

2013-12-09

Simulation Study of CO₂ Injection and Storage in Alberta

Ghaderi, Seyyed Mohammad

Ghaderi, S. M. (2013). Simulation Study of CO₂ Injection and Storage in Alberta (Doctoral thesis, University of Calgary, Calgary, Canada). Retrieved from <https://prism.ucalgary.ca>. doi:10.11575/PRISM/27787
<http://hdl.handle.net/11023/1183>

Downloaded from PRISM Repository, University of Calgary

UNIVERSITY OF CALGARY

Simulation Study of CO₂ Injection and Storage in Alberta

by

Seyyed Mohammad Ghaderi

A THESIS
SUBMITTED TO THE FACULTY OF GRADUATE STUDIES
IN PARTIAL FULFILLMENT OF THE REQUIREMENTS FOR THE
DEGREE OF DOCTOR OF PHILOSOPHY

DEPARTMENT OF CHEMICAL AND PETROLEUM ENGINEERING

CALGARY, ALBERTA

DECEMBER 2013

© Seyyed Mohammad Ghaderi 2013

Abstract

The feasibility of underground injection and storage of CO₂ is associated with many technical and economic challenges. Careful engineering design, economic evaluation, and risk assessment are essential steps towards successful implementation of such complex projects. To address some of these issues, reservoir simulations were conducted on different prototypes with properties relevant to potential storage sites in Alberta. The study covers important aspects of injection into two major types of geological formations: saline aquifers and hydrocarbon reservoirs.

In the case of CO₂ storage into saline aquifers, the two important studied phenomena were (i) the fate of dissolved H₂S in a sour aquifer and (ii) the feasibility of injecting large volumes of CO₂ into a very large aquifer.

In the case of CO₂ storage in hydrocarbon reservoirs, the feasibility of CO₂ EOR/storage in the tight portion of Pembina Cardium field was studied. Various design parameters and operating conditions can affect the performance of a WAG flood. The parameters considered here are those related to development pattern, hydraulic fracture geometry, WAG parameters and the timing of the switch between different schemes. CO₂ EOR performance was assessed based on the oil recovery factor and the amount of stored CO₂. However, to reflect the effect of time, the net present value of the projects was also considered. The effect of all parameters on objective functions was investigated using a compositional simulator. Design of experiment was then utilized to perform a

comprehensive statistical analysis to recognize the most prominent factors in fulfillment of each objective function. Response surfaces were generated to quantify the effect of the factors on the objective functions. Optimization was carried out to find those sets of factors, which provided the highest recovery, storage, and NPV.

To reduce the uncertainty related to CO₂-EOR projects, comprehensive economic studies are required to minimize the risk of failure under different market. Therefore, a rigorous workflow was provided for the industry to evaluate CO₂ EOR and storage in tight oil reservoirs. Based on this workflow, it would be possible to quantify the amount of incentives required to make the coupled CO₂ EOR and storage economically attractive.

Acknowledgements

It would not have been possible to write this doctoral thesis without the help and support of the kind people around me, to only some of whom it is possible to give particular mention here.

Above all, I would like to thank my parents for their support and great patience throughout years of my graduate studies abroad. My family members have given me their unequivocal support throughout, as always, for which my mere expression of thanks likewise does not suffice.

This thesis would not have been possible without the help, guidance and patience of my supervisor, Professor Chris Clarkson. His supportive experience, encouragement and collaboration during the project promoted the work results and directed the research in a fruitful approach. I have learnt much from him about the value of patient and determined action. I am sincerely grateful for his help.

I would also like to thank my initial supervisors, Professor David Keith (now with Harvard University) and Dr. Yuri Leonenko (now with University of Waterloo), who helped steer me towards the subject of study. Likewise, unconditional assistance and guidance from Dr. Hassanzadeh and Dr. Pooladi-Darvish, is greatly appreciated. The blend of encouragement, constructive criticism and direction from all mentioned fellows have been invaluable.

Furthermore, I would also like to acknowledge with much appreciation the crucial

role of the management staff of Penn West Exploration, who gave the permission to use some required data and the necessary materials to complete the task.

A very special thanks goes out to my great companion and wife, Sara Ghandehari, who has been a constant source of motivation and moral support since the first occasion of our acquaintance.

Finally, but importantly, I would like to extend my gratefulness to all my friends who created a warm and friendly environment during my study at the University of Calgary. Specially, I would acknowledge the support from Saeed Taheri, Hamed Tabatabaei, Moslem Hossein Nejad, Mohammad Reza Rahmanian Shahri, Hossein Norouzieh, Mohammad Kariznovy, Mousa Rabiei, Saeed Shad, Amir Ahmad Shirazimanesh, Hashem Salari, Hamid Behmanesh, Danial Kaviani, Amir Shamsa, Farhad Ghanbari, Mervyn Dacosta, Nand Khatri, Petro Babak, and Curtis Fong.

Dedication

*To my divine parents and beloved wife, Sara
for their love, endless support
and encouragements.*

Table of Contents

Abstract	ii
Acknowledgements	iv
Dedication	vi
Table of Contents	vii
List of Tables	x
List of Figures and Illustrations	xii
List of Symbols, Abbreviations, Nomenclatures	xviii
Chapter 1	1
References	6
Chapter 2	8
2-1- Introduction	9
2-2- Model.....	11
2-2-1- Fluid Representation in CMG-GEM	11
2-2-2- Main Features of Simulation Models	14
2-3- Results and Discussion	18
2-3-1- Preliminary Simulation Results	18
2-3-2- Base Case Simulation Results and Observations.....	20
2-4- Sensitivity Analysis	26
2-4-1- Effect of Gas Mobility.....	26
2-4-2- Effect of Gas Injection Rate	27
2-4-3- Effect of Brine Salinity.....	27
2-4-4- Effect of Initial Mole Fraction of Dissolved H ₂ S in Brine	28
2-5- Injection of Acid Gas into Sour Aquifers	32
2-6- Summary	35
Acknowledgments.....	37
References.....	37
Chapter 3	42
3-1- Introduction	43
3-2- Preliminary Conceptual Modeling.....	46

3-3- Detailed Modeling with Full Aquifer Extent.....	48
3-3-1- Dependency of Plume Size and Pressure Field on the Number of Injectors	49
3-3-2- Sensitivity Study of Injection Capacity	52
3-3-3- Some Options to Increase Capacity (Horizontal Injection, Fracturing)	53
3-3-4- Heterogeneity Sensitivity Study	56
3-4- Long-term Fate of CO ₂ Injection.....	62
3-4-1- Pressure Field Evolution during and after Injection	62
3-4-2- Effect of Aquifer Dip on Plume Movement and its Size	64
3-4-3- Estimation of Onset of Convection for Free Phase CO ₂	65
3-4-4- H ₂ S Issue	67
3-5- Summary	67
Acknowledgments.....	68
References.....	69
Chapter 4	71
4-1- Introduction	72
4-2- Base Properties Used in Simulation Models	73
4-3- Modeling Strategy	83
4-4- Simulation Response and Variables	84
4-5- Results and Discussion	88
4-6- Summary	103
Acknowledgements	104
References	104
Appendix 4-A: Sensitivity of Simulation Results to Grid Size.....	107
Chapter 5	110
5-1- Introduction	111
5-2- Base Case Data and Simulation Model	113
5-2-1- Fluid properties and EOS model	113
5-2-2- Reservoir Model and Rock Properties.....	116
5-3- Continuous CO ₂ injection and WAG (with CO ₂) injection	126
5-4- Results and Discussion	128
5-5- Summary	135
Acknowledgment	136
References	136
Chapter 6	139
6-1- Introduction	140
6-2- Properties of Simulation Model.....	142
6-2-1- Fluid Properties and EOS Model.....	142
6-2-2- Reservoir Model and Rock Properties.....	147
6-3- Sensitivity Analysis and Simulation Models.....	153
6-4- Simulation Results and Discussion.....	171
6-5- Summary	182
Acknowledgment	184
References	184
Chapter 7	189
7-1- Introduction	190
7-2- Effect of Reservoir Properties on the Flood Performance.....	193
7-3- Economic Elements in CO ₂ EOR/Storage	205
7-4- Economics of CO ₂ -EOR in Tight Reservoirs	213

7-5- Simulation Models and Assumptions	214
7-6- Economic Model	222
7-7- Results of Economic Sensitivity Analysis.....	223
7-8- Summary	238
Acknowledgement.....	239
References	240
Chapter 8	245
8-1- CO ₂ Injection into Aquifers.....	245
8-2- CO ₂ Injection into Low Permeability Hydrocarbon Reservoirs	247
8-3- Recommendations and Future Work	250
Appendix A: Copyright Permissions.....	252

List of Tables

Table 2-1: Parameters used in equation (2-1) to calculate Henry’s constants for CO ₂ and H ₂ S at different pressures.....	12
Table 2-2: Properties of aquifer and fluids and injection details for the Base Case simulation.....	16
Table 3-1: Properties of the aquifer and water used in WASP study (Hitchon, 1996).....	45
Table 4-1: General properties of the simulation models.....	74
Table 4-2: Fluid properties used in the simulations.....	75
Table 4-3: Factors considered for simulation runs	85
Table 4-4: Simulation runs chosen based on the “D-optimal” design	88
Table 5-1: Reservoir fluid properties	114
Table 5-2: Composition of the fluid (after regression)	115
Table 5-3: Reservoir input for the base case.....	118
Table 5-4: Description of wells and hydraulic fractures.....	121
Table 5-5: Specifications of different tertiary injection scenarios considered in this study	128
Table 6-1: Reservoir fluids properties	143
Table 6-2: Composition of the fluid (after regression)	147
Table 6-3: General properties of the geo-model	150
Table 6-4: Rock properties of different layers	150
Table 6-5: J-function input parameters	153
Table 6-6: Different factors and the associated levels for sensitivity runs	159
Table 6-7: Sensitivity factors and the response values for some of the selected runs	161
Table 6-8: Input parameters for NPV calculations	167
Table 6-9: The optimal values of factors for different responses	182
Table 7-1: Factors and levels for studying the effect of reservoir heterogeneity	197

Table 7-2: Common inputs of simulation models.....	198
Table 7-3: Sensitivity factors and different response values for 16 simulation runs for primary and water-flood scenarios.....	199
Table 7-4: Sensitivity factors and different response values for 16 simulation runs for CO ₂ -WAG scenarios.....	200
Table 7-5: CO ₂ concentration (volume percentage) in the flue gas of power plants with different technologies (from Davison et al. 2001).....	207
Table 7-6: Reservoir properties of the base geo-model used in economic study	216
Table 7-7: Uncertain economic factors for economic evaluation of PR-WF-CO ₂ flood	224
Table 7-8: Table of runs for sensitivity analysis based on the 13 economic factors for scenarios 1&2 (coded factors)	226
Table 7-9: Results of economic evaluation of different recovery schemes for considered reservoir models.....	228
Table 7-10: Uncertain economic factors for economic evaluation of the CO ₂ flood projects.....	234
Table 7-11: Results of economic evaluation of CO ₂ -EOR projects using different incentive schemes	236

List of Figures and Illustrations

- Figure 2-1: Comparison between SUPERTRAPP and CMG predictions for H₂S-CO₂ binary mixtures at 141.8 °F and 1,958 psi for Z factor (a) and mass density (b) as a function of mole fraction of hydrogen sulfide. 13
- Figure 2-2: (a) P-T diagram of H₂S-CO₂ mixtures at four different compositions. The pressure and temperature of the reservoir has also been indicated; (b) Viscosity of H₂S-CO₂ mixtures at reservoir condition (141.8 °F and 1,958 psi) as predicted by SUPERTRAPP which shows the small variation of viscosity between pure CO₂ and a mixture consisting of 0.6 H₂S by mole fraction..... 15
- Figure 2-3: Water-gas relative permeability curves..... 16
- Figure 2-4: Simulation results: (a) gas saturation profile after 100 days; (b) CO₂ mole fraction in the gas phase after 100 days; (c) variation of H₂S mole fraction in the gas phase after 10 days; (d) variation of H₂S mole fraction in the gas phase after 100 days. 20
- Figure 2-5: Development of two sub-regions within the area swept by the CO₂ plume after 100 days of simulation. The solid curve shows the variation of gas saturation versus distance (residual brine saturation is equal to 0.1); the long dashed curve shows the CO₂ mole fraction distribution in the gas phase; the short dashed curve shows the H₂S mole fraction distribution in the gas phase. 23
- Figure 2-6: Variation in the composition of the aqueous phase versus distance in the region swept by the plume after 100 days. The “○” and “□” symbols indicate the equilibrated mole fraction of H₂S and CO₂, respectively, in the aqueous phase in the last block invaded by the gas plume..... 23
- Figure 2-7: Mole fraction of H₂S in the gas plume at different times. Maximum observed H₂S mole fraction (dotted line at different times) is about 0.54. Increase in the width of the second region is determined by measuring the characteristic full width at half maximum (FWHM or “δ”). 24
- Figure 2-8: Moles of H₂S released to the gas phase per unit length versus distance from the injection well after 100 days. The area underneath the curve represents the total amount of H₂S released to the gas phase. 26
- Figure 2-9: Effect of different parameters on the distribution of different phases and components within the aquifer after 100 days; (a) increased gas mobility; (b) increased gas injection rate; (c) comparison of plume extension for two cases with different salinity; (d) use of fresh water instead of saline brine; (e) decreased initial mole fraction of dissolved H₂S to one-fourth of the Base Case value; (f) decreased initial mole fraction

of dissolved H ₂ S to one-eighth of the Base Case value.	31
Figure 2-10: Comparison between phase and component distribution for acid gas injection in two cases; (a, b) the brine is initially saturated with H ₂ S (where, similar to what was displayed in Figure 6, the “○” and “□” symbols indicate the equilibrated mole fraction of H ₂ S and CO ₂ , respectively, in the aqueous phase in the last block invaded by the gas plume); (c, d) the brine is initially free of any dissolved H ₂ S.	34
Figure 3-1: Location of the major CO ₂ emission sources in Alberta and the location of the Wabamun Lake study (redrafted from Karsten et al., 2007).	44
Figure 3-2: Nisku relative permeability curves for gas and water.	46
Figure 3-3: Configuration of injection wells and element of symmetry (cream color area).	47
Figure 3-4: Top view of the Nisku formation in the Wabamun Lake area (study area is outlined by red).	49
Figure 3-5: (a–d) Saturation and (e–h) pressure distribution after 50 years of injection for different numbers of wells in the Nisku study area (wells within the red area in Figure 3-4).	51
Figure 3-6: Pressure buildup and drawdown during CO ₂ injection and after stopping injection for (a) one injector (b) 10 injectors.	52
Figure 3-7: Variation of Nisku capacity with respect to number of wells and formation properties (solid line represents base properties).	53
Figure 3-8: Pressure distribution at the end of injection.	54
Figure 3-9: Comparison of the effect of different well configurations and stimulation on the storage capacity of the model.	55
Figure 3-10: Geo-statistical realizations for porosity and permeability of WASP study area (from Eisinger and Jensen, 2010).	57
Figure 3-11: Object-based realization for porosity.	58
Figure 3-12: (a) Saturation and (b) pressure fields for stochastic-based geomodels after 50 years of injection.	58
Figure 3-13: Injection capacity for 5 different realizations.	59
Figure 3-14: Injection capacity for two different fracture pressures.	60
Figure 3-15: (a) Saturation and (b) pressure fields for object modeling after 50 years of injection.	61
Figure 3-16: Injection capacity for object modeling.	61
Figure 3-17: Pressure build-up (top row) during injection and pressure fall-off (bottom row) after injection stops for an injection scenario with 10 wells each injecting at 0.5	

Mt/year for 50 years.....	63
Figure 3-18: ΔP ($P-P_i$) versus time	64
Figure 3-19: Saturation field for a single injector: (a) base properties; (b) permeability is increased to 150 mD.	65
Figure 3-20: (a) Accumulation of free CO ₂ below the caprock (short-term) and (b) combination of diffusion and natural convection (long-term processes) involved in geological storage of CO ₂ in saline aquifers. (Source of figure: Hassanzadeh et al., 2007)	66
Figure 4-1: Comparison between experimental and simulated PVT behavior of the fluid used in this study (a) oil formation volume factor vs. pressure (b) oil solution gas vs. pressure (c) oil viscosity vs. pressure (d) gas viscosity vs. pressure.	77
Figure 4-2: (a) a close-up view of the simulation model showing the hydraulic fracture planes crossing the well lateral (b) historical oil production data for the subject well (c-d) comparison of gas and water production data from well history and simulation, respectively (e-f) two-phase relative permeability of water-oil and gas-oil obtained from history matching of production data, respectively.....	83
Figure 4-3: Half-normal probability plot of observed effect of factors and their interactions on (a) short-term recovery factors and (b) long-term recovery factor for reservoir model with absolute permeability equal to 0.28 mD.....	91
Figure 4-4: Effect interaction plot between different factors (a) AD, no interaction case (b) AB (c) AF (d) BF.	95
Figure 4-5: (a-b) gas saturation in two models with (a) C=2 and (b) C=3 one year after start of production; (c-d) field oil production rates and the oil recovery factors for the models. Other parameters are as follows: A=6; B=3,000 ft; D=225 ft; E=750 md-ft; F=300 psia.	98
Figure 4-6: Field oil production rates (a) and the oil recovery factors (b) for the models with different levels of E factor; other parameters are as follows: A=4; B=4,500 ft; C=2; D=325 ft; F= 300 psia; G=1.....	99
Figure 4-7: Difference in (a) field oil production rates and (b) the oil recovery factors for the models with different levels of G factor (graph results = “open-hole” results - “cased-hole” results); other parameters are as follows: A=6; B=3000 ft; C=3; D=325 ft;	101
Figure 4-8: Half-normal probability plot of observed effect of factors and their interactions on (a) short-term recovery factors and (b) long-term recovery factor for reservoir model with absolute permeability equal to 0.028 mD.....	102
Figure 4A-1: Grid convergence behavior for parent blocks in x and y directions	108
Figure 4A-2: Grid convergence behavior for number of grid used in construction of local grid refinement representing hydraulic fractures.....	109
Figure 5-1: Comparison of the predicted (PR EOS and LBC correlation) and observed	

values for (a) liquid mixture swelling factor and (b) liquid viscosity with respect to CO ₂ mole percentage in the mixture.....	116
Figure 5-2: (a) Top view (i-j plane) of the model showing the spatial horizontal absolute permeability variation (b) Side view (j-k plane) of the reservoir vertical permeability (c) histogram of the horizontal absolute permeability data.....	117
Figure 5-3: (a) Display of the refined grids which create the hydraulic fracture boundaries and (b) refined grid with higher permeability representing the hydraulic fracture plane.....	120
Figure 5-4: Relative permeability data set used in the primary and water injection scenarios (a) oil-water (b) oil-gas relative permeability.....	122
Figure 5-5: (a) Field oil production rate (b) Recovery factory curve (c) Average reservoir pressure (d) Average reservoir gas saturation at the end of the primary (5 years) and subsequent water-flooding stages.....	124
Figure 5-6: Oil saturation profile at the end of water-flooding stage for (a) top layer and (b) bottom layer of reservoir.....	125
Figure 5-7: Variation of (a) oil recovery factor (b) average reservoir pressure with respect to the HCVP of injected CO ₂ for different injection schemes.....	130
Figure 5-8: Variation of oil saturation at the end of injection scheme (a) continuous CO ₂ injection, top layer (b) continuous CO ₂ injection, bottom layer (c) WAG injection with ratio 2, top layer (d) WAG injection with ratio 2, bottom layer.....	131
Figure 5-9: (a-c) Comparison of different parameters for two WAG process with different cycle length of 9 months and 18 months and identical WAG ratio of 0.5 (d) CO ₂ storage capacity results from different injection scenarios.....	134
Figure 6-1: Comparison of the predicted (PR EOS and Pedersen correlation) and observed values for (a) liquid mixture swelling factor and (b) liquid viscosity with respect to CO ₂ mole percentage in the mixture. (c) comparison of the experimentally measured and sintu.....	146
Figure 6-2: (a) One section of Pembina Cardium reservoir considered as the study area (b) the flattened version of the reservoir model used in reservoir simulations (c) the horizontal permeability map for the top sand layer (Zone 1) (d) the horizontal permeability of the lower shaly-sand layer (Zone 4).....	149
Figure 6-3: Two sets of two-phase relative permeability used for sand (rock type 1) and shaly-sand (rock type 2) rock types (a) two phase oil-water relative permeability (b) two phase oil-gas relative permeability.....	152
Figure 6-4: (a) Oil production rate and (b) oil recovery factors associated with three sequential recovery schemes; primary, water-flood and finally WAG process. Upon WAG completion, the final water-flood injection occurs.....	154
Figure 6-5: The two well patterns used in the simulation models (a) D1 which is comprised of five wells (b) D2 which is comprised of seven wells. The red arrows in both	

figures show the injection wells.....	156
Figure 6-6: Comparison of (a) the recovery factor and (b) the stored CO ₂ volumes of different runs over time.....	167
Figure 6-7: Cross-section view of spatial distribution of different phases in Run 67 (a) oil saturation and (b) water saturation distribution at the end of the water-flood scenario and the beginning of the WAG scheme; (c) oil saturation at the end of the WAG process (d) oil saturation at the conclusion of the project (e) CO ₂ saturation at the end of the WAG process (f) CO ₂ saturation at the conclusion of the project.	171
Figure 6-8: Half-normal probability plots showing the effect of parameters, and their ranking, on (a) oil recovery factor (b) incremental oil recovery factor (c) stored CO ₂ volumes and (d) net present value (NPV) of the projects.....	174
Figure 6-9: (a, b) contour plot and surface response for the incremental oil recovery (c, d) contour plot and surface response for stored CO ₂ volume with respect to fracture half-length and fracture spacing. The other related parameters are A=D1; B=Open-hole; E=1600 psi; F=0.5; G=0.5; H=1.0. (e, f) Variation of NPV with respect to “well pattern” and “well completion” where C=200 ft (e) and C=300 ft(f); D=200 ft; E=1300 psi; F=0.5; G=0.5; H=1.0.	181
Figure 7-1: Prototype of the model with reservoir properties for (a) “Run 1” in (b) “Run 2” in Table 7-3.	196
Figure 7-2: Example response surfaces exhibiting (a) the recovery of water flood (b) the amount of stored CO ₂ as a function of some selected factors. The values of other factors have been indicated in the legend.	202
Figure 7-3: Pareto chart showing the rank of effective parameters on (a) duration of water-flood (b) recovery of water-flood scheme (c) recovery of CO ₂ -WAG scheme and (d) net storage of CO ₂ during WAG process.	204
Figure 7-4: Location of main large CO ₂ emitters in central Alberta (redrafted from Karsten and Bachu, 2007).....	206
Figure 7-5: Flue gas flow rate from power plants using different technologies (redrafted from Nguyen and Allinson, 2002).	207
Figure 7-6: Available technical approaches for CO ₂ separation and capture (derived from Rao and Rubin, 2002).	208
Figure 7-7: (a, b) Variation of capital and “O&M” cost with pipeline specifications (c) minimum required pipeline versus the transportation length for maintaining supercritical state of CO ₂ (d) overall cost of CO ₂ removal from power stations (redrafted from NETL 2010).	212
Figure 7-8: 3D view of the reservoir used in economic evaluation of the CO ₂ -EOR project (a) with base permeability properties and (b) with induced thief zone. Top view of the reservoir with five horizontal wells stimulated with (c) longitudinal (d) transverse fractures in configuration 1 and (e) longitudinal (f) transverse fractures in configuration	

2.....	219
Figure 7-9: Variation in different parameters during continuous CO ₂ injection with adjusted BHP of producers and injection rates of injectors for the “without thief-zone” model with 7 wells (3 injectors and 4 producers) and transverse fractures.....	221
Figure 7-10: Response surfaces of NPV with respect to (a) oil price and discount rate for a primary-waterflood scenario (b) oil price and CO ₂ cost for a primary-waterflood-CO ₂ flood scenario. Other factors are at their mean value.	229
Figure 7-11: (a) probability density function and the best fit function (in red) for NPV (b) cumulative distribution function of NPV (c) Tornado graph of important economic factors of NPV for a primary-waterflood-continuous CO ₂ injection scenario.	232
Figure 7-12: Tornado graph of important economic factors affecting NPV for CO ₂ injection projects.....	237

List of Symbols, Abbreviations, Nomenclatures

Symbol	Definition
Δ_f	Equivalent fracture width in the simulation model
B_o	Oil formation volume factor
D	Diffusion coefficient
D_x	Size of simulation model's grids in the x direction
D_y	Size of simulation model's grids in the y direction
D_z	Size of simulation model's grids in the z direction
F_{cd}	Dimensionless fracture conductivity
H^0	Reference Henry's constant at reference pressure
H_i	Henry's law constant for component i
L_D	Dimensionless well length
N_x	Number of simulation model's grids in the x direction
N_y	Number of simulation model's grids in the y direction
N_z	Number of simulation model's grids in the z direction
P_{avg}	Average reservoir pressure
P_b	Bubble point pressure
P_c	Capillary pressure
P_f	Final reservoir pressure at the end of injection
P_i	Initial pressure
P^0	Reference pressure
P_{wf}	Well flowing pressure
R_s	Solution gas-oil ratio
S_l	Wetting phase saturation
S_{org}	Residual oil saturation in the presence of gas phase
V^*	Partial molar volume
W_f	Fracture width

f_i	Fugacity of component i in gaseous phase
j_e	Entry value of J function
k_h	Horizontal permeability
k_f	Permeability of hydraulic fracture
k'_f	Equivalent permeability of hydraulic fracture in simulation models
k_v	Vertical permeability
$n_{H_2S}^g$	Moles of gaseous H ₂ S
n_r	Number of grids in the radial direction
r_{plume}	Plume radius
r_w	Wellbore radius
s_g	gas saturation
t_{dis}	Time scale of convective dissolution
t_{onset}	Onset time of convection
x_f	Fracture half length
x_i	Mole fraction of component i in aqueous phase
$y_{H_2S}^g$	Mole fraction of H ₂ S in the gas phase
λ_{Dx}	Dimensionless correlation length in horizontal direction
λ_{Dz}	Dimensionless correlation length in vertical direction
ρ_g	Molar density of the gaseous phase
σ_{l-g}	Interfacial tension between gas and liquid
σ_{o-w}	Interfacial tension between oil and water
ΔP_{max}	Maximum pressure deviation from the original pressure
BIC	Binary interaction coefficient
EOS	Equation of state
°F	Degree Fahrenheit
h	Thickness
D	Molecular diffusion coefficient
GOR	Gas oil ratio
Gt	Gigatonnes
$HCPV$	Hydrocarbon pore volume
HF	Hydraulic fracture
Krg	Relative permeability to gas

K_{ro}	Relative permeability to oil
K_{rw}	Relative permeability to water
LHF	Longitudinal hydraulic fracture
MMP	Minimum miscibility pressure
MW	Molecular weight
Mt	Megatonnes
NPV	Net present value
$O\&M$	Operation and maintenance
$OOIP$	Original oil in place
P	Pressure
R	Universal gas constant
Ra	Rayleigh number
SG	Specific gravity
T	Temperature
THF	Transverse hydraulic fracture
Vdp	Dykstra-Parsons coefficient
WAG	Water alternative gas
e	Euler's number (~ 2.7)
g	Acceleration due to gravity
j	Dimensionless Leverett J function
k	Permeability
n	Pore size distribution index
r	Radius
t	Time
δ	Full width at half maximum
λ	Dimensionless correlation length
μ	Viscosity
σ	Interfacial tension
φ	Porosity

Chapter 1

Introduction

Consumption of fossil fuels has continuously increased the level of carbon dioxide and other heat-trapping “green-house” pollutants in the atmosphere. Measurements of CO₂ from the Mauna Loa observatory show that concentrations have increased from about 313 ppm in 1960 to above 400 ppm in 2013 (Tans and Keeling 2013). Presumably, as a result, the climate temperature has gradually increased and most likely will continue to increase over this century. Simulation of climate change indicates that the planet’s temperature could be between 2 to 9.7 °F higher than its current value in 2100 (Herring 2012). The exact value of temperature increase will depend heavily on the energy choices and courses of action we make now and in subsequent decades.

Several options have been suggested to reduce the CO₂ concentration in the atmosphere. Improving the efficiency of energy utilization systems, replacing fossil energy with low CO₂ emitting systems like renewable energy, and capturing/storing CO₂ from fossil fuel combustion are some of these methods. Among the aforementioned methods, underground storage/geological storage of CO₂ is currently the most promising short to medium-term option for reducing the net carbon emissions to the atmosphere

(Bachu and Shaw 2003).

With respect to Alberta, a major North American energy supplier, the annual rate of CO₂ emissions reached 236 Mt in 2010, which was the highest in Canada (Environment Canada 2012). While this level of emissions should be reduced, the sustainability of economic growth should be assured as well (Bachu and Shaw 2003). For Alberta, being a landlocked province, underground storage of CO₂ is the best and probably the only option available for mitigating large emissions rates (Bachu 2003).

Unmineable coal seams, deep saline aquifers, and (depleted) oil and gas reservoirs are usually considered as the most applicable CO₂ storage formations (Bachu 2003). Although there has been significant development of CBM in Alberta in the past 10 years, primarily in the Horseshoe Canyon coals (Bastin et al 2005), coal-seams are not optimal storage targets because there are multiple thin coal seams at a relatively shallow depth. Saline aquifers offer the largest potential for long-term storage, however, the regulatory framework of their application is not clear and the economic/commercial feasibility of aquifer storage is under question (McCoy and Rubin 2009). More importantly, the practicability of injecting large volumes of CO₂ to use up all of this capacity is not clear. The Alberta Geological Survey has identified the Nisku aquifer in the Wabamun Lake area as an attractive potential storage site. This aquifer has been identified due to its large extent and proximity to CO₂ emitters including four coal-fired power plants with emission rates between 3 to 6 Mt/year/plant. As a sour saline aquifer, the fate of dissolved H₂S during CO₂ injection and the technical feasibility of accommodating the total emitted volume of CO₂ from these sources should be evaluated.

The third option, CO₂ storage through enhanced oil and gas recovery (EOR and

EGR), can be quite attractive (Bachu 2003; Gaspar et al. 2005; Ghomian 2008; Singhal 2009; McCoy and Rubin 2009; Jahangiri and Zhang 2011). Over decades of practice, industry has gained enough experience around CO₂ injection operations. When becoming miscible with the in-situ fluids, CO₂ can considerably improve the declining production rates. Because of the integrity of sealing cap-rocks in hydrocarbon reservoirs, secure storage of injected CO₂ can be achieved. Most importantly, the revenue generated from incremental production can partially (if not completely) offset the operating costs of the project.

Based on the performance of Joffre Viking and Weyburn projects in Western Canadian Sedimentary Basin (WCSB), there is good awareness of potential reserve additions by CO₂ flooding which can be applied to other analogous reservoirs. Specifically, with recent increased activity in the exploitation of tight reservoirs with high decline rates, the industry has realized the need for deploying secondary and tertiary recovery schemes. With current high oil prices that may continue for the foreseeable future, CO₂-EOR may become attractive and feasible. CO₂ injection can provide not only an excellent opportunity for improved oil recovery, but also a chance to sequester CO₂ to reduce the environmental footprint. However, restricted flow capacity of low permeability (tight) oil formations imposes unique challenges to the implementation of CO₂-WAG processes in such reservoirs. Application of horizontal wells that have been hydraulically-fractured in multiple stages can substantially improve the injection and production rates. However, there are various design parameters and operating conditions, which can affect the performance of a WAG flood. Parameters such as the development pattern (well spacing and well completion strategy), hydraulic fracture geometry (half-

length and spacing), WAG parameters (WAG ratio and CO₂ slug size) and the timing of the shifts from primary or water-flood to WAG schemes are among the most important considerations.

In this study, CO₂-EOR performance is assessed based on oil recovery factor and as well as the amount of stored CO₂. In other words, the objective is to achieve both goals of enhanced oil recovery and storage of CO₂ in tight oil formations. However, to reflect the effect of time, net present value (NPV) of the projects was also considered. All three of these factors (oil recovery, stored CO₂ quantity, NPV) were therefore included in objective functions to be optimized.

A compositional simulator was used to test various design parameters to understand the effect on these objective functions. A Design of Experiment (DOE) approach was utilized to perform a comprehensive statistical analysis, allowing recognition of the most prominent factors affecting each objective function in a tight oil reservoir (with properties similar to the Pembina Cardium field). Response surfaces were generated to quantify the effect of the factors on the objective functions. Optimization was carried out to find those sets of factors that provided the highest recovery, storage, and NPV.

NPV and profitability of CO₂-EOR processes rely heavily on market conditions and therefore require separate and special attention. The primary obstacle to widespread usage of CO₂-EOR in Alberta is the lack of supply and transportation infrastructure (Singhal 2009). If CO₂ is intended to be supplied by capture from an anthropogenic source (power plants), which is the most likely source of CO₂ in Alberta, CO₂ prices become high and CO₂-EOR projects are not attractive/cost competitive. Therefore, to make these projects economic and compare favorably with other investment opportunities

for business decision-makers, incentives should be implemented in some form by the government. The last part of this study was devoted to exploration of the viability of CO₂-EOR/storage in a typical West Central Alberta tight reservoir, capturing the uncertainty of economic parameters.

In summary, this study examines the important aspects of CO₂ injection into two subsurface targets in Alberta, namely saline aquifers and hydrocarbon reservoirs (with emphasis on tight reservoirs).

This dissertation is divided into eight chapters, and in each chapter (except Chapters 1 and 4), one aspect of underground CO₂ storage into porous media is investigated. Chapter 2 includes an extensive study of the effect of CO₂ storage in a sour saline aquifer (containing dissolved H₂S).

In Chapter 3, the feasibility of injecting large volumes of CO₂ in the Wabamun Area, using numerical simulation, was investigated.

Because large-scale exploitation of tight reservoirs (low permeability reservoirs) with multi-stage fractured horizontal wells (MFHW) is relatively new to Alberta, with most MFHWs under primary production, Chapter 4 is devoted to the examination of primary recovery optimization in such reservoirs.

In Chapter 5, the recovery performance of the CO₂ WAG floods in tight formations is analyzed. The effect of WAG properties (WAG cycle length and WAG ratio) is examined using a symmetric geo-model.

The results of a detailed sensitivity study examining the effect of different operational and design parameters on the performance of CO₂ injection in low permeability portions of the Pembina Cardium field are provided in Chapter 6. The

results of optimization using three different objective functions (maximizing oil recovery, maximizing CO₂ stored mass, and maximizing net present value of the projects) are discussed.

Chapter 7 consists of two different parts. First, the effect of different levels of reservoir heterogeneity on the performance of water-flood and CO₂ flood in tight formations is investigated. Second, the key elements required in the economic assessment of CO₂ floods in Alberta are reviewed, and the proposed economic model used in this study is discussed. Comments on the economic sensitivity and uncertainty are included.

In Chapter 8, the summary and conclusions of the research are provided. The dissertation is concluded with recommendations for future work.

References

- Bachu, S., 2003. Screening and Ranking of Sedimentary Basins for Sequestration of CO₂ in Geological Media in Response to Climate Change. *Environmental Geology*, vol. 44, no. 3, pp. 277-289.
- Bachu, S., and Shaw, J., 2003. Evaluation of the CO₂ Sequestration Capacity in Alberta's Oil and Gas Reservoirs at Depletion and the Effect of Underlying Aquifers. *Journal of Canadian Petroleum Technology*, vol. 42, no. 9, pp. 51-61.
- Bastian, P.A., Wirth, O.F.R., Wang, L., and Voneiff, G.W., 2005. Assessment and Development of the Dry Horseshoe Canyon CBM Play in Canada. Paper SPE 96899 presented at SPE annual technical conference and exhibition in Dallas, Texas, 9-12 October.
- Environment Canada, 2012. Canada's Emission Trends 2012.
- Gaspar, A.T., Suslick, S., Ferreira, D., and Lima, G., 2005. Economic Evaluation

of Oil-Production Project with EOR: CO₂ Sequestration in Depleted Oil Field. Paper SPE 94922 presented at SPE Latin American and Caribbean petroleum engineering conference in Rio de Janeiro, Brazil, 20-23 June.

- Ghomian, Y., Urun, M., Pope, G., and Sepehrnoori, K., 2008. Investigation of Economic Incentives for CO₂ Sequestration. Paper SPE 116717 presented at SPE annual technical conference and exhibition in Denver, Colorado, USA, 21-24 September.
- Herring, D., 2012. Climate Watch Magazine >> Global Temperature Projections. NOAA Climate Portal.
- Jahangiri, H.R., and Zhang, D., 2011. Optimization of the Net Present Value of Carbon Dioxide Sequestration and Enhanced Oil Recovery. Paper OTC 21985 presented at offshore technology conference in Houston, Texas, USA, 2-5 May.
- McCoy, S.T., and Rubin, E.S., 2009. The Effect of High Oil Prices on EOR Project Economics. Energy Procedia, vol. 1, no. 1, pp 4143-4150.
- Singhal, A., 2009. CO₂ Flooding Potential in West-Central Alberta: Generalized Business Case of a Medicine River/Gilby Area Mature Waterflooded Reservoir. Journal of Canadian Petroleum Technology, vol. 48, no. 12, pp. 6-10.
- Tans, P., Keeling, R., 2013. <http://www.esrl.noaa.gov/gmd/ccgg/trends/mlo.html>.

Chapter 2

Evolution of Hydrogen Sulfide in Sour Saline Aquifers during Carbon Dioxide Sequestration¹

Many deep saline aquifers suitable for carbon dioxide (CO₂) sequestration contain measurable concentrations of hydrogen sulfide (H₂S). These aquifers are referred to here as *sour saline aquifers* whereas aquifers with unmeasurable concentrations are referred to as *ordinary saline aquifers*. Sour saline aquifers occur wherever anhydrite or other sulfate sources are present in the formation, even in minor quantities. In this paper, compositional modeling of CO₂ injection into such aquifers is studied. When CO₂ is injected into a sour saline aquifer, the H₂S initially dissolved in the brine will be exsolved and released into an expanding CO₂ plume. At any time after the start of CO₂ injection, the region swept by the plume consists of two sub-regions. The first of these is an inner sub-region extending from the injection well which is characterized by the absence of H₂S in both aqueous and gaseous phases. The dissolved H₂S in this inner sub-region is almost completely removed from the brine via an exsolution process. The second sub-region extends from the outer edge of the inner sub-region to the leading edge of the

¹ This chapter is a modified version of: Ghaderi, S.M., Keith, D.W., Lavoie, R., Leonenko, Y., 2011. Evolution of Hydrogen Sulfide in Sour Saline Aquifers during Carbon Dioxide Sequestration. International Journal of Greenhouse Gas Control, vol. 5(2), pp. 347-355.

plume. In this outer sub-region, the mole fraction of H₂S in the gas plume gradually increases toward the leading edge and reaches a peak value. While the gas plume is expanding the size of the outer sub-region enlarges. Following the discussion of these phenomena, in the next part of the paper, injection of acid gases (mixtures of H₂S and CO₂) into sour saline aquifers and ordinary saline aquifers is explored. In contrast to sour aquifers, unsaturated water in an ordinary aquifer will strip away H₂S from the CO₂ stream and consequently the mole fraction of H₂S toward the gas front decreases. The highly toxic nature of H₂S gas (toxicity of H₂S starts at 4 ppm concentration) suggests the need to account for dissolved H₂S in sour saline aquifers when establishing risk assessment, monitoring, and management strategies at CO₂ storage sites.

Keywords: acid gas injection, CO₂ sequestration, compositional simulation, H₂S exsolution, saline aquifer, sour saline aquifer

2-1- Introduction

Carbon dioxide emissions arising from consumption of fossil fuels are probably the main cause of climate change over the coming century (IPCC, 2007). The use of technologies such as carbon dioxide capture and geologic storage (usually known as CCS), if applied efficiently, can reduce net emissions of CO₂ to the atmosphere. To implement geologic storage at a large scale, injection of nearly pure CO₂ and acid gas (CO₂ and H₂S) must occur over a wide range of aquifer and reservoir characteristics and operating conditions (Bachu and Gunter, 2005). For acid gas injection, the composition of the injected gas can vary widely. At the end of 2003, close to 2.5 Mt CO₂ and 2.0 Mt H₂S (in different composition streams) have been injected into deep saline aquifers and depleted reservoirs in Western Canada at average rates that vary between 35 and 17,500 Mscf/day (Bachu

and Gunter, 2005).

Several studies have reported numerical simulation of the CO₂ storage process, which are often designed to investigate more efficient schemes for storing large volumes of gas (e.g., Kumar et al., 2005; Leonenko and Keith, 2008). Moreover, different aspects of acid gas disposal in saline aquifers have been investigated in recent years (e.g., Adams and Bachu, 2002; Carrol, 2002; Bachu and Carrol, 2005; Bennion and Bachu, 2008). Although some studies have assessed the implications of impurities in the injection stream (Ozah et al., 2005; Bachu and Bennion, 2009; Bachu et al., 2009; Battistelli and Marcolini, 2009), there has been little study of the consequences of injecting CO₂ or acid gas into formations that contain pre-existing impurities in the in-situ brine of the target formation.

Some authors have addressed the presence of gases dissolved in saline aquifers where CO₂ sequestration is planned. The Frio brine formation in the U.S. is believed to be nearly saturated with methane (Doughty et al., 2004; Hovoka et al., 2004) and the Nisku brine formation in Canada contains measurable amounts of dissolved H₂S (Hutcheon, 1999). In addition, the occurrence of non-hydrocarbon gases (CO₂, H₂S, He, and N₂) is quite common in strata of all ages in the Alberta Basin which is part of the Western Canada Sedimentary Basin (Hutcheon, 1999). The Rocky Mountains and the Appalachians North America, are regions where CO₂ injection and geological storage on a large scale is most likely to be implemented in Canada and the United States (Bachu and Gunter, 2005). Battistelli and Marcolini (2009) have demonstrated the exsolution of dissolved CH₄ and its accumulation at the edge of the CO₂ plume can occur during a sequestration process.

2-2- Model

2-2-1- Fluid Representation in CMG-GEM

The dissolution and exsolution of gaseous components into and out of the aqueous phase (water or brine) is calculated in the CMG-GEM model using Henry's law (Li and Nghiem, 1986):

$$f_i = x_i H_i \quad (2-1)$$

in which f_i is the fugacity of component i in the gaseous phase, x_i is its mole fraction in the aqueous phase and H_i is the Henry's law constant of the component. Pressure- and temperature-dependence of the Henry's constant for each component (H (psi)) is expressed by:

$$\ln(H) = \ln(H^0) + \frac{V^*(P - P^0)}{RT} \quad (2-2)$$

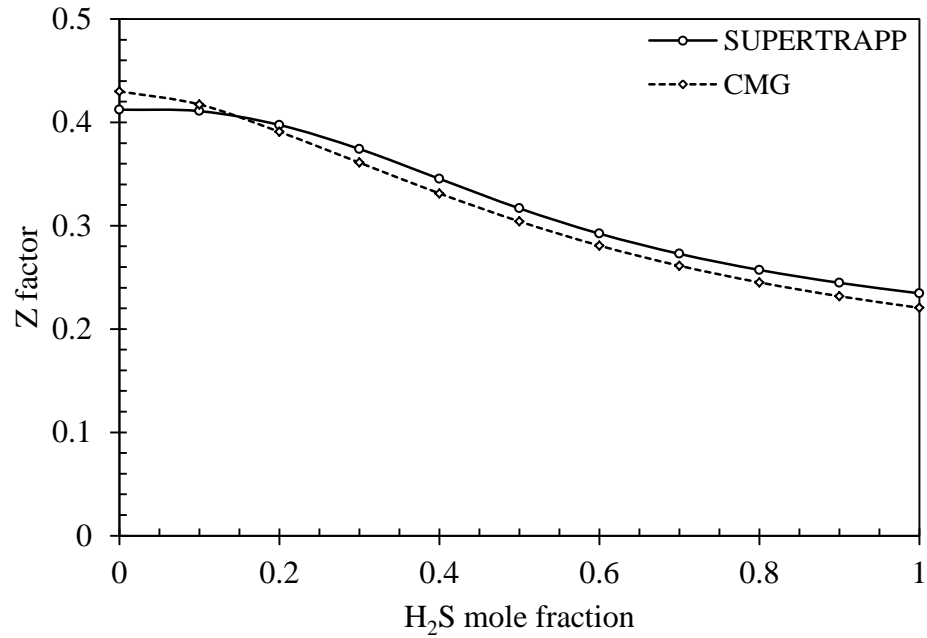
where H^0 (psi) is Henry's constant at the reference pressure P^0 (psi), V^* is the partial molar volume of the component at infinite dilution ($\text{ft}^3/\text{lb-mole}$), P is pressure (psi), T is temperature ($^{\circ}\text{R}$) and R is the universal gas constant ($10.732 \text{ ft}^3 \cdot \text{psi}/^{\circ}\text{R} \cdot \text{lb-mole}$). The greater the value of Henry's constant for a given component, the less soluble it is in the aqueous phase. Table 2-1 shows the set of parameters required for calculating the Henry's constants for CO_2 and H_2S at different pressures and at a constant temperature equal to $141.8 \text{ }^{\circ}\text{F}$ and two different aqueous phase salinities: a brine with zero salinity (fresh water), and a saline brine with salinity equivalent to 7.42 lb of NaCl per cubic foot of solution. The values provided in this table have been verified against experimental data (see Pooladi-Darvish et al. (2009) and Bachu et al. (2009) for more details). The Henry's constants clearly show that solubility of these gaseous components decrease with an

increase in salinity of the formation brine. The Peng-Robinson Equation of State (1976) is used along with Equation (2-2) to model the fugacity of components required in Henry's law. At an initial pressure (1,958 psi), temperature (141.8 °F), and salinity (7.42 lb/ft³), the utilized fluid model in GEM demonstrates that it is possible to dissolve 0.02 H₂S by mole fraction into the brine which is equivalent to a 1.14 molal solution.

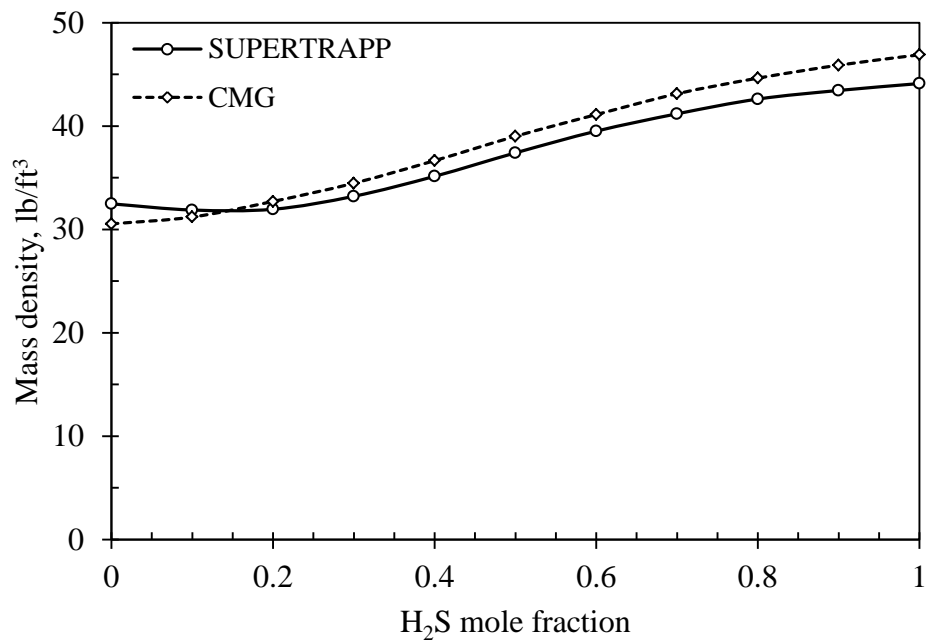
Table 2-1: Parameters used in equation (2-1) to calculate Henry's constants for CO₂ and H₂S at different pressures.

Component	Parameters in Eq. (2-1)	Fresh water	Saline brine
CO ₂	H ⁰ , psi	4.65E+4	6.53 E+4
	V*, ft ³ /lb-mole	5.69E-1	5.64E-1
	P ⁰ , psia	14.7	14.7
H ₂ S	H ⁰ , psi	1.85E+4	2.32E+4
	V*, ft ³ /lb-mole	5.76E-1	5.71E-1
	P ⁰ , psia	14.7	14.7

Figure 2-1-a and Figure 2-1-b show the calculated Z factor and mass density, respectively, at fixed pressure and temperature for binary mixtures of H₂S-CO₂ as functions of H₂S mole fraction. In these figures, the CMG predictions are also compared to calculations performed using the computer program SUPERTRAPP (NIST, 2007) and show acceptable accuracy and consistency. These figures illustrate the smooth change in properties of the CO₂-H₂S binary mixtures as the mole fraction of H₂S increases. Therefore, at pressures greater than the critical pressure (which is the case in the present simulations), of all possible binary mixtures of H₂S and CO₂, using a single phase approach for these mixtures of varying composition is valid. In this study, this single phase is referred to either as a gas phase or more generally a non-aqueous phase.



(a)



(b)

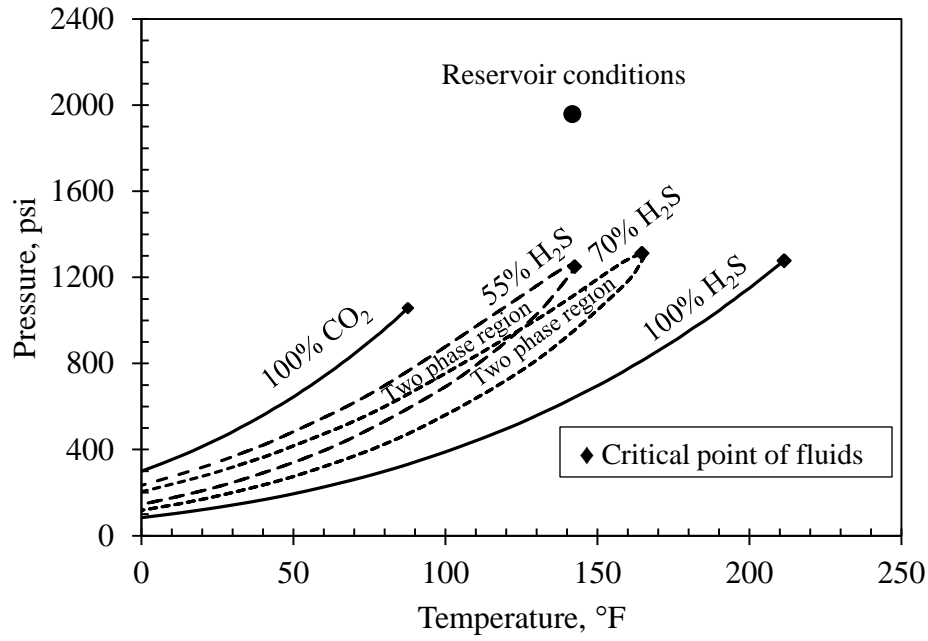
Figure 2-1: Comparison between SUPERTRAPP and CMG predictions for H₂S-CO₂ binary mixtures at 141.8 °F and 1,958 psi for Z factor (a) and mass density (b) as a function of mole fraction of hydrogen sulfide.

CMG predictions for P-T diagrams of this binary system have been displayed in Figure 2-2-a. This figure also shows the initial pressure and temperature of the aquifer. Since the variation in the viscosity of the CO₂-H₂S mixtures in the composition range applicable for this study was not considerable (Figure 2-2-b), the viscosity of the non-aqueous phase mixtures was set to a constant value equal of 0.05 cp. Using this average value in comparison with the highest and lowest values gives rise to only a 5% error in estimating plume extension. Viscosity of the brine was calculated according to Bachu and Carroll (2005) and for fresh water that same viscosity was used.

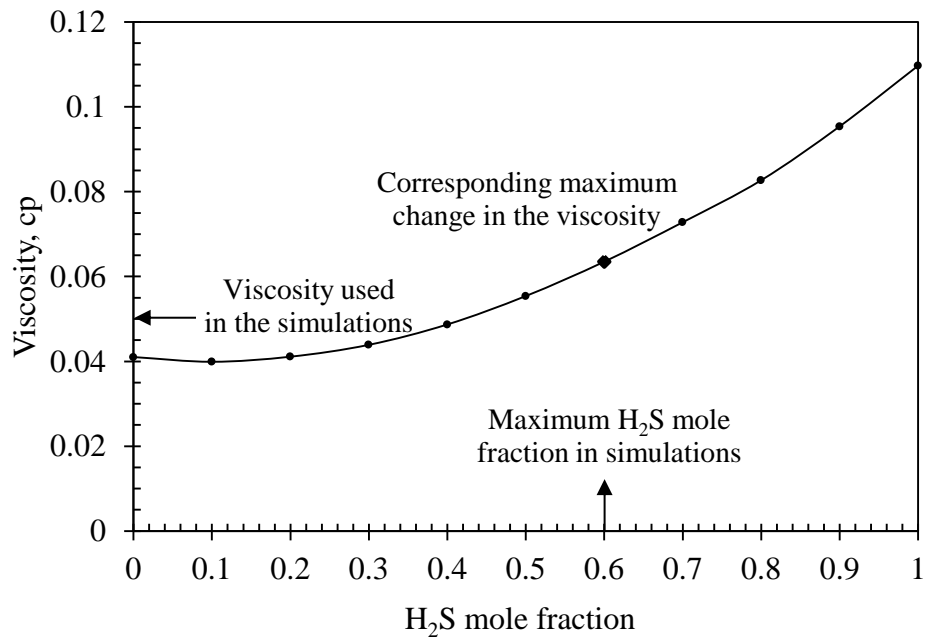
2-2-2- Main Features of Simulation Models

All simulations were performed using a one-dimensional radial model, with an assumed absolute permeability of 5000 mD, a porosity of 30%, a radius of 328 feet, and a thickness of 3.28 feet (see Table 2-2 for a full list of aquifer properties). The initial pressure, temperature, and salinity of the brine are the same as the values that were used in the numerical simulations by Bachu (Bachu et al., 2009).

The relative permeability curves were modeled using the Corey correlation (1954) with exponents of 2.0 and 1.5 for the gas and water relative permeability curves, respectively. Figure 2-3 presents the curves used in the simulations. The residual brine saturation was set equal to 0.1, and two different end-point relative permeability values for the gas phase of 0.4 and 1.0 were considered for the Base Case and one sensitivity analysis, respectively.



(a)



(b)

Figure 2-2: (a) P-T diagram of H₂S-CO₂ mixtures at four different compositions. The pressure and temperature of the reservoir has also been indicated; (b) Viscosity of H₂S-CO₂ mixtures at reservoir condition (141.8 °F and 1,958 psi) as predicted by SUPERTRAPP which shows the small variation of viscosity between pure CO₂ and a mixture consisting of 0.6 H₂S by mole fraction.

Table 2-2: Properties of aquifer and fluids and injection details for the Base Case simulation

Property	Value/Specification
Radius, ft	328
Thickness, ft	3.28
Absolute permeability, mD	5,000
Porosity	0.30
Rock compressibility, 1/psi	3.45E-6
Temperature, °F	141.8
Initial pressure, psi	1,958
Brine salinity, lb/ft ³	7.42
Initial mole fraction of dissolved H ₂ S	0.02
Grid system	1D-Radial
n _r	2,000
Aqueous phase viscosity, cp	0.58
Non-aqueous phase viscosity, cp	0.05
Injection gas composition	Pure CO ₂
Injection rate ft ³ /day	141.25
Injection period, day	100

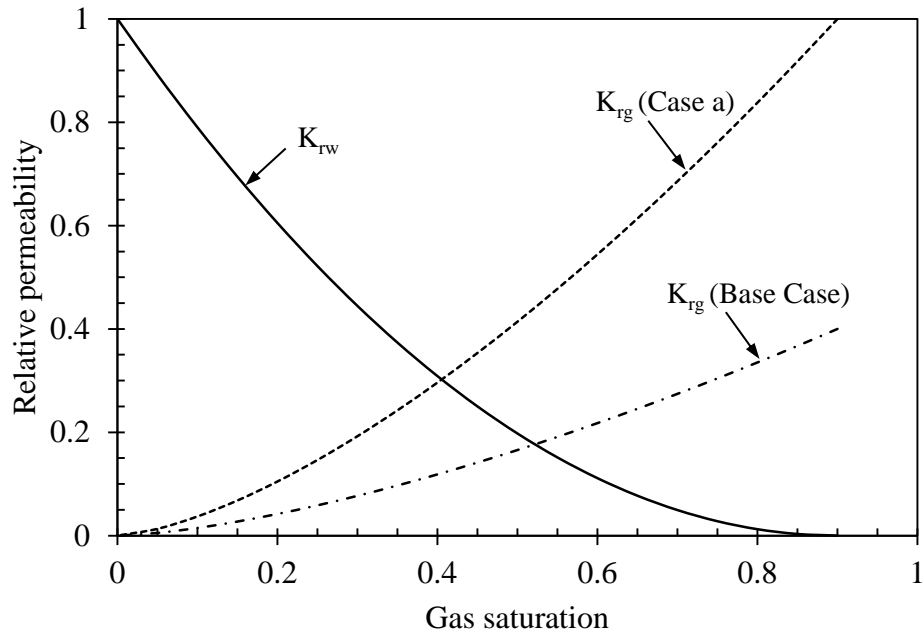


Figure 2-3: Water-gas relative permeability curves

The model employed a single vertical injection well, with constant injection rate located at the center of a bounded radial model, and a production well at the boundary to mimic a constant pressure boundary condition. Injection simulations of pure CO₂ and an

80% CO₂-20% H₂S mixture at supercritical conditions were performed for 100 days. The injection rate was fixed at 141.25 ft³/day (\approx 38.8 Mscf/day). The high value of absolute permeability and injection rate ensure propagation of the gas plume in a reasonable time while producing minimum pressure disturbance in the models.

It is worth mentioning some of the other relevant features and assumptions of the simulation models. First, GEM is an isothermal simulator in which the temperature of the injected fluids, as well as the temperature of the reservoir, remains constant at the user specified value, thereby neglecting all possible thermal effects. Second, true representation of the reservoir in the z direction may require using a multi-layered system which can capture any possible gravity segregation and hence saturation distribution. However, to reduce the degree of complexity of the problem, a one-layer system was used. Third, although molecular diffusion can play a role when there is a concentration gradient and also can cause back-mixing of the dissolved components with the (newly) injected gas, it was neglected in the current study. Fourth, the vaporization of water and related side effects such as formation dry-out, salt precipitation, and reductions in permeability and porosity (Pruess 2009; Zeidouni et al., 2009) were ignored. This further implies that the water component is only present in the aqueous phase and not in the non-aqueous phase. At the temperature and pressure of interest in this study, the ultimate mole fraction of water in the non-aqueous phase cannot exceed 2% to 3% (Li and Firoozabadi, 2009). Lastly, capillary forces were not considered in this study.

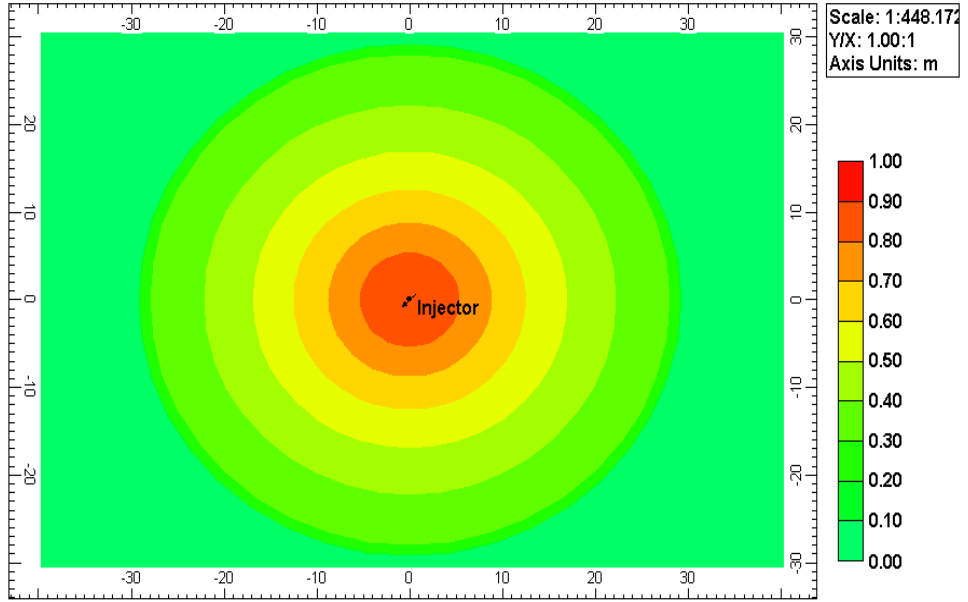
2-3- Results and Discussion

2-3-1- Preliminary Simulation Results

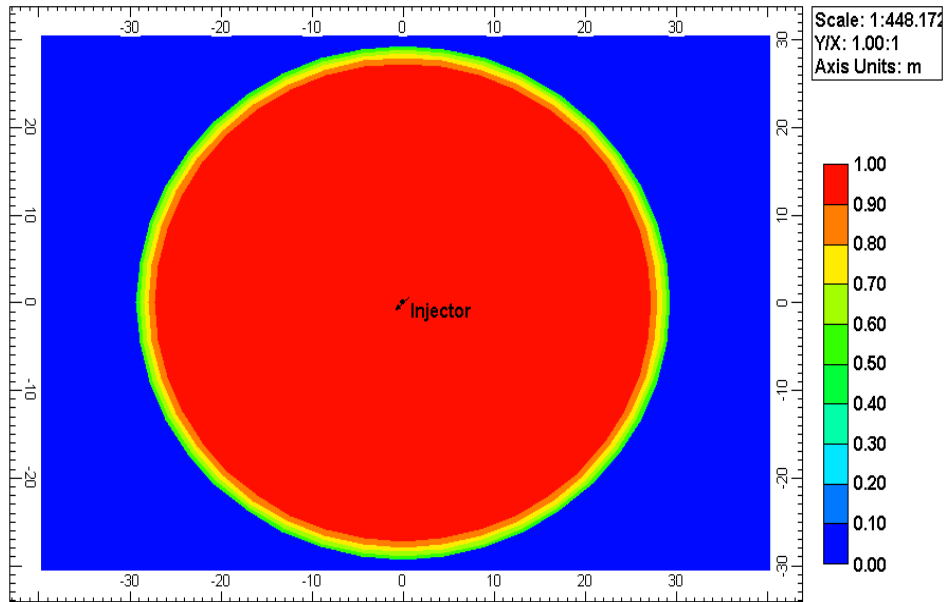
Preliminary simulation results indicate that injection of pure CO₂ into a saline aquifer, which is initially saturated with H₂S (Table 2-2), causes the exsolution and release of dissolved H₂S into the expanding CO₂ plume. Moreover, the expanding CO₂ plume (or acid gas plume) delivers all of the exsolved H₂S progressively towards the leading edge of the plume.

The effect of discretization on solution accuracy was investigated by conducting simulations with different degrees of grid refinement. It was concluded that fine grids are required to accurately capture the gas plume radius at any time, and to evaluate its composition correctly; therefore, two thousand grid cells (each 3.28 ft thick and 0.16 ft of radial extent) were used for all simulation models.

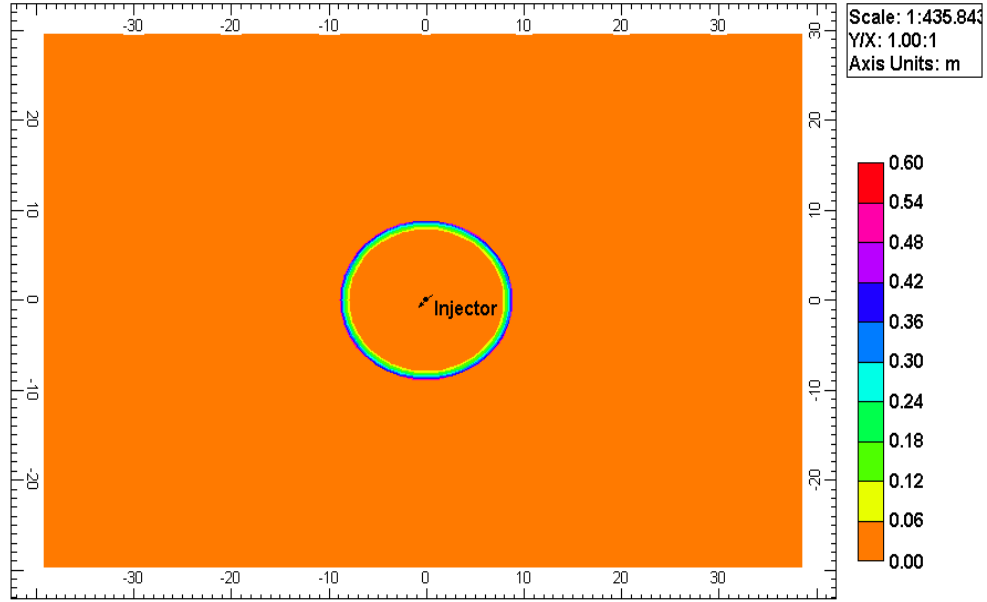
Figure 2-4-a shows the gas saturation variation within the aquifer after 100 days. As can be seen in Figure 2-4-b, the mole fraction of CO₂ within this plume changes from 1.0 at the point of injection and gradually decreases toward zero close to the outer boundary of the plume. Figure 2-4-c and Figure 2-4-d illustrate the variation in the H₂S composition of the plume after 10 days and 100 days, respectively, indicating a substantial increase in the radial extent of the evolved region. Since the plume expansion is symmetrical in the radial models, 2D graphs will be used to illustrate the development of gas saturation and H₂S evolution as the gas exsolution progresses.



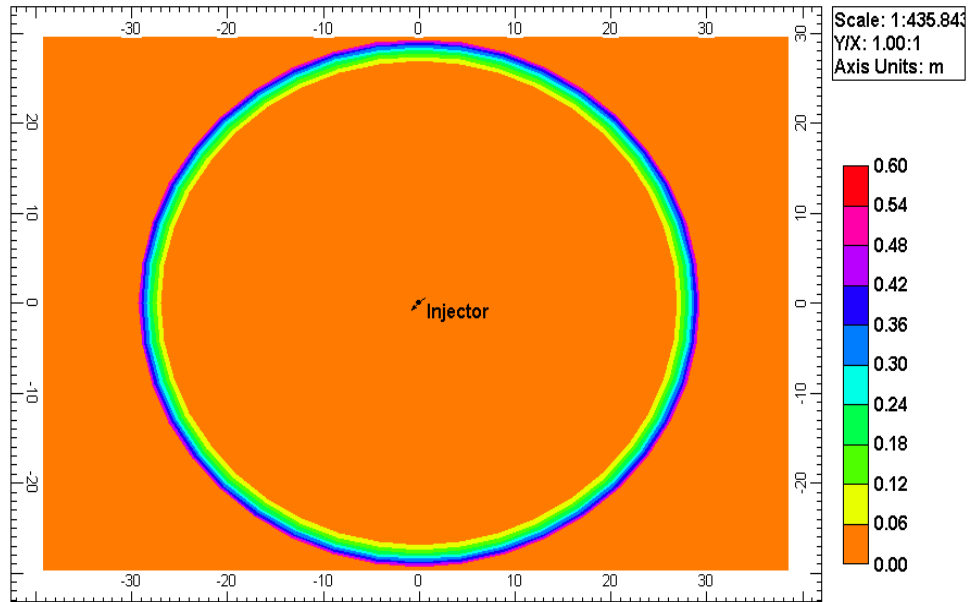
(a) Gas saturation after 100 days



(b) CO₂ mole fraction in the gas phase after 100 days



(c) H₂S mole fraction in the gas phase after 10 days



(d) H₂S mole fraction in the gas phase after 100 days

Figure 2-4: Simulation results: (a) gas saturation profile after 100 days; (b) CO₂ mole fraction in the gas phase after 100 days; (c) variation of H₂S mole fraction in the gas phase after 10 days; (d) variation of H₂S mole fraction in the gas phase after 100 days.

2-3-2- Base Case Simulation Results and Observations

As mentioned above, 2000 grid cells in the radial direction was chosen as the Base Case.

This grid was utilized to investigate the consequences of injection of CO₂ into brine which is saturated with (dissolved) H₂S at the initial conditions described in Table 2-2. For the Base Case scenario, pure CO₂ is injected at a rate of 141.25 ft³/day into a vertical well located at the center of the model. As previously described, when the injected CO₂ comes into contact with saturated brine, H₂S is progressively exsolved out of the aqueous phase into the gas phase of the advancing CO₂ plume. The CO₂ plume pushes the mobile portion of the brine, as well as the exsolved H₂S, toward the outer boundary of the domain, while CO₂ continuously dissolves into the brine. As observed from the simulations, at any time after injection starts, the region swept by the plume consists of two sub-regions: an inner radial sub-region extending from the injection well, characterized by the absence of H₂S in both aqueous and non-aqueous phases; and, an outer sub-region, where the mole fraction of H₂S in the gas plume gradually increases towards a peak value near the leading edge.

The peak value of H₂S (at the leading edge) is defined by thermodynamic equilibrium at the gas-liquid boundary (based on the fundamental assumption of instantaneous thermodynamic equilibrium, which is employed in CMG-GEM calculations). For the ternary system of H₂S-CO₂-H₂O flash calculations indicate that at the temperature, pressure and salinity used in this study, a gas mixture of 54% H₂S and 46% CO₂ is in equilibrium with an aqueous phase consisting of 1.30% H₂S, 0.7% CO₂, and 98% water (all by mole percent). These results of flash calculations are consistent with the experimental results of Bachu et al. (2009) in which they have shown that at the prevailing conditions, the solubility of H₂S is about two times greater than the solubility of CO₂ in aqueous phase. The results of simulations also suggest that the maximum mole

fraction of H₂S in the gas phase is 0.54, which is consistent with above data. It should be noted that this result is valid only within assumption and simplification made and discussed previously. If for example the vaporization of water to the gas phase were accounted for, it is expected that the H₂S concentrations would be greater. However, the quantification of such is not the main purpose of this study; instead, emphasis has been placed on understanding the mechanisms involved in the evolution of the very toxic and hazardous H₂S component.

Figure 2-5 and Figure 2-6 show the simulation results for the Base Case scenario after 100 days of injection. From Figure 2-5, it is inferred that, after 100 days, the plume radius will reach approximately 96.1 feet. The first sub-region is about 84.6 feet in radius, and the second sub-region is about 11.5 feet. Figure 2-6 clearly shows that the CO₂ has been dissolved into the brine, while H₂S has been exsolved and released into the gas phase. Considering both of these figures together, the occurrence of the equilibrium composition between the two phases (gas and aqueous) at the leading edge is identifiable. As time passes, subsequent to increasing radius of the plume, the extent of the second sub-region, which contains a gaseous H₂S concentration, also increases. The evolution of H₂S into the gas phase is a dynamic process beginning when CO₂ injection is initiated at the injector. This phenomenon was previously noted and illustrated in Figure 2-4-c and Figure 2-4-d.

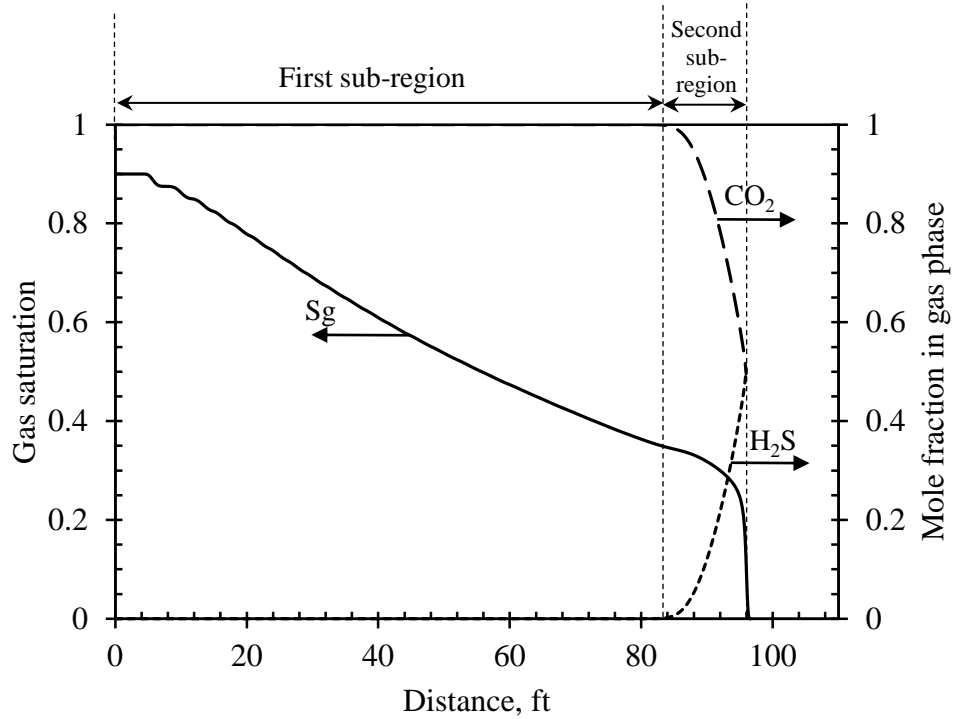


Figure 2-5: Development of two sub-regions within the area swept by the CO₂ plume after 100 days of simulation. The solid curve shows the variation of gas saturation versus distance (residual brine saturation is equal to 0.1); the long dashed curve shows the CO₂ mole fraction distribution in the gas phase; the short dashed curve shows the H₂S mole fraction distribution in the gas phase.

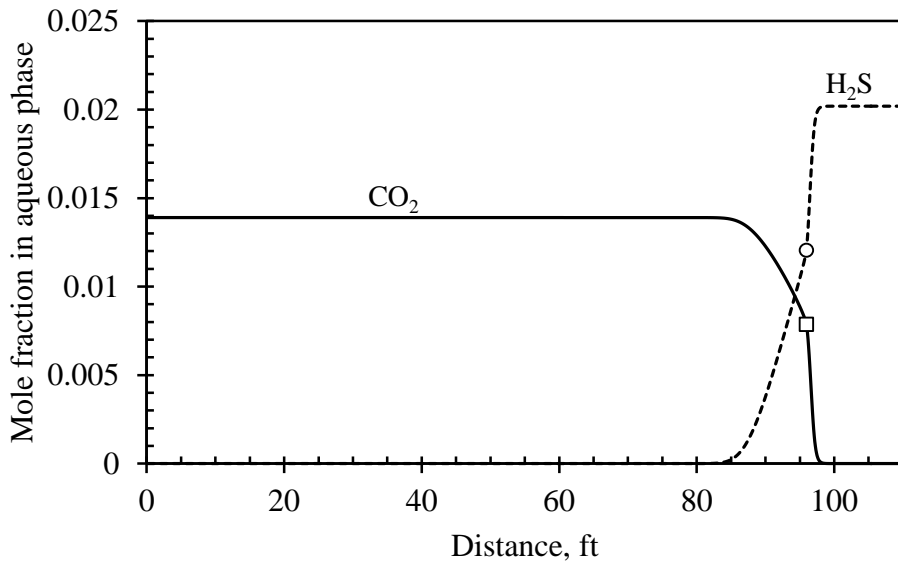


Figure 2-6: Variation in the composition of the aqueous phase versus distance in the region swept by the plume after 100 days. The “○” and “□” symbols indicate the equilibrated mole fraction of H₂S and CO₂, respectively, in the aqueous phase in the last block invaded by the gas plume.

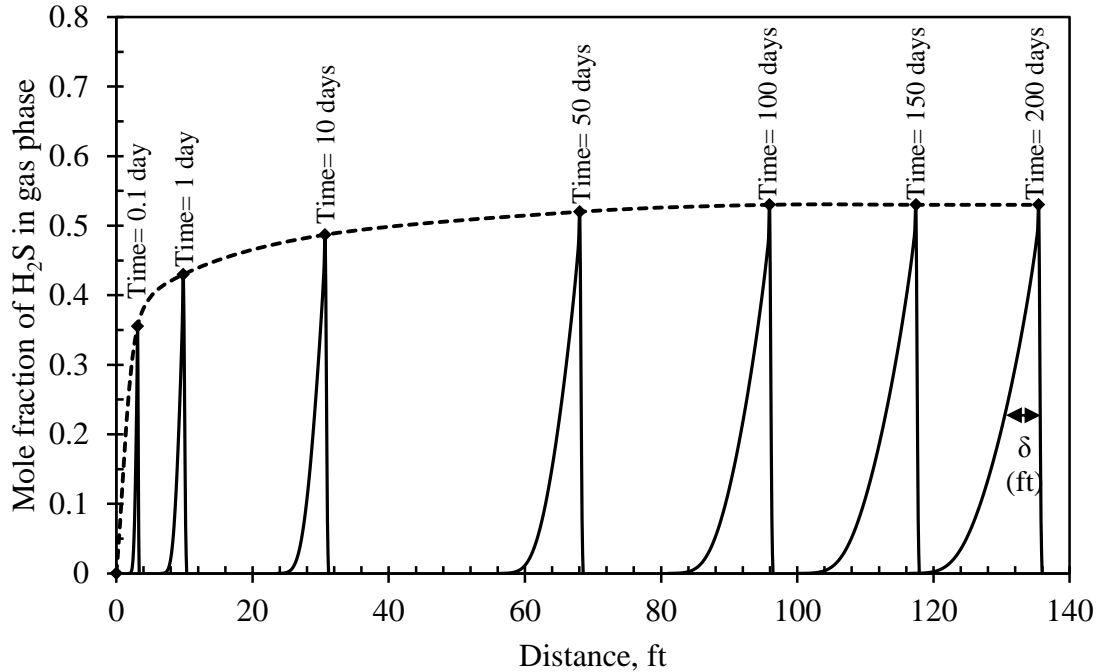


Figure 2-7: Mole fraction of H₂S in the gas plume at different times. Maximum observed H₂S mole fraction (dotted line at different times) is about 0.54. Increase in the width of the second region is determined by measuring the characteristic full width at half maximum (FWHM or “ δ ”).

Figure 2-7 demonstrates the gradual development of the outer sub-region. Its width continues to grow and the concept of FWHM (full width at half maximum, δ in Figure 2-7) is used to estimate the rate of width growth after stabilization of the peak value, as given by:

$$\frac{\Delta\delta}{\Delta t} = \frac{\delta_2 - \delta_1}{t_2 - t_1} = \frac{4.43 - 3.43}{200 - 100} = 0.01 \left(\frac{\text{ft}}{\text{day}} \right) \quad (2-3)$$

where δ (m) represents the FWHM of the graphs in Figure 2-7 corresponding to times when the peak value has been reached.

One point should be emphasized here: in the vicinity of the injection well in the presence of a strong convective process (strong CO₂ flux), the H₂S concentration gradient is confined within a very thin boundary layer near the edge. The layer’s width is increasing from zero (at the well) to scales (far enough from the well) comparable to

simulation grid size and at some point this layer becomes observable. Layer visibility occurs when dotted line on Figure 2-7 starts flattening and the equilibrium boundary mole fraction (54%) is reached (after 50 days).

From the simulation results, it is also possible to calculate the number of moles of H₂S in the gas phase at any specific time by evaluating the following integral (which is only valid for 1-D flow model):

$$n_{H_2S}^g = \int_{r_w}^{r_{plume}} (s_g \rho_g y_{H_2S}^g \varphi 2\pi h r) dr \quad (2-4)$$

where $n_{H_2S}^g$ (lb-mole) is the moles of gaseous H₂S, s_g is the gas saturation, ρ_g (lb-mole/ft³) represents the molar density of the gaseous phase, $y_{H_2S}^g$ is the mole fraction of H₂S in the gas phase, φ is the porosity, h (ft) is the thickness of the reservoir, and r (ft) is the radius from the injection well. The integration is carried out over a distance from the wellbore radius (r_w) to the plume radius r_{plume} .

Figure 2-8 shows the graph of the integrand in Equation (2-4) after 100 days of injection. The amount of H₂S released to the gas phase at this time (obtained by numerical integration of this graph) is equal to about 0.48 lb-mole. Knowing that the molecular weight of hydrogen sulfide is equal to 34.1 lb/lb-mole, the molar release value noted above is equivalent to about 16.4 lb of H₂S.

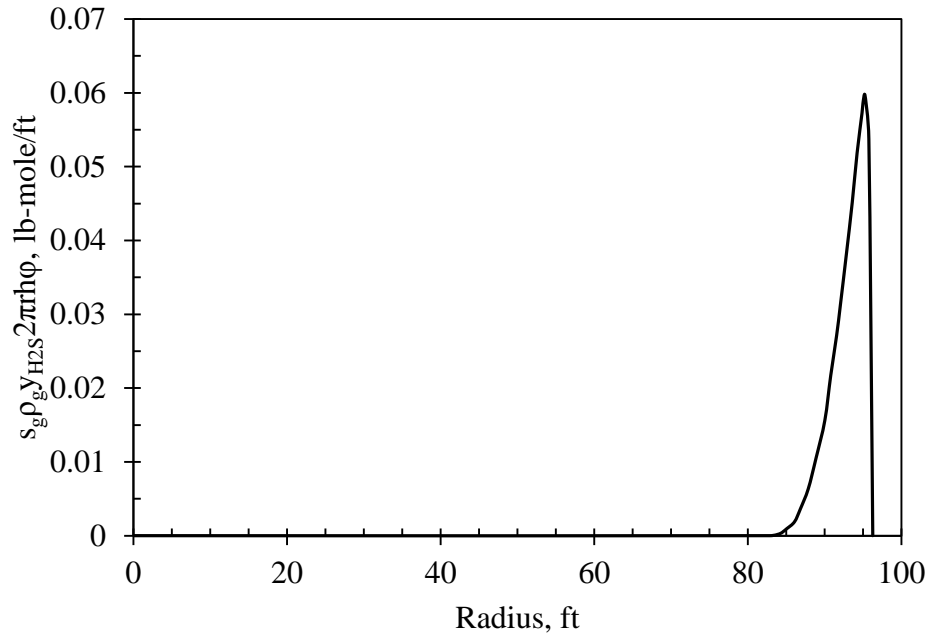


Figure 2-8: Moles of H₂S released to the gas phase per unit length versus distance from the injection well after 100 days. The area underneath the curve represents the total amount of H₂S released to the gas phase.

2-4- Sensitivity Analysis

Simulations were conducted to investigate the effect of flow conditions on the distribution of two phases and two components, and specifically to investigate the evolution of H₂S at the leading edge of the plume. Flow conditions are affected by gas mobility, gas injection rate, salinity of the brine, and initial mole fraction of dissolved H₂S. For simplicity, only the results after 100 days of injection are presented, as illustrated in Figure 2-9.

2-4-1- Effect of Gas Mobility

The effect of gas mobility was examined by changing the gas relative permeability and by increasing the end point of gas relative permeability from 0.4 to 1.0 (Figure 2-3, K_{rg} (Case a)). In the case of a more adverse mobility ratio (i.e., a higher gas mobility), at any

given time the gas spreads over a larger contact area with the aqueous phase (larger radius of plume) in comparison with the Base Case, thereby stripping H₂S more effectively from the brine in contact with the advancing gas front (Figure 2-9-a). For this case, after 100 days, δ would be 5.41 ft, which is 1.98 ft greater than the Base Case at the same point in time. It should also be noted that at 100 days, the gas plume has advanced 5 m further than for the Base Case model.

2-4-2- Effect of Gas Injection Rate

The effect of gas injection rate was investigated by increasing the injection rate from 141.25 ft³/day to 353.12 ft³/day. The effect of increasing the gas rate is similar to that of increasing the gas relative permeability. However, these two cases are different in one important aspect. Any change in relative permeability curves causes direct change in the characteristic fractional flow curve which in turn changes the phase saturation distributions. However, increasing the injection rate does not have any effect on the fractional flow curve. Instead, increasing the injection rate causes the plume to propagate faster and to contact a larger area at a specific time in comparison with the Base Case. Figure 2-9-b demonstrates that, after 100 days, the plume has passed 150.9 ft. The results also reveal that the rate of increase in the width of characteristic FWHM or δ increases and reaches a value of 0.015 ft/day (similar calculation to Equation (2-3))

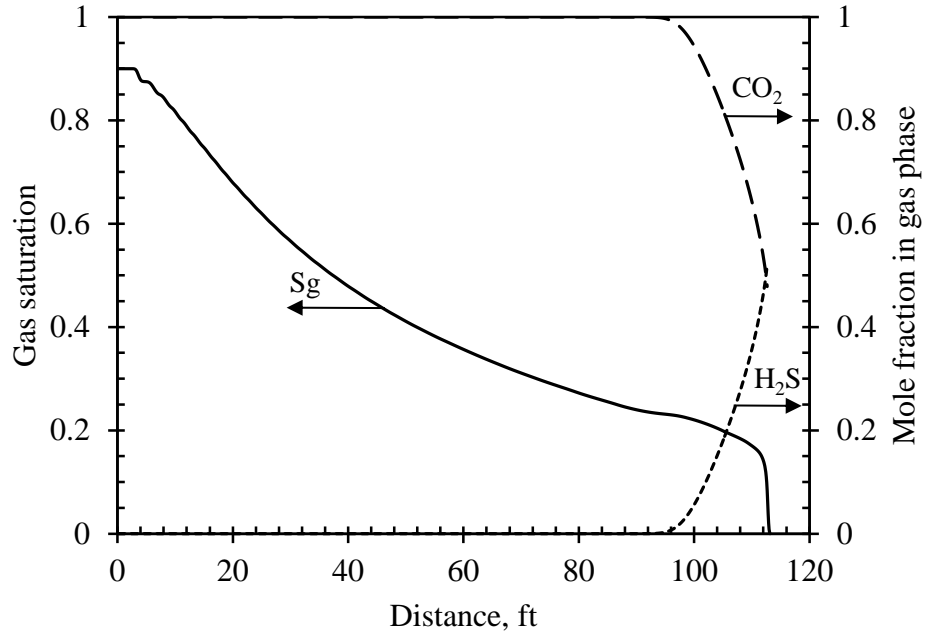
2-4-3- Effect of Brine Salinity

As has been pointed out by several researchers, the solubility of CO₂ and H₂S in brine will decrease with an increase in brine salinity (e.g., Enick and Klara, 1990; Duan et al. 2007). The effect of salinity was examined by considering fresh water instead of brine. It

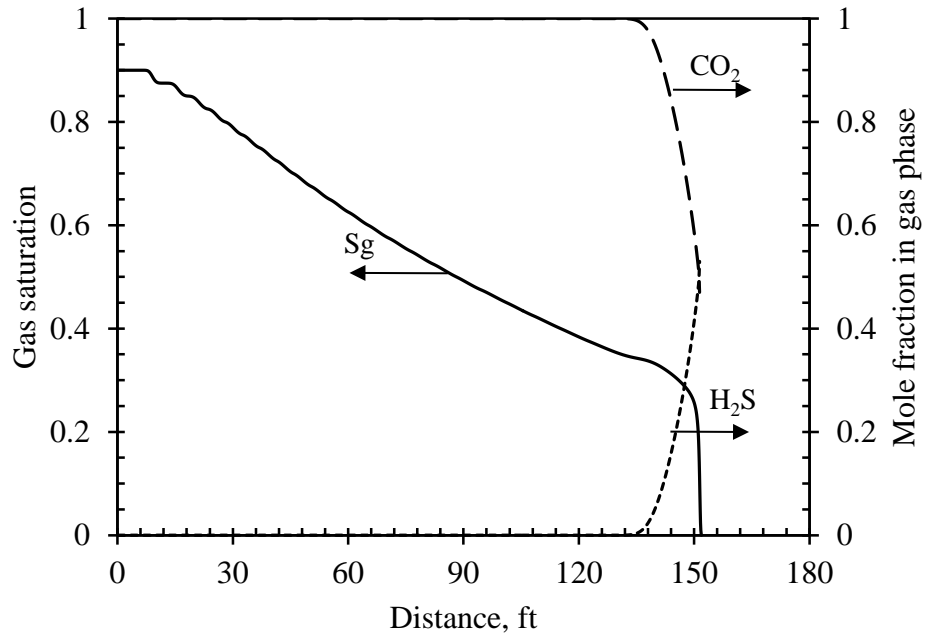
was assumed that the initial mole fraction of dissolved H₂S was equal to the saturated brine value in the Base Case (i.e., 0.02). The data in the third column of Table 2-1 (“Fresh water”) was used in the simulation models to reflect the higher solubility of gaseous components in the fresh water. The higher solubility of the gaseous components into fresh water relative to the brine case causes the ultimate radius of the CO₂ plume to shrink from 96.1 feet in the Base Case to 94.8 feet in this fresh water case (see Figure 2-9-c). This means that less H₂S is released for the fresh water case (see Figure 2-9-d).

2-4-4- Effect of Initial Mole Fraction of Dissolved H₂S in Brine

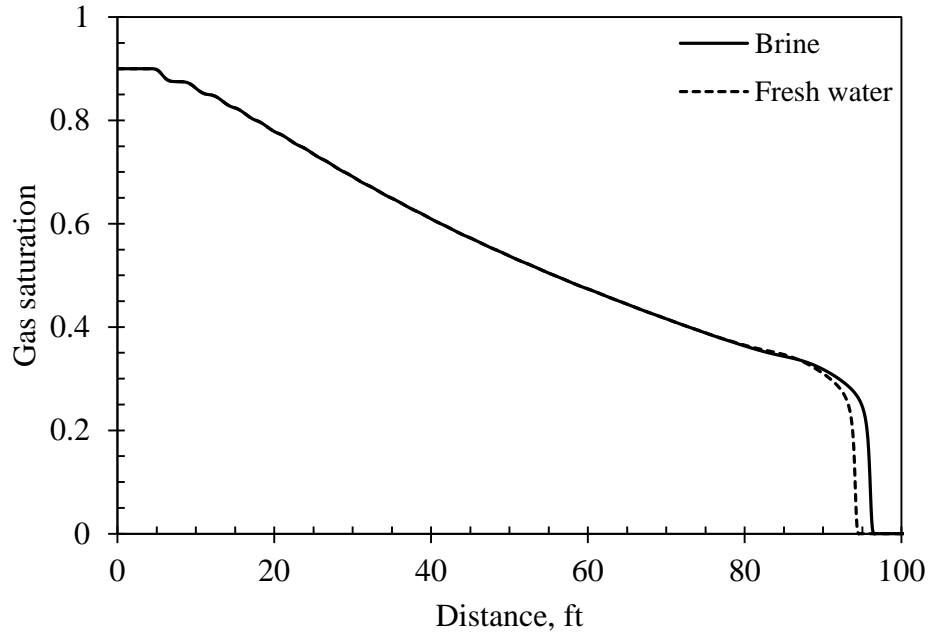
Simulations were run for two cases where the initial mole fraction of the dissolved H₂S in brine was substantially decreased. In the first case (Figure 2-9-e), the initial mole fraction of dissolved H₂S was equal to 0.005 and, for the second one (Figure 2-9-f), the initial mole fraction was equal to 0.0025 (i.e., one-fourth and one-eighth of the Base Case value, respectively). The evolution of H₂S in these cases is clearly different than the Base Case. The brine in the Base Case is saturated with H₂S; hence, dissolution of H₂S into the aqueous phase does not occur. However, in the cases of unsaturated brine, part of the exsolved H₂S, which remains as a gaseous accumulation, would be consumed in the dissolution process. Therefore (at least at the gas front), dissolution and exsolution of H₂S happen simultaneously; this causes a significant delay in the final composition being reached for different components, meaning less H₂S is released to the gas phase.



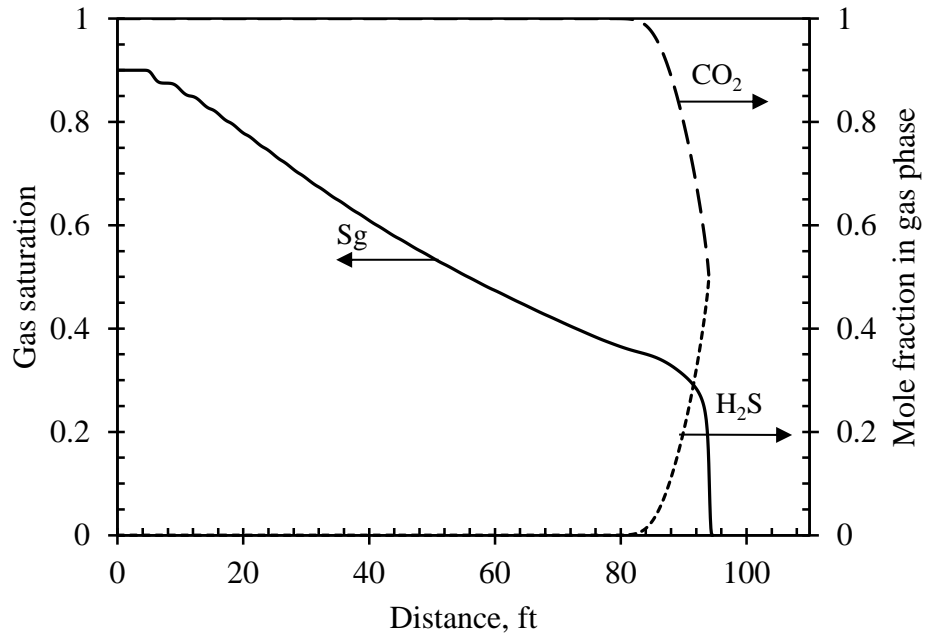
(a) Increased gas mobility



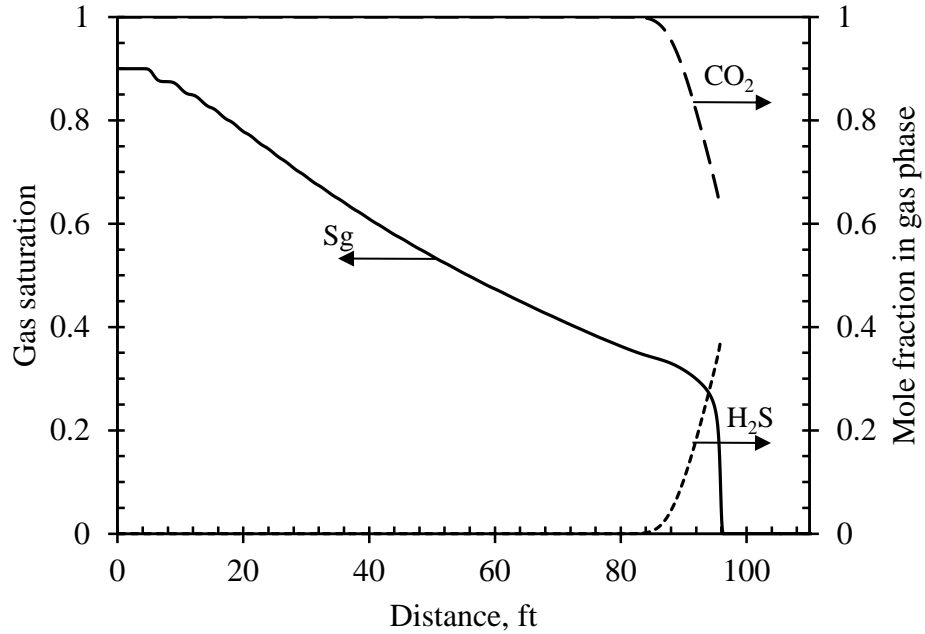
(b) Increased injection rate



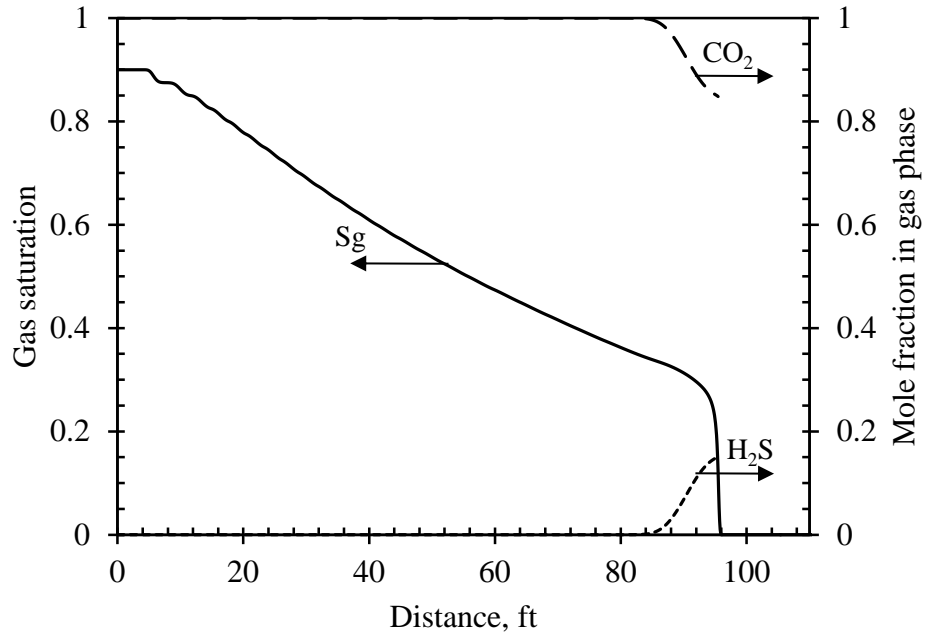
(c) Plume extension in fresh water vs. brine



(d) Using fresh water instead of brine



(e) Decreased mole fraction of dissolved H_2S by 4



(f) Decreased mole fraction of dissolved H_2S by 8

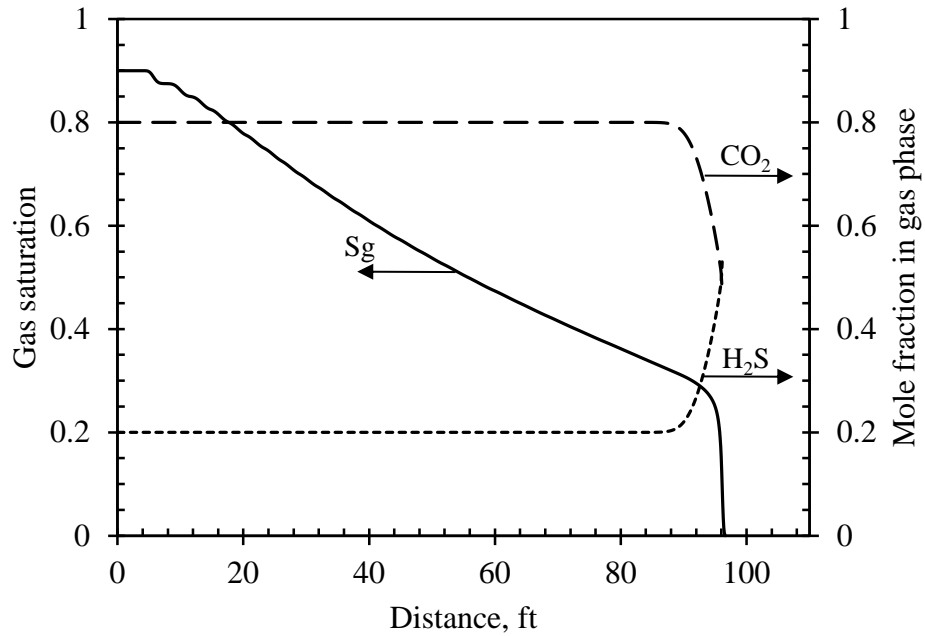
Figure 2-9: Effect of different parameters on the distribution of different phases and components within the aquifer after 100 days; (a) increased gas mobility; (b) increased gas injection rate; (c) comparison of plume extension for two cases with different salinity; (d) use of fresh water instead of saline brine; (e) decreased initial mole fraction of dissolved H_2S to one-fourth of the Base Case value; (f) decreased initial mole fraction of dissolved H_2S to one-eighth of the Base Case value.

2-5- Injection of Acid Gas into Sour Aquifers

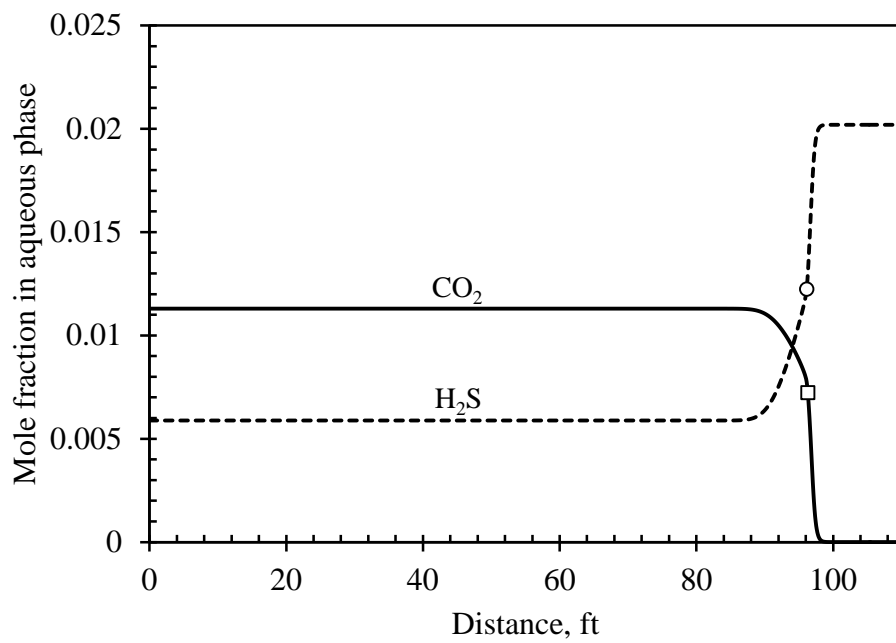
Acid-gas injection operations represent a commercial-scale analogue to geological storage of CO₂, which is one of the most promising means of reducing anthropogenic CO₂ emissions into the atmosphere in the short-to-medium term (IPCC, 2007). Due to the importance of the operation, it is worth studying the impact of acid gas injection in sour aquifers and comparing these results with those of injection into pure brine (i.e., a saline aquifer with no other impurities).

Injection of a mixture of 80% CO₂ and 20% H₂S for 100 days into saline aquifers with properties in Table 2-2 was studied. The same simulations were repeated for brine with the same salinity but in the absence of initial dissolved H₂S.

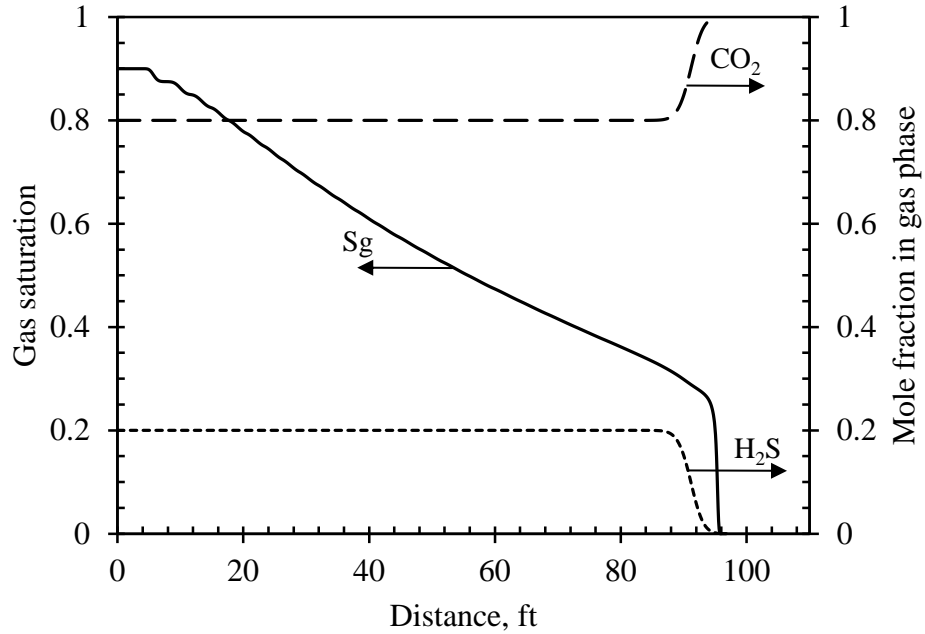
Figure 2-10-a and Figure 2-10-b show the results of the injection process in the sour aquifer. As can be seen, the injected streams strip away the dissolved H₂S and, at the same time, both CO₂ and H₂S are simultaneously approaching equilibrium in the in-situ brine. Figure 2-10-c and Figure 2-10-d illustrate the results associated with injection of acid gas into a saline aquifer, which is initially free of any H₂S. As expected, as the gas continues to flow away from the injection well, it comes into contact with unsaturated formation water; the higher H₂S solubility in brine causes the chromatographic separation of the two gases, resulting in H₂S being stripped off at the leading edge of the gas plume (Bachu and Bennion, 2009). In this situation, the zone with high composition of H₂S in the gas plume does not appear. The depicted results in these two figures are similar to the results previously reported by Bachu (Bachu et al., 2009).



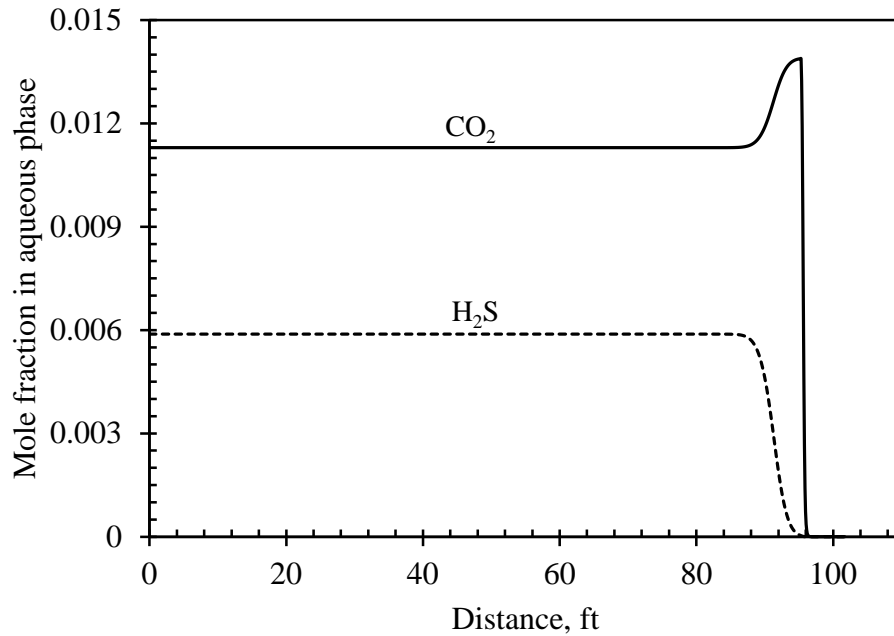
(a) Brine is initially saturated with H₂S



(b) Brine is initially saturated with H₂S



(c) Pure brine



(d) Pure brine

Figure 2-10: Comparison between phase and component distribution for acid gas injection in two cases; (a, b) the brine is initially saturated with H₂S (where, similar to what was displayed in Figure 6, the “○” and “□” symbols indicate the equilibrated mole fraction of H₂S and CO₂, respectively, in the aqueous phase in the last block invaded by the gas plume); (c, d) the brine is initially free of any dissolved H₂S.

2-6- Summary

Compositional numerical simulations were performed to characterize the exsolution of H_2S during carbon dioxide and acid gas sequestration in saline aquifers containing pre-existing dissolved H_2S as an impurity. Simulation results confirm the formation of two distinguishable sub-regions in the volume swept by the gas plume. For pure CO_2 injection, the first sub-region is characterized by the absence of H_2S in both aqueous and gaseous phases. This sub-region occupies the interior cylindrical region centered at the injection point. On the other hand, in the outer cylindrical sub-region surrounding the first sub-region, the H_2S mole fraction gradually increases toward the leading edge of the advancing gas front. The size of the evolved sub-region increases over time. The maximum H_2S mole fraction in gas phase is affected by the reservoir conditions under investigation, including the pressure, temperature, and salinity. Because this was a characterization study, precise quantification of the results was not pursued as a goal of this study; therefore, the results would be subject to minor changes if, for example, the vaporization of water or flow in vertical direction are considered.

Sensitivity analysis was performed to explore the effects of flow conditions and fluid characteristics on the sizes of these sub-regions and particularly the alteration of the H_2S mole fraction profile in the second sub-region. The study was limited to the main parameters such as gas mobility, gas injection rate, brine salinity, and initial mole fraction of dissolved H_2S impurity. Gas mobility, which is controlled by relative permeability of gas, had a direct effect on the size of the plume. Increasing the gas mobility causes the plume size to increase and consequently enhances the release of H_2S . Injection rate changes the rate of growth of the second sub-region. Brine salinity influences gas solubilities which accordingly affect the evolution of the H_2S dissolved species. Increased

solubility reduces the exsolution of dissolved hydrogen sulfide. Although the initial mole fraction of dissolved H₂S has a direct effect on the amount of exsolvable H₂S, a low initial mole fraction is not a serious barrier for H₂S to reach appreciable levels near the leading edge of the plume.

Injection of a mixture of 80% CO₂ and 20% H₂S as an acid gas into a sour aquifer was also explored. The results show that, in contrast with the injection of pure carbon dioxide, the injection of the acid gas mixture is accompanied by the simultaneous exsolution and dissolution of H₂S from and into the aqueous phase. For low mole fraction of hydrogen sulfide in the injection fluid, the dissolution of this component causes no practical change in the mole fraction profile of H₂S in comparison with injection of pure CO₂ into sour saline aquifers. Injection of an acid gas mixture into an ordinary brine aquifer gives rise to the formation of sour brine in the swept region as unsaturated water easily strips away H₂S from the injected sour gas stream.

The results of this study are important in establishing monitoring strategies for CO₂ storage sites, and in evaluating the risks associated with the possible leakage of evolved H₂S during CO₂ and acid gas injection into sour saline aquifers. This research also establishes the level of corrosivity represented by CO₂ and H₂S concentrations (affecting pH levels and partial pressures of corrosive elements, etc.) in both the aqueous and gas phases when the plume intersects wells that penetrate the injection horizon. The effect of other impurities such as CH₄, N₂, and SO₂, either as in-situ components or as constituents of the injection stream, can be studied in a similar manner and should be the subject of future studies.

Acknowledgments

Financial support for this work was provided by NSERC Strategic Grant and AERI with additional funding from industry partners through Wabamun Area CO₂ Sequestration Project (WASP, <http://people.ucalgary.ca/~keith/wasp.html>) led by University of Calgary. Simulation software (GEM) was donated by the Computer Modelling Group. This support is gratefully acknowledged. Finally, we also wish to express our particular thanks to Drs. Pooladi-Darvish and Hassanzadeh for their extremely helpful discussions and generous suggestions for improvements to this paper.

References

- Adams, J.J., Bachu, S., 2002. Equations of State for Basin Geofluids: Algorithm Review and Intercomparison for Brines. *Geofluids*, vol. 2, pp. 257-271.
- Ahmed, T., 1989. *Hydrocarbon Phase Behaviour*. Gulf Publishing Company, Houston.
- Bachu, S., Carroll, J.J., 2005. In-situ Phase and Thermodynamic Properties of Resident Brine and Acid Gases (CO₂ and H₂S) Injected into Geological Formations in Western Canada. In: Rubin, E.S., Keith, D.W., Gilboy, C.F. (Eds.), *Proceedings of the 7th International Conference on Greenhouse Gas Control Technologies*, vol. I. Elsevier, London, U.K., pp. 449-457.
- Bachu, S., Gunter, W.D., 2005. Overview of Acid Gas Injection Operations in Western Canada. In: Rubin, E.S., Keith, D.W., Gilboy, C.F. (Eds.), *Proceedings of the 7th International Conference on Greenhouse Gas Control Technologies*, vol. I. Elsevier, London, U.K., pp. 443-448.
- Bachu, S., Bennion, D.B., 2009. Chromatographic Partitioning of Impurities

Contained in a CO₂ Stream Injected into a Deep Saline Aquifer: Part 1- Effect of Gas Composition and In-situ Conditions. *Int. J. Greenhouse Gas Control*, doi:10.1016/j.ijggc.2009.01.001.

- Bachu, S., Pooladi-Darvish, M., Hong, H., 2009. Chromatographic Partitioning of Impurities (H₂S) Contained in a CO₂ Stream Injected into a Deep Saline Aquifer: Part 2 - Effect of Flow Conditions. *International J. of Greenhouse Gas Control*, doi:10.1016/j.ijggc.2009.01.002.
- Battistelli A., Marcolini, M., 2009. TMGAS: A New TOUGH2 EOS Module for the Numerical Simulation of Gas Mixtures Injection in Geological Structures. *Int. J. Greenhouse Gas Control*, vol. 3(4), pp. 481-493.
- Bennion, D.B., Bachu, S., 2008. Drainage and Imbibition Relative Permeability Relationships for Supercritical CO₂/Brine and H₂S/Brine Systems in Intergranular Sandstone, Carbonate, Shale and Anhydrite Rocks. *SPE Res. Eng. Eval.* 11 (3), pp. 487-496, doi: 19.2118/99326PA.
- Carrol, J.J., 2002. Phase Equilibria Relevant to Acid Gas Injection, Part 1 - Non-aqueous Phase Behaviour. *JCPT*, June 2002, vol. 41(6).
- Carrol, J.J., 2002. Phase Equilibria Relevant to Acid Gas Injection: Part 2 - Aqueous Phase Behavior. *JCPT*, June 2002, vol. 41(7).
- Computer Modeling Group (CMG), 2008. User's Guide-GEM: Advanced Compositional Reservoir Simulator. Version 2008.12. Computer Modeling Group Ltd., Calgary, AB, Canada.
- Corey, A.T., 1954. The Interrelation between Gas and Oil Relative Permeabilities. *Producers Monthly* (November), pp. 38-41.

- Doughty, C., Pruess, K., Benson, S.M., Freifeld, B.M., Gunter, W.D., 2004. Hydrological and Geochemical Monitoring for a CO₂ Sequestration Pilot in a Brine Formation. LBNL Report 55104, Lawrence Berkeley National Laboratory, Berkeley, CA.
- Duan, Z., Sun, R., Liu, R., Zhu, C., 2007. Accurate Thermodynamic Model for the Calculation of H₂S Solubility in Pure Water and Brine. *Energy and Fuels*, vol. 21, pp. 2056-2065.
- Enick, R.M., Klara, S.M., 1990. CO₂ Solubility in Water and Brine under Reservoir Conditions. *Chem. Eng. Commun.*, vol. 90, pp. 23-33.
- Hovorka, S.D., Doughty, C., Holtz, M., 2004. Testing Efficiency of Storage in the Subsurface: Frio Brine Pilot Experiment. LBNL Report 55730, Lawrence Berkeley National Laboratory, Berkeley, CA.
- Hutcheon, I., 1999. Controls on the Distribution of Non-Hydrocarbon Gases in the Alberta Basin. *Bulletin of Canadian Petroleum Geology*, vol. 47(4), pp. 573-593.
- Intergovernmental Panel on Climate Change (IPCC), 2007. In: Core Writing Team, Pachauri, R.K., Reisinger, A. (Eds.), *Climate Change 2007: Synthesis Report. Contribution of Working Groups I, II and III to the Fourth Assessment Report of the Intergovernmental Panel on Climate Change*. IPCC, Geneva, Switzerland.
- Kumar, A., Ozah, R., Noh, M., Pope, G.A., Bryant, S., Sepehrnoori, K., Lake, L.W., 2005. Reservoir Simulation of CO₂ Storage in Deep Saline Aquifers. *SPE J.*, vol. 10(3), pp. 336-348.

- Leonenko, Y., Keith, D.W., 2008. Reservoir Engineering to Accelerate The Dissolution of CO₂ Stored in Aquifers. *Environmental Science & Technology*, vol. 42, pp. 2742-2747.
- Li, Y., Nghiem, L.X., 1986, Phase Equilibria of Oil, Gas and Water/Brine Mixtures from a Cubic Equation of State and Henry's Law. *The Canadian Journal of Chemical Engineering*, vol. 64 (3), pp. 486-496.
- Li, Z., Firoozabadi, A., 2009. Cubic-Plus-Association Equation of State for Water-Containing Mixtures: Is "Cross Association" Necessary? *AIChE Journal*, vol. 55, pp. 1803-1813.
- NIST, 2007. Standard Reference Database 4. NIST Thermophysical Properties of Hydrocarbon Mixtures, Program SUPERTRAPP – Version 3.2. Gaithersburg, MD 20899, USA
- Ozah, O.C., Lakshminarasimhan, S., Pope, G.A., Sepehrnoori, K., Bryant, S.L., 2005. Numerical Simulation of the Storage of Pure CO₂ and CO₂-H₂S Gas Mixtures in Deep Saline Aquifers. *SPE 97255*.
- Rowe, A.M., Chou, J.C.S., 1970. Pressure-Volume-Temperature-Concentration Relation of Aqueous NaCl Solutions. *J. Chem. Eng. Data*, vol. 15(1970), pp. 61-66.
- Peng, D.Y., Robinson, D.B., 1976. A New Two-constant Equation of State. *Ind. Eng. Chem. Eng. Fundam.*, vol. 15, pp. 59-64.
- Pooladi-Darvish, M., Hong, H., Stocker, R.K., Bennion, D.B., Theys, S., Bachu, S., 2009. Chromatographic Partitioning of H₂S and CO₂ in Acid Gas Disposal. *JCPT*, vol. 48(10), pp. 52-57.

- Pruess, K., 2009. Formation Dry-Out from CO₂ Injection into Saline Aquifers: 2. Analytical Model for Salt Precipitation. *Water Resour. Res.* 45, W03403, doi:10.1029/2008WR007102.
- Zeidouni, M., Pooladi-Darvish, M., Keith, D.W., 2009. Analytical Solution to Evaluate Salt Precipitation during CO₂ Injection in Saline Aquifers. *International J. of Greenhouse Gas Control*, vol. 3(5), pp. 600-611.

Chapter 3

Reservoir Modeling for Wabamun Lake Sequestration Project

A study, entitled “Wabamun Lake Sequestration Project” or “WASP”, was performed to evaluate large-scale CO₂ storage opportunities in the Wabamun area including potential risks. The project examined the feasibility of storing 20 megatons (Mt) of CO₂ per year over 50 years. This scale is one order of magnitude larger than the typical benchmark (1 Mt/year) used in academic research and commercial projects that are currently in place or under review. The study was conducted by a group of researchers from several universities as well as industry consultants. This paper presents an overview of the reservoir modeling part of this study, which the author was responsible for. The main objectives of the reservoir modeling were: i) estimation of storage capacity (traditionally, this value is projected based on the available pore space, but we have an additional practical consideration: the maximum amount one can inject within a short period of time (~50 years) and within a localized injection area (~18.5 mi × 37 mi)); ii) investigation of CO₂ plume movement and pressure distribution during and after injection including the effect of formation dip angle on the plume shape and its migration; iii) investigation of the long-term fate of injection associated with free phase CO₂ and aquifer pressurization;

iv) investigation of the phase behaviour of H₂S initially available and dissolved in brine during CO₂ sequestration process. These simulation sensitivities led to a few important findings. The most important one is that, when CO₂ is being injected into a sour aquifer, initially dissolved H₂S will release into the expanding CO₂ plume and accumulate at the leading edge of the plume. Also, the large scale injection scheme (20 Mt/year), which requires multi well injectors, provides very different pressure response compared to a one well (1 Mt/year) scenario.

Keywords: Large scale CO₂ sequestration, reservoir simulation, H₂S evolution, fate of injected CO₂

3-1- Introduction

Carbon dioxide emissions arising from consumption of fossil fuels are probably the main cause of climate change over the coming century (IPCC, 2007). The use of technologies such as carbon dioxide capture and geologic storage (usually known as CCS), if applied efficiently, can reduce net emissions of CO₂ to the atmosphere. However, for this technology to play a significant role in managing global emissions it should be carried out at very large scales. Although aquifers offer a large storage potential for CCS, the injection of large volumes to fill up this capacity can be complicated. In this study, we performed a comprehensive numerical simulation of injection into the Nisku aquifer located in Wabamun Lake Area, Alberta, Canada, where large CO₂ emitters are present (Figure 3-1).

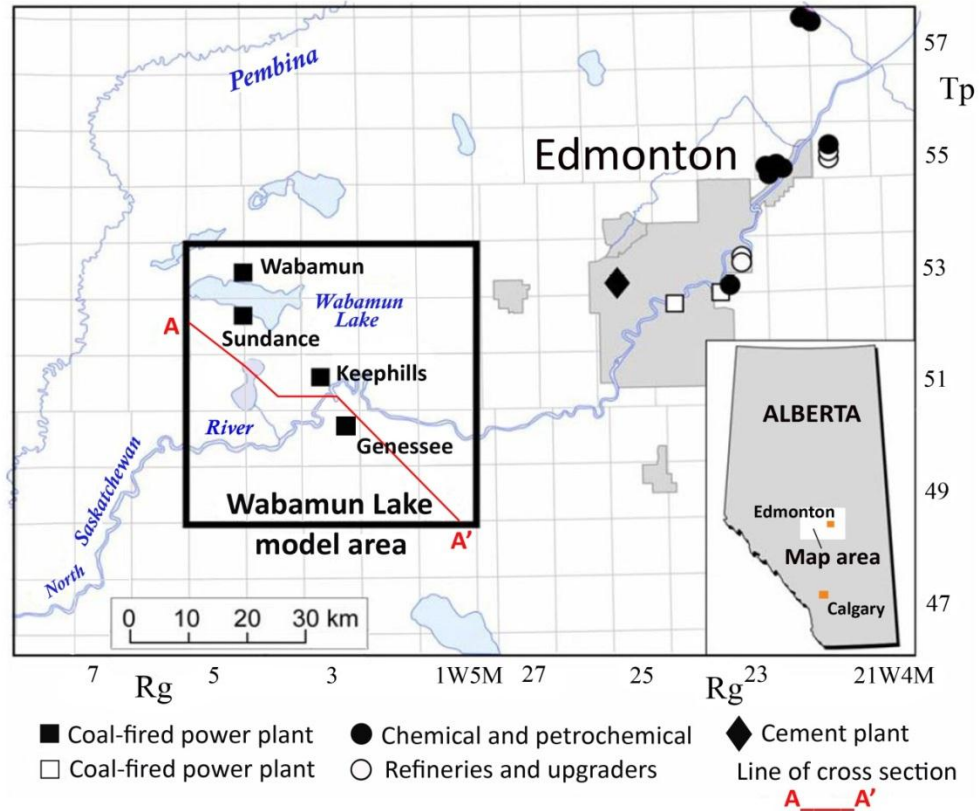


Figure 3-1: Location of the major CO₂ emission sources in Alberta and the location of the Wabamun Lake study (redrafted from Karsten et al., 2007).

Together the four coal-fired power plants in the Wabamun study area emit approximately 30 Mt CO₂ per year. The Alberta Geological Survey has identified this area as a potential storage site with different underground storage targets. Identification of the targets was based on evaluation of a variety of parameters such as stratigraphy and lithology, fluid composition, rock properties, geothermal, geomechanical and pressure regimes. One of these targets, the Nisku Formation in the Devonian Winterburn Group, was selected for WASP study. The Nisku was deposited at the edge of a carbonate shelf. From southeast to northwest, relatively pure platform carbonates change into interbedded limestone and shale of ramp and ultimately basin slope characteristics. The depth to the top of the Nisku formation ranges between 5250 ft in the northeast and gradually

increases to 7050 ft in the southeast (Karsten et al., 2007). The salinity of the formation water is equivalent to 11.86 lb of NaCl/ft³. The temperature of the formation is 140 °F and, at these conditions, the water viscosity is equal to 0.84 cp. The net thickness of the aquifer is estimated to be 230 ft and pressure at aquifer top is approximately 2,320 psi. These reservoir and water data were taken from Hitchon (Hitchon, 1996) and used for building simulation models. Table 3-1 summarizes aquifer and fluid properties used in the study.

Table 3-1: Properties of the aquifer and water used in WASP study (Hitchon, 1996)

Property	Value
Depth, ft	6,100
Thickness, ft	230
Pressure at aquifer top, psi	2,320
Temperature, °F	140
Permeability, mD	30
Ratio of vertical to horizontal permeability	0.27
Porosity, %	10
Salinity of formation water, lb/ft ³	11.86
Density of formation water, lb/f ³	72.14
Viscosity of formation water, cp	0.84
Rock compressibility, 1/psi	3.1E-6

Pressure-dependency of fluid density and viscosity was determined using the black oil model presented by Hassanzadeh (Hassanzadeh et al., 2008). The characteristic relative permeability curves of the Nisku carbonate, which have been measured at in-situ conditions of pressure, temperature and brine salinity are shown in Figure 3-2 (Benion and Bachu, 2008).

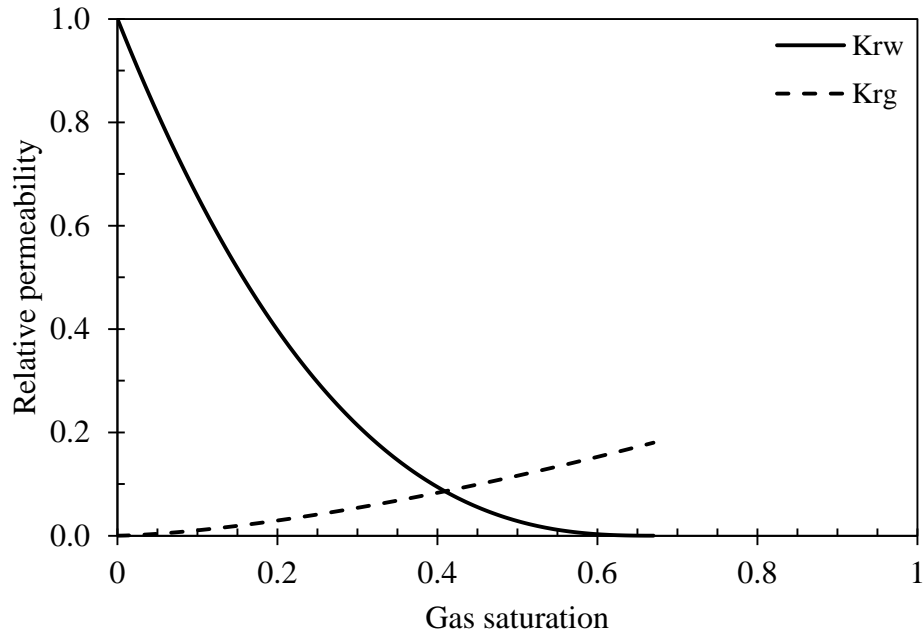


Figure 3-2: Nisku relative permeability curves for gas and water.

In the following sections, the results of reservoir simulation of saturation (plume size) and pressure distributions in a simplified conceptual homogeneous model, as well as full size homogeneous and heterogeneous reservoir models, are presented. Secondly, the effect of reservoir dip on plume evolution is discussed. Thirdly, the long-term fate of average reservoir pressure and CO₂ in the free gas phase is investigated. Finally, the phenomena of H₂S exsolution during CO₂ injection into a sour aquifer is briefly addressed.

3-2- Preliminary Conceptual Modeling

To develop a benchmark at the beginning of the project, a simplified conceptual model was developed assuming homogeneous properties (provided above) and an infinite acting aquifer. A square (125 mi × 125 mi) simulation domain was chosen to represent the aquifer (the results were not sensitive to an increase in model size to 155 mi × 155 mi).

By setting the model to these dimensions, the aquifer behaves as though it were infinite acting for the injection of the target volume of CO₂. Figure 3-3 shows the model configuration for different numbers of vertical injector wells (1-25). All wells are perforated from the top to the bottom of the aquifer. The number of wells (n) and placement configuration were designed to allow the use of an element of symmetry and hence reduce the total number of grid cells by a factor of four. The distance between the wells in x and y directions are the same and equal to λ . The total cumulative amounts of injected CO₂ (denoted as Q1, Q4, Q9, Q16 and Q25), increase with the number of wells and these amounts are split equally between injectors in each case. For example, in the case of 9 wells, the yearly flow rate per each well is $Q9/(9 \text{ wells} \times 50 \text{ years})$.

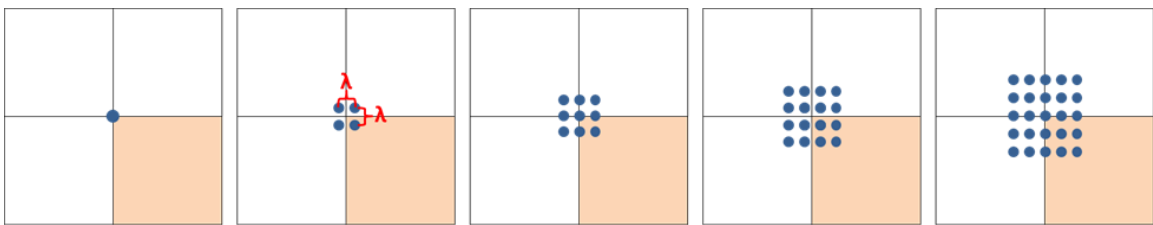


Figure 3-3: Configuration of injection wells and element of symmetry (cream color area).

In all cases, the injection time is chosen as 50 years and injection capacity is defined as the maximum amount, which is possible to inject without exceeding the reservoir fracture pressure (assumed to be 5,800 psi as discussed later in the paper).

Simulation results demonstrate that, for a single injector completed in the whole formation interval and at the center of the reservoir, the plume radius reaches 2.8 miles after 100 years. Most plume propagation takes place during the injection period and virtually stops after 100 years from the start of injection (50 years after injection stops). The injection rate capacity was found to be ~1 Mt/year for this vertical injectors (constrained by fracture pressure), while horizontal wells each 0.62 mi in length and completed open-hole, can improve the injectivity to ~1.5 Mt/year.

For the multiple wells ($n > 1$) injection scenario, CO₂ saturation plumes do not interfere and n individual plumes each having a radius 2.5-3 mi is observed. However, the pressure field behavior is completely different from the saturation field. By the end of CO₂ injection period, there are no individual pressure plumes. Instead, different pressure plumes merge into a single large (scale of hundred km) pressure envelope. Injection capacity increases with the number of wells but this effect is rapidly vanishing after $n \sim 10$. These phenomena will be discussed in detail later, when a full Nisku aquifer geomodel is considered.

3-3- Detailed Modeling with Full Aquifer Extent

In this section, simulation results for CO₂ injection into the Nisku formation are presented. First, a homogenous model is used to investigate injectivity into a semi-infinite formation. Then, a heterogeneous model is populated with realistic permeability and porosity fields in order to demonstrate the effect of heterogeneity and reservoir dip angle on the evolution of a CO₂ plume as well as the impact on reservoir pressure.

Figure 3-4 shows a top view of the Nisku aquifer. The illustrated area is approximately 280 mi \times 400 mi while the area outlined in red corresponds to the injection area (930 mi²). The injection site is chosen to be near wells with available core and log data. The base properties used for homogeneous model are the same as for the conceptual model (base case).

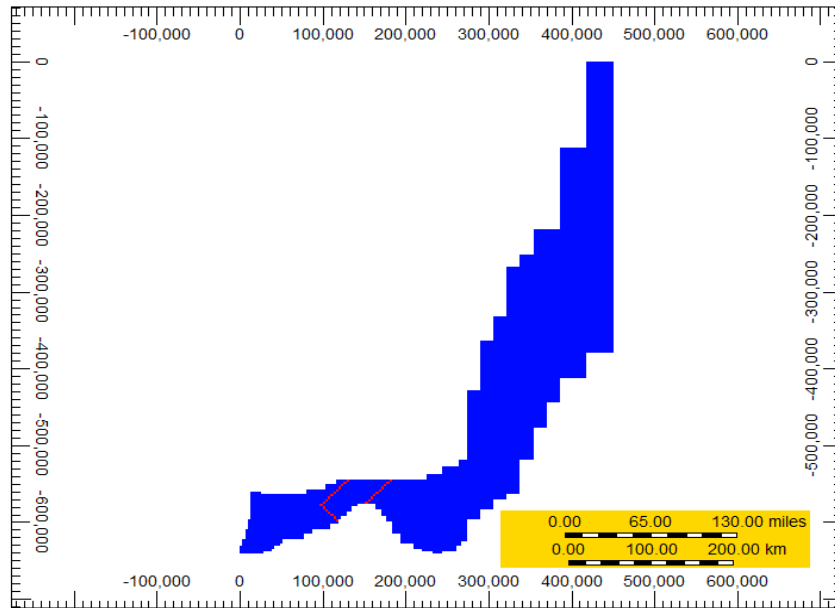
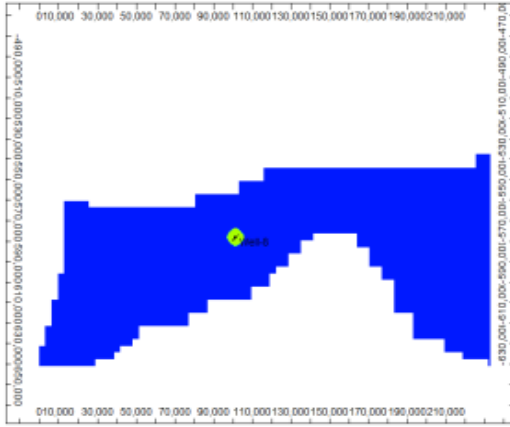


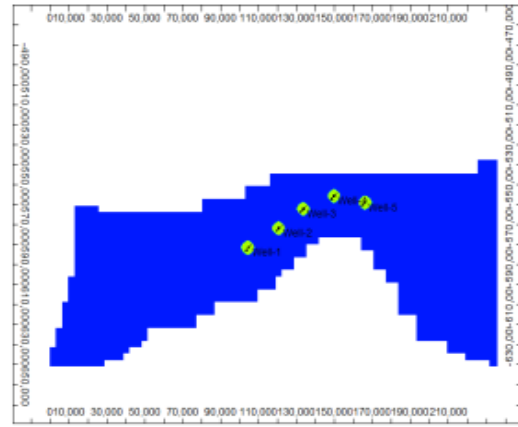
Figure 3-4: Top view of the Nisku formation in the Wabamun Lake area (study area is outlined by red).

3-3-1- Dependency of Plume Size and Pressure Field on the Number of Injectors

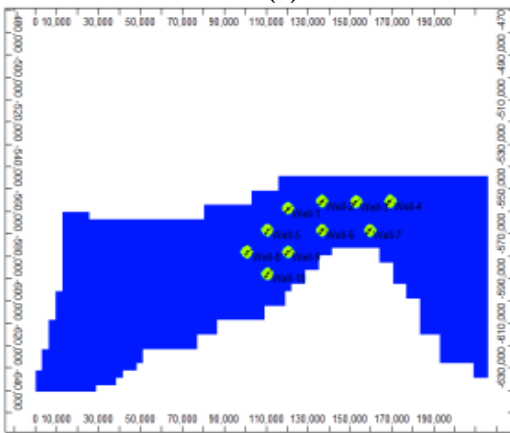
Figure 3-5 presents the plume extension and pressure distribution after 50 years of injection using base case properties. For the case with one well, the plume radius in the top layer is about 2.8 mi, which is consistent with the conceptual model as well as analytical solution radius (Nordbotten et al., 2005). It is noticeable that the size of “*pressure plume*” is much larger (about 40 mi), even for one well. In the cases of n number of injectors, one can see the existence of n individual plumes for CO₂ saturation. As the number of wells increases, the individual injector flow-rate decreases (fracture pressure constraint) and consequently the plume radius decreases. For pressure, however, strong interference between injectors occurs leading to pressurization of the total area covered by injectors and far beyond that.



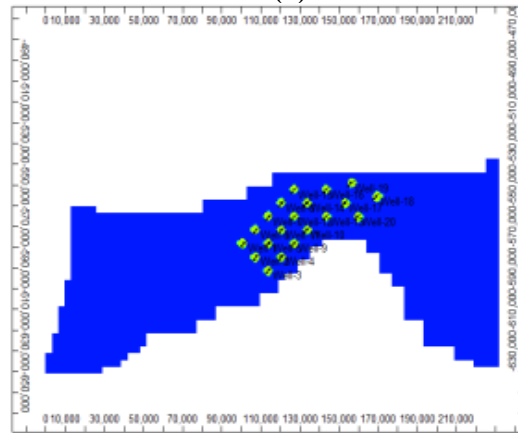
(a)



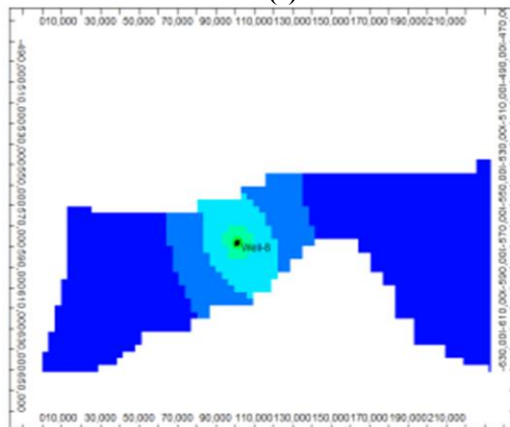
(b)



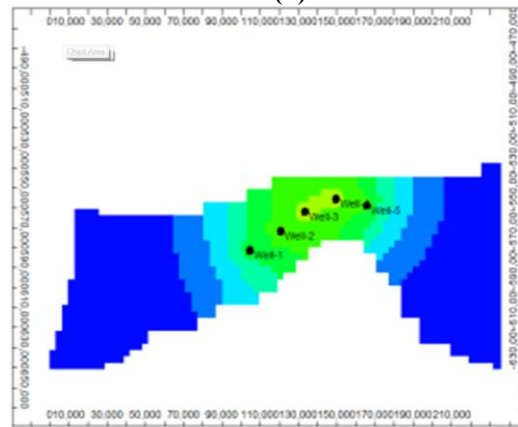
(c)



(d)



(e)



(f)

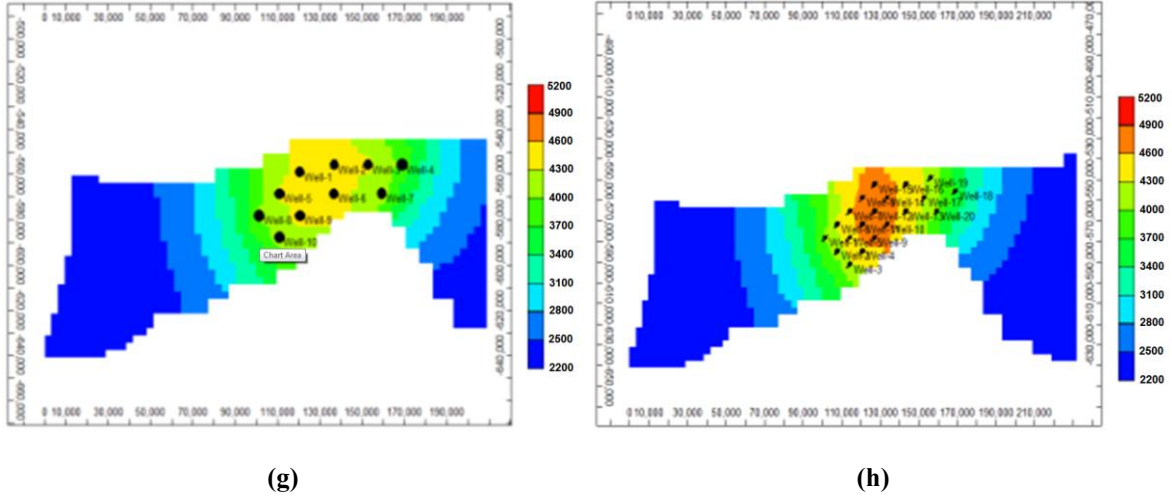
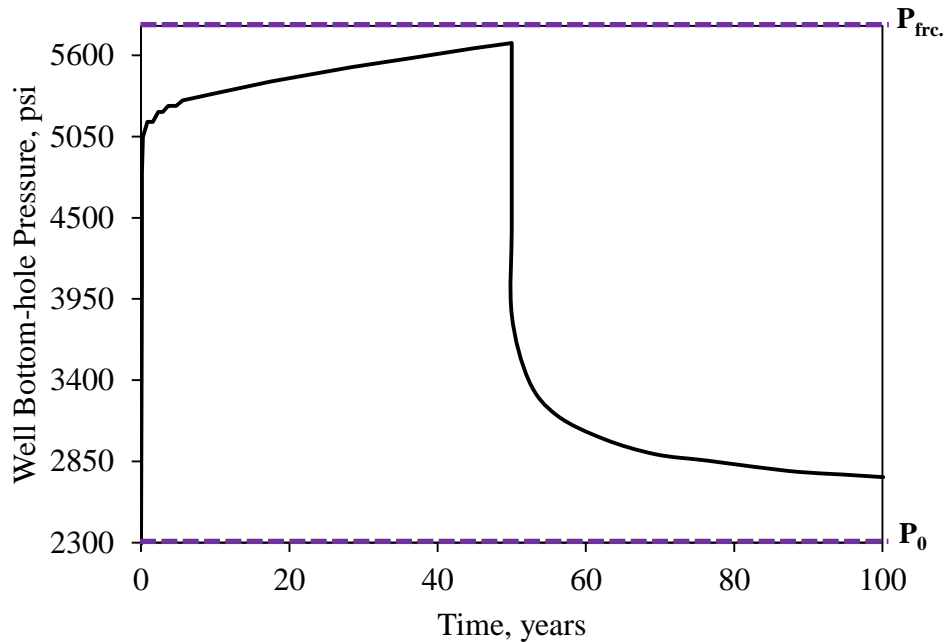


Figure 3-5: (a–d) Saturation and (e–h) pressure distribution after 50 years of injection for different numbers of wells in the Nisku study area (wells within the red area in Figure 3-4).

It is very important to mention that the dynamics of the pressure field is very different for one well injection and for multiple injection wells, as depicted in Figure 3-6. One can see that the pressure fall-off after ending CO₂ injection is much quicker for a single well than multiple wells. The pressure fall-off for multiple wells is much slower because of the larger area of pressure influence.



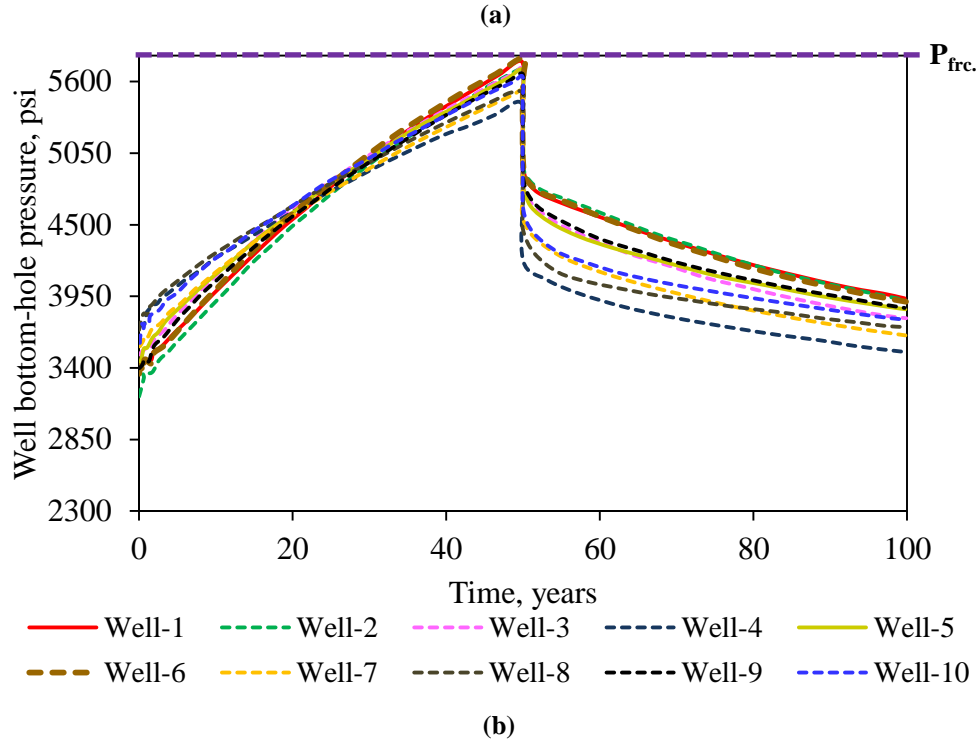


Figure 3-6: Pressure buildup and drawdown during CO₂ injection and after stopping injection for (a) one injector (b) 10 injectors.

3-3-2- Sensitivity Study of Injection Capacity

Starting with one well, the maximum achievable rate was determined to be as high as 1.1 Mt CO₂/year (matches the results of conceptual), which is equivalent to 0.055 Gt after 50 years. This flow rate causes the bottom-hole pressure to reach 5800 psi (fracture pressure of capping formation) at the end of the injection period. This value for the formation fracture pressure was assumed by WASP team at the beginning of the project based on some literature data for Alberta reservoirs. Later, midway through the project, the Geomechanical Simulation Group (part of the WASP team) estimated this value to be around 5100-5300 psi. Because our original assumption was very close to this estimate, the 5800 psi estimate was kept in our reservoir numerical modeling (a sensitivity of capacity to different fracture pressures within the range of 4300 to 5800 psi is presented

later in this section). When the next five wells are placed in the zone, the corresponding flow rate for each well reduces to 0.625 Mt/year per well with cumulative injection of 0.15 Gt. Increasing the number of wells to ten, brings the flow rate to 0.418 Mt/year per well with total injected CO₂ of 0.209 Gt. Finally, the values for 20 wells are equal to 0.476 Mt/year and 0.238 Gt, respectively. These results are shown in Figure 3-7 (solid-line curve). In addition, we estimated the reservoir properties required to achieve the target storage of 1.0 Gt. The dashed-line curve on Figure 3-7 presents the injection capacity of the focus area with the following aquifer properties: porosity of 20%, horizontal permeability of 90 mD. Although these values cause significant difference in the outcome, the limitation in injectivity improvement for more than 10 wells still exists.

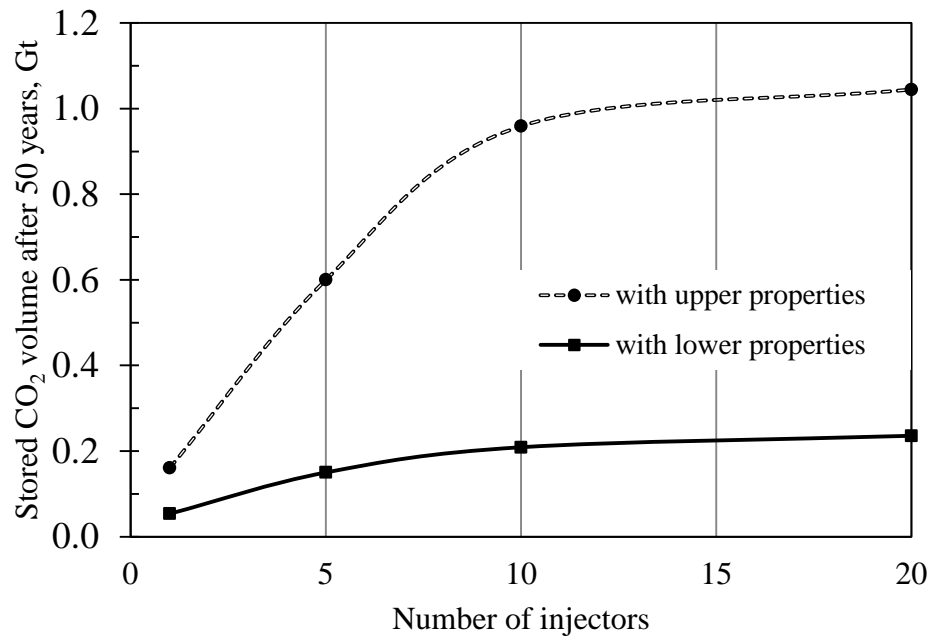


Figure 3-7: Variation of Nisku capacity with respect to number of wells and formation properties (solid line represents base properties).

3-3-3- Some Options to Increase Capacity (Horizontal Injection, Fracturing)

In the storage process, the term “capacity” could have two meanings. The *apparent*

capacity is the available and accessible pore volume of the aquifer. However, the *injection capacity* is the amount of CO₂ that can be injected realistically into the formation and is a function of the number of wells and the fracture pressure of the formation. As discussed earlier, for a restricted injection area, such as one in the Nisku study, increasing the number of wells beyond a certain limit (which is controlled by formation properties and injection site area) has a minor effect on the injection capacity. A few methods that could increase injection capacity are discussed below.

The first method is using horizontal wells instead of vertical wells. For vertical wells, it is preferable to use fully penetrated wells over the whole thickness of the aquifer. To find the minimum length of the horizontal well that would increase the injection capacity over vertical wells, the effective radius of pressure disturbance around the vertical injection well, which is again a function of formation properties, should be determined. After the start of injection through a vertical well, the pressure around the wellbore increases rapidly and causes the development of a narrow width pressure peak in the vicinity of the well, Figure 3-8.

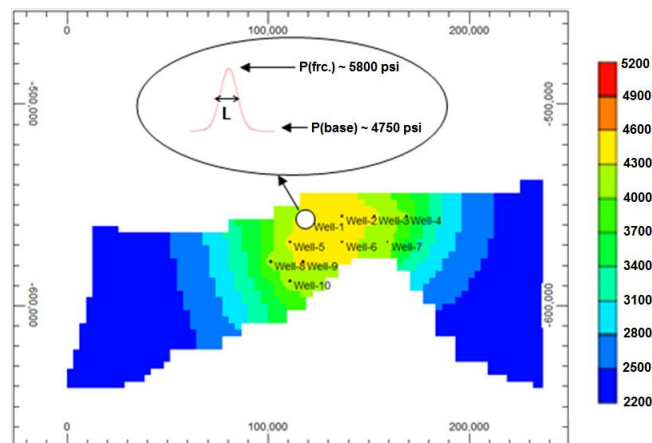


Figure 3-8: Pressure distribution at the end of injection.

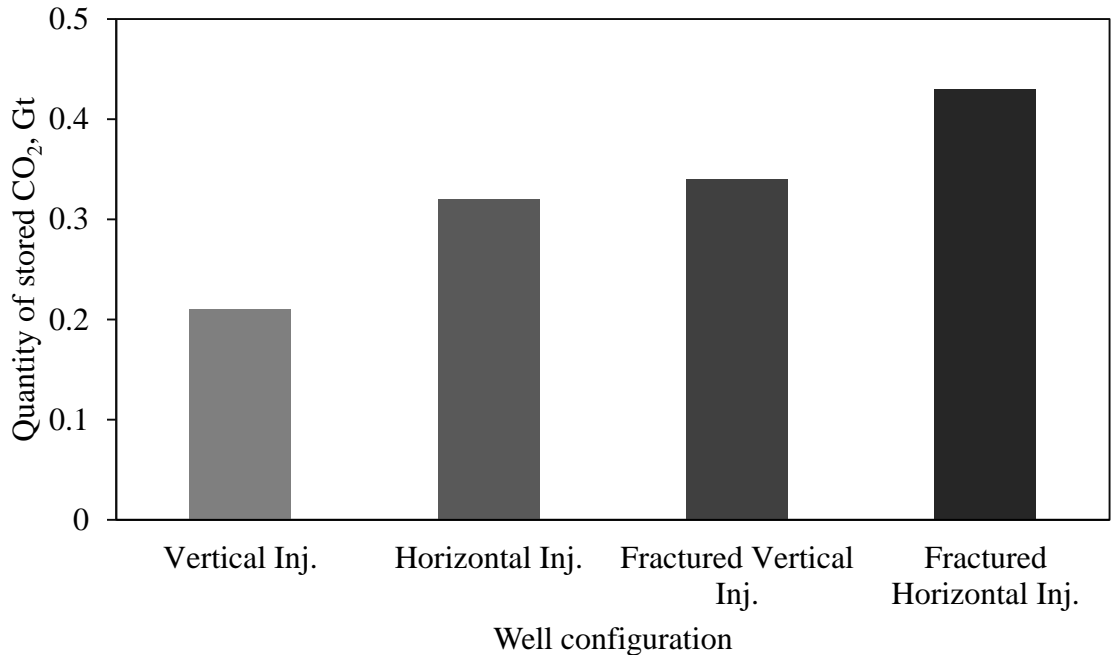


Figure 3-9: Comparison of the effect of different well configurations and stimulation on the storage capacity of the model.

Using horizontal wells with a total length greater than the scale of the vertical injector’s pressure peak “L” (Figure 2-8) will diminish these high-pressure peaks in the vicinity of the well bore and cause the injectivity to increase. For the Nisku formation, this minimum required well length was estimated to be 9,800 ft.

Figure 3-9 compares the effect of different well configurations on the achievable CO₂ injection capacity. While the vertical injectors provide the minimum capacity, their replacement with the horizontal wells will increase storage capacity by approximately 50%. Application of stimulation techniques such as hydraulic fracturing (HF) can also improve injectivity, with the results depicted as the last two bars in Figure 3-9. Nevertheless, the technical feasibility of implementing these techniques requires careful geomechanical characterization of the formation. For example, maintenance of the caprock integrity is a major concern in using such techniques for secure underground storage of CO₂. The details of simulation for hydraulic fracturing can be found

somewhere else (Ghaderi et al., 2009).

3-3-4- Heterogeneity Sensitivity Study

Two different heterogeneity modeling methods were considered in this study: stochastic and object based modeling. The stochastic modeling was based on existing quantitative data (wireline sonic and density logs, acoustic impedance) and geo-statistical tools. It relies on resistivity-derived porosities and permeabilities (nearly 60 wells). For this study, 5 equi-probable realizations of properties were generated, Figure 3-10. Porosity ranges from 1.3 – 28.6 % (mean 4.9%) and permeability from 3.1 – 393 mD (mean 22.37 md). Details of the development of the geostatistical realizations, generated by a geo-statistics group for the WASP project, are presented in the Geomodeling Section (Eisinger and Jensen, 2010) of WASP report. It should be noted that the presented geo-models only cover the study area (see Figure 3-4); however, the pore volume of the boundary grids (far from the well locations) have been modified such that the total pore volume of the complete model is still honored. This is an important consideration for running such a huge model without sacrificing the accuracy of the results.

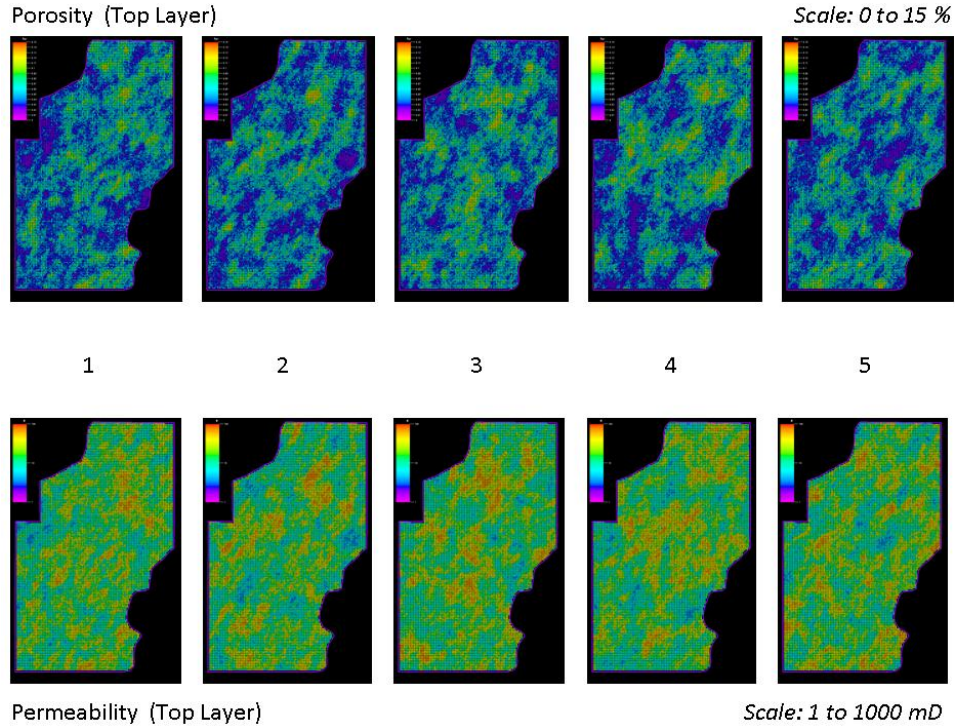


Figure 3-10: Geo-statistical realizations for porosity and permeability of WASP study area (from Eisinger and Jensen, 2010).

Object based models use “objects” (of same size) with higher porosity and permeability zones. The geometry and distribution of the objects in this study were constrained by dimensions of existing modern carbonate analogs, conceptual understanding of the Nisku carbonate in the Wabamun area, wireline log data and seismic data.

Two kinds of objects were used: i) dark blue (minor width = 1650 ft, major/minor ratio = 5, and thickness = 16.5 ft) and ii) light blue (minor width = 980 ft, major/minor ratio = 5, and thickness = 6.5 ft). These are oriented along dip and distributed in each zone (upper, middle, and lower, Figure 3-11- left) of the Nisku. Figure 3-11- right shows the trend in layering of these zones (upper third has 13 layers with average vertical grid size $z = 5.6$ ft; middle third has 5 layers with $z = 14.6$ ft and lower third has 12 layers with average $z = 6.1$ ft).

For stochastic modeling examples (realizations 4 and 5), the saturation and pressure fields are shown on Figure 3-12.

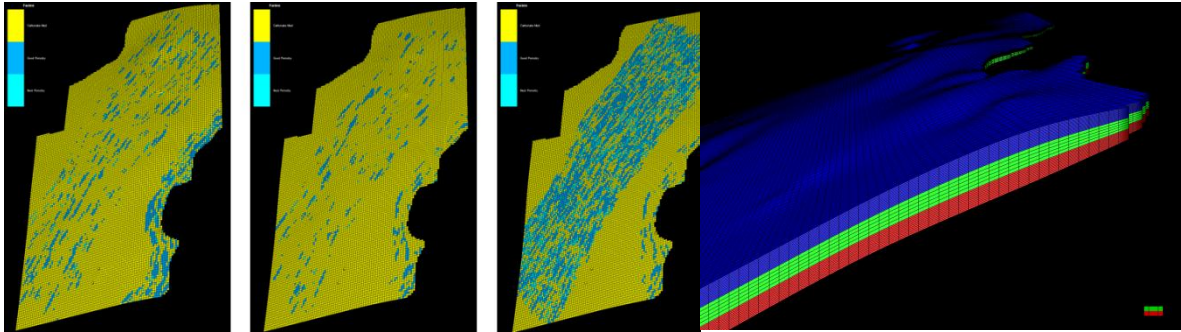


Figure 3-11: Object-based realization for porosity.

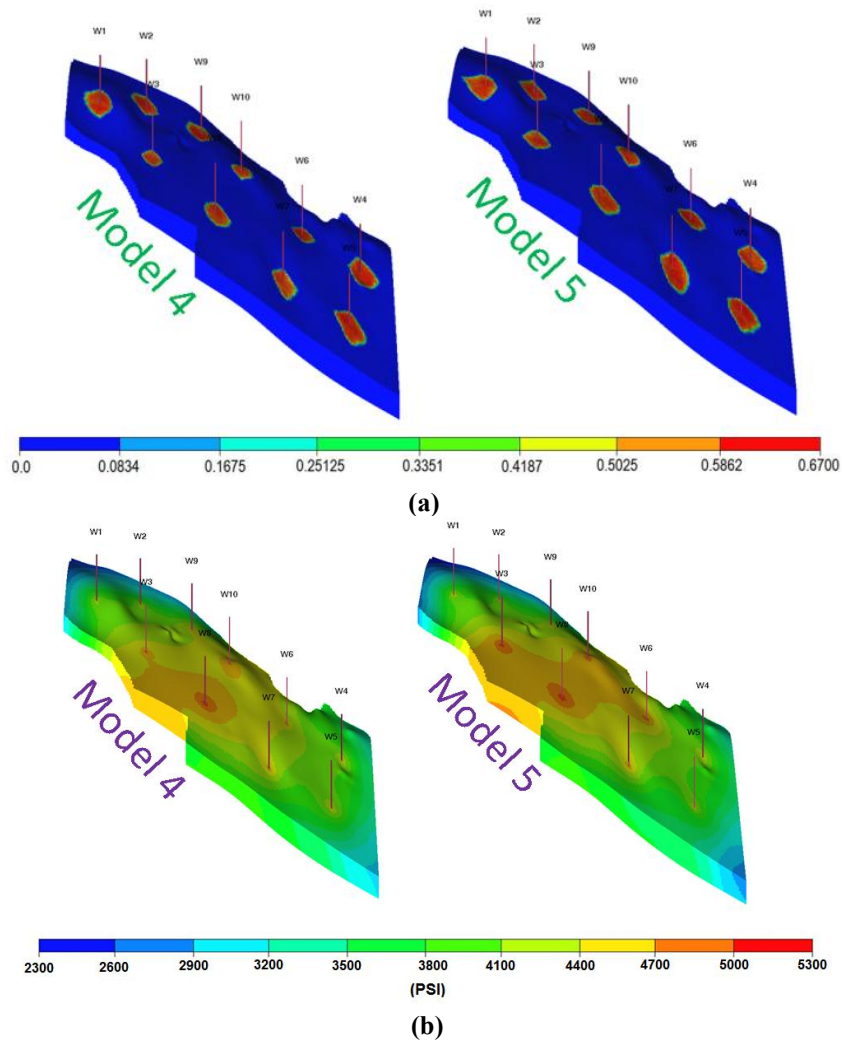


Figure 3-12: (a) Saturation and (b) pressure fields for stochastic-based geomodels after 50 years of injection.

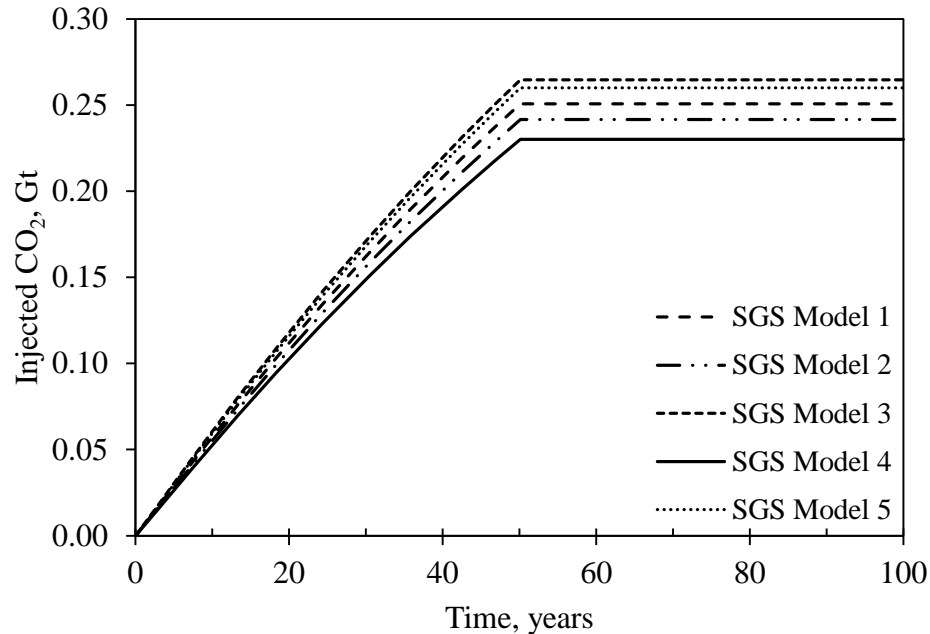


Figure 3-13: Injection capacity for 5 different realizations.

Although one can see some differences on a small scale for saturation and pressure fields of these two models, the injection capacities for all cases are almost identical (Figure 3-13) and very close to the homogeneous model (Figure 3-7, for 10 wells injection).

The above results represent the storage capacity when the fracture pressure was set to 5800 psi. To investigate the effect of fracture pressure limit on the storage capacity, simulations were run with sequential Gaussian simulation (SGS) model 1 in Figure 3-13. Sensitivity of capacity to fracture pressure is shown on Figure 3-14; a 25% reduction in fracture pressure will reduce the aquifer capacity by 40%, which is significant.

For object modeling, the saturation and pressure fields are shown in Figure 3-15. Injection capacity, as in the case of stochastic modeling, is very close to the homogeneous model, Figure 3-16.

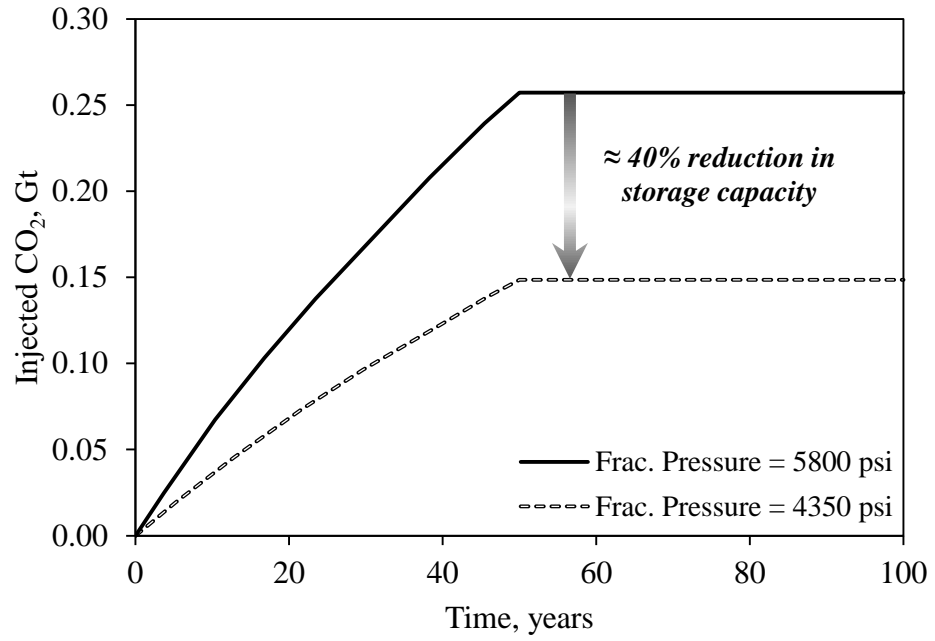
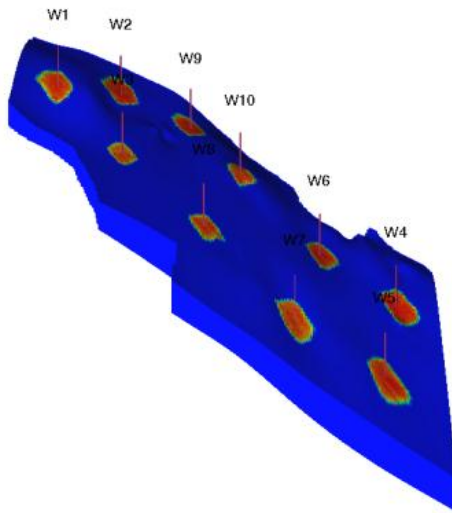
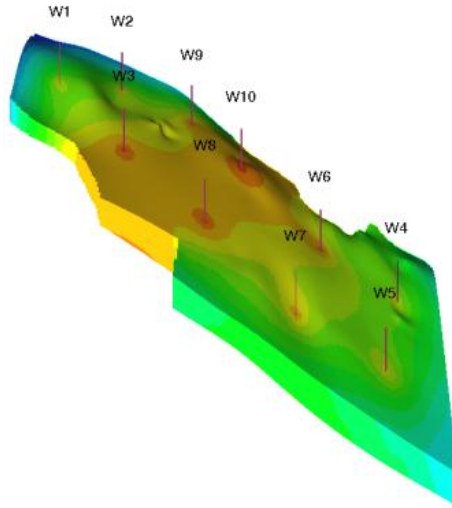


Figure 3-14: Injection capacity for two different fracture pressures.



(a)



(b)

Figure 3-15: (a) Saturation and (b) pressure fields for object modeling after 50 years of injection.

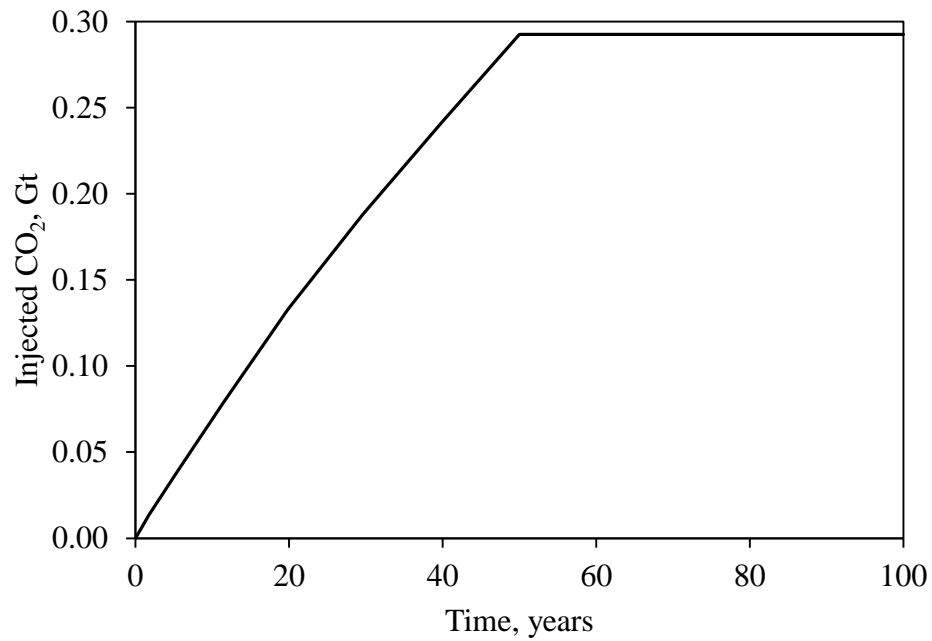


Figure 3-16: Injection capacity for object modeling.

Based on this limited number of realizations, it is tentatively concluded that the small scale heterogeneity (compared to plume size) considered in this study does not exert a strong control on pressure and saturation fields or on overall capacity of the injection site.

However, it is expected that for layered systems, and for objects comparable to plume size, the effect of heterogeneity will be substantial. This heterogeneity will especially affect selective placement of injectors. Such a study would require more detailed knowledge of the property distribution within the aquifer.

3-4- Long-term Fate of CO₂ Injection

In this section, the long-term fate of CO₂ injection is discussed in association with the following phenomena:

- Increased aquifer pressure during and after injection
- Migration of CO₂ beyond injection area due to dip
- Buoyancy of CO₂ over long period of time (leakage risk)
- H₂S issues

3-4-1- Pressure Field Evolution during and after Injection

As discussed in the previous sections, the pressure in the aquifer (within and around injection area) increases rapidly during the injection period and then gradually decreases toward the initial pressure distribution after injection stops, due to the very large volume of the Nisku aquifer. It is important to know how long it will take for a substantial pressure disturbance to dissipate. The simulation results of a 10-well scenario are presented in Figure 3-17.

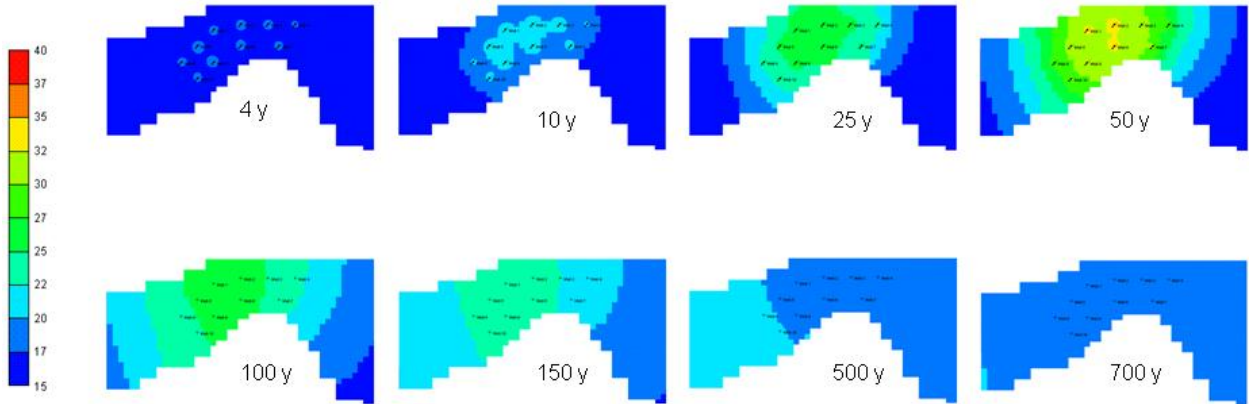


Figure 3-17: Pressure build-up (top row) during injection and pressure fall-off (bottom row) after injection stops for an injection scenario with 10 wells each injecting at 0.5 Mt/year for 50 years.

One can see that pressure does not reach initial reservoir pressure ($P_i = 2,320$ psi) even 650 years after injection stops, although the difference in $\Delta P = P - P_i$ is small compared to the maximum difference ($\Delta P_{\max} = 3480$ psi = $P_f - P_i$ at the end of injection). The graph of ΔP vs. time is presented in Figure 3-18, which allows estimation of the time scale of pressure decay. From this graph, it can be inferred that ΔP falls e (~ 2.7) times at ~ 120 years, when the pressure fall-off curve starts to level off and thereby providing the time scale for the fate of pressure under injection design.

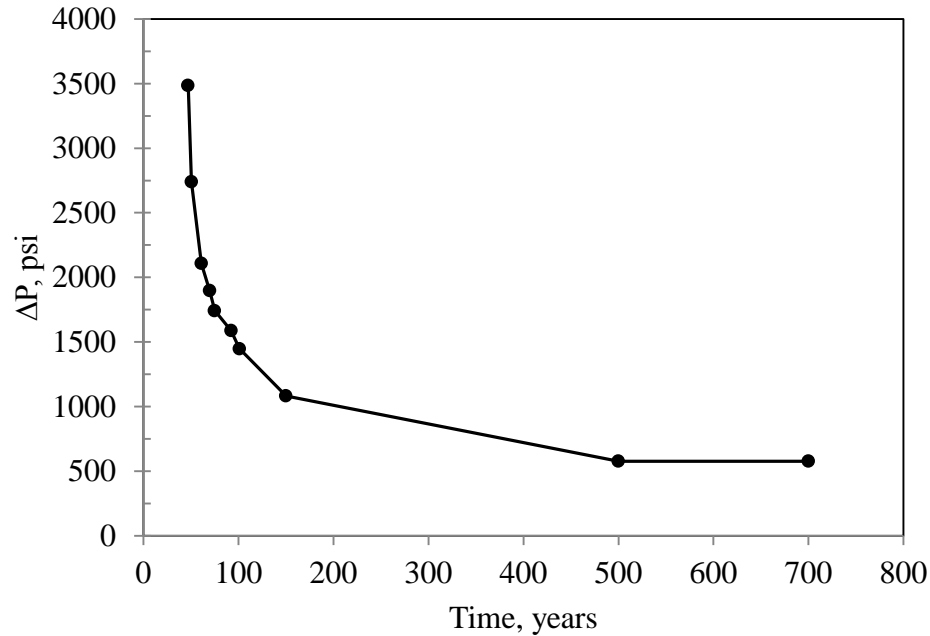


Figure 3-18: ΔP (P-P_i) versus time

3-4-2- Effect of Aquifer Dip on Plume Movement and its Size

The effect of aquifer dip was evaluated with simulation runs using the base Nisku properties (Figure 3-4) and a single well injection rate of 1 Mt/year for 50 years. Simulations were run up to 1000 years after injection started, and two cases were considered for comparison: i) dip angle = 0° and ii) dip angle = 0.5°. The second case corresponds to the average dip angle of Nisku formation. The results of CO₂ saturation at the top layer vs. time are shown in Figure 3-19. One can see that at base conditions the effect of dip angle on the plume movement is marginal (Figure 3-19-a), although when permeability was increased (while all other parameters remained the same) noticeable plume migration along dip was observed (Figure 3-19-b).

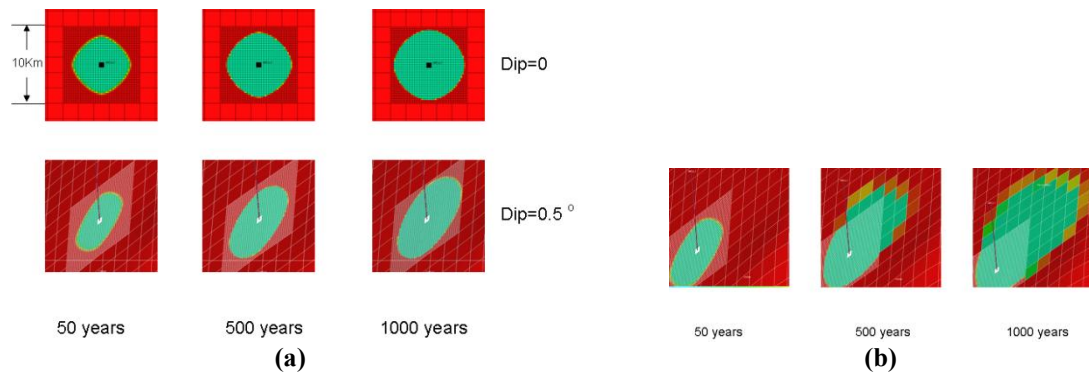


Figure 3-19: Saturation field for a single injector: (a) base properties; (b) permeability is increased to 150 mD.

The above results suggest that if the plume reaches regions with higher permeability, it will migrate upwards, and this should be taken into consideration for management of leakage risk.

3-4-3- Estimation of Onset of Convection for Free Phase CO₂

The CO₂ injected into a deep aquifer is typically 10-40% less dense than the resident brine. Driven by density contrasts, CO₂ will flow vertically first and then horizontally spreading under the caprock (Leonenko and Keith, 2008). If there are breaches in the caprock, leakage could occur through these high permeability zones or through artificial penetrations such as abandoned wells. It is very important to know how long the CO₂ remains as a free phase beneath the caprock and how long complete dissolution of CO₂ into the brine phase will take because this determines the timescale over which free phase CO₂ has a chance to leak out. After injection, free-phase CO₂ (gas or supercritical fluid) will be partially trapped as residual saturation and the rest will slowly dissolve in the brine (Hassanzadeh et al., 2006). Depending on reservoir properties, different mechanisms may be responsible for dissolution. Here we estimate the dissolution mechanisms at Nisku conditions and the associated time scales of dissolution. In the short

term (Figure 3-20-a), during and after injection, some amount of CO₂ is residually trapped and the remainder may be dissolved by natural convection (Figure 3-20-b). The amount of trapped CO₂ depends on rock fluid properties (relative permeability curves), and in the Nisku case, is about 30%. The amount of dissolved CO₂ depends on reservoir pressure and temperature as well as brine salinity, and in the Nisku case, is about 3-5%. The remaining amount of free CO₂ (~65%) will slowly dissolving into the brine by a combination of diffusion and natural convection.

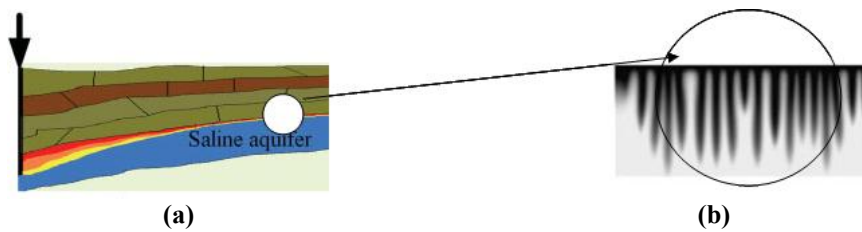


Figure 3-20: (a) Accumulation of free CO₂ below the caprock (short-term) and (b) combination of diffusion and natural convection (long-term processes) involved in geological storage of CO₂ in saline aquifers. (Source of figure: Hassanzadeh et al., 2007)

The important parameter to describe convection is the porous medium Rayleigh number, defined as $Ra = kgh\Delta\rho/(\mu\phi D)$, where k is permeability, ϕ is porosity, g is acceleration due to gravity, h is aquifer thickness, μ is viscosity, $\Delta\rho$ is the density difference (CO₂ saturated and fresh brine) and finally D is the molecular diffusion coefficient. If $Ra > 49$ then natural convection occurs. At Nisku conditions, $Ra \sim 400$, from which we estimated the onset of convection at these conditions ($t_{\text{onset}} \sim 80$ years) and time scale of convective dissolution ($t_{\text{dis}} \sim 3000$ years). Estimations are made based on Hassanzadeh's model (Hassanzadeh et al., 2007). One can see that the time scale for possible leakage is very long and this can be a serious obstacle for implementation of an injection project due to regulatory and monitoring issues. Active reservoir engineering might be needed (for example, see Leonenko and Keith, 2008) to reduce the dissolution time to the scales of hundreds years.

3-4-4- H₂S Issue

While working on the WASP project, we discovered that when CO₂ is injected into a sour saline aquifer, the H₂S initially dissolved in the brine will be exsolved and released into an expanding CO₂ plume. A comprehensive study of this phenomenon has been made and all detailed results were discussed in Chapter 2.

3-5- Summary

In this study we performed numerical modeling of injection of large volumes of CO₂ (1 Gt target over 50 years) into the Nisku Formation located in Alberta. Injection modeling was performed within localized injection area of 18.5 mi × 37 mi. The main objectives of the study were to:

- estimate the injection capacity and CO₂ plume movement and pressure distribution during and after injection;
- estimate the time scale of pressure relief upon injection, time scale of CO₂ dissolution, effect of dip angle on plume shape and its migration; and
- assess the possible H₂S evolution in the CO₂ plume over time and space.

The following observations were made in this study:

- The capacity of injection is limited not by available pore space but by ability to inject without exceeding the fracture pressure of the formation. The capacity increases with the number of injectors but increasing the number of wells has a limit even considering a large well spacing. Very strong interference between pressure plumes was observed with no substantial benefits beyond 10 wells. Horizontal injection wells and aquifer fracturing may be considered as alternative options to increase the capacity. Sensitivity of capacity to reservoir permeability,

rock compressibility and well placement was investigated.

- For multiple injection scenarios (n wells), CO₂ saturation plumes have no interference; we see n individual plumes of radius 2.5-3 mi for each injector. The pressure field behavior is totally different from the saturation field. There are no individual pressure plumes but a single large (scale of hundred km) pressure envelope.
- The dip in the Nisku formation does not affect the results (i.e. no substantial plume movement) although free phase CO₂ may migrate along the dip if it reaches a zone with higher permeability above 100 mD. We estimated that at Nisku conditions, the time scale for pressure relief is 120 years and time scale for free phase CO₂ dissolution is ~3000 years where the mechanism of dissolution is natural convection.
- H₂S dissolved in aquifer brine will be released into the CO₂ plume during injection and will reach a high mole fraction at the outer edge of the CO₂ front.

Acknowledgments

Financial support for this work was provided by NSERC Strategic Grant and AERI with additional funding from industry partners through Wabamun Area CO₂ Sequestration Project (WASP) led by the University of Calgary. Simulation software (CMG) was donated by Computer Modeling Group. This support is gratefully acknowledged. We also wish to thank Long Neighem and Vijay Shrivastava for their help with the new version of GEM and for useful discussions of its applications to this study.

References

- Bennion, B., Bachu, S., 2008. Drainage and Imbibition Relative Permeability Relationships for Supercritical CO₂/brine and H₂S/brine Systems in Intergranular Sandstone, Carbonate, Shale, and Anhydrite Rocks. SPE Reservoir Evaluation & Engineering, vol. 11(3), pp. 487-496.
- Eisinger, C.L., Jensen, J.L., 2010. Data Integration, Petrophysics, and Geomodeling, in Wabamun Area CO₂ Sequestration Project. Report @ <http://www.ucalgary.ca/wasp/Geology%20and%20Geomodeling.pdf>.
- Ghaderi, S.M., Keith, D.W., Leonenko, Y., 2009. Feasibility of Injecting Large Volumes of CO₂ into Aquifers. Energy Procedia, vol. 1(1), pp. 3113-3120.
- Ghaderi, S.M., Keith, D.W., Lavoie, R., Leonenko, Y., 2011. Evolution of Hydrogen Sulfide in Sour Saline Aquifers during Carbon Dioxide Sequestration. International Journal of Greenhouse Gas Control, vol. 5(2), pp. 347-355.
- Hassanzadeh, H., Pooladi-Darvish, M., Elsharkawy, A.M., Keith, D.W., Leonenko, Y., 2008. Predicting PVT Data for CO₂-brine Mixtures for Black-oil Simulation of CO₂ Geological Storage. International Journal of Greenhouse Gas Control, vol. 2 (1), pp. 65-77.
- Hassanzadeh, H., Pooladi-Darvish, Keith, D.W., 2006. Stability of a Fluid in a Horizontal Saturated Porous Layer: Effect of Non-linear Concentration Profile, Initial, and Boundary Conditions. Transport in Porous Media, vol. 65(2), pp. 193-211.
- Hassanzadeh, H., Pooladi-Darvish, Keith, D.W., 2007. Scaling Behavior of Convective Mixing, with Application to Geological Storage of CO₂. AIChE

Journal, vol. 53(5), pp. 1121-1131.

- Hitchon, B., 1996. Aquifer Disposal of Carbon Dioxide, Hydrodynamic and Mineral Trapping: Proof of Concept, Geoscience Publishing Ltd., Sherwood Park, Alberta, Canada.
- Intergovernmental Panel on Climate Change (IPCC), 2007. In: Core Writing Team, Pachauri, R.K., Reisinger, A. (Eds.), Climate Change 2007: Synthesis Report. Contribution of Working
- Leonenko, Y., Keith, D.W., 2008. Reservoir Engineering to Accelerate the Dissolution of CO₂ Stored in Aquifers. Environmental Science and Technology, vol. 42(8), pp. 2742-2747.
- Karsten, M., Bachu, S., and Buschkuehle, B.E., 2007. Assessment of a Carbonate Aquifer for CO₂ Geological Storage in the Wabamun Lake Area. CSPG/CSEG convention, May 14-17.
- Nordbotten, J.M., Celia, M.A., Bachu, S., 2005. Injection and Storage of CO₂ in Deep Saline Aquifers: Analytical Solution for CO₂ Plume Evolution during Injection. Transport in Porous Media, vol. 58(3), pp. 339-36.

Chapter 4

Investigation of Primary Recovery in Low-Permeability Oil Formations: A Look at the Cardium Formation, Alberta¹

Tight oil formations (permeability <1 mD) in Western Canada have recently emerged as a reliable resource of light oil supply owing to the use of multi-fractured horizontal wells. The Cardium Formation, which contains 25% of Alberta's total discovered light oil (according to Alberta Energy Resources Conservation Board), consists of conventional and unconventional (low-permeability or tight) play areas. The conventional play areas have been developed since 1957. Contrarily, the development of unconventional play is a recent event, due to considerably poorer reservoir properties, which increase the risk associated with capital investment. This in turn implies the need for a comprehensive and critical study of the area before planning any development strategy.

This chapter presents performance results from the low permeability portions of the Cardium Formation where new horizontal wells have been drilled and stimulated in multiple stages to promote transverse hydraulic fractures. Development of the tight Cardium Formation using primary recovery is considered. The production data of these

¹ This chapter is modified version of: Ghaderi, S.M., Clarkson, C.R., Kaviani, D., 2013. Investigation of Primary Recovery in Low-Permeability Oil Formations: A Look at the Cardium Formation, Alberta (Canada). Journal of Oil & Gas Science and Technology, DOI: 10.2516/ogst/2012091

wells was first matched using a black oil simulator. The calibrated model presented was used for performance predictions based on sensitivity studies and investigations that encompassed design factors such as well spacing, fracture properties, and operational constraints.

4-1- Introduction

Economic production of hydrocarbons from reservoir rocks requires reservoir-specific solutions. Until recently, oil and gas exploitation was restricted to relatively high permeability and porosity reservoirs. In such reservoirs, wellbore contact through vertical wells was sufficient to obtain economic rates and recovery. Recent advances in drilling and completion technology have enabled commercial production from reservoirs with poorer properties. The low-permeability area of the Pembina Cardium Field in Western Canada, referred to as a “Halo Oil” play by Clarkson and Pedersen (2011), is an example.

The Pembina Cardium field is the principal conventional oil pool in Canada covering an area of over 3,000 km² with more than 6,100 (approximately 4,400 producers and 1,700 injectors which are mainly vertical). OOIP is in excess of 7,780 MMbbl with recovery of less than 17% to date. The field is located in a stratigraphic trap of northwest-southeast oriented shoreface sands with the eastern up-dip margin being defined by shale out of the sands and the western downdip margin by decreasing reservoir quality (Krause et al. 1987). Horizontal wells have been drilled in both the Cardium sands and conglomerates within the Pembina field with limited success (Adegbesan et al. 1996).

In 2008, the first horizontal well with seven hydraulic fracture stages was completed in the unconventional (low-permeability) portion of the Cardium. The production rates from this well were so promising (average production rates of approximately 123 bbl/day

without any water production) that another 12 wells were drilled in 2009 (Viau and Nielsen, 2010). Since then, more and more multi-fractured horizontal wells are being completed or planned in the area by different companies.

Because the unconventional portion of the Pembina is at early stages of production and development, more detailed studies are required for better management and exploitation of the resources. In this study, our purpose is to determine the major parameters that will affect the recovery of oil from these reservoirs under primary production scheme when fractured horizontal wells are being used. Oil production rates from the wells are usually high at the beginning, however limited reservoir permeability impedes favorable rates over the long term. Therefore short-term and long-term production performance will be considered separately in this work. As part of the study, extensive numerical simulations were performed using the ECLIPSE 100™ simulator¹ (Schlumberger, 2010). The “design of experiment” approach was employed to define the simulation scenarios and the parameters involved. In each simulation run, several parameters can be varied simultaneously to capture the effect of all main parameters and their likelihood of interaction. The oil recovery from simulation runs will be the main response in the statistical interpretation of the results. Simulation strategies and results will first be discussed.

4-2- Base Properties Used in Simulation Models

The properties required for generating simulation models were obtained from one of the active operators in the area. To avoid issues related to reservoir heterogeneity, all reservoir properties are considered constant at their average values. Some of these

¹ ECLIPSE 100, ECLIPSE, and PVTi are trademarks of Schlumberger.

properties are summarized in Table 4-1 (modified from Clarkson and Pederson, 2010).

Table 4-1: General properties of the simulation models

Property	Value
Thickness, ft	16.4
Porosity, %	12
Absolute permeability, mD	0.28
Initial reservoir pressure, psia	2,017
Initial oil saturation, %	86
Initial water saturation, %	14
Reservoir temperature, °F	115
Model area, acres	640
Number of blocks, NX×NY×NZ	105×105×3
Dimension of blocks, ft×ft×ft	50×50×5.46

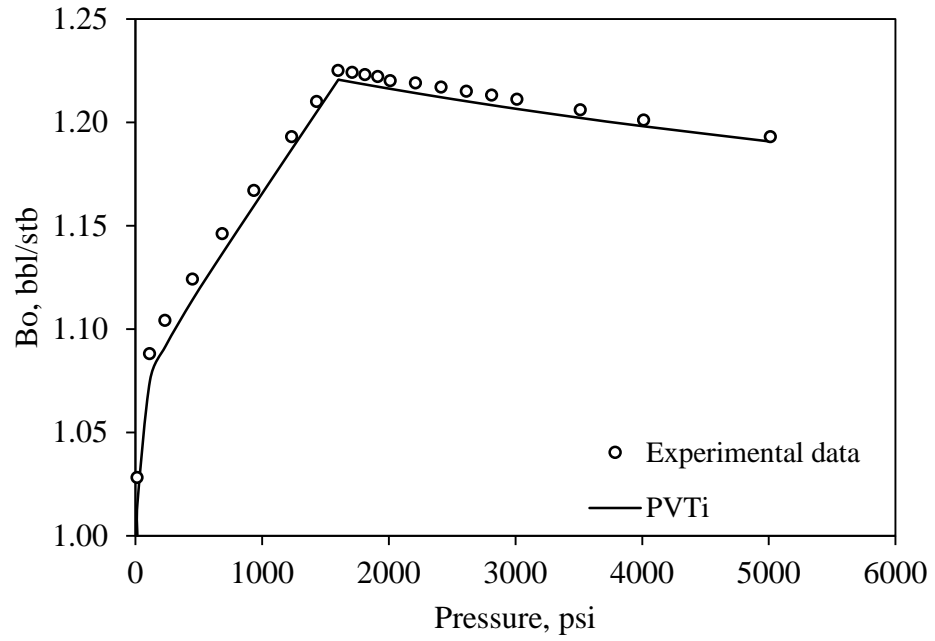
The data in this table have been obtained from an area of Cardium where the pay zone varies between 16 to 26 ft and the reservoir rock consists of muddy fine-grained sandstones with low permeability (≈ 0.3 mD) but relatively suitable porosity (≈ 0.12). It is also known that the reservoir is not supported by any initial gas cap (note the initial reservoir pressure and oil bubble point pressure in Table 4-1 and Table 4-2) or bottom water support and therefore the main mechanism of primary production would be through solution gas drive (Clarkson and Pederson, 2010).

Table 4-2 provides the fluid data used in the simulation models which are based on the real data obtained from one of the wells in the study area. The oil is relatively light with °API equal to 37.

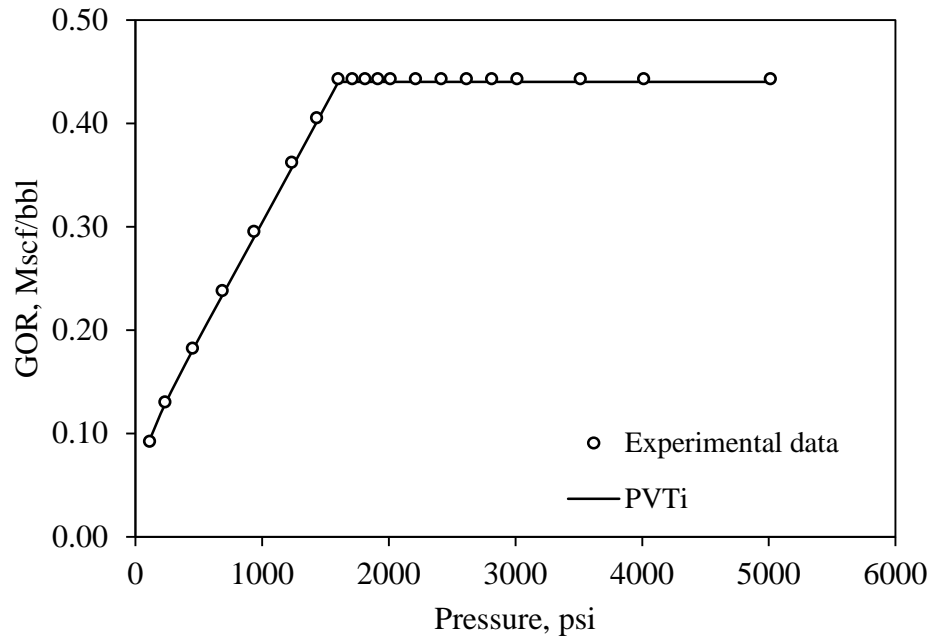
Table 4-2: Fluid properties used in the simulations

Phase/Property	Value
Oil	
Pb (psia)	1,602
Rs at Pb (scf/stb)	430
Viscosity at Pb (cp)	1.43
Bo at Pb (bbl/stb)	1.22
Density at STP (lb/ft ³)	51.8
Gas	
Ave. Viscosity (cp)	0.011
Density at STP (lb/ft ³)	0.069
Water	
Viscosity (cp)	0.58

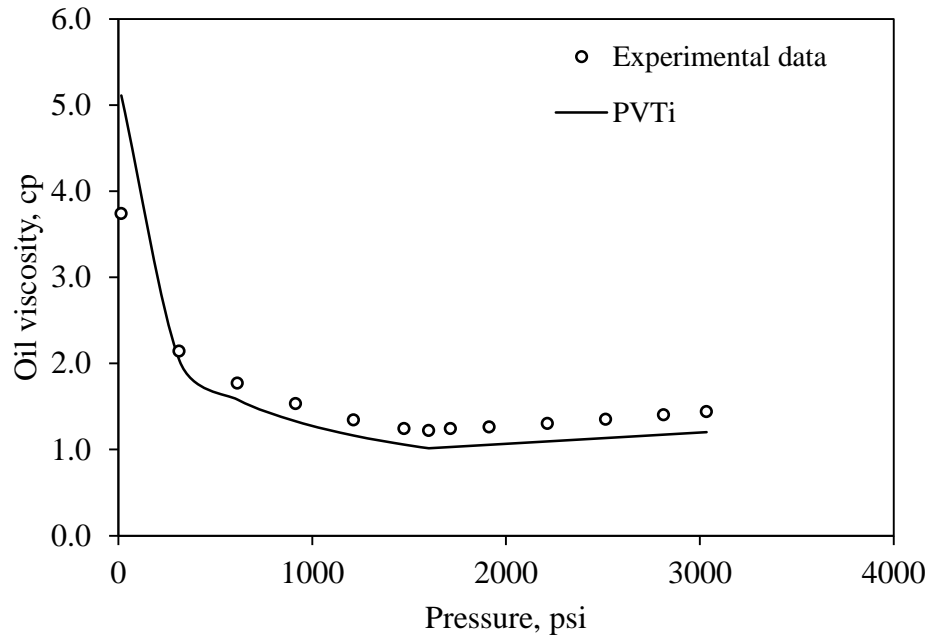
Figure 4-1 depicts the results obtained from the simulation of the PVT data for oil and gas using the PVTi™ module of Eclipse (Schlumberger, 2010). Figure 4-1-a and Figure 4-1-b show the results of the differential liberation test, and the viscosity measurements (Figure 4-1-c and Figure 4-1-d) obtained from constant composition expansion test. Pedersen's correlation (Pedersen et al. 1984) was used to match the viscosity data. For the range of pressure applicable to this study (200-2,000 psia), the match of the PVT data is acceptable. The results of Table 4-2 are similar to what was used by Clarkson and Pedersen (2010) using standard correlations.



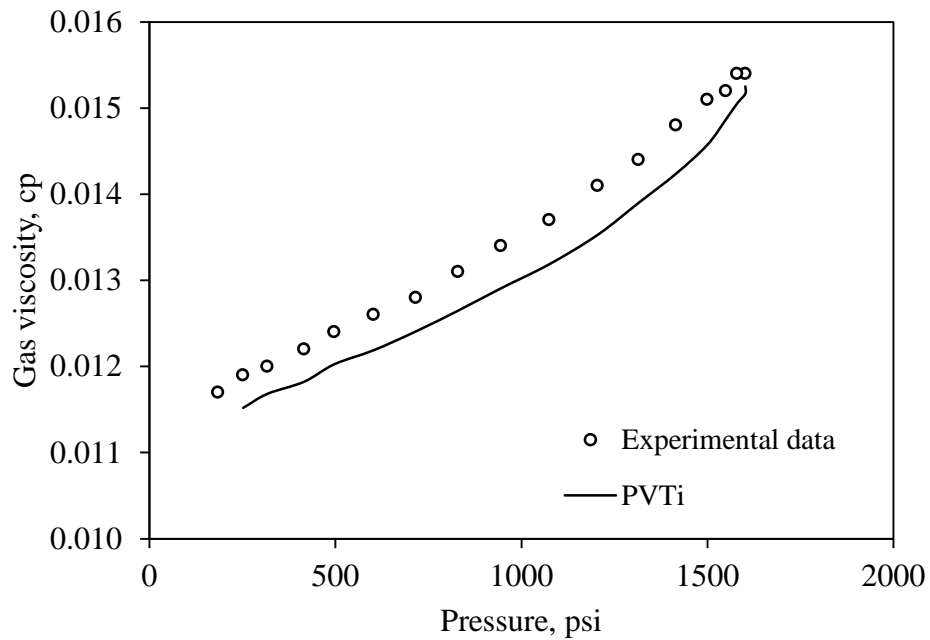
(a)



(b)



(c)



(d)

Figure 4-1: Comparison between experimental and simulated PVT behavior of the fluid used in this study (a) oil formation volume factor vs. pressure (b) oil solution gas vs. pressure (c) oil viscosity vs. pressure (d) gas viscosity vs. pressure.

One missing element in our simulation models was a relative permeability data set.

To obtain the relative permeability, or at least a rough estimate of its shape, we tried to

history match the production data of the wells in the study area and used the relative permeability data as the matching parameter. We received about one year production data for three separate wells in the region from an operator. For the well selected for analysis, the pressure is somewhat less than the virgin pressure (approximately 2,500 psi), suggesting that some depletion due to offsetting vertical wells may have occurred. Nonetheless, we analyzed the well individually, realizing that a field simulation may be justified.

Well completion data were obtained from the operator. The length of the horizontal well is 3,865 ft and its wellbore diameter is 7.2 inches. It was frac'd in 10 stages with an average fracture spacing of 429 ft (assuming 1 fracture per stage). We estimate the fracture half-length to be equal to 181 ft and fracture conductivity close to 300 md-ft. The well is completed open-hole (Clarkson and Pedersen 2010).

Figure 4-2-a displays a close-up view of the simulated transverse fractures planes which are perpendicular to the well trajectory. To precisely capture the physics of the fluid flow in the models, the local grid refinement (LGR) feature is used to explicitly construct the hydraulic fractures along the well. However, exact duplication of the fractures' width in a simulation model will require extremely refined grids which results in computationally very expensive models (Shaoul et al. 2007). Therefore, a sensitivity study was performed to determine the optimal degree of refinement for the fractures blocks as well as the parent block dimensions (see Appendix 4A). Also, transmissibility of the fractures blocks should be adjusted such that following relationship holds:

$$k_f \times w_f = k'_f \times \Delta_f \quad (4-1)$$

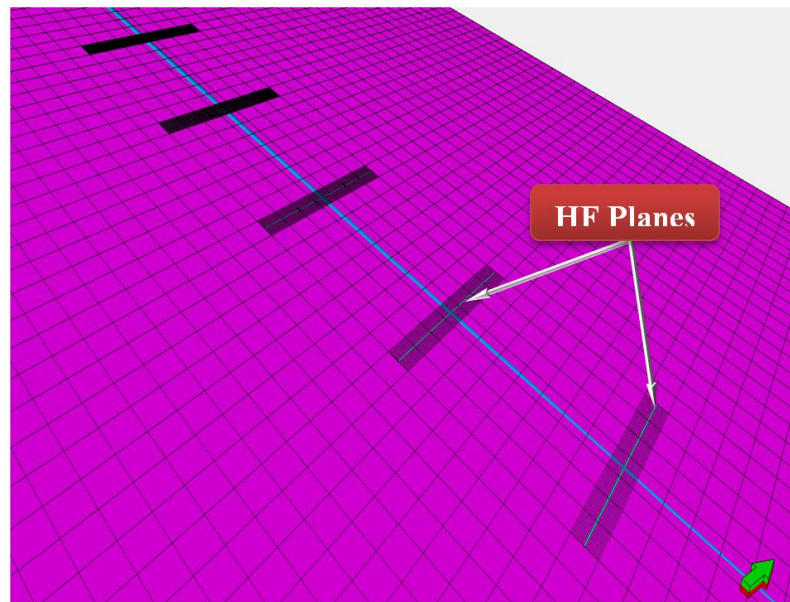
where $k_f \times w_f$ is the product of fracture permeability and width and $k'_f \times \Delta_f$ is the corresponding product in the simulation model. The hydraulic fractures in our study have a constant width equal to 2.0 ft which are obtained by dividing the parent grid block into 25 parts in the direction perpendicular to the fracture orientation.

Figure 4-2-b shows the historic oil production rates from the subject well for almost one year. It should be noted that in Figure 4-2 time zero corresponds to the time when the well has reached the “pump-off state”, signified by a stabilized fluid level in the annulus. As the well bottom-hole pressure (BHP) was estimated from periodic fluid shots combined with casing pressure, a stabilized fluid level in the annulus indicates that the well is producing under constant BHP. For the period of production displayed in Figure 4-2-b, this BHP is close to 250 psia (the pressure data is not shown).

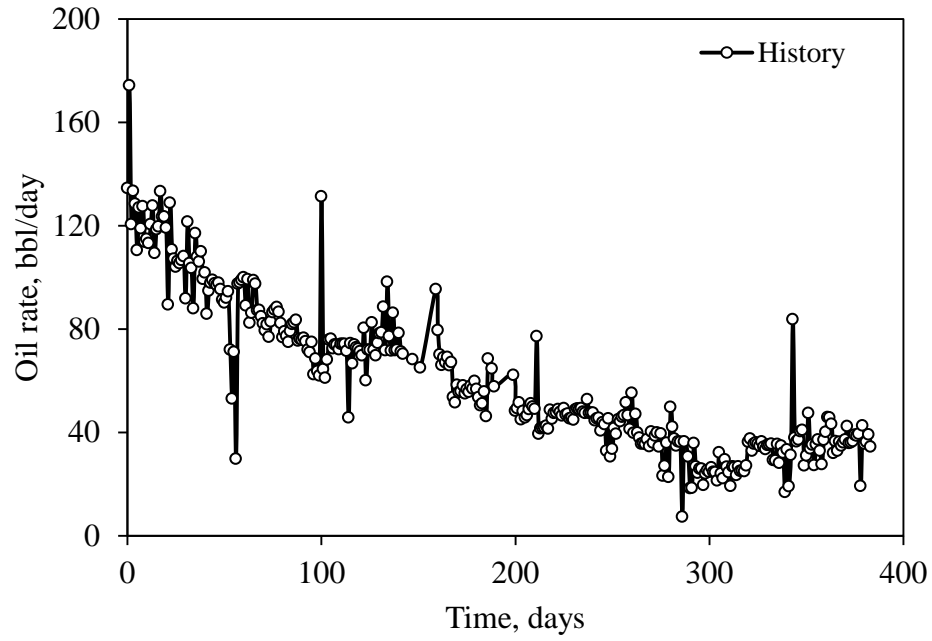
For history-matching, oil production rate and flowing pressure were honored in the simulator and gas and water production rates were predicted. Figure 4-2-c shows the gas production history from the well and the simulation results from the history-matching process, while Figure 4-2-d shows the water production rate match (initial water production is actually the flowback water which was injected during the implementation of frac job). Although the overall match in both graphs looks acceptable and the trends are honored, there is a period (between 185 to 240 days) in which the simulation results are quite different from the historical data. The anomalous well production during this period is due to an unknown operational change in the well and is ignored in the simulation model.

Figure 4-2-e and Figure 4-2-f show the two phase water-oil and gas-oil relative permeability curves which were obtained as a result of history-matching the production

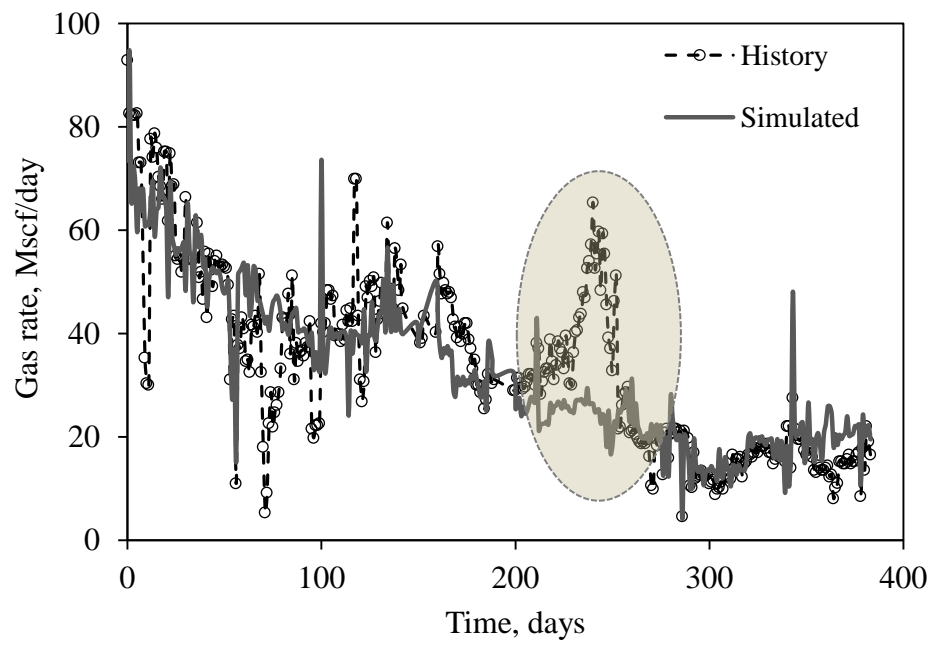
data. The curves were generated with the Corey correlation for initial simulations. These were then adjusted for matching historical water and gas rate measurements. It is important to note that because the changes in the gas rate follow the changes in the oil rate (compare Figure 4-2-b and Figure 4-2-c) and also the gas rate has stabilized at the end of the matching period, the reservoir is interpreted to be above the bubble point pressure (if the pressure falls below the bubble point pressure we will experience a sharp increase in gas rate and consequently gas-oil ratio). As also noted by Clarkson and Pedersen (2011), the GOR is relatively flat through the production history. Therefore, because only oil and water are flowing in the reservoir, the production data are not ideal for deriving the gas-oil relative permeability curve. Nonetheless, the best match was obtained by using this set of permeability data and we continue using it in the rest of this study.



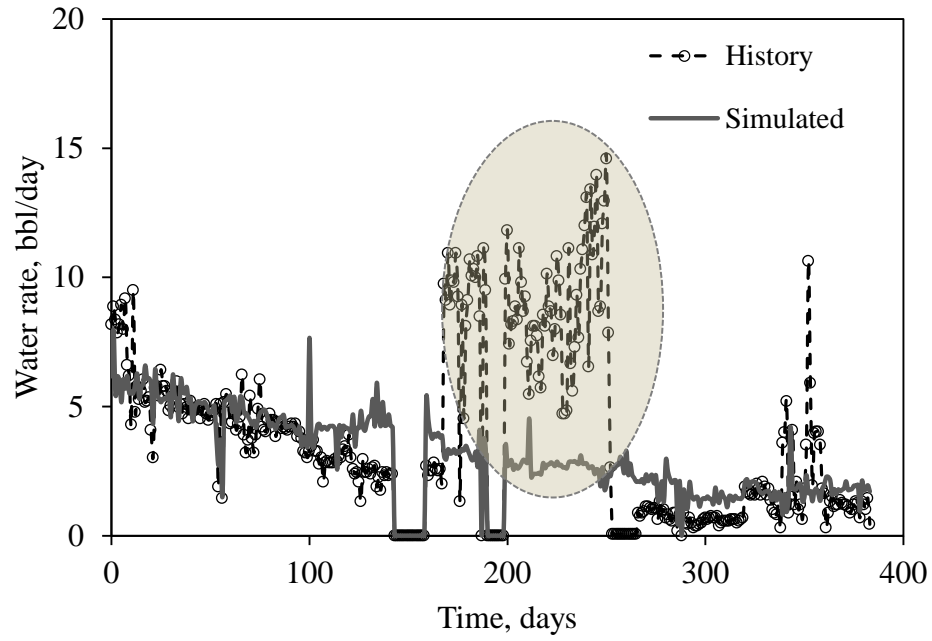
(a)



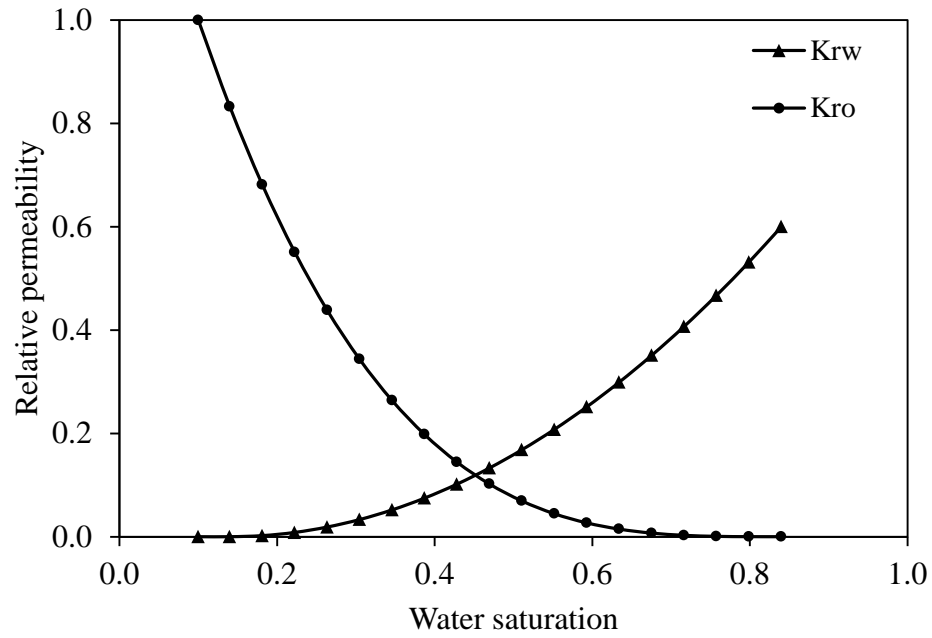
(b)



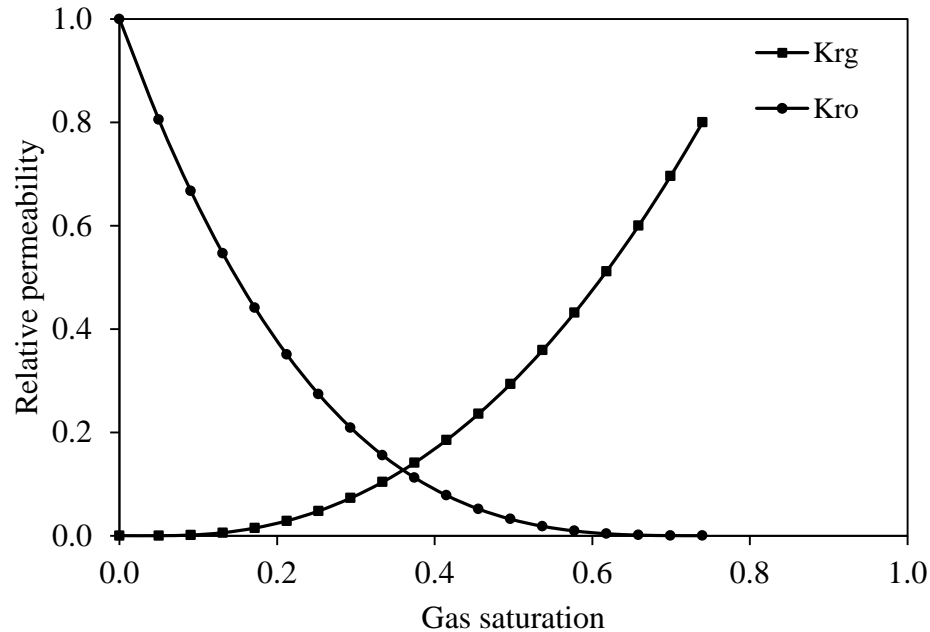
(c)



(d)



(e)



(f)

Figure 4-2: (a) a close-up view of the simulation model showing the hydraulic fracture planes crossing the well lateral (b) historical oil production data for the subject well (c-d) comparison of gas and water production data from well history and simulation, respectively (e-f) two-phase relative permeability of water-oil and gas-oil obtained from history matching of production data, respectively.

From the history-matching process, we have obtained base values for our simulation runs. In the next section, we will define the modeling strategy for our sensitivity study and the parameters considered.

4-3- Modeling Strategy

To fully understand the requirements for successful exploitation of low-permeability reservoirs, one should perform extensive simulation runs. Before any simulation, the objective function or response (e.g. cumulative oil production) should be defined and all impactful factors (those which are believed to affect the response, which might be as many as tens) should be determined. These factors usually require two to three levels (values) to cover all possible range of variations under different circumstances. An

important question is that, in each simulation run, which parameters should be used in the sensitivities and which level(s) (high, medium and low) should be employed.

Design of experiment (DOE) is a formal structured technique for studying any situation that involves a response that varies as a function of one or more independent variables (Mathews 2005). DOE is specifically designed to address complex problems where more than one variable may affect the response and two or more variables may interact with each other. DOE replaces inferior methods such as the traditional method of studying the effect of one variable at a time (OVAT). Compared to DOE, the OVAT method is an inefficient use of resources and is incapable of detecting the presence of or quantifying interactions between variables (Mathews 2005).

Application of DOE and response surface (RS) in reservoir engineering where an optimization problem, history match, or uncertainty analysis is of interest, has recently received considerable attention (such as works done by Zabalza-Mezghani, 2004; Feraille and Busby, 2009; Feraille and Marrel, 2012). DOE can considerably reduce the number of runs during a risk assessment problem which is an imperative concern for potentially expensive fluid flow simulations (Scheidt et al., 2007). Therefore, we use the DOE technique for determining the variables and their associated levels for each simulation run and the sequence in which these runs should be performed.

4-4- Simulation Response and Variables

The main objective function that we are interested in is the final oil recovery factor (recovery efficiency) of the reservoir. However, production from multi-fractured horizontal wells starts with relatively high rates followed by a rapid decline. Therefore, short-term recovery factors (recovery at the end of 5 years) and long-term recovery

factors (recovery at the end of 20 years) are considered separately as the responses. Seven factors, which seem to affect the recovery in tight oil formations the most, were chosen. These factors and their different levels are summarized in Table 4-3.

Table 4-3: Factors considered for simulation runs

Factor	Unit	Low	Medium	High
A: Number of wells	Number/section	2	4	6
B: Length of well	Ft	1500	3000	4500
C: Density of HF*	# HF/(500 ft well)	2	-	3
D: Half-length of HF	Ft	125	225	325
E: Conductivity of HF	md-ft	250	750	1250
F: Well operating BHP	Psi	300	600	1200
G: Completion method	N/A	Open-hole (“1”)	-	Cased-hole (“2”)

* HF stands for hydraulic fracture

Five parameters are assigned three levels and the two remaining ones get two levels. In the following, we provide a brief description of the response, selected factors and their levels and the rationale for these choices.

Recovery factor (Response): The ultimate objective of any reservoir engineering design is to obtain the highest possible recovery from the reservoir, subject to economic viability of the design. However, we intentionally neglect the economic factors, as this is the focus of the second part of this study, which will be looking for the optimal design.

Number of wells per section (factor A): The number of wells and the spacing between them are important factors in management of recovery. As the number of wells increases, the cumulative drainage area of the wells increases as does the recovery efficiency. To simplify the problem, in all conducted simulations, the wells are aligned in the same direction and are evenly spaced in the reservoir section.

Length of well lateral (factor B): As the well length increases, more volume of the reservoir would participate in production leading to increased recovery. The minimum and maximum well lengths are 1,500 ft and 4,500 ft, respectively.

Density of hydraulic fractures (factor C): The main goal of generating hydraulic fractures from the horizontal well is to increase the contacted area with the reservoir. It is reasonable to increase the number of fractures per well (to a point) in favor of obtaining higher recoveries. In this study, the hydraulic fractures will be evenly spaced along the well. Factor C controls the number of fractures along the well, which can be calculated from Equation (4-2).

$$\#HF/Well = \begin{cases} L_D + 1; C = 2 \\ 2L_D + 1; C = 3 \end{cases} \quad (4-2)$$

where L_D is the well length(B)/500ft. For instance, if a well is 3,000 ft in length, the number of fractures is 7 and 13 for C equals to two and three, respectively.

Half-length of hydraulic fractures (factor D): In the case of transverse hydraulic fractures, increasing the fracture half-length also increases the contacted area for each horizontal well. In simulation runs, one of these values may be encountered: 125 ft (short), 225 ft (moderate), or 325 ft (long).

Conductivity of hydraulic fractures (factor E): This factor is important in determining the dimensionless fracture conductivity parameter as given in Equation (4-3):

$$F_{cd} = \frac{k_f \times w_f}{k \times x_f} \quad (4-3)$$

where $k_f \times w_f$ is the conductivity of the hydraulic fracture, k is the matrix permeability and x_f is the fracture half-length. Considering a matrix permeability equal to 0.28 mD the range of possible F_{cd} in this study will be between 2.7 (for lowest fracture conductivity and highest fracture half-length) to 35.7 (for highest fracture conductivity and lowest fracture half-length). This range covers a spectrum of finite to almost infinite

conductivity; i.e. $F_{cd} > 20$ (Economides et al. 2002).

Well operating BHP (factor F): BHP values closer to the oil bubble point pressure hinder the formation of two phase flow of oil and gas and keep oil effective permeability at higher values, but restrict the overall flow rates. BHP values closer to atmospheric pressure on the other hand have a reverse effect. Thus, this factor may also have a two-sided effect on the recovery factors and needs to be considered.

Completion strategy (factor G): In an “open-hole” completion, the whole length of the horizontal well + the hydraulic fractures contribute to the fluid flow while in the “cased-hole” method, the production only occurs through the hydraulic fractures to the well. This restricted flow path may adversely influence the productivity index of the well.

If OVAT technique is used to design the simulation runs, a total of 972 ($= 3^5 \times 2^2$) runs will be required. However, if an “optimal design” scheme through DOE is used, far fewer runs will be required to obtain the same level of information. By an optimal design, we mean a design that is “best” with respect to some criterion.

There are several popular design optimality criteria like A , D , and I just to name a few (Montgomery, 2007). In this study, we used the “D-optimal” design which is the most widely used and is a suitable choice for deterministic computer simulation models. However, it should be mentioned that “Optimal design” is only one of the available algorithms in DOE and other methods such as “factorial design”, “Latin hypercube” or more sophisticated techniques have been used in dealing with demanding reservoir simulation runs (e.g., see Manceau et al., 2001, Feraille and Busby, 2009; Maschio et al. 2010; Ghomian et al., 2010).

4-5- Results and Discussion

The collection of simulation runs and the order in which these runs performed are tabulated in Table 4-4. As can be seen in this table, a total of 79 runs were carried out which is only 9% of the total runs required if the OVAT method were used. In each scenario, several factors may change simultaneously and acquire different levels. The design of the runs was performed using the Design-Expert[®] software (Stat-Ease, 2010). As can be seen in this table, no special pattern in the chosen factor levels from one run to the next can be recognized, thus the random nature of selections is honored.

Table 4-4: Simulation runs chosen based on the “D-optimal” design

Run No.	Factor							Response	
	A	B	C	D	E	F	G	Rec. (%) Short-term	Rec.(%) Long-term
1	4	4500	3	225	250	1200	1	5.2	7.8
2	6	4500	2	225	1250	600	2	12.2	17
3	4	4500	2	225	1250	1200	2	4.4	7.4
4	2	3000	2	325	250	600	2	3.2	6.4
5	6	1500	2	225	750	600	2	5	8.1
6	2	1500	2	325	250	1200	1	1.1	2.3
7	6	3000	2	325	250	300	1	10.5	14.3
8	2	1500	3	225	1250	1200	1	1.2	2.3
9	4	1500	3	225	750	600	1	4	6.8
10	2	1500	3	225	750	300	1	2.3	4.5
11	2	1500	3	225	250	1200	2	1.1	2.2
12	6	1500	3	225	1250	600	1	5.6	7.9
13	4	3000	2	125	250	1200	1	2.9	5.2
14	2	3000	2	225	750	600	1	3.3	6.2
15	4	1500	2	325	1250	300	1	5.1	8.1
16	2	3000	3	125	1250	600	1	2.9	5.8
17	6	4500	2	225	750	300	1	14.1	18.5
18	4	1500	2	225	250	300	2	3.6	7.2
19†	6	4500	3	225	250	300	2	14.9	18.7
20	4	1500	2	125	750	300	2	3.1	6.7
21	6	4500	3	125	250	600	2	11.2	16.2
22	2	4500	2	225	250	1200	2	2	4.1
23	6	1500	3	325	1250	600	2	6.3	8.5
24	2	3000	3	325	250	600	1	4	6.8
25	6	4500	3	225	750	1200	2	7.4	9.1
26	2	3000	3	325	750	300	2	5	8.2
27	2	1500	2	225	1250	600	2	1.9	3.9
28	6	3000	3	325	1250	1200	1	5.9	7.2
29	4	3000	3	325	750	1200	2	4.6	6.4

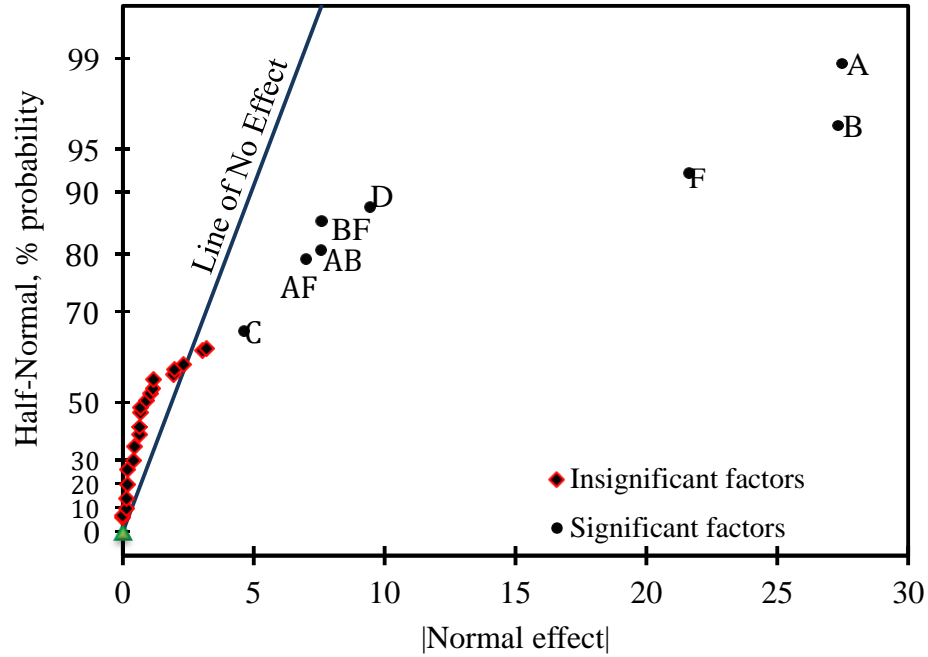
Run No.	Factor							Response	
	A	B	C	D	E	F	G	Rec. (%) Short-term	Rec. (%) Long-term
30	6	4500	3	125	1250	1200	2	6.1	8.7
31	4	3000	3	225	250	600	2	6.7	10.7
32	4	4500	2	225	250	600	1	8.5	14.1
33	2	4500	3	125	750	300	2	4.6	8.7
34	4	4500	3	325	1250	600	1	12.1	15.4
35	4	4500	3	125	250	1200	2	4.2	7.1
36	2	1500	2	325	250	300	2	2.1	4.5
37	2	3000	2	125	1250	1200	2	1.3	2.8
38	2	4500	2	325	750	300	1	6	10
39	6	1500	3	225	1250	300	2	6.4	9
40	6	3000	3	225	750	600	2	9.9	12.8
41	6	1500	2	325	250	600	2	4.9	8.1
42	4	3000	2	225	750	300	2	6.9	12.1
43	4	3000	3	125	750	600	2	5.7	10.2
44	4	3000	3	325	1250	300	2	9.7	13.2
45	6	3000	2	125	250	600	1	7.7	12.1
46	6	1500	2	125	750	300	1	5.1	8.5
47	4	1500	2	325	750	600	1	4.4	7.2
48	4	4500	2	125	250	300	1	8.4	15.2
49	4	1500	3	225	250	300	1	4.3	7.4
50	6	1500	2	125	1250	1200	2	2	3.9
51	2	4500	2	225	1250	300	1	5.1	9.3
52	4	4500	2	125	750	1200	1	4.2	7.1
53	6	3000	2	325	750	1200	1	5.3	7.1
54	2	1500	2	125	250	300	1	1.8	3.9
55	6	1500	3	225	750	200	1	3	4.4
56	2	3000	2	125	1250	300	1	3.1	6.4
57	6	4500	3	125	750	600	1	11.5	16.2
58	6	1500	3	125	250	1200	1	2.5	4.1
59	6	4500	2	125	750	300	2	10.9	18
60	6	3000	2	225	250	1200	1	4.6	6.7
61	2	4500	2	325	1250	1200	2	2.8	5
62	6	4500	3	325	250	1200	2	7.5	9.2
63	4	1500	2	325	1250	1200	2	2.3	3.9
64 $\frac{1}{2}$	2	1500	3	125	750	1200	2	0.9	2
65	4	1500	2	125	1250	600	2	2.8	6
66	2	3000	3	225	1250	300	2	4.1	7.3
67	2	4500	2	125	250	600	1	3.8	7.6
68	6	3000	3	125	750	1200	1	4.4	6.5
69	6	3000	3	125	250	300	2	8.9	13.5
70	2	1500	2	225	750	1200	2	1	2.1
71	6	3000	2	325	1250	300	2	11	15
72	4	3000	2	225	1250	600	1	6.5	10.8
73	4	1500	3	125	1250	1200	1	1.8	3.4
74	6	4500	2	325	1250	600	1	14.1	16.9
75	2	4500	3	325	750	600	2	6.2	9.7
76	4	4500	3	325	750	300	2	13.3	17.4
77	2	4500	3	125	250	1200	1	2.3	4.2

Run No.	Factor							Response	
	A	B	C	D	E	F	G	Rec. (%) Short-term	Rec.(%) Long-term
78	4	1500	3	325	250	600	2	4.5	7
79	2	4500	3	325	1250	300	1	7	10.9

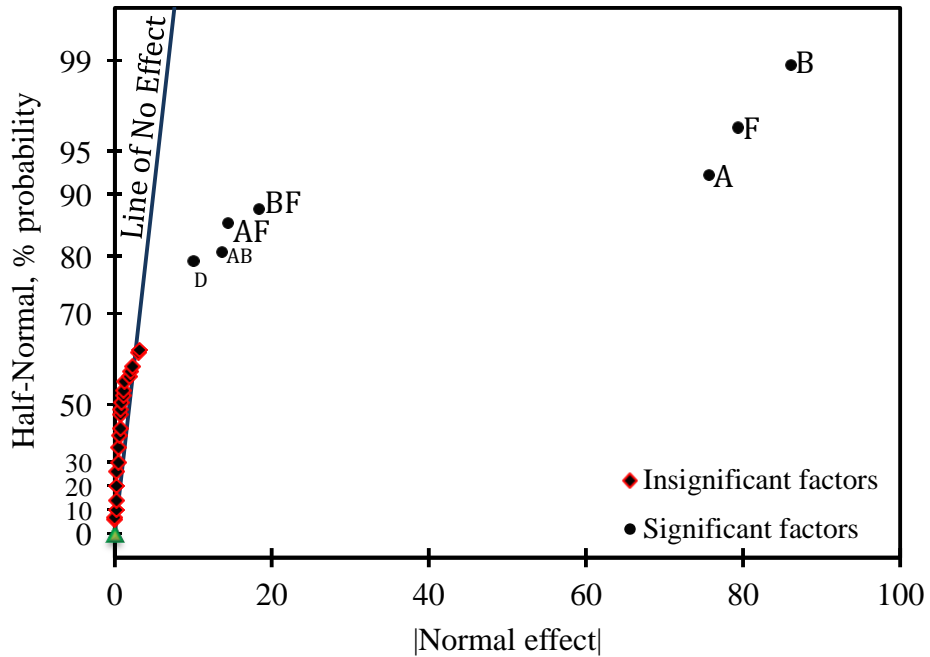
Despite the significant difference in the time-span of the two model responses, as can be seen in Table 4-4, for the majority of the simulation runs, the recovery factor at the end of 20th year (long-term recovery) is not considerably higher than that at the end of the 5th year. Therefore, it is reasonable to analyze these two responses separately. According to these results, the short-term recovery factor ranges between 0.9% (Run 64) and 14.9% (Run 19) and between 2% and 18.7% for the long-term recovery for the same set of runs.

A half-normal probability plot is used to determine whether the entire set of factors and interaction effects are by coincidence (and, thus, shows no effect significantly different from zero) or whether some factors and/or interactions have significant effect. This is a plot of the absolute value of the effect estimates against their normal cumulative probabilities. Any factors or interactions whose observed effects are due to chance are expected to be randomly distributed around zero. These effects will tend to fall along a straight line called “line of no effect”. The straight line on this plot always passes through the origin and should also pass close to the fiftieth percentile data value. The effects that might be significant have average values different from zero and are located a substantial distance away from the straight line that represents no effect (Montgomery 2007).

Figure 4-3 displays the half-normal probability plot of the factors that might affect the short-term recovery factors in simulation runs.



(a)



(b)

Figure 4-3: Half-normal probability plot of observed effect of factors and their interactions on (a) short-term recovery factors and (b) long-term recovery factor for reservoir model with absolute permeability equal to 0.28 mD.

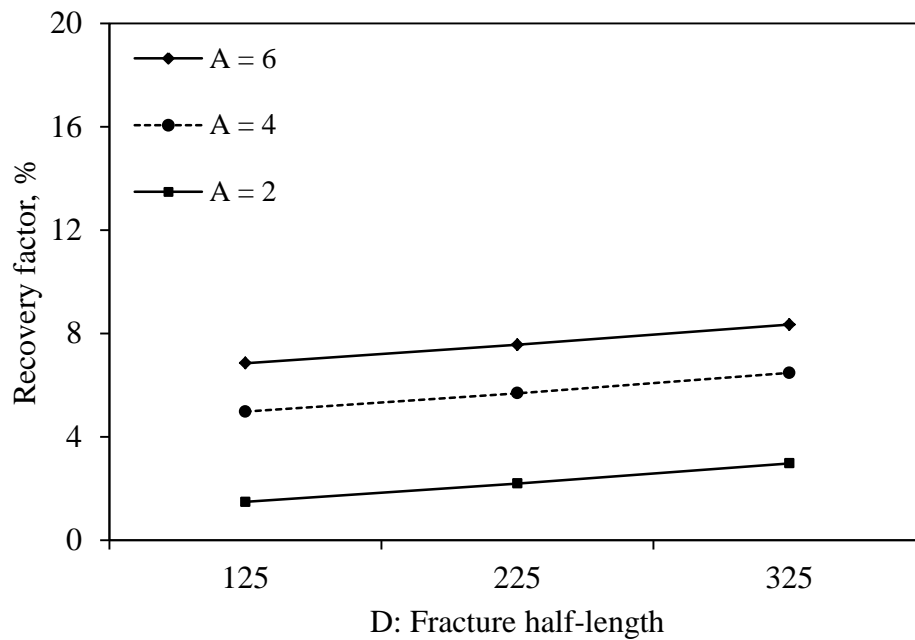
As this figure suggests, with the model properties used in this paper (see Table 4-1), only 5 factors out of 7 have a significant effect on the recovery. The order of their

significance is: (1) the number of wells (factor A); (2) the length of the well (factor B); (3) operating BHP of the wells (factor F); (4) half-length of hydraulic fracture¹ (factor D); (5) density of HF (factor C). Interestingly, the conductivity of the fractures and the completion strategy in comparison with the other five factors have only a minor effect on the objective function (they are statistically insignificant). In other words, although increasing fracture conductivity and using the open-hole completion scheme may increase the recovery factor (which is the case for our simulation runs), investment in the other five factors possibly will yield better results. Figure 4-3-b is similar graph but for the long-term recovery factors. The same factors as in the short-term recovery cases have emerged as significant, except the density of HF (factor C). We will discuss the reasons for this difference later in the text.

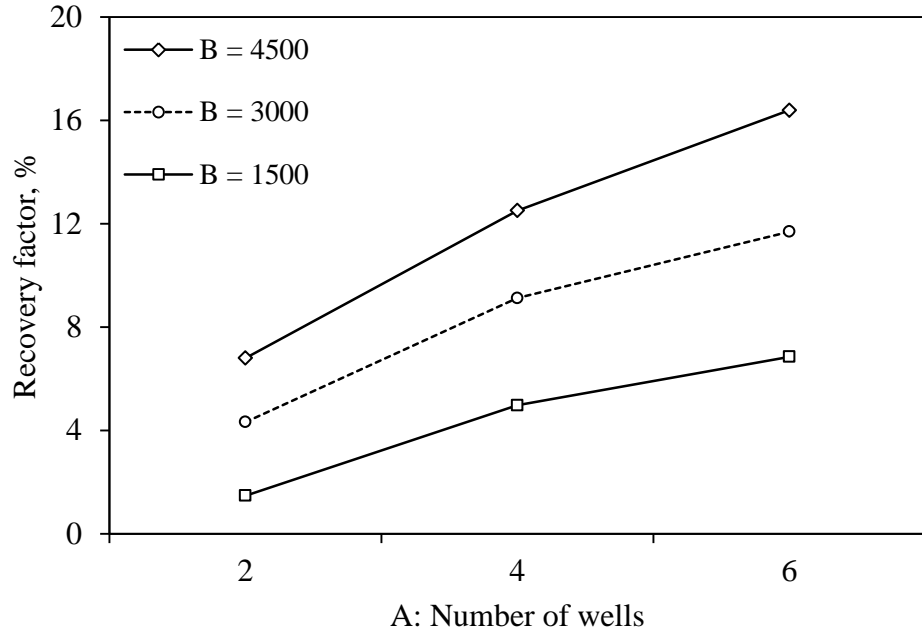
In some situations, the difference in response between the levels of one factor is not the same at all levels of the other factors. When this occurs, there is interaction between the factors. For example, in Figure 4-3 we see that interaction exists between A and B, denoted as AB, and this interaction is contributing to the recovery. However, factor D has no interaction with other factors. To clarify the interaction effect, consider Figure 4-4-a in which recovery is plotted versus fracture half-length (factor D) at three different levels of factor A. The three depicted curves are approximately parallel to each other indicating that regardless of the level of A, increasing/decreasing the level of D from one level to the next one always causes the same amount of increase/decrease in recovery (or the slope of the curves). Since D has no interaction with any other factor, a similar plot will be obtained if the alternative factors (B, F, and etc.) are used instead of A. The general trend is similar; if the level of factor D increases the recovery factor will increase and

¹ The term “Hydraulic fracture(s)” will be henceforth abbreviated as HF.

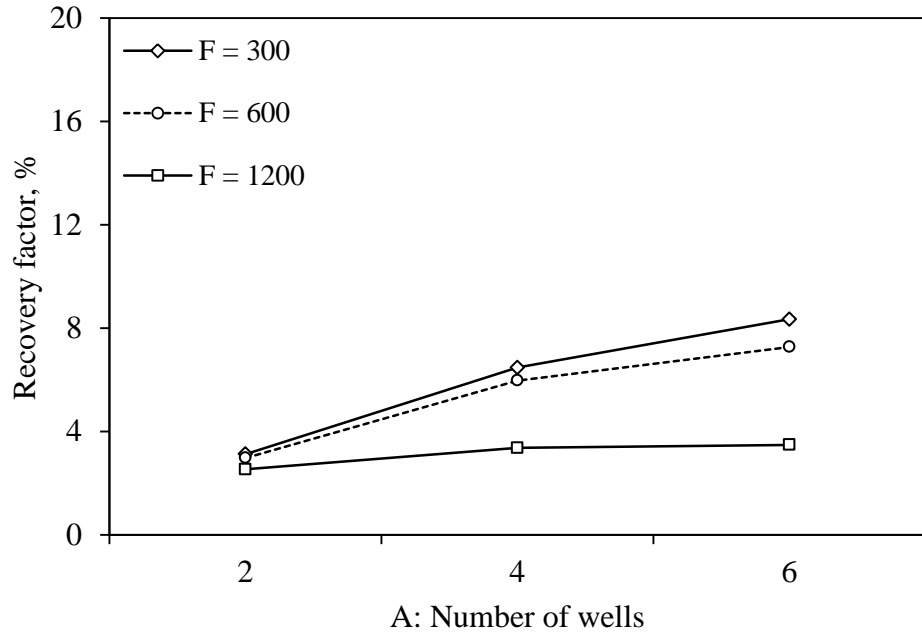
vice versa. Conversely, we see in Figure 4-4-b that the curves describing the recovery factor versus the number of wells at different levels of B is non-linear; the amount of increase/decrease in the recovery factor depends on the changes in levels of both factors. For Figure 4-4-c and Figure 4-4-d, similar comments can be made. Another possible conclusion from these figures is that increasing both the number and the length of the wells (Figure 4-4-a), increasing the number of wells and decreasing the BHP, increasing the well length, and decreasing the BHP causes an increase in the achievable recovery factor. Therefore, more wells with longer laterals which are operating at lower BHP when stimulated with longer hydraulic fractures increases both short and long-term recovery.



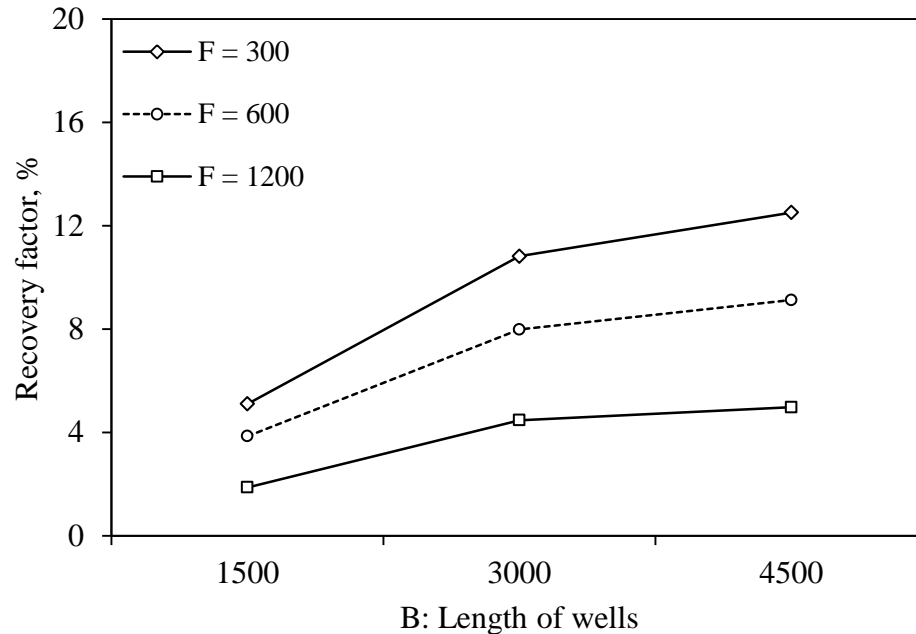
(a) For: B=1500; C=2; E=250; F=300; G=1



(b) For: $C=2$; $D = 125$; $E = 250$; $F = 300$; $G=1$



(c) For: $B=1500$; $C=3$; $D=325$; $E=250$; $G=1$



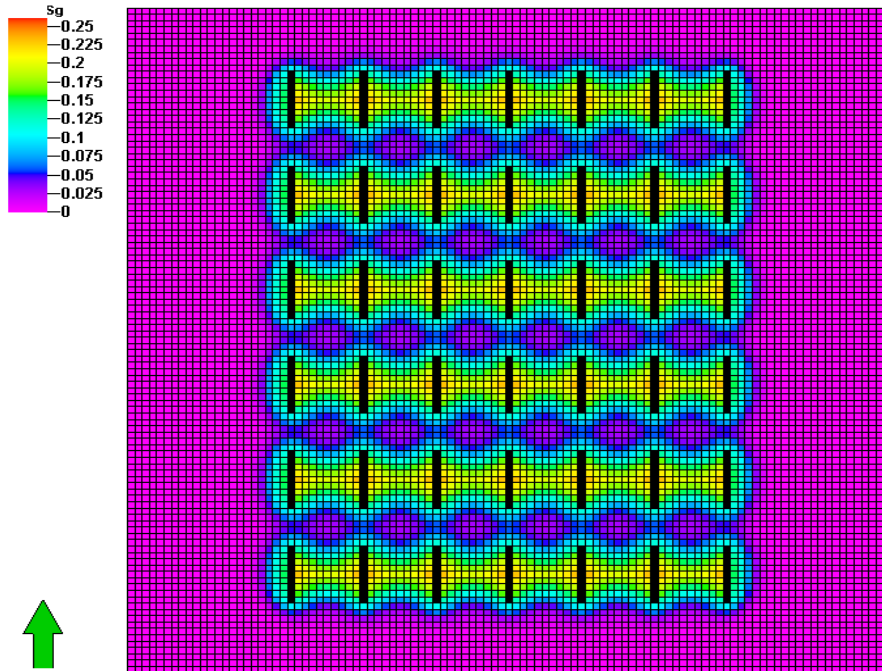
(d) For: A=4; C=2; D=125; E=250; G=1

Figure 4-4: Effect interaction plot between different factors (a) AD, no interaction case (b) AB (c) AF (d) BF.

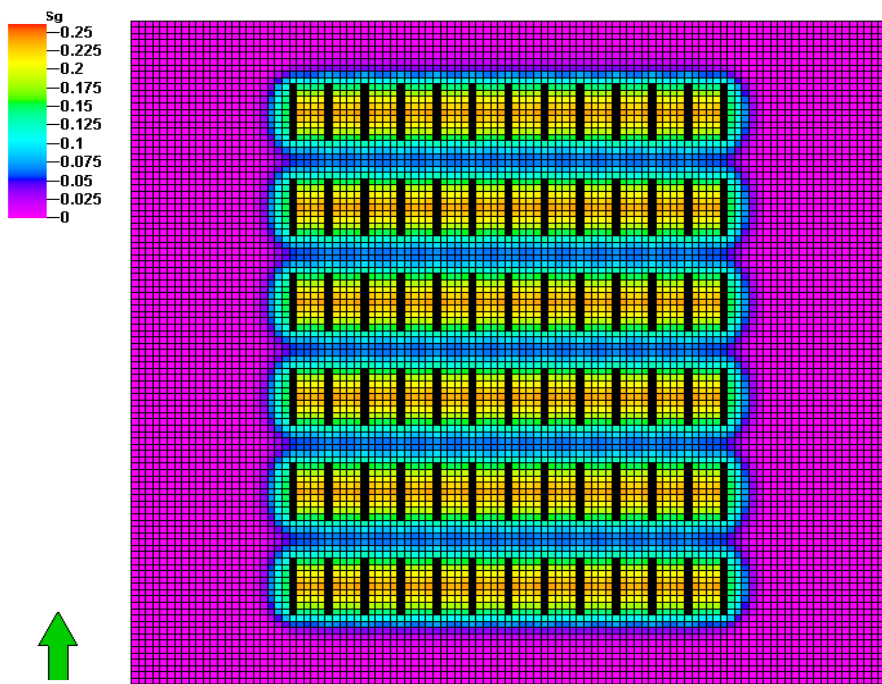
It is worth looking at the effect of factors which were recognized as having an insignificant impact on primary recovery, namely fracture density (factor C) for the long-term recovery efficiency, and fracture conductivity (factor E) and completion strategy (factor G) for both long-term and short-term efficiencies. Increasing the number of fractures per well, although improving the contacted area with the reservoir, causes the spacing between the fractures to reduce. Under constant BHP operation ($p_{wf} < p_b$) this may accelerate the pressure depletion between the fractures and the formation of the two phase flow regimes in this region. This can adversely reduce the oil effective permeability. Nevertheless, the amount of reduction in the oil effective permeability is a function of the relative permeability characteristics and especially the oil relative permeability end points and critical gas saturation. If the critical gas saturation is so high that it takes a long time to reach that gas saturation between the fractures, then increasing

the number of fractures (neglecting economic factors) would be favorable, otherwise there is not much benefit expected. However, since the low-permeability reservoirs should be produced under very low-BHP conditions, this critical value of the gas saturation between the fractures will pass soon after the start of the production and higher mobility of the gas with respect to oil hinders the sustainability of high oil production rates.

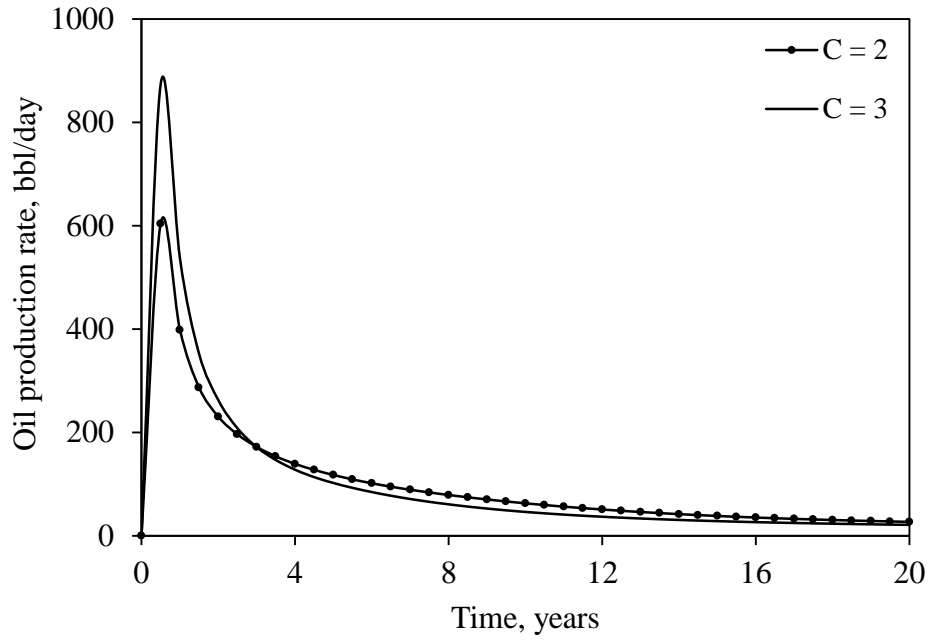
Figure 4-5-a and Figure 4-5-b show the gas saturation distribution in the reservoir (top-view) after one year from start of production for two simulation runs which differ only in the number of fractures per well. The spacing between the fractures in Figure 4-5-a is 500 ft and in Figure 4-5-b is 250 ft. For the run with closer hydraulic-fracture spacing, the amount of the evolved gas saturation between fractures and also the extension of two phase oil-gas region is greater, both of which augment two phase flow interference. This in turn causes lower mobility to oil and hence reduces recovery efficiency. Figure 4-5-c demonstrates that oil production rates from the model with larger number of fractures will produce oil at higher rates early on (short-term effect), but at later times the two-phase flow interference becomes important and productivity drops off (long-term effect). The recovery curves (Figure 4-5-d) are consistent with the oil production rates and the results from two half-normal probability plots. According to this figure, there is a statistically significant difference between the short-term recovery factors but this difference gradually diminishes over time. There is therefore an optimum number for the fracture density which primarily depends on the reservoir characteristics and secondly on the economic concerns.



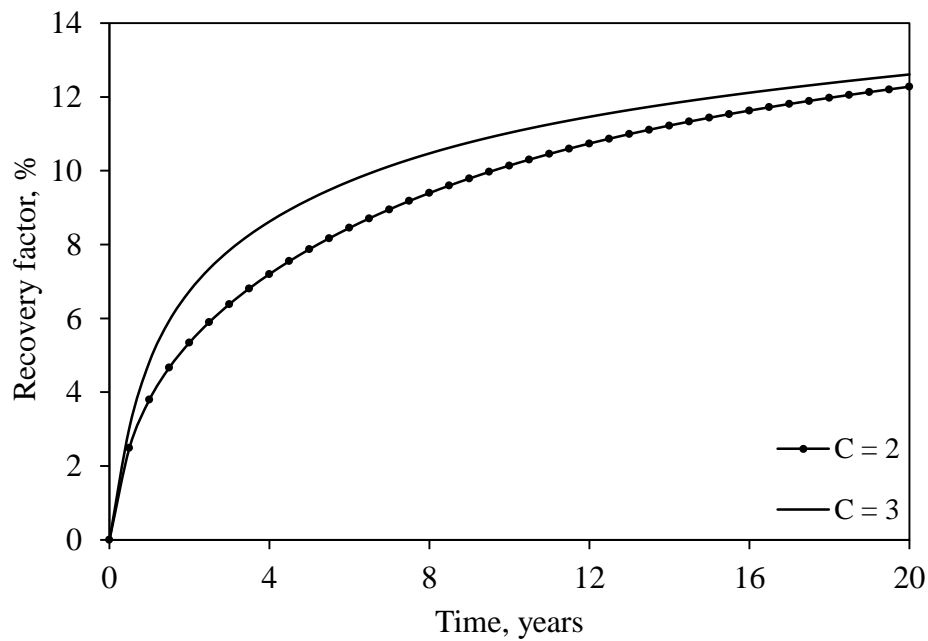
(a)



(b)



(c)

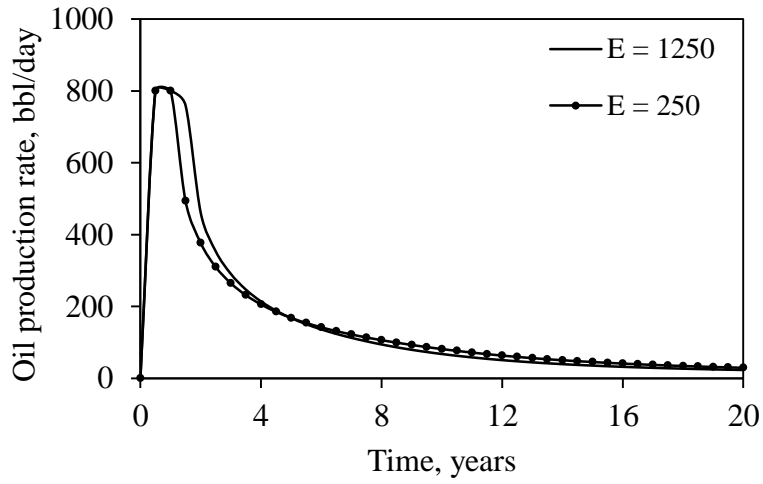


(d)

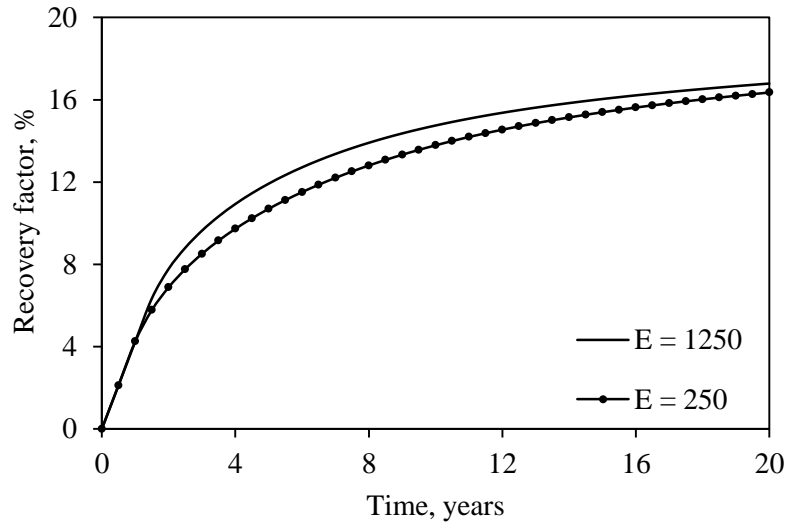
Figure 4-5: (a-b) gas saturation in two models with (a) C=2 and (b) C=3 one year after start of production; (c-d) field oil production rates and the oil recovery factors for the models. Other parameters are as follows: A=6; B=3,000 ft; D=225 ft; E=750 md-ft; F= 300 psia.

Our simulation results confirm that similar comments made for fracture spacing can be made for the effect of fracture conductivity, as this factor was also recognized as

insignificant for recovery efficiency. Figure 4-6-a compares the oil production rate from two models which differ only in fracture conductivity. Figure 4-6-b demonstrates the corresponding recovery factors for the models. Embedding more conductive fractures will result in higher production rates earlier in the life of the project which might shorten the project pay-back period.



(a)

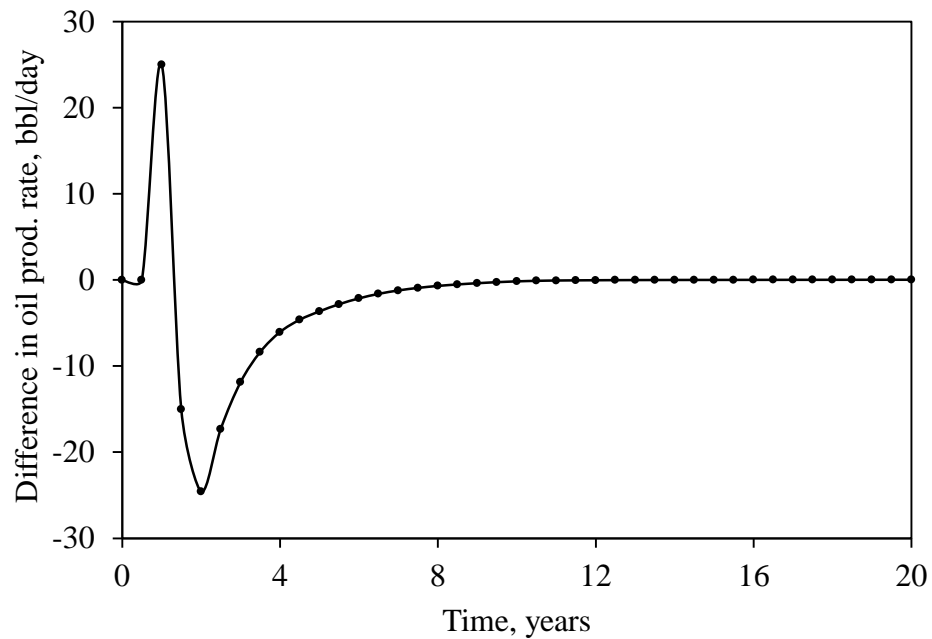


(b)

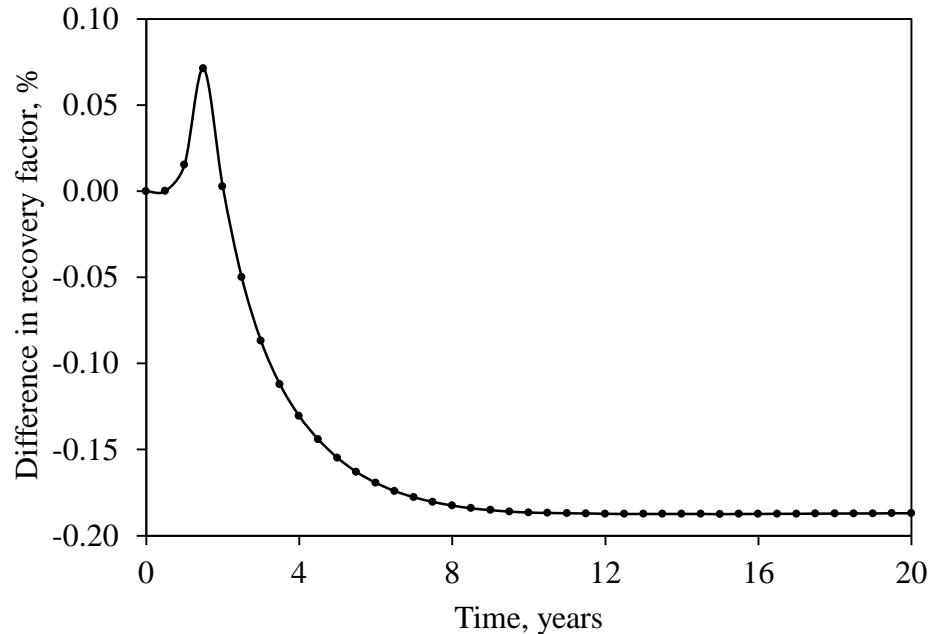
Figure 4-6: Field oil production rates (a) and the oil recovery factors (b) for the models with different levels of E factor; other parameters are as follows: A=4; B=4,500 ft; C=2; D=325 ft; F= 300 psia; G=1.

Finally, the difference in results for the open-hole and cased-hole methods (factor G)

is depicted in Figure 4-7 and confirms the outcome of the previous analysis which demonstrated that there is little difference between the two completion methods. The largest contribution to production occurs through the highly conductive fracture conduits and the contribution from other perforations along the horizontal well is of subtle importance. It should be also noted that a minor difference in the recovery factors between two models in Figure 4-7-b may arise from the numerical errors.



(a)

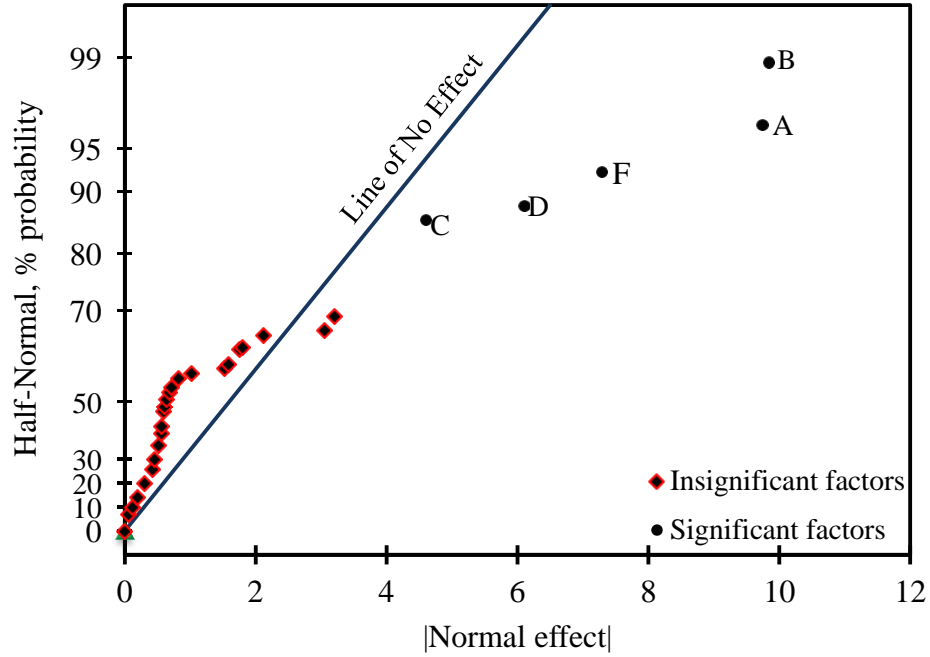


(b)

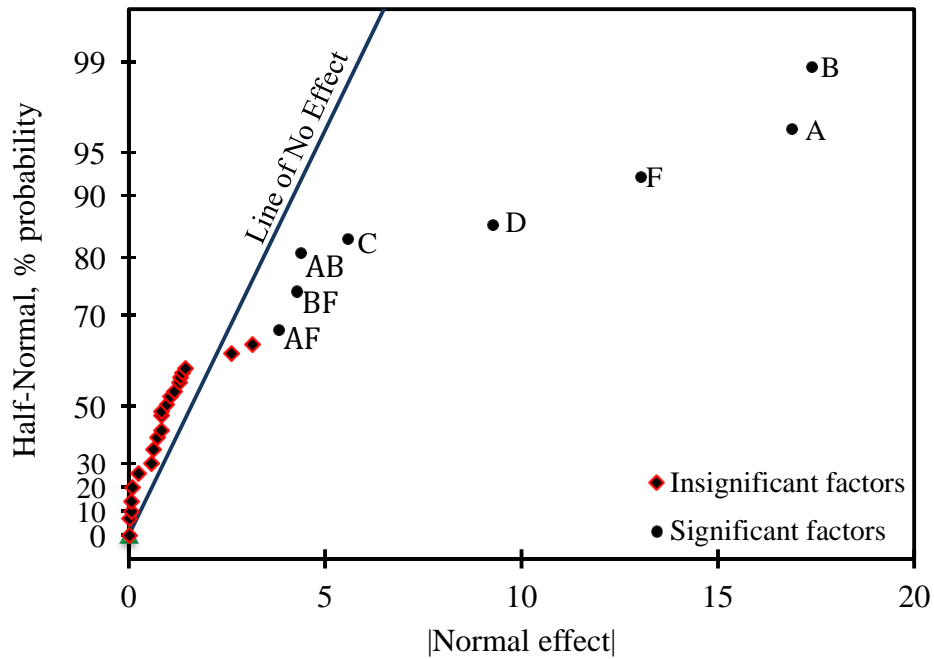
Figure 4-7: Difference in (a) field oil production rates and (b) the oil recovery factors for the models with different levels of G factor (graph results = “open-hole” results - “cased-hole” results); other parameters are as follows: A=6; B=3000 ft; C=3; D=325 ft;

Because the conventional methods for measurement of permeability sometimes fail when applied to tighter formations, there is risk in the estimation of this property. Therefore, we repeated the analysis above, but with absolute permeability reduced one order of magnitude (absolute permeability = 0.028 mD). The half-normal probability plot of the factor effects is given in Figure 4-8. It is interesting to note that once more the same significant factors appear on both graphs, but now factor C is significant for short and long-term recovery efficiency (compare Figure 4-8 and Figure 4-3). Also comparing the two figures, we see that factor C either does not appear as a significant factor or it sits very close (in comparison with other factors) to the “line of no effect”. There is a good chance that if the reservoir properties change, particularly the relative permeability data, fracture density may be totally removed from the list of significant factors and hence it should be treated carefully and optimized for the formation under consideration. This

result emphasizes the importance of accurate reservoir characterization for tight formations.



(a)



(b)

Figure 4-8: Half-normal probability plot of observed effect of factors and their interactions on (a) short-term recovery factors and (b) long-term recovery factor for reservoir model with absolute permeability equal to 0.028 mD.

4-6- Summary

In this work, a systematic method for establishing the most important factors affecting primary recovery (short- and long-term) using multi-fractured horizontal wells is provided. The combination of design-of-experiment (DOE) and numerical simulation used in this work is superior to the one-variable-at-a-time approach (OVAT) used in many studies because a) fewer runs are required and b) the interaction between factors can be established and quantified.

For reservoir and fluid properties typical of the low-permeability Pembina Cardium, the most important factors controlling primary recovery in order of significance are: the number of wells per section; the length of the well; operating BHP pressure of the wells. Fracture conductivity has a lesser effect on recovery factor, but will impact early time production rates. Higher fracture density may accelerate oil production, but also accelerates gas saturation between fractures, which reduces oil mobility and impairs long term oil production. Further, whether or not fracture density has a significant impact on recovery depends on the combination of reservoir properties, particularly relative and absolute permeability, underpinning the need for careful reservoir characterization. The difference in long-term recovery factor due to completion method (open-hole versus cased-hole) appears to be insignificant. However, it should be noted that phenomenon like non-darcy flow of fluids within hydraulic fractures, if it can be truly characterized and accounted for, may change these results to some extent.

Although we performed our sensitivity runs at two different matrix permeability levels, we recognize that there is also considerable uncertainty in relative permeability characteristics – we will perform our analysis using different relative permeability scenarios in the future.

In future work, reservoir heterogeneity and changes in relative permeability will be considered. Economic criteria will also be incorporated into the analysis. Finally, a similar approach will be used to establish critical factors controlling CO₂-EOR in this tight oil play; CO₂-EOR in this play is worthy of investigation because of not only the potential for increased of oil recovery, but also the possibility for CO₂ storage.

Acknowledgements

This research was made possible by funding provided by ISEEE-NRCan (project title “Co-optimization of CO₂ Sequestration and Oil Recovery in Tight Oil Formations”). Chris Clarkson would like to acknowledge Encana and AITF for support of his Chair position in Unconventional Gas and Light Oil research at the University of Calgary, Department of Geosciences. He would also like to acknowledge the sponsors of Tight Oil Consortium (TOC), hosted at the University of Calgary. The authors would like to acknowledge ARC Resources for contributions of the Cardium well production.

References

- Adegbesan, K.O., Costello, J.P., Elsborg, C.C., King, D.A., Mills, M., King, R.W., 1996. Key Performance Drivers for Horizontal Wells under Waterflood Operations in the Layered Pembina Cardium Reservoir. *Journal of Canadian Petroleum Technology*, vol. 35 (8), pp. 25-35. DOI: 10.2118/96-08-02.
- Clarkson, C.R., Pedersen, P.K., 2010. Tight Oil Production Analysis: Adaptation of Existing Rate-Transient Analysis Techniques. Paper CSUG/SPE 137352 presented at the Canadian Unconventional Resources & International Petroleum Conference held in Calgary, Alberta, Canada, 19-21 October. DOI:

10.2118/137352-MS.

- Clarkson, C.R., Pedersen, P.K., 2011. Production Analysis of Western Canadian Unconventional Light Oil Plays. Paper CSUG/SPE 149005 presented at the Canadian Unconventional Resources Conference held in Calgary, Alberta, Canada, 15-17 November.
- Economides, M.J., Oligney, R.E., Valkó, P., 2002. Unified Fracture Design: Bridging the Gap between Theory and Practice. Alvin, Texas: Orsa Press.
- Feraille, M., Marrel, A., 2012. Prediction under Uncertainty on a Mature Field, Oil Gas Sci. Technol. – Rev. IFP Energies nouvelles, vol. 67(2): pp. 193-206.
- Feraille, M., Busby, D., 2009. Uncertainty Management on a Reservoir Workflow. International Petroleum Technology Conference, Doha, Qatar, 7-9 December.
- Ghomian, Y., Sepehrnoori, K., Pope, G.A., 2010. Efficient Investigation of Uncertainties in Flood Design Parameters for Coupled CO₂ Sequestration and Enhanced Oil Recovery. SPE Paper 139738 presented at SPE International Conference on CO₂ Capture, Storage, and Utilization held in New Orleans, Louisiana, USA, 10-12 November.
- Krause, F.F., Collins, H.N., Nelson, D.A., Machelmer, S.D., French, P.R., 1987. Multiscale Anatomy of a Reservoir: Geological Characterization of Pembina-Cardium Pool, West-central Alberta, Canada: American Association of Petroleum Geologists Bulletin, vol. 71, pp. 1233-1260.
- Manceau, E., Mezghani, M., Zabalza-Mezghani, I., Roggero, F., 2001. Combination of Experimental Design and Joint Modeling Methods for

Quantifying the Risk Associated with Deterministic and Stochastic Uncertainties - An Integrated Test Study. Paper SPE 71620-MS presented at Annual Technical Conference and Exhibition, 30 September - 3 October, Louisiana, New-Orleans, USA.

- Maschio, C., Viegas de Carvalho, C.P., Schiozer, D.J., 2010. A New Methodology to Reduce Uncertainties in Reservoir Simulation Models Using Observed Data and Sampling Techniques. *J. Petrol. Sci. Eng.*, vol. 72(1), pp. 110-119.
- Mathews, P., 2005. *Design of Experiments with MINITAB*. Milwaukee, Wisconsin: ASQ Quality Press.
- Montgomery, D.C., 2007. *Design and Analysis of Experiments*. Seventh Edition, John Wiley & Sons Inc.
- Pedersen, K.S., Fredenslund, A., Christensen, P.L., Thomassen, P. 1984. Viscosity of Crude Oils, *Chemical Engineering Science*, vol. 39(6): pp 1011-1016.
- Schlumberger, 2010. *Eclipse (version 2010.1) Reference Manual*.
- Schlumberger, 2010. *PVTi (version 2010.1) Reference Manual*.
- Shaoul, J.R., Behr, A., Mtchedlishvili, G., 2007. Developing a Tool for 3D Reservoir Simulation of Hydraulically Fractured Wells. *SPE Res Eval & Eng* 10(1): pp 50-59. SPE-108321-PA. DOI: 10.2118/108321-PA.
- Stat-Ease, Inc. 2010. *Design-Expert (version 8.0.6), Reference Manual*.
- Scheidt, C., Zabalza-Mezghani, I., Feraille, M., Collombier, D., 2007. Toward a Reliable Quantification of Uncertainty on Production Forecasts: Adaptive Experimental Designs. *Oil & Gas Science and Technology*, vol. 62(2): pp 207-

224.

- Viau, C., Nielsen, K., 2010. Unconventional Oil Production in the Cardium Formation, East Pembina Area, Alberta, Canada. Presented at the CSPG core conference held in Calgary, Alberta, Canada, 16-17 September.
- Zabalza-Mezghani, I., Manceau, E., Feraille, M., Jourdan, A., 2004. Uncertainty Management: From Geological Scenarios to Production Scheme Optimization. Journal of Petroleum Science and Engineering special issue: Risk Analysis Applied to Petroleum Exploration and Production, vol. 44(1-2): pp. 11-25.

Appendix 4-A: Sensitivity of Simulation Results to Grid Size

In this appendix, the results of sensitivity study regarding the optimum degree of refinement for the grid blocks of the simulation models are presented. A symmetric simulation model with the following parameters and properties are considered:

Model Area: 128 acres (1/5 of a section)

A- Number of wells: 1

B- Well length: 4500 ft

C- Number of fractures: 19

D- Length of HF: 325 ft

E- Conductivity of HF: 1250 md-ft

F- Well operation BHP: 300 psia

G- Well completion: open-hole

Since this is a sensitivity study with respect to number of grids (or grid size) the considered model consists of one well. However, the well is located in the middle of a smaller area to see the boundary effect. The well length and fracture geometry are set at

their maximum and the well bottom-hole pressure is set at its minimum value to make sure the extreme cases have been considered. Open-hole completion is the ultimate exposure of a fractured well to a reservoir and hence was considered in the sensitivity study.

To do a sensitivity on the number of grids in the x or y direction (which are equal in the current models) a fixed fractures' width of 1 ft (dividing each parent block into 50 sub-blocks in the x direction as local grid refinement) was used and the number of blocks in the x and y direction were varied to screen the oil recovery factor. Figure 4A-1 shows the results of recovery factor versus $1/N_x$. According to this figure, when the number of grids reaches 105 the recovery factors almost gets flat and therefore this number was chosen as the optimal number of grids in the x and y directions. Similar approach was taken for grid construction in the z direction.

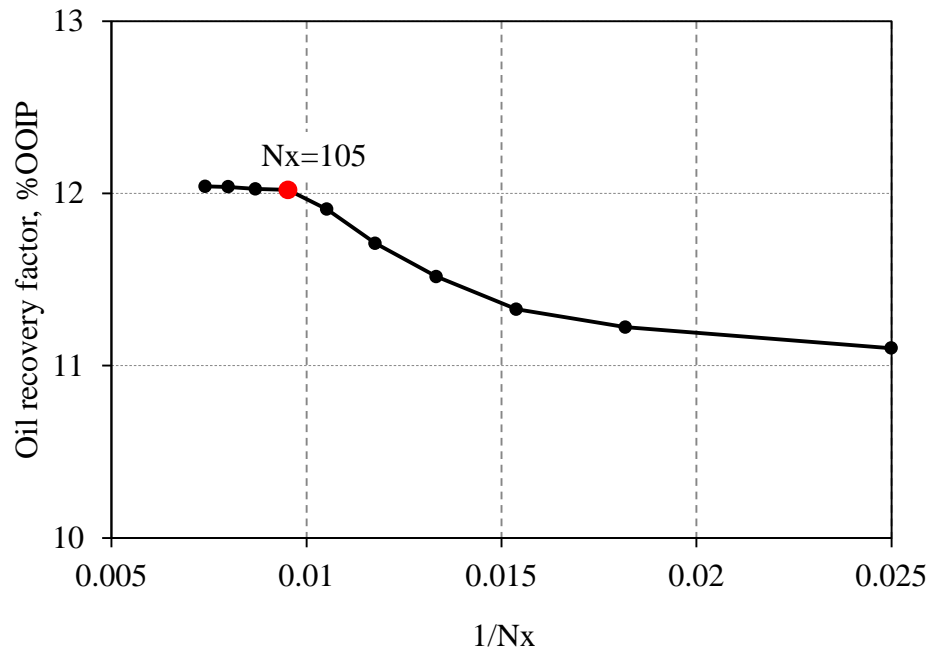


Figure 4A-1: Grid convergence behavior for parent blocks in x and y directions

Since local grid refinement is used to represent the hydraulic fractures, it is necessary

to do similar study for the number of division that should be applied for a stable simulation response. Figure 4A-2 displays such a sensitivity when the number of grids in the x and y directions are fixed at 105. As this figure suggests 25 division (fracture width of 2 feet) should be satisfactory for the simulation of primary recovery scheme.

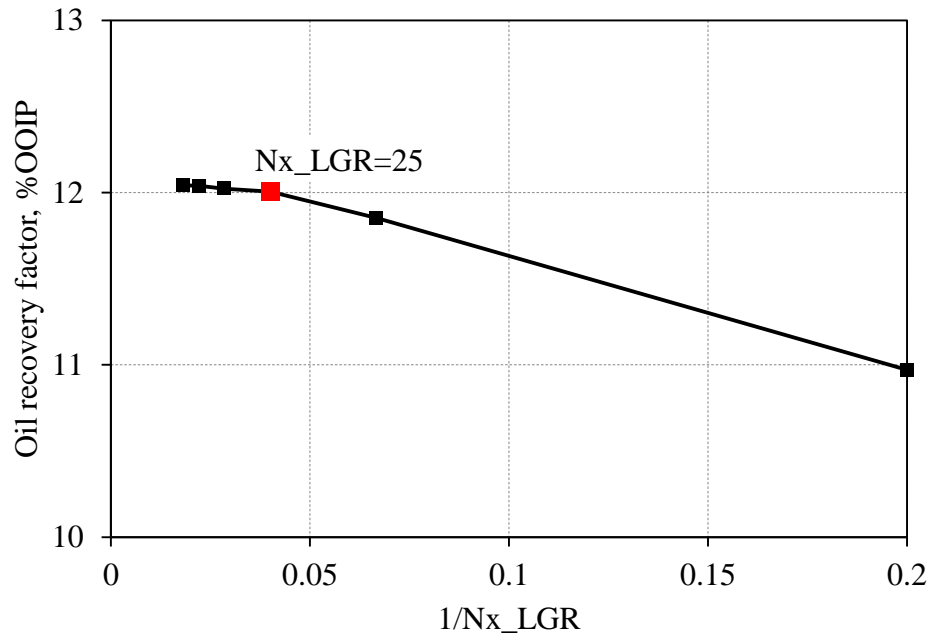


Figure 4A-2: Grid convergence behavior for number of grid used in construction of local grid refinement representing hydraulic fractures.

In summary, considering the computational expenses and time we used $105 \times 105 \times 3$ blocks in the x, y, and z direction, respectively and 25 blocks for local grid refinements.

Chapter 5

Evaluation of Recovery Performance of Miscible Displacement and WAG Process in Tight Oil Formations¹

Recent advances in well design and production techniques have brought considerable attention to exploitation of tight (low permeability, absolute permeability <1 mD) oil resources. Drilling of long horizontal wells and deployment of hydraulic fractures along these wells (multi-fractured horizontal wells) can substantially improve the primary production rates from such reservoirs. Nevertheless, the low effective permeability of these reservoirs to oil hinders the sustainability of favorable oil rates and at some point applying some EOR technique becomes inevitable.

In the current study, CO₂ miscible flooding and WAG process in a tight oil reservoir are investigated. Although several studies have investigated different aspects of the process in conventional oil plays, the design of an effective scheme in tight oil formations is more complex. These complexities are related to the proper design of the fractures (half-length, conductivity, orientation (transverse vs. longitudinal), etc.) and their relative

¹ This chapter is a modified version of: Ghaderi, S.M., Clarkson, C.R., Chen, S., and Kaviani, D., 2012. Evaluation of Recovery Performance of Miscible Displacement and WAG Processes in Tight Oil Formations, Paper SPE 152084, presented at SPE/EAGE European Unconventional Resources Conference and Exhibition, Vienna, Austria, 20-22 March.

placement along producers and injectors and the operational constraints on each well or segment of the well.

In this work, we utilize an EOR scheme design where multi-fractured horizontal wells are used for both injection and production, and the hydraulic fracturing stages are staggered to delay breakthrough and improve sweep efficiency. For a set of defined parameters, compositional simulations are conducted to investigate the effect of the CO₂ slug size, WAG ratio and cycle length on the recovery efficiency of the model. The recovery from the aforementioned EOR process is then compared with its corresponding base case in which the reservoir has gone through periods of primary and water-flooding stages. The results of this study show that the incremental oil recovery from WAG process in tight formation can reach as high as 20%.

5-1- Introduction

The low permeability portion of Pembina Cardium field, referred to as a “Halo Oil” play by Clarkson and Pedersen (2011), is currently being exploited under primary recovery using multi-fractured horizontal well technology. The play has several attractive attributes such as high quality oil (around 36 °API) and sweet gas, low water production rates with accessible infrastructure in the area. The Pembina Cardium field has a large OOIP (an ERCB estimated 7.78 billion barrels in the main Cardium area alone, plus great potential in the “Halo Oil” play), long life reserves, repeatability and relatively low risk (Viau and Nielsen, 2010). However, obtaining a good economic return from the low permeability portion of the play can be quite challenging. Hydraulic fracturing techniques combined with horizontal well technology have enabled commercial production from these plays (e.g. Cox et al., 2008).

Hydraulic fracturing raises well productivity by improving its contact area with the target formation. Depending on the state of the stress in the reservoir, either longitudinal or transverse fractures can be developed (Economides et al., 2002). However, in the low-permeability formations, due to the low mobility of the oil and rather quick pressure interference between the fractures, the depletion of the reservoir is almost confined to the near fracture space. The initial high production rates will rapidly decrease with time and at the end of the primary production stage, the remaining oil saturation could be significant. Therefore, an EOR scheme is vital to recover the remaining oil in place. In this study, we will investigate CO₂ flooding of the low-permeability formations, using multi-stage fractured horizontal wells as injectors.

The ability of CO₂ to develop miscibility and high solubility in reservoir oil, which results in swelling of the oil and significant viscosity reduction are a few advantages of CO₂ EOR (Jarrel et al., 2002). From a carbon storage point of view, CO₂ injection in high permeability oil systems is not desirable due to the possibility of its early breakthrough to producers. Lower permeability oil reservoirs offer the opportunity for more efficient storage capacity due to reduced mobility of CO₂. However, in such systems, achieving injection levels adequate for carbon storage and incremental oil recovery is a challenge using conventional oilfield technologies. The adoption of multi-stage fractured horizontal wells in such a situation is an effective strategy to increase injectivity.

To increase the sweep efficiency, and hence oil recovery, the configuration of hydraulic fractures and their orientation should satisfy two conditions: maximizing contact area with the reservoir matrix and maximizing distance between the producer fractures and injector fractures. One solution that can offer such an opportunity is to

stagger transverse fractures along the injectors and producers. Therefore, the focus of this study is the investigation of CO₂ EOR, either through injection of pure CO₂ or WAG injection, in such configurations.

In this paper, compositional simulation of CO₂ EOR in a tight oil reservoir, with properties similar to the low permeability portion of the Pembina Cardium field, is performed and the results are summarized. A commercial compositional simulator is used to examine the amount of incremental recovery that can be obtained in such a reservoir after the secondary recovery stage. The results of the CO₂ storage capacity of these plays under different injection schemes will be provided.

5-2- Base Case Data and Simulation Model

5-2-1- Fluid properties and EOS model

The reservoir oil is undersaturated light oil with stock tank gravity of 38 °API and an initial solution gas-oil-ratio (GOR) of 730 scf/stb. The original reservoir pressure at the reference depth of 5279 ft is 2520 psi. The bubble point of the reservoir at reservoir temperature of 127 °F is approximately 2450 psi. The CO₂ minimum miscibility pressure (MMP) was determined experimentally to be 2320 psia. Table 5-1 summarizes the important properties of the reservoir fluid.

Table 5-1: Reservoir fluid properties

Parameter	Value
Pb, psia	2,450
Rs at Pb, scf/stb	730
Oil viscosity at Pb, cp	0.63
Bo at Pb, bbl/stb	1.37
Oil density at STP, lb/ft ³	52.1
Average gas viscosity, cp	0.01
Average gas density at STP, lb/ft ³	0.065
Water viscosity, cp	0.57

A crucial part of a compositional reservoir simulation of miscible or even immiscible EOR scenarios is prediction of the phase equilibria between the in-situ reservoir fluid and the injected fluid. To achieve this, an equation of state (EOS) is usually tuned via experimental PVT data. The tuning of EOS in this work followed the methodology suggested by Khan et al. (1992) to characterize CO₂-oil mixtures. The two-parameter Peng-Robinson EOS (Peng and Robinson, 1976) was selected to regenerate the fluid properties because it has proven to be suitable for low-temperature CO₂-oil mixtures (Khan et al., 1992). The viscosity correlation selected to match the oil viscosity was the modified Lohrenz-Bray-Clark (LBC) model (Lohrenz et al., 1964) which is capable of predicting both oil and gas viscosities.

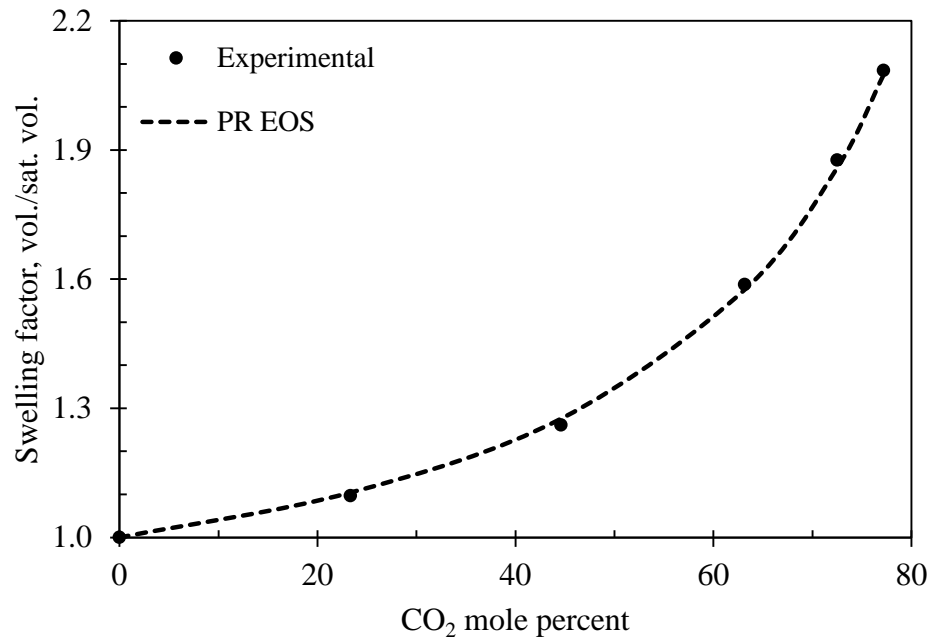
PVT laboratory data was from differential liberation (DL), constant composition expansion (CCE) and separator tests, and very importantly, a swelling test. These test results were used to tune the EOS, which is capable of characterizing the CO₂-hydrocarbon system above the MMP. Table 5-2 presents the composition of final pseudo-components obtained as a result of the regression process.

Table 5-2: Composition of the fluid (after regression)

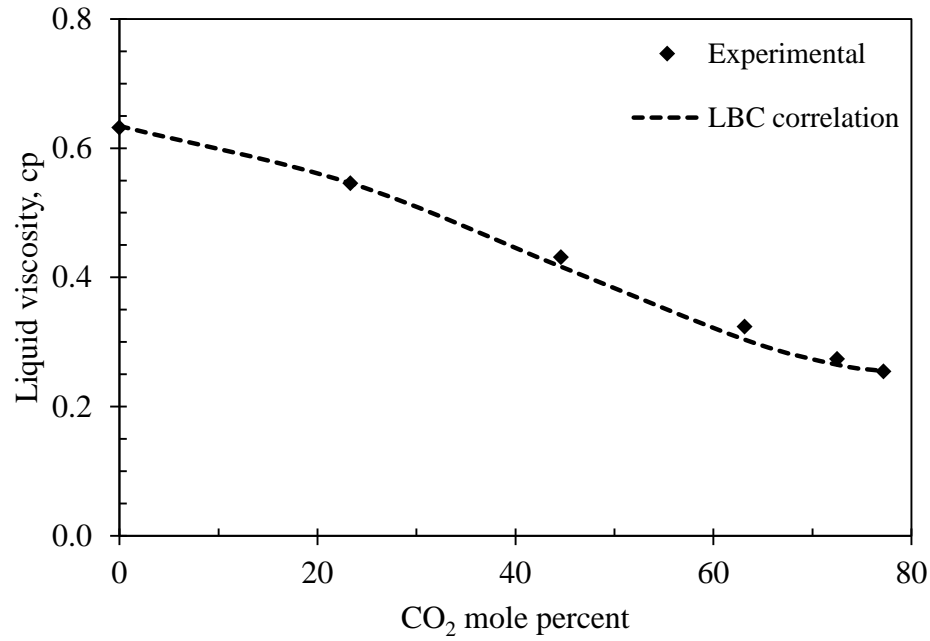
Component	Mole fraction
CO ₂	0.001
N ₂ -C ₁	0.414
C ₂	0.076
C ₃	0.059
C ₄ -C ₅	0.061
C ₆	0.026
C ₇ P*	0.363

* MW = 238 lb/lb-mole ; SG = 0.86

The effect of CO₂ injection on the swelling of oil as well as its viscosity reduction for the fluid of interest has been depicted in Figure 5-1-a and Figure 5-1-b, respectively. These figures also illustrate the good match between the tuned PR EOS and LBC correlation to these critical PVT tests.



(a)

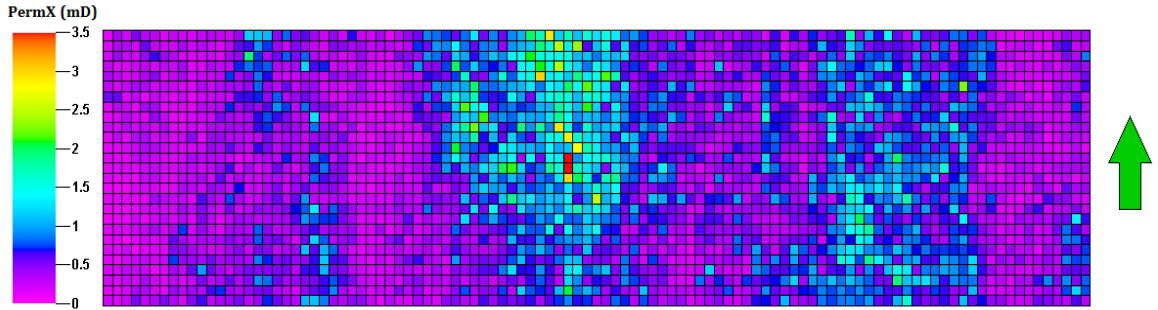


(b)

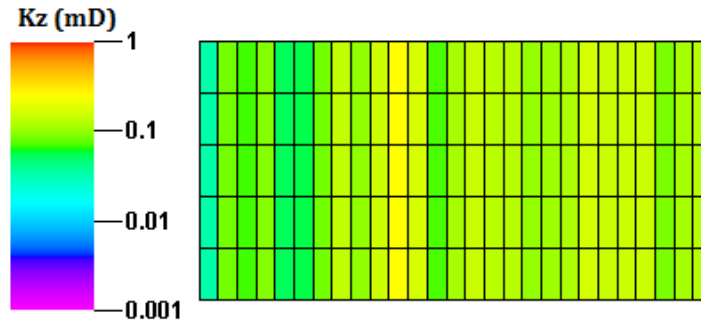
Figure 5-1: Comparison of the predicted (PR EOS and LBC correlation) and observed values for (a) liquid mixture swelling factor and (b) liquid viscosity with respect to CO₂ mole percentage in the mixture.

5-2-2- Reservoir Model and Rock Properties

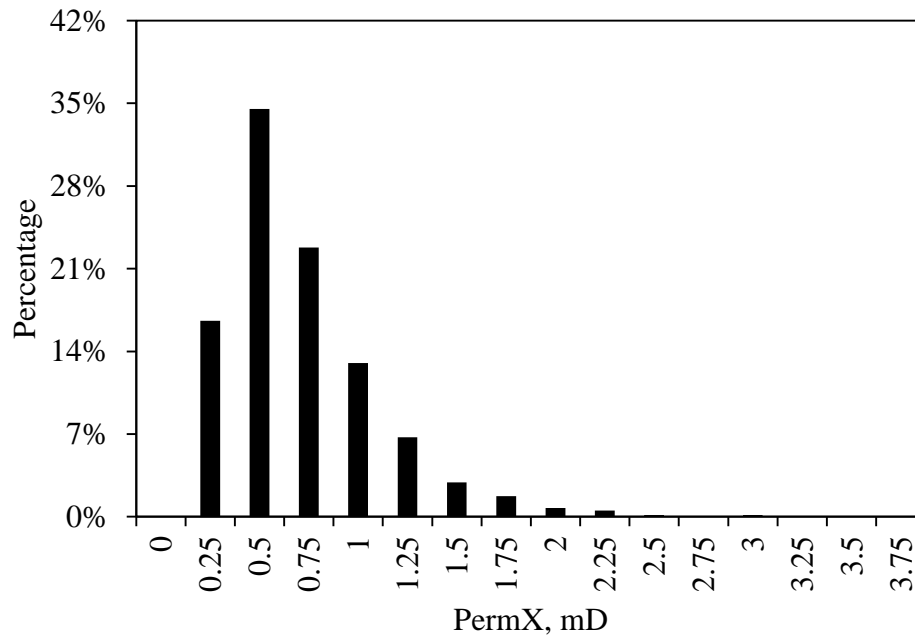
The considered reservoir geometry is a symmetric model with an area equal to one quarter of a reservoir section (160 acres) and with a uniform reservoir thickness of 15 ft. The absolute permeability in the horizontal direction is variable and its distribution was generated using Gaussian geostatistical simulation. Figure 5-2-a shows the horizontal permeability distribution and Figure 5-2-b displays the vertical permeability, which is 0.1 times the horizontal permeability, in cross section view. Figure 5-2-c shows the histogram of the horizontal permeability (mean value of 0.62 mD, standard deviation of 0.41 mD).



(a)



(b)



(c)

Figure 5-2: (a) Top view (i-j plane) of the model showing the spatial horizontal absolute permeability variation (b) Side view (j-k plane) of the reservoir vertical permeability (c) histogram of the horizontal absolute permeability data.

Table 5-3 lists the input parameters for the reservoir model.

Table 5-3: Reservoir input for the base case

Property	Value
Length, ft	5,250
Width, ft	1,350
Thickness, ft	15
Depth at the top of formation, ft	5,297
Initial reservoir pressure, psi	2,520
Initial water saturation, %	25
Initial oil saturation, %	75
Reservoir temperature, °F	127
Average porosity, %	12
Average horizontal permeability, mD	0.61
Vertical to horizontal permeability ratio	0.1
Reservoir pore volume, bbl	2.2E+6
Reference pressure, psi	1,000
Rock compressibility at P ⁰ , psi ⁻¹	5.0E-6
Number of grids (Nx×Ny×Nz)	105×27×5
Grid size (Dx×Dy×Dz), ft	50×50×3

The three horizontal wells used in the model are assumed to be hydraulically fractured in the transverse direction. Therefore, the planes of hydraulic fractures are perpendicular to the well trajectory. To precisely capture the physics of the fluid flow in the models, the local grid refinement feature is used to construct the hydraulic fractures along the well. The parent blocks enclosing the fractures are refined (divided into odd number of finer grids) in the direction parallel to the well path and also in the vertical direction. The central sub-grid in the refined area after modification of its transmissibility represents a real fracture. Transmissibility of the fracture blocks was adjusted such that following relationship holds (Shaoul et al. 2007):

$$k'_f \times \Delta_f = k_f \times w_f \quad (5-1)$$

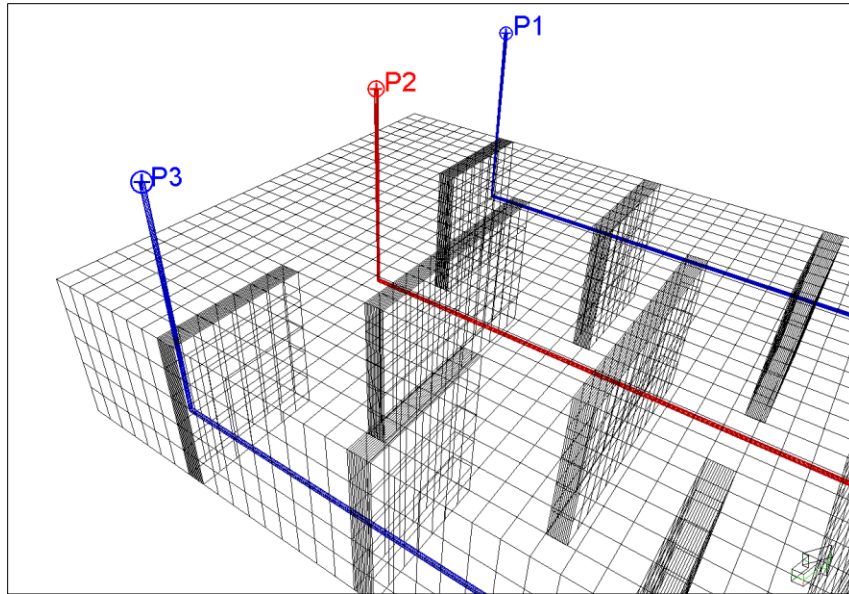
where $k'_f \times \Delta_f$ is the product of fracture permeability and width (fracture conductivity) and $k_f \times w_f$ is the corresponding product in the simulation model. The hydraulic fractures in our study have a constant width equal to 2.0 ft and their conductivity is

around 150 md-ft. The considered grid dimension was obtained based on the sensitivity analysis of the recovery factor of both water-flood and WAG flood scenarios and follow the same process as presented in Appendix 4A.

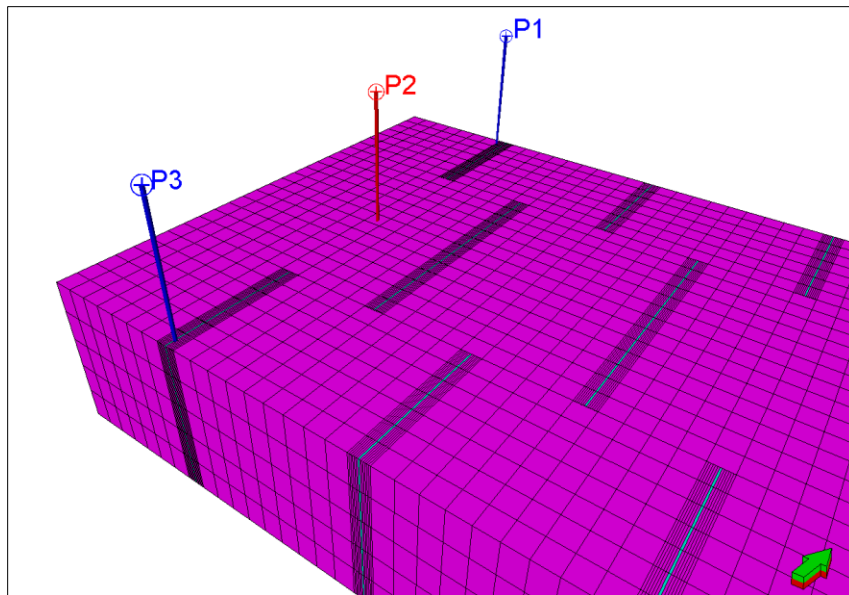
Figure 5-3-a shows a transparent display of the 3-D view of parent blocks enclosing the refined fractures in the model. Figure 5-3-b, displays the sub-grid in the refined region with modified transmissibility equal to that of a real fracture. One inner well at the center (P2 with complete fracture plane) and two boundary located wells (P1 and P3 with one wing of fracture plane) cover the whole drainage area. Table 5-4 summarizes the properties of the wells and their surrounding hydraulic fracture planes.

A combination of initial primary recovery (all wells are producers) and subsequent water-flooding (P2 is converted to water injector) is simulated as a base case for comparison with miscible gas flooding and WAG process. The primary recovery is continued until the recovery reaches a plateau (~15%) and the subsequent water-flooding is active until the water cut at producers reaches 95%. The water injection operation will last for 15 years.

The set of relative permeability curves used for the base case are shown in Figure 5-4. The critical water saturation is equal to 0.25 (the same as initial water saturation) and critical gas saturation is 0.05. The residual oil saturation for both gas and water phases are equal to 0.25 and the maximum relative permeability for gas and water are 0.50 and 0.35, respectively. Capillary pressure, however, is neglected.



(a)



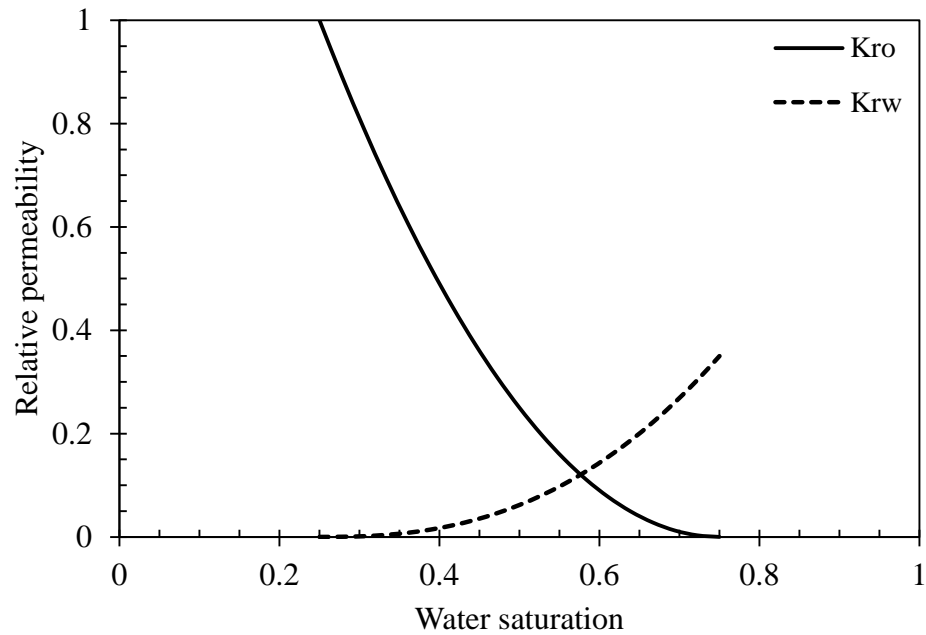
(b)

Figure 5-3: (a) Display of the refined grids which create the hydraulic fracture boundaries and (b) refined grid with higher permeability representing the hydraulic fracture plane.

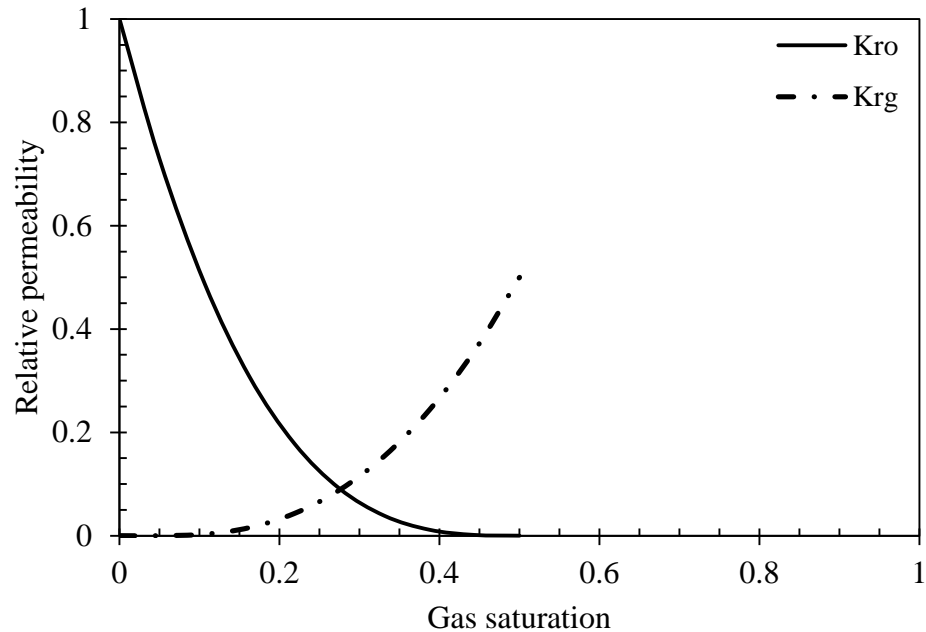
Table 5-4: Description of wells and hydraulic fractures

Property	Value
Well diameter, ft	0.6
Well length, ft	3,650
Well spacing, ft	650
Bottom hole pressure of producers, psia	300
Injection rate, rb/day	320
Duration of primary recovery, year	5
Duration of water flooding stage, year	15
Number of HF* along producers	13
Number of HF along injectors	12
Spacing between consecutive HF, ft	300
HF half-length, ft	225
HF height, ft	15
Conductivity of HF, md-ft	150
HF orientation	transverse
HF arrangement	staggered

* HF is abbreviated form of Hydraulic Fracture(s)



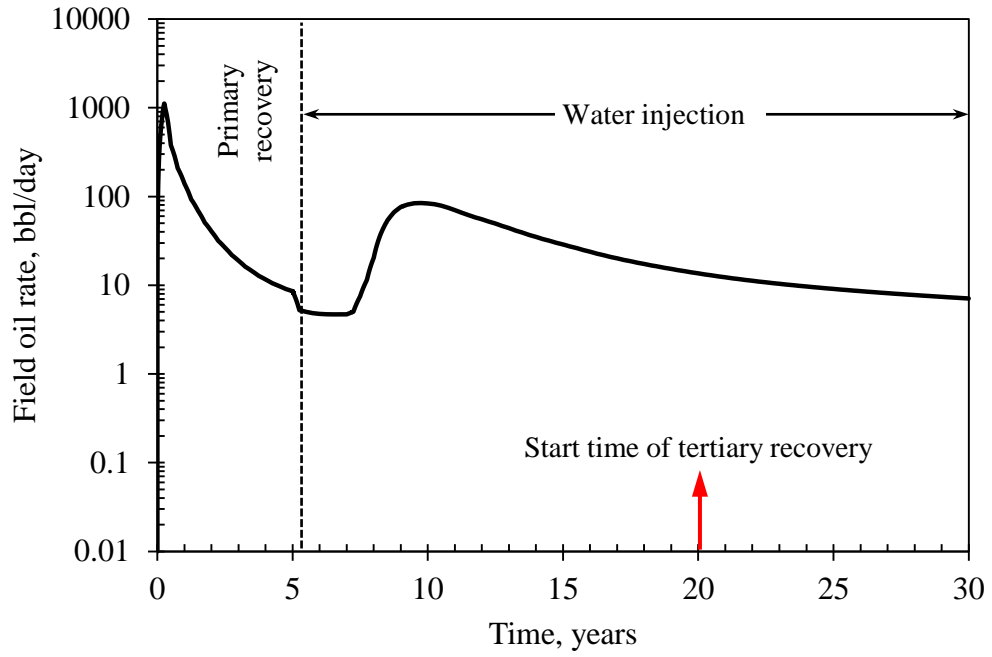
(a)



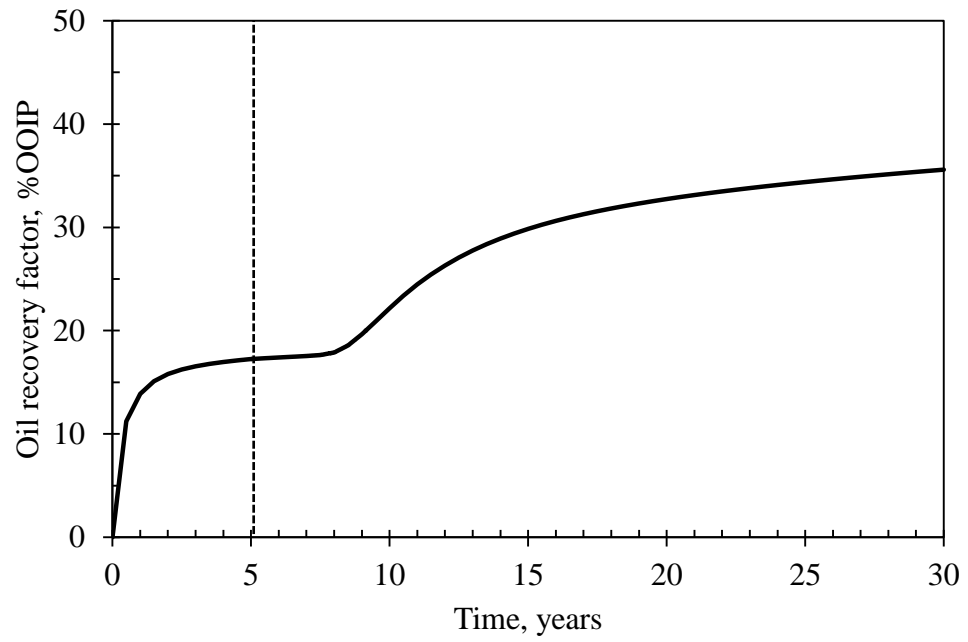
(b)

Figure 5-4: Relative permeability data set used in the primary and water injection scenarios (a) oil-water (b) oil-gas relative permeability.

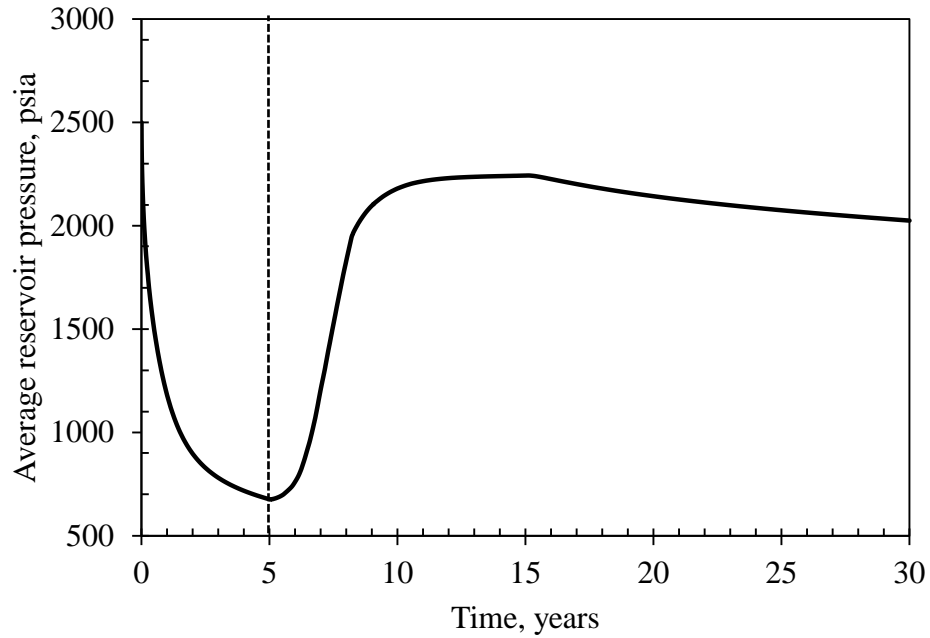
Figure 5-5 depicts various aspects of the first two stages of simulated oil recovery. According to Figure 5-5-a, just after primary recovery stage and at the beginning of water-flooding stage (converting the central well into injector), there is an abrupt reduction in the oil production rate as one of the producers is eliminated. Limited permeability of the reservoir matrix, and hence restricted flow capacity of the injector, causes considerable delay for water to first reach the producers and substantially increase the oil production rates. In this example, under the water injection rate of 300 stb/day, the breakthrough will happen after two and a half years. At the breakthrough time the average reservoir pressures is close to its peak value (Figure 5-5-c).



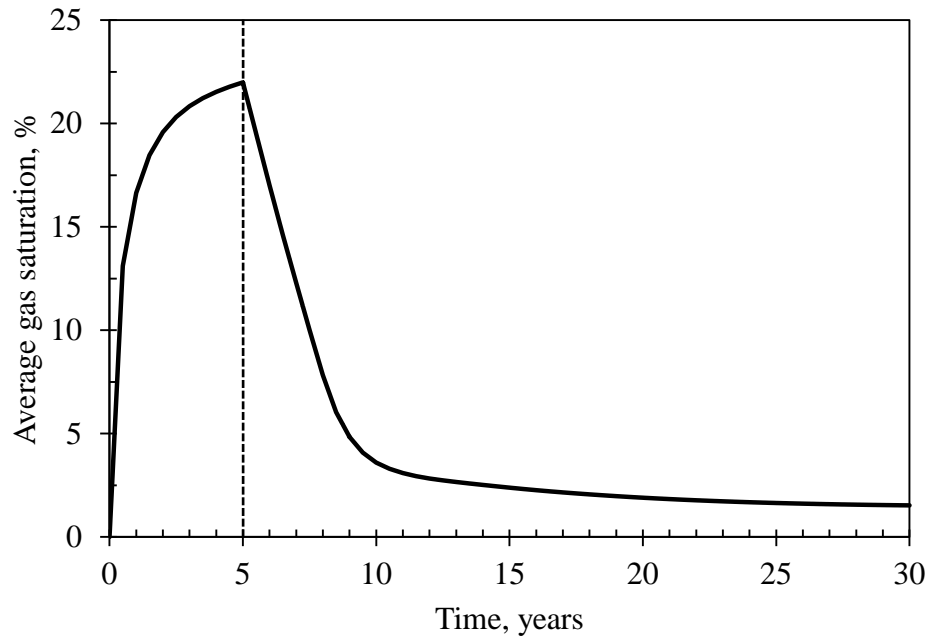
(a)



(b)



(c)



(d)

Figure 5-5: (a) Field oil production rate (b) Recovery factor curve (c) Average reservoir pressure (d) Average reservoir gas saturation at the end of the primary (5 years) and subsequent water-flooding stages.

For the base case, after 15 years of water-flooding, the water cut reaches 95%, where the pressure is around 2100 psi (not far from the MMP, Figure 5-5-c) and the gas

saturation approaches negligible values and is mostly associated with gas accumulation near the producers (Figure 5-5-d). Figure 5-6 displays the oil saturation distribution in the reservoir at the end of water-flooding. It shows that water flows favorably through high permeability zones first, and that the flooding front is not uniform. Despite the very low vertical absolute permeability, gravity segregation causes the average water saturation in the lower part of the reservoir to be higher than the upper part of the reservoir. After 0.8 PV (pore volumes) of water injection, the residual oil is mainly concentrated in the upper portion of the reservoir and low permeability zones.

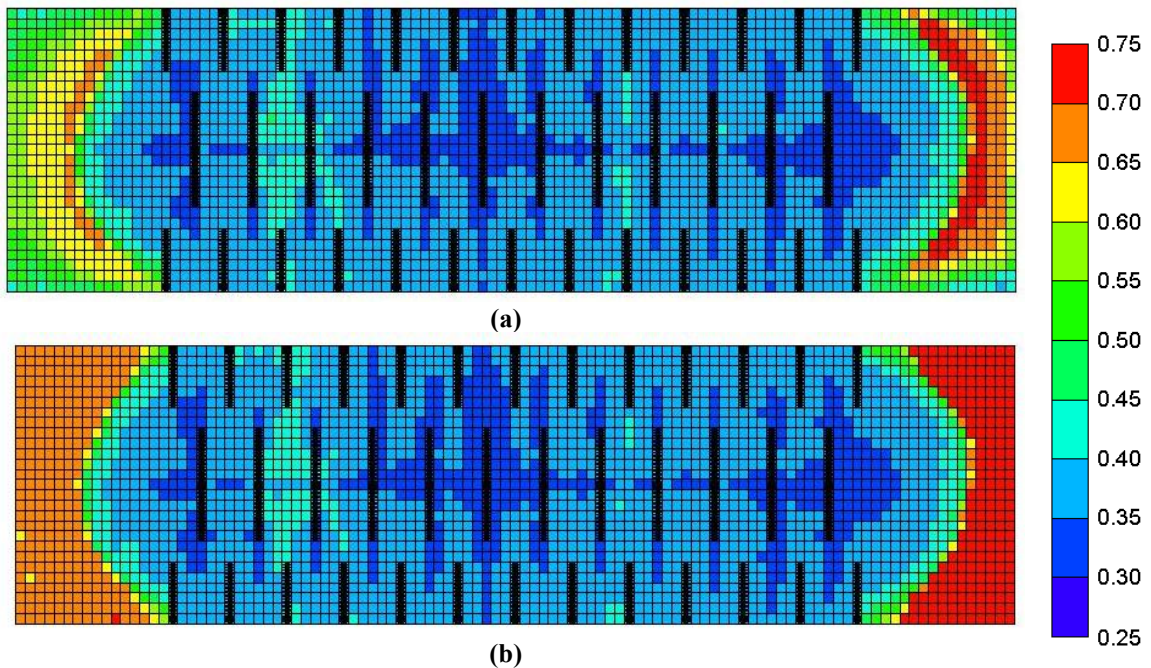


Figure 5-6: Oil saturation profile at the end of water-flooding stage for (a) top layer and (b) bottom layer of reservoir.

One important consideration for the waterflood scenario is the unexpected high recovery factor at the end of the process. We believe the main reason for such a high value is the symmetric nature of the model which keeps all the oil between the injector and the producer and leads to high sweep efficiency. In this respect, the effects of the relative permeability curves are also critical.

5-3- Continuous CO₂ injection and WAG (with CO₂) injection

In typical gas injection processes, the mobility ratio between injected gas and the displaced oil bank is very unfavorable because of low viscosity of the injected fluids. This results in viscous fingering (abridged breakthrough) and reduced sweep efficiency. To overcome these problems, alternating injection of gas and water with specified volume, known as the WAG process, has been developed. Improvement of sweep efficiency as a result of mobility contrast is the key element in the success of WAG process (Green and Whillhite, 1998). Moreover, injection of water as a slightly incompressible fluid can maintain the reservoir pressure level, which is necessary for development of miscibility between gas and oil and acceleration of gas solubility in oil (and therefore oil viscosity reduction). Because of the density contrast, the injected gas and water usually tend to sweep different portions of the reservoir. The upper portion of the pore space will tend to be swept by gas while water will push the oil in the lower parts (Jarrel et al., 2002).

To optimize the WAG process, there are several parameters that should be designed carefully. The following key factors should be considered (among others):

- *Slug Size*: Slug size, which refers to the cumulative volume of injected gas, is expressed as percentage/fraction of the hydrocarbon pore volume (HCPV). Generally, the more miscible gas injected, the higher the incremental oil recovery. Nevertheless, a larger injected volume will suppress the project economic return (Shing-Ming et al., 1984).
- *WAG Ratio*: WAG ratio, which is the ratio of the volume of injected water to that of gas, is one of the most important parameters in the WAG process. However, the optimized value for this ratio is quite reservoir-dependent, because the overall

performance of the WAG scheme depends strongly on the permeability distribution, gravity segregation (determined by fluid properties), and flow behavior of different phase (determined by two and three phase relative permeabilities). Gas availability as well as wetting state of the reservoir is also an important consideration in this respect (Wu et al., 2004).

- *Cycle Length*: The timing of switch between gas and water alternates may have considerable effect on the recovery factor as it determines the time span over which the phase redistribution (for example override of gas and underdrive of water) can occur within the reservoir (Wu et al., 2004).

Before performing any miscible flood simulation, the relative permeability and the amount of residual oil saturation with respect to CO₂ should be adjusted. The residual oil saturation in a field scale CO₂/WAG miscible flood varies between 5%-15% (Jarrel et al., 2002). To comply with this observation, the oil-gas relative permeability was modified to yield $S_{org} = 0.05$, resulting in $K_{rg} = 0.55$.

To study the effect of WAG ratio on recovery for this specific reservoir model, four cases with WAG ratio of 0.5, 1.0, 2.0 and 0 (continuous CO₂ injection) were considered. Each injection scenario will be continued until the HCPV of injected CO₂ reaches 1.0. To consider the effect of cycle length, an additional case for the WAG ratio of 0.5 will be provided. Table 5-5 provides a summary of the injection scheme in each case. The injection rate of fluids is however fixed at 320 rbbl/day except for scenario 1.

Table 5-5: Specifications of different tertiary injection scenarios considered in this study

Inj. scenario	WAG ratio	WAG cycle length	CO ₂ inj. length	Water inj. length
	[fraction]	[months]	[months]	[months]
1	0	NA	NA	NA
2	0.5	18	12	6
3	1.0	12	6	6
4	2.0	18	6	12
5	0.5	9	6	3

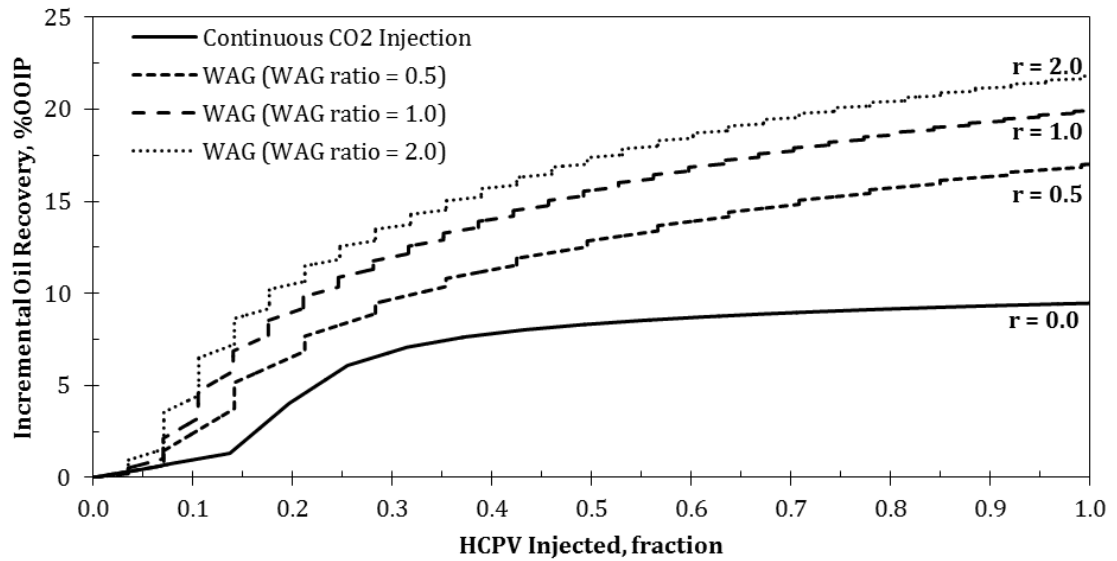
The simulation results indicate that in the case of continuous solvent injection, CO₂ will quickly reach the high permeable fractures along the producers hence the average reservoir pressure rapidly falls after the CO₂ breakthrough. To get a better sweep efficiency in this case, the injection may start with a lower rate and increase when the breakthrough was observed. Therefore, the proposed initial and final injection rates are set as 0.5 Mscf/day and 1.5 Mscf/day for continuous injection scenario.

5-4- Results and Discussion

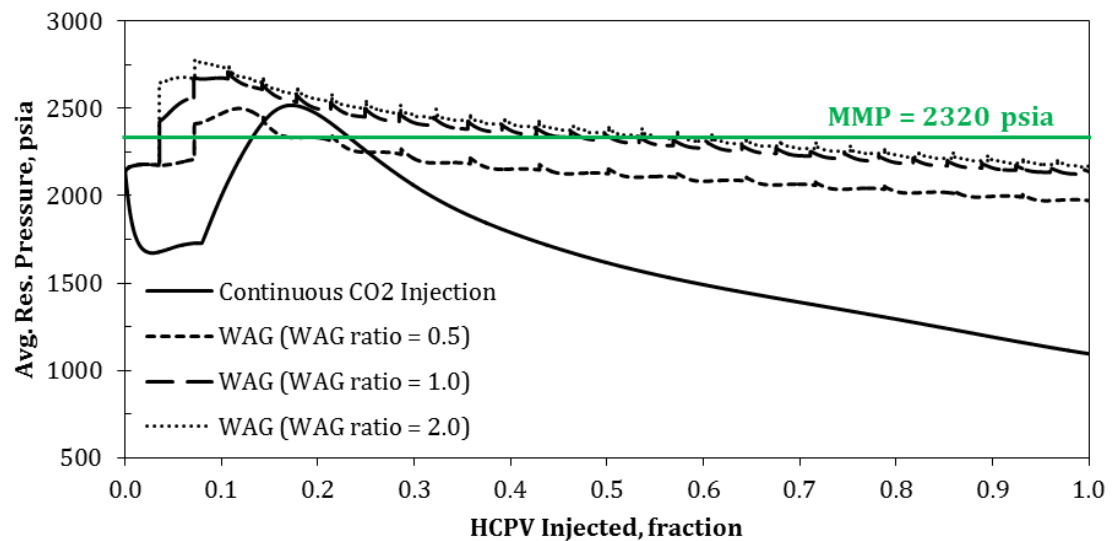
Referring to Figure 5-5-b and Figure 5-5-c, it is seen that the tertiary recovery scheme starts when 32% of OOIP has been recovered and the reservoir pressure has reached 2140 psia. Figure 5-7-a shows the incremental oil recovery associated with the first 4 scenarios in Table 5-5 with respect to HCPV injected. According to this figure, WAG performs better than continuous CO₂ injection, and applying higher WAG ratio brings about superior results. Moreover, at higher WAG ratios the difference between the recovery performance decreases. For example, the recovery factory at 100% HCPV for WAG ratios of 0.5, 1.0, and 2.0 are 16.7%, 19.8% and 21.7% respectively.

Figure 5-7-b depicts the average reservoir pressure for each injection scheme. In this figure, the line of minimum miscibility pressure has been drawn as well. The pressure trends in this figure are in line with the results obtained for the recovery factors. For any

injection scheme, depending on how far the pressure is below the MMP and hence less favorable miscible process, the corresponding recovery factor would also be less. In other words, as the difference between pressures (i.e. $MMP - P_{avg}$) increases, the CO₂ EOR efficiency goes down. Therefore, the smallest recovery factor is obtained in continuous CO₂ injection scenario and much better results are obtained in WAG process. In addition, for this model, as the WAG ratio increases, it would be easier to maintain MMP, but harder for CO₂ and oil to stay in contact, hence reducing the miscibility. Therefore, there should be an optimal WAG ratio for achieving best tertiary recovery.



(a)



(b)

Figure 5-7: Variation of (a) oil recovery factor (b) average reservoir pressure with respect to the HCPV of injected CO₂ for different injection schemes.

The comparison between the sweep efficiency of two cases with WAG ratio of 0.0 and 2.0 after injection of 100% HCPV of CO₂ is displayed in Figure 5-8. As expected, reservoir heterogeneity plays an important role in dictating the preferential flow paths. For continuous injection scenario, the high mobility CO₂ seeks out the path of least resistance through high permeable fractures along the producers and will travel the same

path for the entire process. Therefore, the recovery is confined mostly to the region between the producers and injectors fractures' tips. For WAG process, however, the recovery region is expanded substantially in both vertical and areal directions. Further, due to buoyancy effects and upward movement of CO₂, recovery from the top of the reservoir would be more than from the bottom.

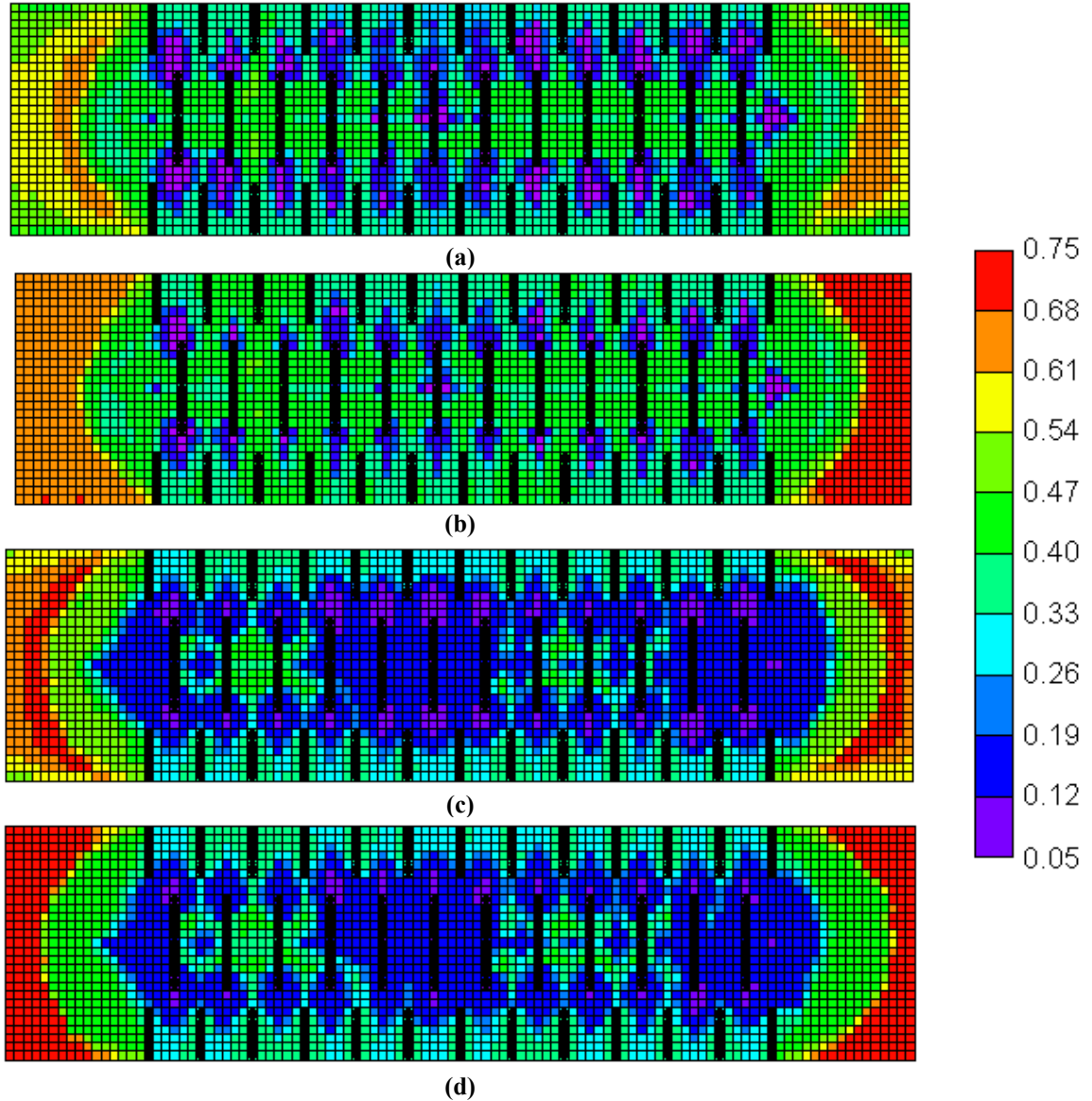
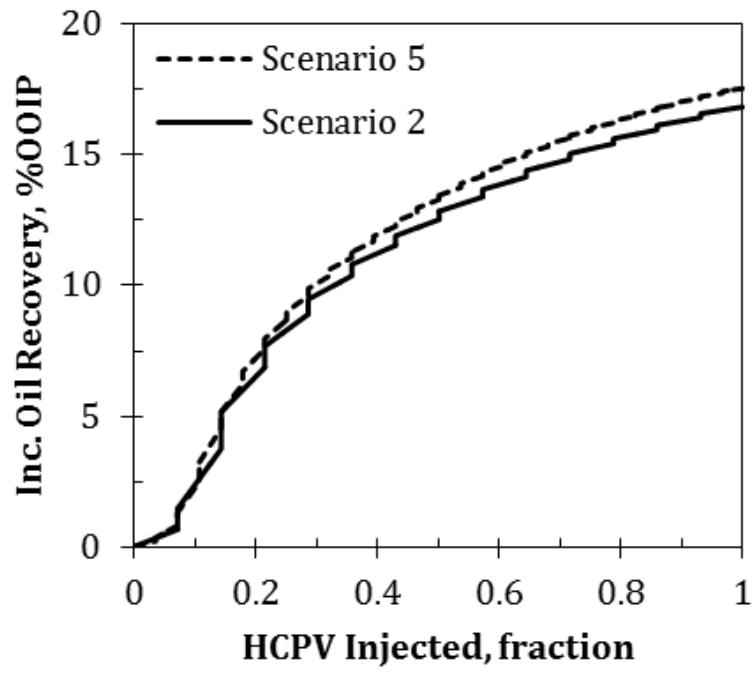


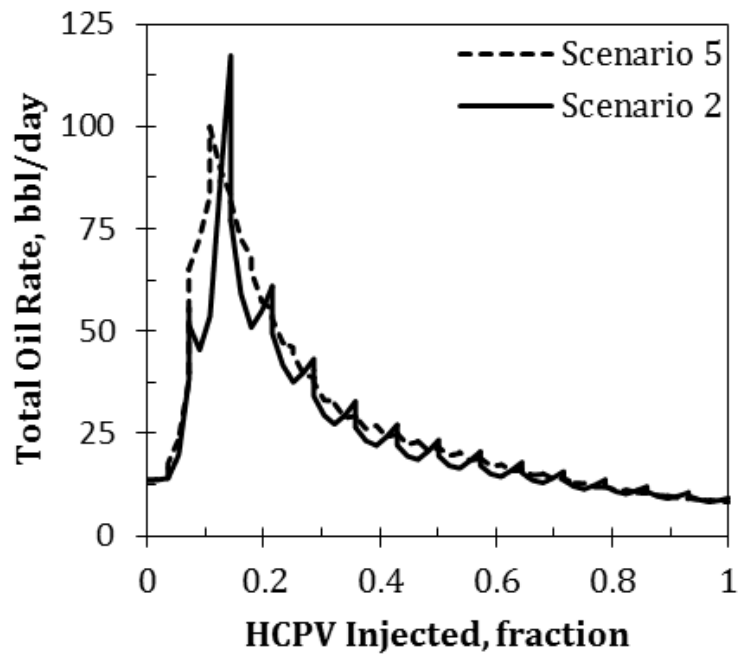
Figure 5-8: Variation of oil saturation at the end of injection scheme (a) continuous CO₂ injection, top layer (b) continuous CO₂ injection, bottom layer (c) WAG injection with ratio 2, top layer (d) WAG injection with ratio 2, bottom layer.

To investigate the effect of cycle length (with identical WAG ratio) on the performance of WAG injection, the results for scenarios 2 and 5 are compared in Figure 5-9-a through Figure 5-9-c. From these figures, it is concluded that decreasing the cycle length increases recovery factors from the WAG process. This may be due to the fact that decreasing the cycle length causes increase in water injection frequency which consequently keeps the average pressure at higher values. Higher pressures simply mean better sweep efficiency with respect to both maintaining miscibility conditions and also maintaining pressure gradient between producers and injectors.

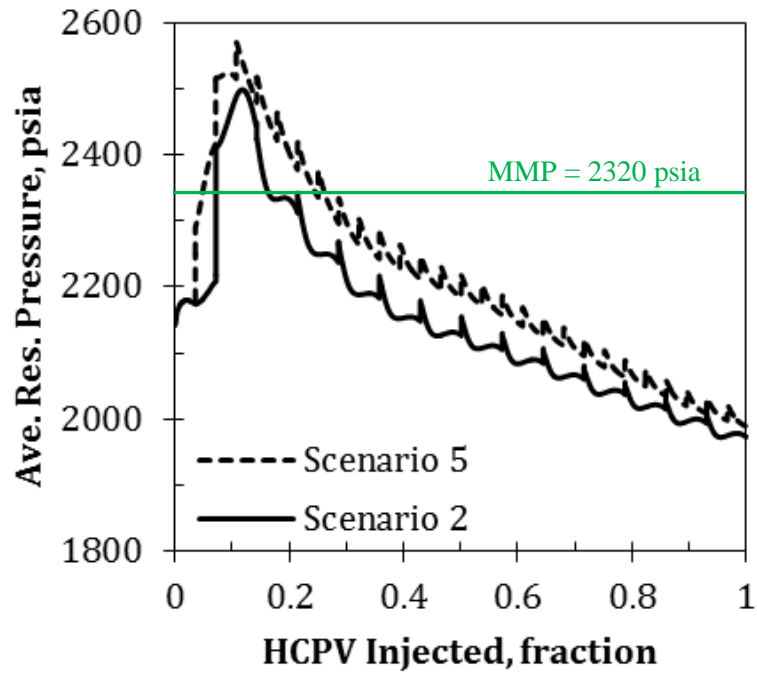
From storage point of view, Figure 5-9-d shows the average CO₂ saturation at the end of injection periods for different scenarios in the reservoir. The results demonstrate that the less efficient recovery scheme (continuous CO₂ injection) is the preferred one in this respect. In the WAG process the injected solvent has enough time and more of a tendency (due to higher pressures) to dissolve into the in-situ oil and will be produced in the subsequent water injection cycle. However, it should be noted that the effect of important parameters like the solubility of CO₂ into water and relative permeability hysteresis effect on the storage capacity of different schemes have been neglected in this study. These important parameters may alter to some extent the oil recovery factors.



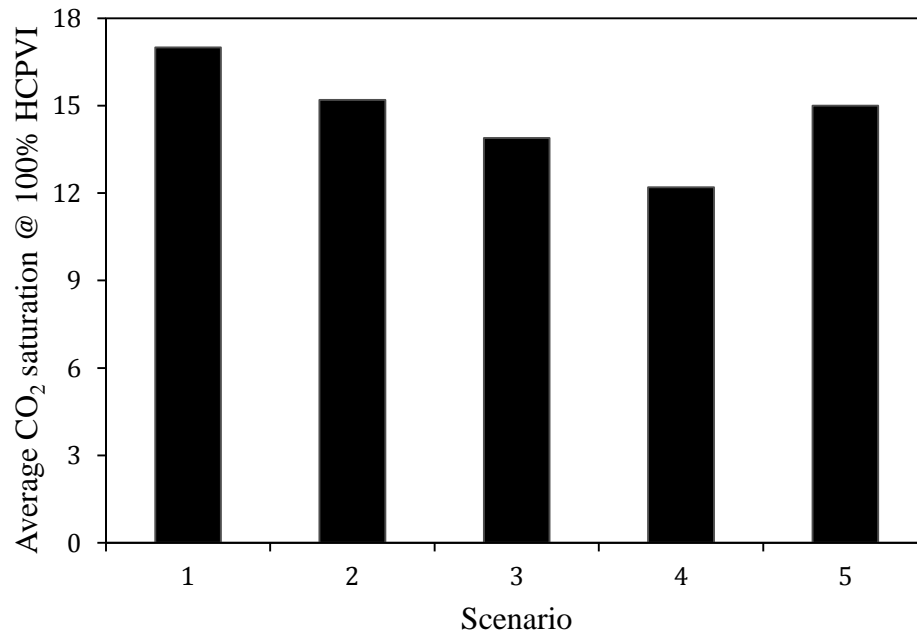
(a)



(b)



(c)



(d)

Figure 5-9: (a-c) Comparison of different parameters for two WAG process with different cycle length of 9 months and 18 months and identical WAG ratio of 0.5 (d) CO₂ storage capacity results from different injection scenarios.

5-5- Summary

In this chapter, a quarter section of a tight oil reservoir with a stochastic permeability distribution is set up and a compositional simulator is used to investigate CO₂ EOR process. The three horizontal wells in the model (two edge producers and one middle injector) have transverse fractures in a staggered configuration. This configuration has the advantage of maximizing contact area with the formation as well as maximizing distance between the fractures, which is important in delaying the breakthrough of the injected fluids and improving sweep efficiency. At the end of primary and secondary (water-flooding) recovery, almost 70% of the original oil in place remains trapped in the inter-fracture spaces of this symmetric model.

To recover this remaining oil saturation, CO₂ injection, either through injection of pure CO₂ or WAG, was considered. The results indicate that recovery factors from injection scenarios (with constant rate constraint on injectors), is substantially influenced by the reservoir heterogeneity and also the mobility of the injected fluids. For continuous CO₂ injection, high mobility of the gas causes a fast breakthrough at the producers. As such, once the connection between the injectors and producers fractures (path of least resistance) was established, the average reservoir pressure falls rapidly below the MMP, thereafter the process would remain immiscible and not gaining the benefit of miscible flood.

WAG injection, on the other hand, can substantially improve the recovery by maintaining the pressure around the MMP and therefore develop an efficient miscible process. With reservoir and fluid properties used in this study, as the WAG ratio increases, it would be easier to maintain pressure levels higher than MMP and therefore recovery increases. However, it should be noted that under this circumstance it would be

also harder for CO₂ and oil to stay in contact, hence reducing the miscible flood benefits. Therefore, an optimal WAG ratio could be designed through simulation. In this study, even after water-flood, the incremental recovery of CO₂ flood in tight oil formation, with WAG ratio of 2.0, could be as high as 21.7%.

Decreasing the cycle length (with identical WAG ratio) causes increase in water injection frequency, which consequently keeps the average pressure at higher values and therefore improves the sweep efficiency. Like the WAG ratio, there should be an optimal value for this parameter which is quite reservoir dependent.

Results from this study show that the CO₂ EOR potential in tight oil formations is significant. The parametric compositional model has proved to be a very efficient proxy in similar projects. Multiple sensitivities and optimal design can be investigated within a reasonable time frame while CO₂ production/storage can also be monitored.

Acknowledgment

This research was made possible by funding provided by ISEEE-NRCan (project title “Co-optimization of CO₂ Sequestration and Oil Recovery in Tight Oil Formations”). Chris Clarkson would like to acknowledge Encana and AITF for support of his Chair position in Unconventional Gas and Light Oil research at the University of Calgary, Department of Geoscience. He would also like to acknowledge the sponsors of Tight Oil Consortium (TOC), hosted at the University of Calgary.

References

- Clarkson, C.R., Pedersen, P.K., 2011. Production Analysis of Western Canadian Unconventional Light Oil Plays. Paper CSUG/SPE 149005 presented at the

Canadian Unconventional Resources Conference held in Calgary, Alberta, Canada, 15-17 November.

- Cox, S.A., Cook, D.A., Dunek, K., Daniels, R., Jump, C., Barree, B., 2008. Unconventional Resource Play Evaluation: A Look at the Bakken Shale Play of North Dakota. Paper SPE 114171 presented at the SPE Unconventional Reservoirs Conference held in Keystone, Colorado, 10-12 February.
- Economides, M.J., Oligney, R.E., Valkó, P., 2002. Unified Fracture Design: Bridging the Gap between Theory and Practice. Alvin, Texas: Orsa Press.
- Green, W.D., Willhite, G.P., 1998. Enhanced Oil Recovery. SPE, Richardson, Texas.
- Jarrel, P.M., Fox, C.E., Stein, M.H., Webb, S.L., 2002. Practical Aspects of CO₂ Flooding, Monograph Series, SPE, Richardson, Texas.
- Khan, S.A., Pope, G.A., Sepehrnoori, K., 1992. Fluid Characterization of Three-Phase CO₂/Oil Mixtures, paper SPE/DOE 24130 presented at the 8th Symposium Oil Recovery, Tulsa, OK, 22-24 April.
- Lohrenz, J., Bray, B.G., Clark, C.R., 1964. Calculating Viscosity of Reservoir Fluids from their Composition, J. Pet. Tech. page 1171; Trans., AIME 231.
- Peng, D.Y., Robinson, D.B., 1976. A New Two-Constant Equation of State, Ind. & Eng. Chem. Fund. 15, No. 1, 59-64.
- Shing-Ming, C., Allard, D.R., Anli, J., 1984. Factors Affecting Solvent Slug Size Hydrocarbon Miscible Flooding Requirements in Hydrocarbon Miscible Flooding, SPE paper 12636 presented at the 4th Symposium on Enhanced Oil Recovery, Tulsa, OK, 15-18, April.

- Shaoul, J.R., Behr, A., Mtchedlishvili, G., 2007. Developing a Tool for 3D Reservoir Simulation of Hydraulically Fractured Wells. SPE Res Eval & Eng 10(1):50-59. SPE-108321-PA. DOI: 10.2118/108321-PA.
- Viau, C., Nielsen, K., 2010. Unconventional Oil Production in the Cardium Formation, East Pembina Area, Alberta, Canada. Presented at the CSPG core conference held in Calgary, Alberta, Canada, 16-17 September.
- Wu, X., Ogbe, D.O., Zhu, T., Khataniar, S., 2004. Critical Design Factors and Evaluation of Recovery Performance of Miscible Displacement and WAG Process, SPE paper 2004-192 presented at Canadian International Petroleum Conference, Calgary, Alberta, 8 June.

Chapter 6

Optimization of WAG Process for Coupled CO₂ EOR-Storage in Tight Oil Formations: An Experimental Design Approach¹

Restricted flow capacity of low permeability oil formations imposes unique challenges to the implementation of CO₂-WAG processes in such reservoirs. Application of multi-stage fractured horizontal wells can substantially improve the injection and production rates. However, there are various design parameters and operating conditions which can affect the performance of a WAG flood. The parameters considered in this study are those related to development pattern (well spacing and well completion strategy), hydraulic fracture geometry (half-length and spacing), WAG parameters (WAG ratio and CO₂ slug size) and the timing of the switch from primary or water-flood to WAG scheme. In this study, CO₂ EOR performance is assessed based on the oil recovery factor and also the amount of stored CO₂; in other words, the objective is to achieve both the goals of enhanced oil recovery and storage of CO₂ in the tight oil formation. However, to reflect the effect of time, the net present value (NPV) of the projects was also considered. All

¹ This chapter is a modified version of : Ghaderi, S.M., Clarkson, C.R., and Chen, Y., 2012. Optimization of WAG Process for Coupled CO₂ EOR-Storage in Tight Oil Formations: An Experimental Design Approach, Paper SPE 161884, presented at SPE Canadian unconventional resources conference in Calgary, Alberta, Canada, 30 October-1 November 2012.

three of these parameters were therefore included in objective functions to be optimized.

The effect of all aforementioned parameters on objective functions was investigated using a compositional simulator. Design of experiment (DOE) was then utilized to perform a comprehensive statistical analysis to recognize the most prominent factors in fulfillment of each objective function in a tight reservoir with properties similar to Pembina Cardium field. Response surfaces were generated to quantify the effect of the factors on the objective functions. Optimization was carried out to find those sets of factors which provided the highest recovery, storage, and NPV. Searching for optimal values can be extended to any combination of objective functions which are obtained by applying weighting multipliers to each individual objective function.

6-1- Introduction

Careful implementation of CO₂-EOR in depleted or partially depleted oil reservoirs can provide two simultaneous benefits: (1) an environmental benefit by permanent storage and retention of part of the injected CO₂ volume; (2) an economic benefit by noticeable improvement in oil production rates and hence incremental oil recovery.

In CO₂-EOR, a portion of the injected CO₂ dissolves into the oil and water that remains in the reservoir. Therefore, not all the injected gas can be recycled back to the surface. The capillary process will trap an additional fraction of CO₂ underground, a process known as non-wetting phase capillary trapping (Lake, 1989). Although very dependent on the reservoir properties and injection/production strategy, typical estimates for CO₂ storage of EOR schemes are between 30% to 50% of the injected quantity (Smyth, 2008; Han et al., 2010; Hovorka, 2010). The ability of CO₂ to dissolve in reservoir oil (causing swelling of the oil), and reduce oil viscosity are the mechanisms for

increased oil production rates using CO₂-EOR (Jarrel et al., 2002). In many floods, water is introduced episodically to augment a CO₂ flood as a chase fluid, a process known as water alternating gas or WAG process. WAG is used to reduce the amount of required expensive CO₂, as well as increasing the amount of contacted oil (Lake, 1989; Green and Whillhite, 1998).

To date, the majority of the CO₂-EOR projects are designed to minimize the amount of gas injected per barrel of oil produced, hence, minimizing the CO₂ purchase and making the most profit possible. However, when the goal is aimed toward storage of injected carbon dioxide, the design challenges and considerations change significantly (Kovscek, 2002; Kovscek and Cakici 2005). The design and implementation of the process in tight formations becomes even more complicated because obtaining commercial production/injection rates is a serious concern in such reservoirs.

Recent advances in drilling and completion technology, such as the utilization of multi-staged fractured horizontal wells, have enabled commercial production from reservoirs with poorer properties. Nevertheless, proper design of the fractures with respect to different properties (e.g., number of stages and half-length) is necessary to ascertain good economic return for the required relatively large capital investment. Moreover, if future secondary and/or tertiary recovery schemes are planned to be executed under such circumstances, selection of proper design parameters becomes vital.

Feasibility of CO₂ EOR/storage in the low permeability portion of Pembina Cardium field, referred to as a “Halo Oil” play by Clarkson and Pedersen (2011), is the main focus of this study. This play has several attractive attributes such as high quality oil (around 36 °API), sweet gas, and low water production rates with accessible infrastructure in the area

(Viau and Nielsen, 2010).

We present a methodology to find the operational conditions and design parameters under which the highest oil recovery and highest CO₂ storage in a tight reservoir can be achieved. This approach is based on design of experiment (DOE) and, encompasses comprehensive statistical analysis of the results of extensive compositional simulation runs. Each run consists of four sequential stages of primary recovery, water-flood, CO₂-WAG, and the final water-flood recovery. The timing of switch from one scheme to the next is different for each run. Therefore, the effect of timing on the oil recovery and storage capacity is considered by accounting for the time value of money or NPV of the projects. The situations under which the NPV turns out to be optimal will be investigated as well. Response surfaces are then generated to quantify the effect of different factors on different objective functions.

The paper is organized as follows: First, the reservoir and fluid properties used in the simulation models are presented. Second, the considered parameters for the sensitivity runs are defined and the different levels associated with each factor are declared. Third, the sensitivity results are presented, analyzed and discussed. Finally, the summary and conclusion are provided.

6-2- Properties of Simulation Model

6-2-1- Fluid Properties and EOS Model

The reservoir oil is an undersaturated light oil with a stock tank gravity of 38 °API and an initial solution gas-oil-ratio (GOR) of 730 scf/stb. The original reservoir pressure at the reference depth of 5279 ft is 2520 psi. The bubble point of the reservoir at reservoir

temperature of 127 °F is approximately 1620 psi Table 6-1 summarizes the important properties of the reservoir fluid.

Table 6-1: Reservoir fluids properties

Property	Value
Pb, psia	1,620
Rs at Pb, scf/stb	730
Oil viscosity at Pb, cp	0.63
Bo at Pb, bbl/stb	1.37
Oil density at STP, lb/ft ³	52.1
Average gas viscosity, cp	0.01
Water viscosity, cp	0.57
Water salinity, ppm	50,000

Simulation of the WAG and CO₂ injection processes requires compositional simulation which can account for the phase equilibria between the injected and in-situ fluids. The first step for any compositional simulation is proper tuning of an EOS such that all important interactions can be captured. The tuning of the EOS in this work followed the methodology suggested by Khan et al. (1992) to characterize CO₂-oil mixtures. The two-parameter Peng-Robinson EOS (Peng and Robinson, 1976) was selected to regenerate the fluid properties because it was proven to be suitable for low-temperature CO₂-oil mixtures (Khan et al., 1992). The modified Pedersen model (Pedersen and Fredenslund, 1987) was used to predict both oil and gas viscosities.

To determine the binary interaction coefficients (BIC) between CO₂ and different oil components, and to check the accuracy of the tuned EOS, a 1-D slim tube experiment was simulated. The slim tube experiment is the most typical method for measuring the minimum miscibility pressure between a solvent gas and oil (Danesh, 1998). The CO₂ minimum miscibility pressure (MMP) was measured experimentally as 2320 psia.

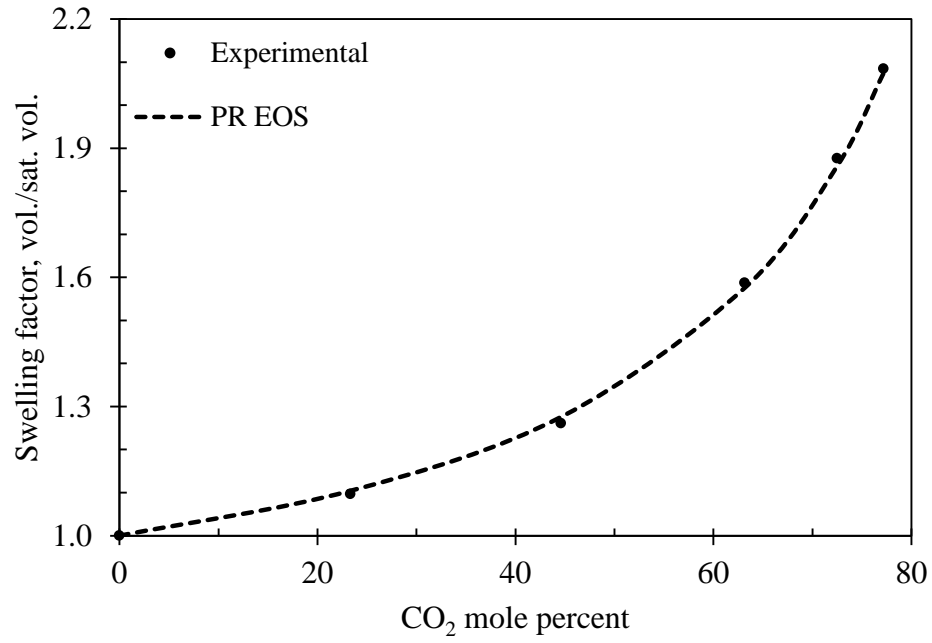
To account for the solubility of CO₂ into water, which has an impact on CO₂ storage,

Henry's law was used (Li and Ngheim, 1986). Therefore, the fugacity, f_i , of gaseous components soluble in aqueous phase was calculated as:

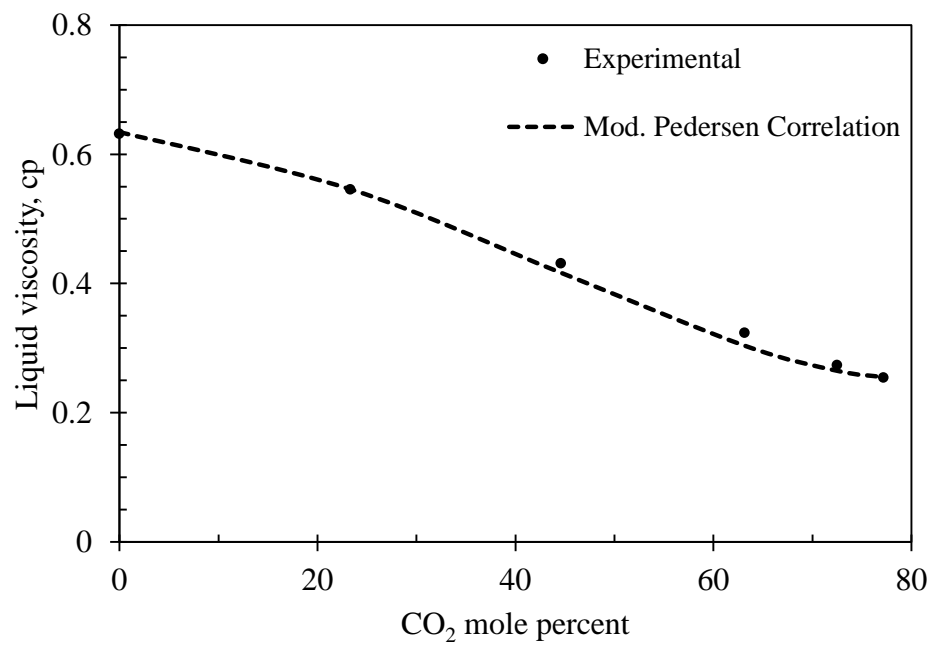
$$f_i = x_i \times H_i \quad (6-1)$$

where H_i is the Henry's constant of component i and x_i is the mole fraction of component i in the aqueous phase. Henry's constant is a function of pressure, temperature and salinity therefore the Harvey's correlation (Harvey, 1996) was used to describe this dependency for CO₂ and water.

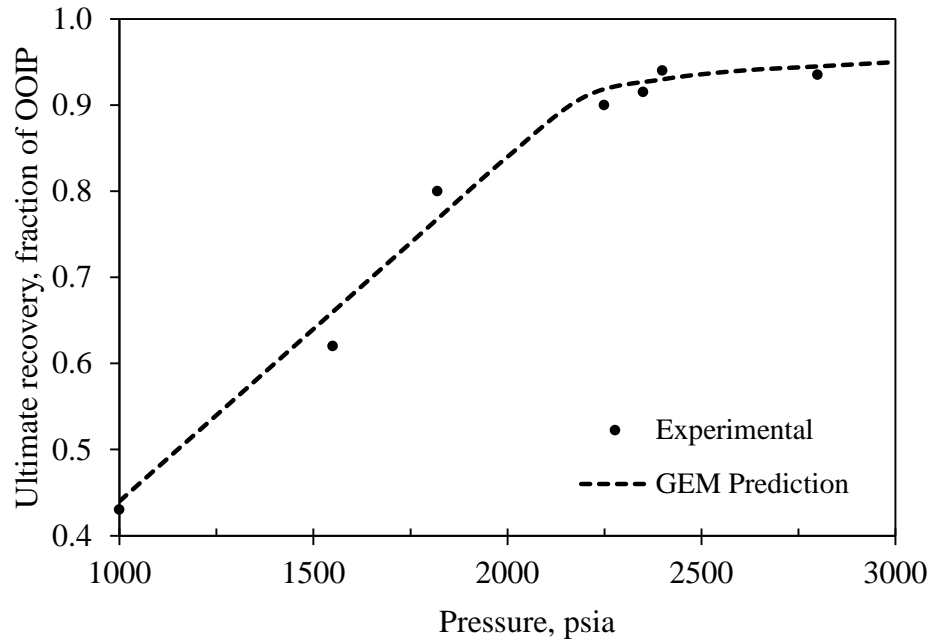
Figure 6-1-a shows the experimental and PVT simulation results for oil swelling caused by CO₂ solution, and Figure 6-1-b shows the viscosity trend. Figure 6-1-c represents the results of the slim tube experiment and the prediction for MMP which closely matches the experimental value. Figure 6-1-d illustrates the variation of CO₂ solubility in saline water versus pressure at a constant temperature of 127 °F. The composition of the final fluid with the properties of the heavy fraction is tabulated in Table 6-2.



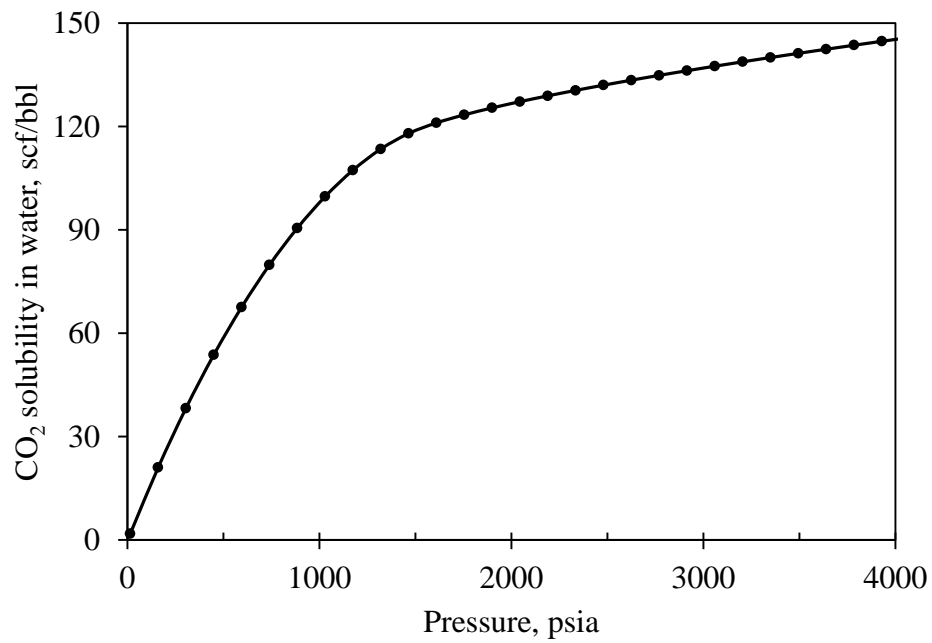
(a)



(b)



(c)



(d)

Figure 6-1: Comparison of the predicted (PR EOS and Pedersen correlation) and observed values for (a) liquid mixture swelling factor and (b) liquid viscosity with respect to CO₂ mole percentage in the mixture. (c) comparison of the experimentally measured and sintu

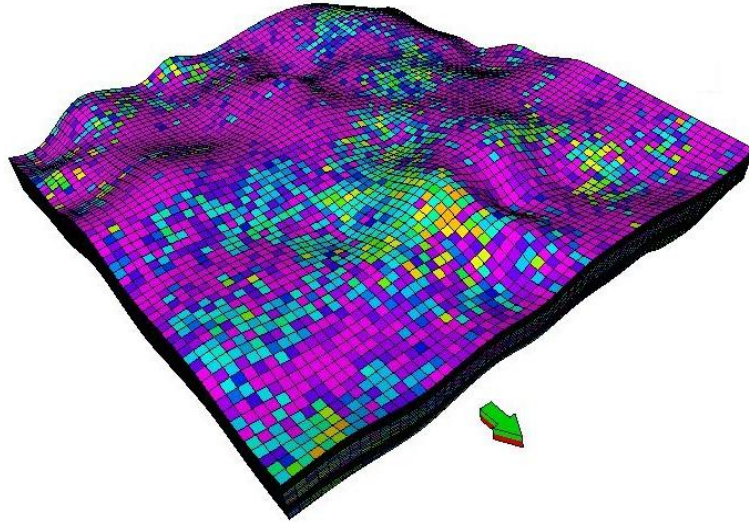
Table 6-2: Composition of the fluid (after regression)

Component	Mole fraction
CO ₂	0.001
COMP1	0.414
COMP2	0.076
COMP3	0.059
COMP4	0.061
COMP5	0.026
HFRC*	0.363

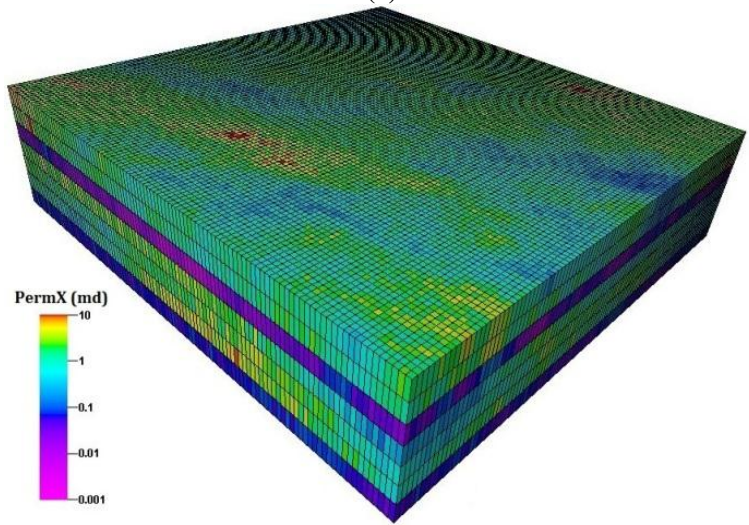
* MW = 238 lb/lb-mole ; SG = 0.86

6-2-2- Reservoir Model and Rock Properties

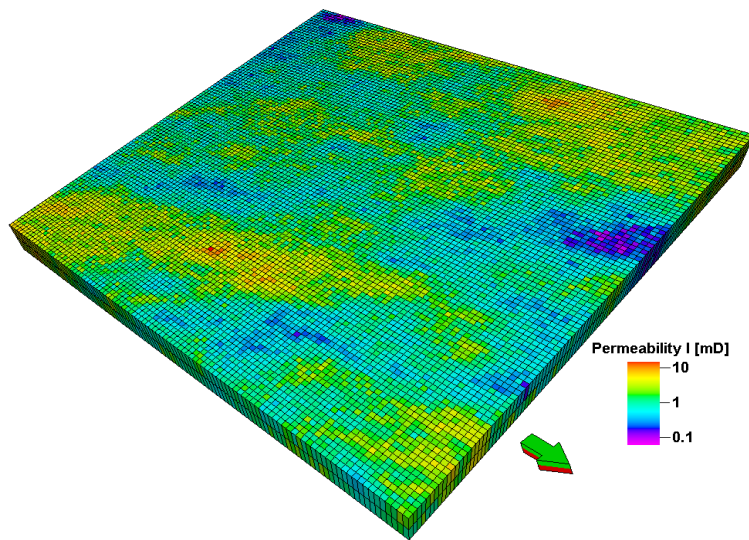
The original 3-D geological reservoir model considered for this study was one section (640 acres) of the Pembina Cardium field, where the structure and the heterogeneity of permeability and porosity were modeled based on real core and log data. Figure 6-2-a presents a close-up view of this 3-D model. However, since local grid refinement is used to capture the fluid flow through the hydraulic fractures which exacerbates the run time of compositional simulation, the reservoir model was flattened (Figure 6-2-b) to allow some flexibility with respect to handling sensitivities of the fracture spacing and fracture half-length.



(a)



(b)



(c)

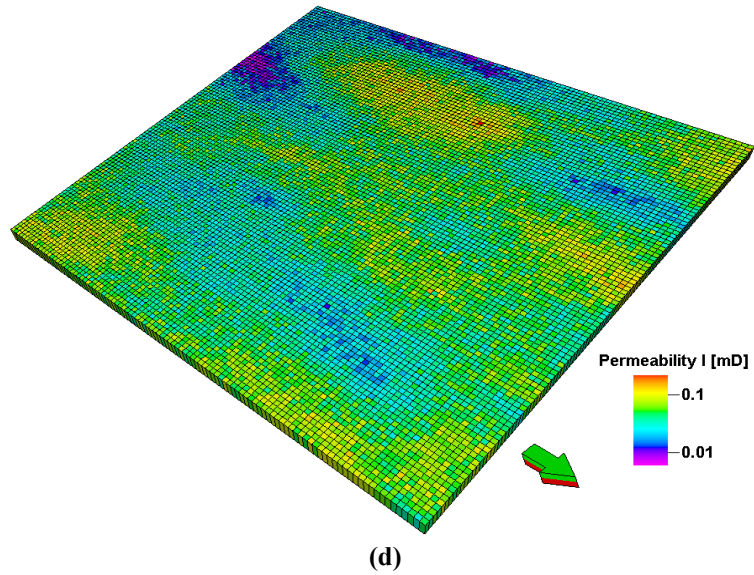


Figure 6-2: (a) One section of Pembina Cardium reservoir considered as the study area (b) the flattened version of the reservoir model used in reservoir simulations (c) the horizontal permeability map for the top sand layer (Zone 1) (d) the horizontal permeability of the lower shaly-sand layer (Zone 4).

Different properties of the final geo-model used in the simulations are tabulated in Table 6-3. The reservoir is supposed to be surrounded by four sealing faults at its edges. Also, pressure support and contribution from the aquifer beneath the reservoir is minor and therefore neglected.

The geo-model consists of two rock types, sand and shaly-sand (mixed of shale and sand). There are four zones in the model: Zone 1 (top zone) and Zone 3 have sand, while Zone 2 (which is between Zone 1 and Zone 3), and Zone 4 (bottom zone), are shaly sand. Figure 6-2-c and Figure 6-2-d show spatial variation of the horizontal permeability for the top sand and bottom shale-sand layers, respectively. The vertical to horizontal permeability ratio was considered a constant at 0.1. Each layer has a permeability distribution associated with its porosity variation as well. The average rock properties for each layer can be found in Table 6-4.

Table 6-3: General properties of the geo-model

Property	Value
Length, ft	5,250
Width, ft	5,250
Thickness, ft	24.1
Depth at the top of formation, ft	5,297
Initial reservoir pressure, psi	2,520
Initial water saturation, %	25
Initial oil saturation, %	75
Reservoir temperature, °F	127
Average porosity, %	9.1
Average horizontal permeability, mD	1.44
Horizontal to vertical permeability ratio	0.1
Reservoir pore volume, bbl	9.3E+6
Reference pressure, psi	1,000
Rock compressibility at reference pressure, psi ⁻¹	5.0 E-6
Number of grids (Nx×Ny×Nz)	105×105×7
Average grid size (Dx×Dy×Dz), ft	50×50×3

Table 6-4: Rock properties of different layers

Geological layer*	S1	SS1	S2	SS2
\bar{h} , ft	8.4	2.9	9.3	3.5
$\bar{\varphi}$, %	11.2	3.1	8.4	3.8
\bar{k} , mD	1.621	0.029	2.211	0.047
Number of layers in simulation model	2	1	3	1
* <u>S</u> stands for sand and <u>SS</u> stands for shaly-sand				

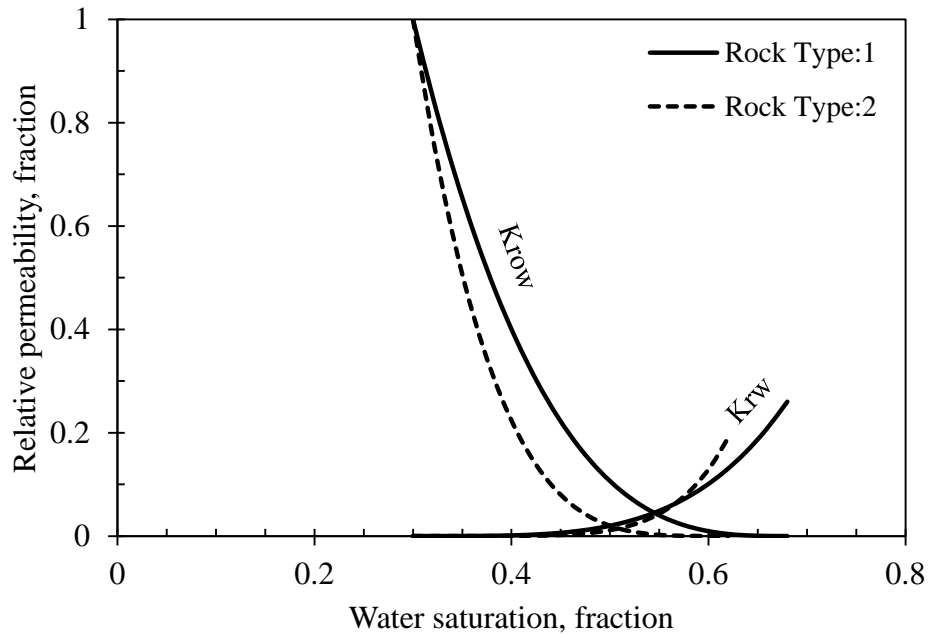
The horizontal wells used in the model have the same horizontal length of 4650 ft. The hydraulic fractures along the wells are in the transverse direction and vertically extend from the top to the bottom of the reservoir. The local grid refinement features are used to create the hydraulic fractures along the well. The transmissibility of the refined grid representing the fracture plane should be adjusted to honor the following equality (Shaoul et al., 2007):

$$k'_f \times \Delta_f = k_f \times w_f \quad (6-2)$$

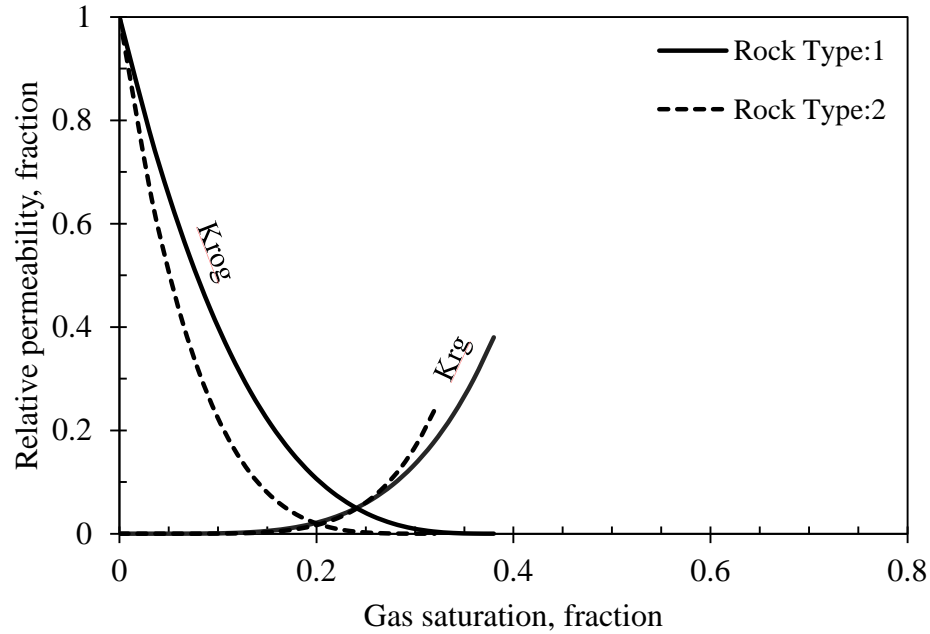
where $k'_f \times \Delta_f$ is the product of fracture permeability and width (fracture conductivity)

and $k_f \times w_f$ is the corresponding product in the simulation model. The hydraulic fractures in our study have a constant width (W_f) equal to 1.0 ft and their conductivity is around 200 md-ft.

The two sets of two-phase relative permeability data used for the two rock types are shown in Figure 6-3. Here, rock type 1 represents sand and rock type 2 represents shaly-sand. The maximum relative permeabilities to water are 0.27 and 0.19 for rock type 1 and 2, respectively. These values for the gas phase are 0.24 and 0.38. However, due to lack of data for Pembina Cardium, relative permeability hysteresis was neglected. From CO₂ storage point of view, hysteresis can account for trapped and immobile portion of injected CO₂ which resides in the reservoir for a long period of time (Ozah et al., 2005; Spiteri et al., 2005, Ghomian at al., 2008). Therefore our assumption of reversibility will lead to less CO₂ trapping than may be expected. The three-phase relative permeability is calculated based on staggered model (GEM, 2011).



(a)



(b)

Figure 6-3: Two sets of two-phase relative permeability used for sand (rock type 1) and shaly-sand (rock type 2) rock types (a) two phase oil-water relative permeability (b) two phase oil-gas relative permeability.

Two-phase capillary pressure for different rock types was modeled using Leverett J function (GEM, 2011) as:

$$P_c = \sigma \sqrt{\frac{\varphi}{k}} j \quad (6-3)$$

where φ is the porosity, k is the permeability, σ is the interfacial tension between water-oil and that of gas-liquid at reservoir temperature and j is the dimensionless Leverett J function:

$$j = S_l^{-n} + j_e - 1 \quad (6-4)$$

where S_l is the wetting phase saturation, j_e is the entry value of J function, and n is the pore size distribution index (Ghomian, 2008). Therefore, J function enables the calculations of capillary pressure within each grid block separately. Input data for different parameters is provided in Table 6-5.

Table 6-5: J-function input parameters

Rock Type	RT1	RT2
σ_{l-g} , dyne/cm	17	17
σ_{o-w} , dyne/cm	26	26
Je (gas phase)	6	6
Je (water phase)	12	12
n	1	1

6-3- Sensitivity Analysis and Simulation Models

Using the aforementioned reservoir and fluid models, compositional simulation runs were carried out to investigate the effect of different parameters on the performance of the WAG flood. To represent real world cases, each WAG injection scheme is preceded by two stages of primary and water injection scenarios. However, from an economic point of view, the switching time from primary to water-flood, and subsequently from water-flood to WAG, may have a considerable effect on the project viability. Also, after the conclusion of the WAG process, the resident CO₂ can still provide some opportunities for recovery improvement and therefore the production is switched back to water-flood.

As an example, Figure 6-4 demonstrates the effect of different schemes on the oil production rate and oil recovery factor for one of the runs (Run 67). As can be seen from Figure 5-4, the ultimate achievable recovery from primary production is around 20%. Switching to water-flood after 4 years of primary production can improve this recovery to 43%. If the water-flood is switched to WAG injection after 10 years, an incremental recovery of 13.5% can be obtained; all comparisons are based on the equal producing life of 80 years.

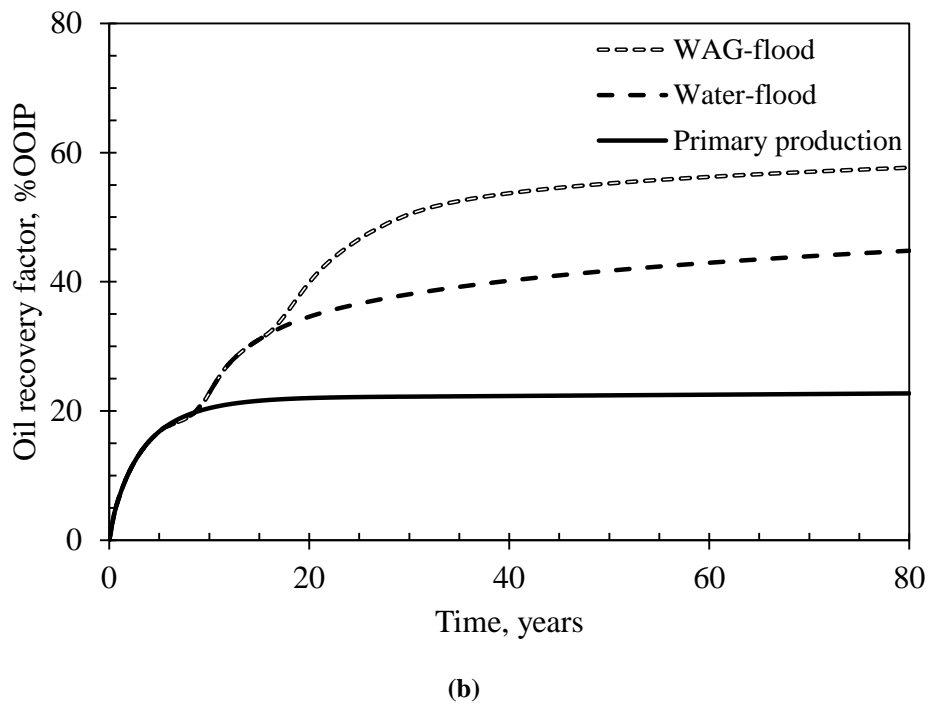
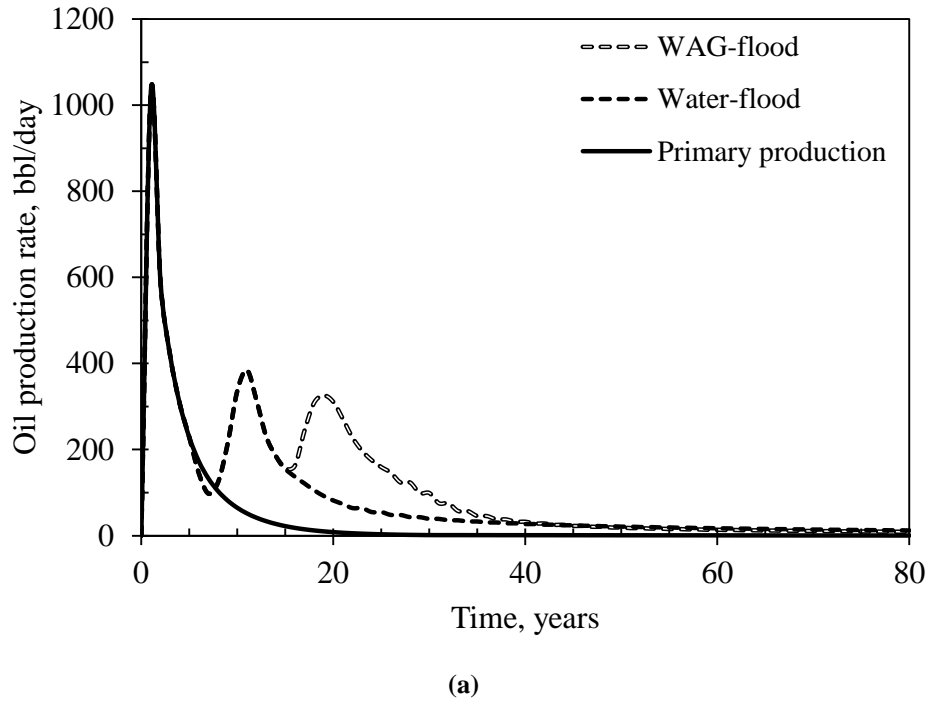
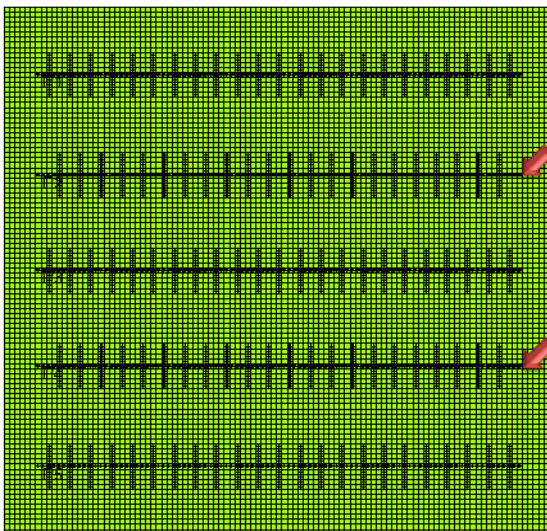


Figure 6-4: (a) Oil production rate and (b) oil recovery factors associated with three sequential recovery schemes; primary, water-flood and finally WAG process. Upon WAG completion, the final water-flood injection occurs.

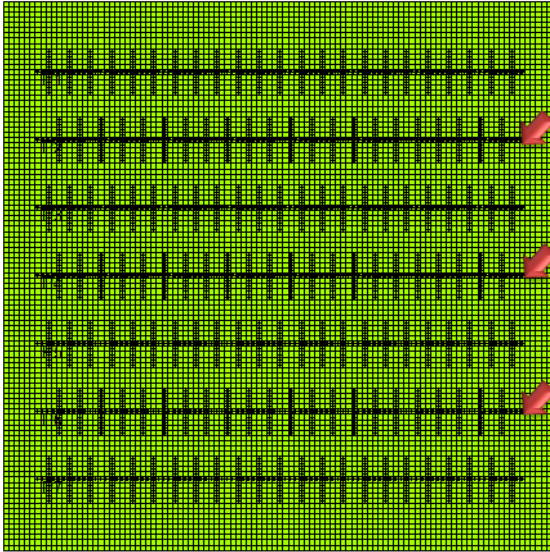
In order to perform a comprehensive study of the effect of different parameters on the WAG process performance, the objective functions (or desired responses) should be

specified. In this study, the design and operational conditions under which the maximum oil production in the form of oil recovery factor and also the maximum CO₂ storage occur are the two main objective functions. Therefore, it is necessary to recognize the most influential parameters that affect these two objective functions. Some of those critical factors which were reflected in this study are listed below.

Factor A (Well Pattern): The number of wells (producers and injectors) and also the well spacing are two deterministic factors for the recovery factor as well as the time length over which this recovery is achieved. In this study, we combine these two factors into one variable and call it “well pattern”. Two well patterns are considered and thereafter referred to as D1 and D2. D1 consists of 5 wells with a well spacing of 1000 ft, while D2 has 7 wells with a spacing of 650 ft. Injection schemes will be formed by converting two wells into injectors in D1 pattern and 3 wells in D2 pattern. Figure 6-5 shows the top view of the reservoir with the two patterns and the location of all injectors and producers.



(a)



(b)

Figure 6-5: The two well patterns used in the simulation models (a) D1 which is comprised of five wells (b) D2 which is comprised of seven wells. The red arrows in both figures show the injection wells.

Factor B (Well Completion): In a cemented well completion, the flow of fluids is restricted to the intersection point of the hydraulic fracture plane with the well trajectory. In open-hole completion, however, the whole length of the lateral is contributing to the fluid flow. These two completions may alter the timing of the recoveries from a reservoir and therefore should be considered.

Factor C (Fracture Spacing): Decreasing the fracture spacing, or equivalently increasing the number of fractures, will increase the well contact area with the reservoir and consequently improve the productivity/injectivity of the wells. Three fracture spacings of 200 ft, 300 ft and 400 ft were considered for this factor. The corresponding numbers of fractures are 23, 16, and 11 for the smallest to largest fracture spacing.

Factor D (Fracture Half-Length): In addition to well and fracture spacing, fracture half-length may have a profound effect in controlling the fluid flow direction and sweep efficiency. Long transverse fractures leave a short gap between the fractures tips and

hence shortens the breakthrough time of the injected fluid and undermines the sweep efficiency. However, longer fractures accelerate the production rate during the primary recovery stage. The values associated with this factor are 100 ft, 200 ft, and 300 ft.

Factor E (Average Reservoir Pressure While Switching to Water-Flood): The further away the average reservoir pressure is from the oil bubble point pressure ($\Delta P = P_b - P_{avg.}$), the more gas accumulates within the reservoir, and the more viscous the oil becomes. The resulted higher in-situ gas saturation leads to multi-phase flow of the liquid and gas phases, therefore, lowers the mobility of the oil phase. In the case of water-flood this will leave less accessible oil volume for encroaching water, and, due to increased viscosity of oil, the mobility ratio will be less favorable. Therefore, timing of the switch to water-flood scenario with respect to average reservoir pressure should be considered. ΔP of 20 psi, 320 psi and 620 psi were considered as minor, moderate and major levels of departure from bubble point pressure respectively in this regard. These values correspond to average reservoir pressure of 1600 psi, 1300 psi, and 1000 psi, respectively.

Factor F (WCUT While Switching to WAG): The transition from water-flood scheme to CO₂ injection scheme can occur at varying water cuts. Once water breakthrough occurs the average reservoir pressure starts to decline. A pressure drop below the minimum miscibility pressure of CO₂ and oil would be detrimental to the miscible process. Also, higher water-cut implies that more oil has been pushed to the producers and hence less has been left for CO₂ to recover. We will consider 0.5, 0.7, and 0.9 WCUT fractions as the starting point of CO₂/WAG injection.

Factor G (CO₂ Slug Size): Slug size, which refers to the cumulative volume of injected gas, is expressed as percentage/fraction of the initial hydrocarbon pore volume

(HCPVi). Generally, the more miscible gas injected, the higher the incremental oil recovery. Nevertheless, a larger injected volume will suppress the project economic return (Shing-Ming et al., 1984). The three levels associated with this factor in this study are 0.25, 0.50, and 0.75 of HCPVi.

Factor H (WAG Ratio): WAG ratio, which is the ratio of the volume of injected water to that of gas at reservoir conditions, is one of the most important parameters in the WAG process. However, the optimized value for this ratio is quite reservoir-dependent, because the overall performance of the WAG scheme depends strongly on the permeability distribution, gravity segregation, and flow behavior of different phases (Wu et al., 2004). A WAG ratio of 0, 1, and 2 were considered in the simulation models. Needless to say, WAG ratio of zero implies continuous CO₂ injection until the designated slug size volume is fulfilled.

Table 6-6 provides a summary of all factors considered and the levels associated with each of them. Cycle length or the time over which one cycle of gas plus water injection is completed is another factor that may influence the WAG project objectives (Jarrel et al., 2002; Wu et al., 2004). In this work, a constant cycle length of one year was used. This is equivalent to six months of CO₂ injection alternating with six months of water injection for WAG ratio of 1 and four months of CO₂ injection alternating with eight months of water injection for WAG ratio of 2.

Table 6-6: Different factors and the associated levels for sensitivity runs

Factor	L1	L2	L3
A: Well pattern	D1	D2	
B: Well completion	Cemented	Open-hole	
C: Fracture spacing, ft	200	300	400
D: Fracture half-length, ft	100	200	300
E: \bar{P} at WF switch, psi	1,000	1,300	1,600
F: WCUT at WAG switch, fraction	0.50	0.70	0.90
G: CO ₂ slug size, fraction	0.25	0.50	0.7
H: WAG ratio	0	1	2

Considering all the above parameters and the number of levels associated with each factor, a total of 2916 ($=2^2 \times 3^6$) is needed if the classical way of doing sensitivity analysis is pursued. Design of Experiment (DOE), as an alternative approach, can efficiently handle any situation which involves a response that varies as a function of one or more independent variables/factors (Mathews, 2005). With DOE, it is possible to identify any possible interaction between two or more variables and therefore it is superior to the traditional method of studying the effect of one variable at a time (OVAT). The main advantage of experimental design however is its capability of generating response surfaces (RS) which are able to predict the effect of variation of factors on objective functions in mathematical form. There are a variety of methods, like two and three level factorial design, and some optimal designs such as *A*, *D*, and *I* to perform a successful experimental design study (Montgomery, 2007).

Because the number of levels for different factors is not equal, we used an optimal method to design the matrix of required runs. This method is the “D-optimal” design, which is widely used in deterministic computer simulation models (Stat-Ease, 2010). With this method, only 105 runs are required to understand the effect of all considered parameters on WAG process. Therefore, this 96% reduction in the total number of runs

creates a vast computational time savings which is critical for demanding compositional simulation runs.

The collection of simulation runs are tabulated in Table 6-7. The assigned value to any parameter in each run, and the order in which these runs should be performed, is determined by DOE. Two factors, namely E and F which determine the switching time between different recovery schemes, may also have a significant effect on the total project life time and the response of the two objective functions.

Table 6-7: Sensitivity factors and the response values for some of the selected runs

Run	Factors								Responses			
	A	B	C	D	E	F	G	H	Oil Rec. Factor (%OOIP)	Inc. Oil Rec. Factor (%OOIP)	Stored CO ₂ Volume (bcf)	NPV (MM\$)
1	D1	Open-Hole	200	200	1300	0.9	0.5	1	53.47	10.1	2.51	29.2
2	D1	Open-Hole	400	100	1600	0.5	0.25	2	58.56	14.8	1.91	31.7
3	D1	Cemented	400	200	1300	0.7	0.5	1	58.21	14.7	1.93	19.4
4	D1	Open-Hole	200	100	1600	0.9	0.75	0	48.22	4.7	0.2	29.8
5	D1	Cemented	200	300	1300	0.5	0.25	2	49.8	8.2	1.25	22.2
6	D1	Cemented	300	300	1300	0.7	0.5	2	54	11.1	2.47	19.4
7	D1	Open-Hole	200	200	1000	0.5	0.25	2	51.75	8.9	1.58	29.9
8	D1	Cemented	200	100	1600	0.9	0.25	1	55.35	12.1	1.57	23
9	D2	Open-Hole	400	200	1600	0.5	0.25	2	53.53	12.22	1.65	32.9
10	D1	Cemented	400	200	1600	0.9	0.25	0	50.62	7.6	1.05	16.7
11	D2	Open-Hole	200	200	1000	0.7	0.25	0	42.83	2.08	0.49	25.9
12	D2	Open-Hole	400	300	1300	0.7	0.25	2	51.62	10.41	1.46	30.5
13	D2	Cemented	200	100	1000	0.9	0.5	0	43.11	3.16	0.38	19.9
14	D1	Open-Hole	300	100	1000	0.7	0.5	2	57.1	15.2	3.12	29.1
15	D2	Open-Hole	300	200	1600	0.9	0.25	1	50.72	9.53	1.4	26.8
16	D1	Open-Hole	300	300	1300	0.5	0.5	0	45.1	2.3	0.42	28.7
17	D1	Open-Hole	200	100	1300	0.7	0.25	2	56	12.5	1.72	33.2
18	D2	Cemented	400	300	1600	0.9	0.25	2	49.72	10.06	1.44	10.7
19	D1	Open-Hole	400	300	1300	0.5	0.5	1	57.62	13.6	1.91	31.1
20	D1	Open-Hole	400	300	1000	0.9	0.75	2	56.82	13.3	2.81	23.4
21	D1	Open-Hole	400	300	1600	0.5	0.75	0	44.5	2.8	0.52	27.6
22	D2	Open-Hole	300	100	1000	0.9	0.25	0	46.45	6.35	0.9	30.1
23	D1	Open-Hole	200	300	1000	0.7	0.75	1	47.72	7.8	2.2	27.1
24	D2	Open-Hole	200	100	1300	0.5	0.25	0	45.9	4.55	0.72	36

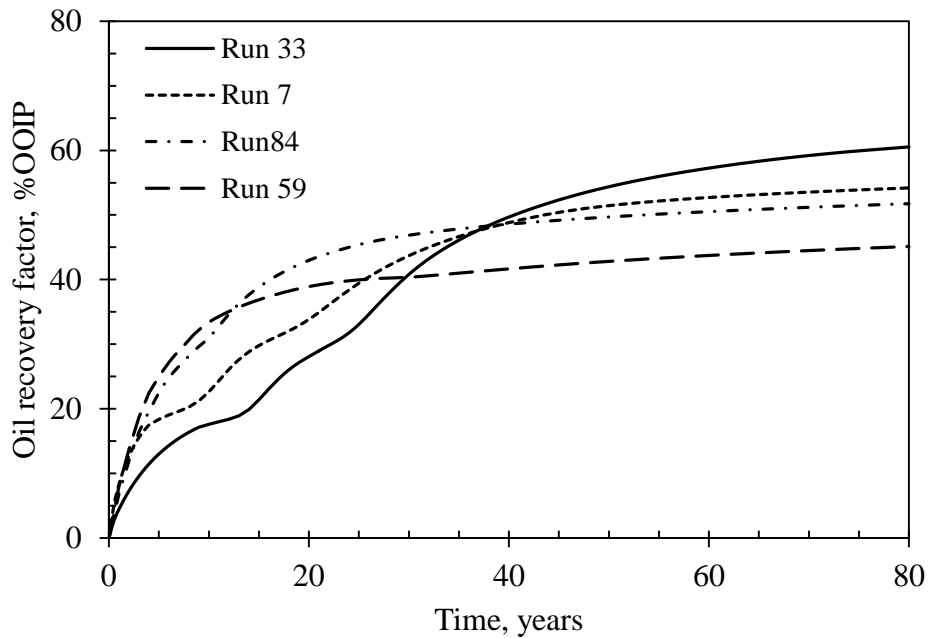
Run	Factors								Responses			
	A	B	C	D	E	F	G	H	Oil Rec. Factor (%OOIP)	Inc. Oil Rec. Factor (%OOIP)	Stored CO ₂ Volume (bcf)	NPV (MM\$)
25	D2	Cemented	300	300	1300	0.7	0.75	2	49.45	8.65	1.97	19.1
26	D2	Open-Hole	300	200	1300	0.5	0.5	2	52.82	11.06	2.31	36.4
27	D1	Open-Hole	300	100	1600	0.7	0.75	1	57.97	15	3.2	32.4
28	D2	Open-Hole	200	100	1600	0.5	0.5	1	53.95	11.54	1.7	38.1
29	D2	Cemented	300	200	1600	0.7	0.75	1	52.46	11.38	2.46	21.5
30	D1	Cemented	300	200	1300	0.9	0.5	0	48.09	4.16	0.56	21
31	D1	Open-Hole	400	300	1000	0.9	0.25	0	49.22	6.95	1.02	23.4
32	D1	Open-Hole	200	200	1000	0.9	0.5	2	52.8	11	2.45	27
33	D1	Cemented	400	100	1000	0.5	0.75	1	58.28	17.12	3.52	17.7
34	D1	Cemented	300	100	1000	0.9	0.75	2	57.64	14.98	3.03	20.1
35	D1	Open-Hole	300	100	1600	0.5	0.25	0	49.22	7.01	0.94	32.2
36	D2	Open-Hole	300	100	1600	0.9	0.5	2	54.44	13.15	2.67	29.6
37	D2	Cemented	400	200	1600	0.7	0.5	2	54.43	13.3	2.68	20.2
38	D2	Cemented	200	100	1300	0.5	0.5	2	52.77	11.27	2.39	28.8
39	D2	Open-Hole	300	200	1000	0.9	0.75	2	52.18	10.83	2.28	27.8
40	D2	Cemented	400	300	1600	0.5	0.5	1	50.5	11.63	1.59	22.6
41	D2	Open-Hole	200	300	1600	0.9	0.75	1	42.17	2.76	1.21	17.6
42	D2	Cemented	200	200	1600	0.9	0.5	1	47.98	7.23	2.08	14.4
43	D2	Open-Hole	300	200	1300	0.7	0.5	0	44.05	2.35	0.46	31
44	D2	Cemented	400	300	1000	0.9	0.75	1	49.86	11.29	2.35	12
45	D1	Open-Hole	300	200	1000	0.5	0.75	1	54.6	12.98	2.94	29.8
46	D1	Open-Hole	300	200	1600	0.5	0.5	1	56.92	13.52	1.9	32
47	D1	Cemented	300	300	1000	0.7	0.25	0	45.25	4.92	0.74	18.2
48	D2	Open-Hole	300	100	1300	0.7	0.75	1	55.29	13.24	2.86	38.1
49	D2	Cemented	400	100	1600	0.9	0.75	0	43.23	4.79	2.61	15.4

Run	Factors								Responses			
	A	B	C	D	E	F	G	H	Oil Rec. Factor (%OOIP)	Inc. Oil Rec. Factor (%OOIP)	Stored CO ₂ Volume (bcf)	NPV (MM\$)
50	D2	Cemented	300	200	1000	0.5	0.25	0	44.11	4.95	0.74	20.3
51	D1	Open-Hole	200	300	1300	0.7	0.5	0	41.65	2.24	0.24	27
52	D2	Cemented	200	100	1600	0.7	0.5	0	43.4	3.2	0.34	21.2
53	D2	Open-Hole	400	100	1000	0.7	0.75	0	39.94	4.04	2.17	28.4
54	D2	Cemented	200	100	1300	0.9	0.75	1	52.6	10.51	2.48	23.9
55	D1	Cemented	200	300	1600	0.7	0.75	2	50.35	8.55	2.08	18.8
56	D1	Cemented	200	100	1000	0.5	0.25	0	47.01	6.04	0.86	23.4
57	D1	Cemented	200	200	1000	0.7	0.25	2	51.55	10.78	1.59	21.8
58	D1	Cemented	400	100	1000	0.9	0.5	2	58.35	16.01	3.3	15.3
59	D2	Open-Hole	200	200	1600	0.5	0.75	0	39.9	0.38	0.17	27.6
60	D2	Cemented	200	100	1000	0.5	0.75	2	52.01	11.55	2.41	25.7
61	D2	Open-Hole	400	200	1300	0.9	0.75	0	42.25	3.51	2.16	27.1
62	D1	Open-Hole	200	200	1600	0.7	0.25	1	52.25	10.2	1.42	30.5
63	D2	Open-Hole	400	200	1000	0.9	0.5	2	55.35	13.65	2.81	26.6
64	D2	Open-Hole	200	300	1600	0.5	0.5	2	43.55	4.23	1.43	24
65	D1	Cemented	400	200	1300	0.5	0.25	0	49.85	7.62	1.03	20
66	D1	Open-Hole	300	100	1000	0.9	0.5	1	58.15	15.54	1.98	28.1
67	D2	Open-Hole	400	100	1000	0.7	0.25	1	53.45	13.63	1.61	31.4
68	D2	Open-Hole	400	300	1000	0.7	0.5	0	44.56	4.05	0.67	25.5
69	D2	Open-Hole	300	300	1600	0.5	0.25	1	47.12	7.25	1.02	30.8
70	D2	Cemented	300	300	1300	0.9	0.5	1	48.9	7.7	1.91	15
71	D2	Cemented	200	200	1300	0.5	0.5	1	47.69	7.86	2.2	27.3
72	D1	Cemented	300	300	1000	0.5	0.75	2	52.85	12.13	2.5	20
73	D2	Open-Hole	200	200	1300	0.9	0.25	2	49.4	8.3	1.33	28.4
74	D1	Open-Hole	400	300	1600	0.9	0.5	1	58.78	13.51	1.95	24.1

Run	Factors								Responses			
	A	B	C	D	E	F	G	H	Oil Rec. Factor (%OOIP)	Inc. Oil Rec. Factor (%OOIP)	Stored CO ₂ Volume (bcf)	NPV (MM\$)
75	D1	Cemented	300	100	1300	0.5	0.25	1	55.55	13.38	1.72	27
76	D2	Cemented	200	300	1600	0.5	0.25	0	40.02	0.46	0.31	8.6
77	D2	Cemented	300	300	1300	0.7	0.25	0	43.8	3.2	0.58	16.2
78	D1	Cemented	400	200	1000	0.9	0.25	1	54.1	12.75	1.65	14.9
79	D1	Open-Hole	400	200	1600	0.7	0.5	0	49.35	5.66	0.69	27.9
80	D2	Cemented	300	100	1600	0.7	0.25	2	54.25	12.86	1.7	24.1
81	D2	Cemented	400	200	1000	0.7	0.75	0	36.98	3.92	2.2	14.3
82	D1	Open-Hole	400	100	1300	0.7	0.5	0	49.7	5.76	0.66	29.4
83	D2	Cemented	300	100	1300	0.5	0.75	0	45.3	2.91	0.36	25.3
84	D2	Open-Hole	300	300	1600	0.7	0.25	1	46.82	6.93	1.07	26.4
85	D1	Cemented	400	300	1300	0.9	0.5	0	43.65	4.41	2.33	15
86	D2	Open-Hole	200	300	1000	0.5	0.75	0	38.62	1.42	0.17	22.7
87	D1	Open-Hole	200	200	1300	0.7	0.75	2	54.25	10.48	2.42	28.9
88	D1	Cemented	200	200	1000	0.9	0.75	0	45.1	3.48	0.22	19.5
89	D1	Cemented	300	300	1600	0.9	0.5	0	46.47	3.32	0.5	15.8
90	D2	Open-Hole	200	200	1000	0.7	0.5	1	46.85	7.9	2.16	31.1
91	D2	Cemented	400	100	1300	0.9	0.25	1	52.27	12.37	1.61	17.2
92	D2	Open-Hole	200	100	1000	0.7	0.25	2	51.6	11.32	1.53	34.6
93	D1	Open-Hole	300	300	1300	0.9	0.75	0	46.43	3.03	0.28	26.3
94	D2	Cemented	300	300	1000	0.9	0.5	2	48.8	8.61	1.94	14.4
95	D2	Open-Hole	200	300	1000	0.9	0.25	1	42.32	3.36	0.81	22.2
96	D2	Cemented	400	200	1300	0.9	0.75	2	53.35	12.42	2.62	15.1
97	D1	Open-Hole	300	200	1000	0.9	0.25	2	54.15	12.01	1.78	26.9
98	D1	Cemented	200	300	1000	0.5	0.5	1	49.44	8.81	1.43	21
99	D1	Open-Hole	200	100	1300	0.5	0.75	2	56.42	13.14	2.89	34.5

Run	Factors								Responses			
	A	B	C	D	E	F	G	H	Oil Rec. Factor (%OOIP)	Inc. Oil Rec. Factor (%OOIP)	Stored CO ₂ Volume (bcf)	NPV (MM\$)
100	D2	Cemented	300	100	1000	0.7	0.5	1	55.85	14.73	1.88	25.1
101	D2	Cemented	200	300	1300	0.7	0.25	1	42.58	3.45	0.7	15.6
102	D1	Open-Hole	400	100	1300	0.9	0.75	1	60.62	16.01	3.59	28.2
103	D1	Cemented	400	300	1300	0.7	0.75	1	55.6	12.94	2.86	17.9
104	D1	Cemented	300	200	1600	0.5	0.5	2	56.25	13.49	2.76	23.6
105	D2	Cemented	400	100	1000	0.5	0.5	0	38.42	4.42	2.66	16

To clarify, Figure 6-6-a and Figure 6-6-b display recovery factor and CO₂ storage associated with four different runs. The switching time from primary to water-flood is 5 years for Run 33 and 5 months for Run 59. 15 years later, the water-flood is converted into WAG flood for Run 33 and 4 years later for Run59. Run 33 starts with the lowest recovery factor and but achieves the highest value among four presented cases. Run 59, on the other hand, starts with a high recovery factor but levels off relatively quickly. From the CO₂ storage point of view, Figure 6-6-b suggests that the amount of stored CO₂ volume is affected by the project's termination time. Hence, it is critical to include the factor of time as another criterion to account for its effect on the previously projected objective functions. An appropriate method to apply the effect of time is through net present value (NPV) determination for each run as the third objective function. Some of the key economic factors for NPV calculation are presented in Table 6-8.



(a)

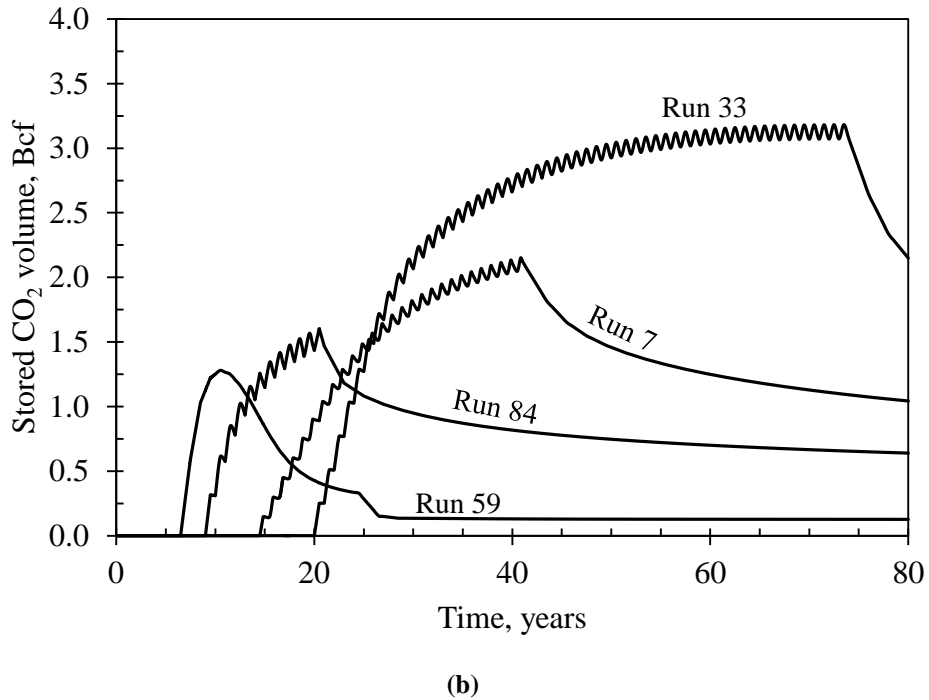


Figure 6-6: Comparison of (a) the recovery factor and (b) the stored CO₂ volumes of different runs over time.

Table 6-8: Input parameters for NPV calculations

Parameter	Value
Oil price, \$/bbl	80
Royalty*, %	variable
CO ₂ price, \$/Mscf	1.0
CO ₂ recycle cost, \$/Mscf	0.52
Oil lifting cost, \$/oil bbl	15
Operating cost of producers, \$/Well/year	24,000
Operating cost of Injectors, \$/Well/year	30,000
Operating cost cut-off, \$/boe	60

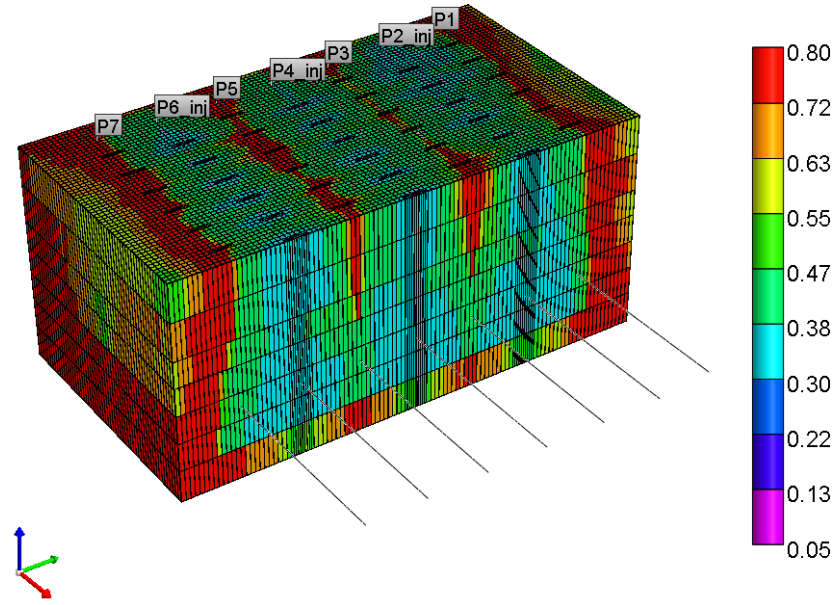
*Royalty calculation follows the Alberta regulations and includes royalty holidays, e.g. oil royalty is generally a function of oil volume and oil price.

Each simulation scenario continues until the operating cost cut-off (see Table 6-8) is met, which corresponds to approximately 12 STB of oil per day at field level. Therefore, different projects have different termination times, which affects all three objective functions. Moreover, since the main objective of this study is the WAG performance evaluation, it is worth comparing the incremental recovery associated with WAG

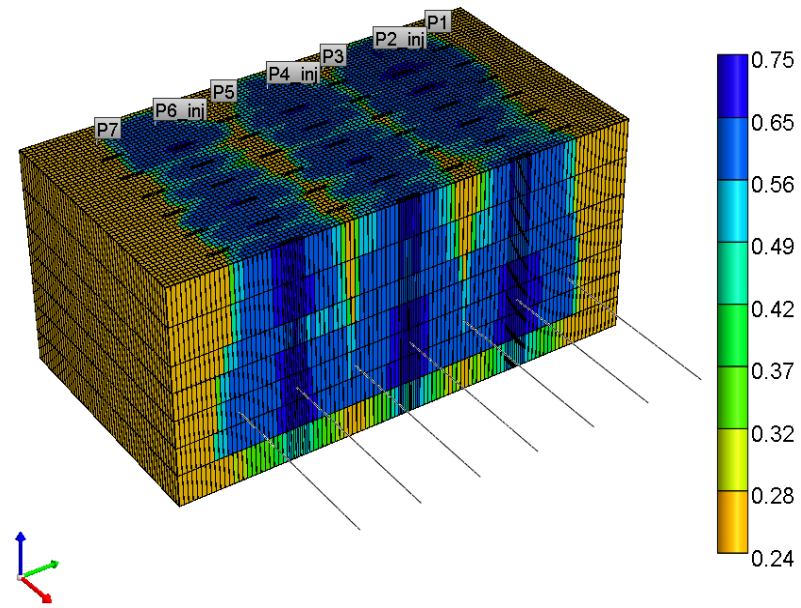
injection with the continued water-flood at the point of termination. The second column in the responses section of Table 6-7 is allocated to these values.

Visualization of the fluid movement and phase distribution provides better insight into the WAG process in tighter reservoirs exploited by multi-fractured horizontal wells. Figure 6-7-a, for example, shows a cross-section view (cut in the middle plane in the x direction) of the oil saturation at the end of water-flood and hence the beginning of the WAG flood for Run 67. Non-uniform distribution of the oil signifies the importance of the permeability heterogeneity in governing the fluid flow in the direction of higher permeability. Figure 6-7-b displays the water saturation distribution at that time. The conical shape of the vertical distribution of water along the injectors illustrates the gravity effect during water injection. Figure 6-7-c shows the oil saturation at the end of the WAG cycle and Figure 6-7-d shows the oil saturation profile at the end of the post-WAG water-flood. The effect of reservoir heterogeneity is greater on a WAG depletion scheme than for straight water-flood. Also, the sweep is mostly confined to the space between the fractures. Considerable change in the oil saturation of the upper portion of the reservoir (Figure 6-7-d) shows the benefit of CO₂ flooding in improving the recovery factors for the post-WAG water-flood scenario. Figure 6-7-e and Figure 6-7-f indicate the spread of the free CO₂ phase at the end of the WAG and the final water-flood schemes, respectively. The distribution at the top layer of Figure 6-7-e suggests that the CO₂ breakthrough pathways between the fractures are well established. Figure 6-7-f illustrates upward movement of CO₂ after WAG termination (note the CO₂ plume expansion at the top layer), however the overall saturation of free CO₂ decreases as the water pushes some of the CO₂ to the producers which gradually reduces the storage volume during the final

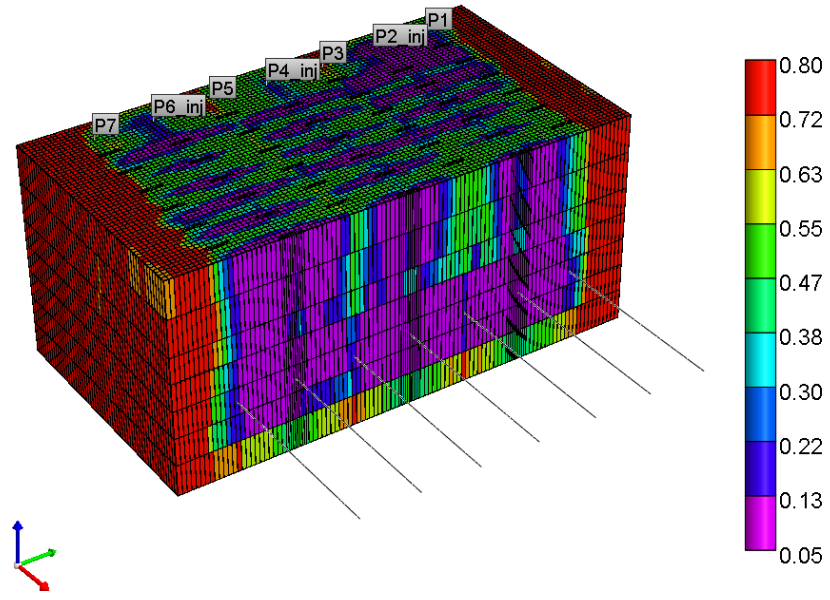
water-flood stage.



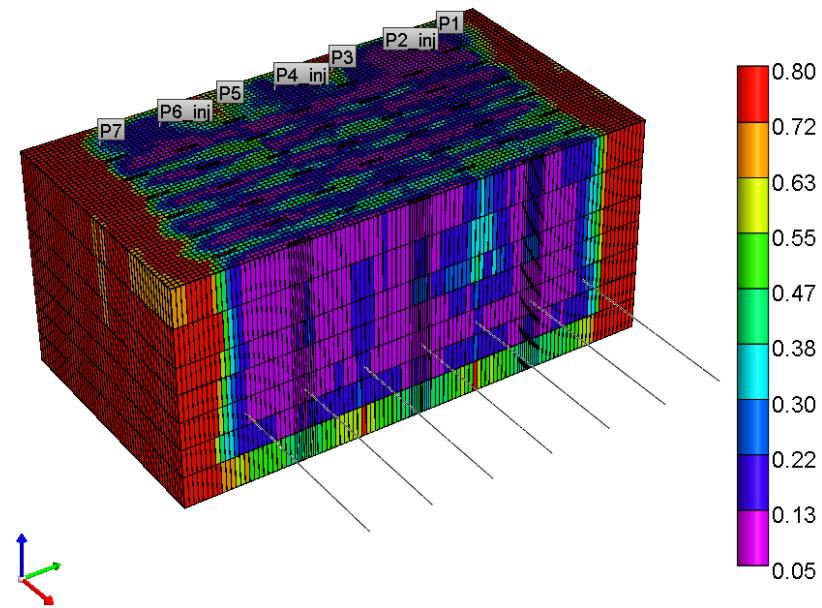
(a)



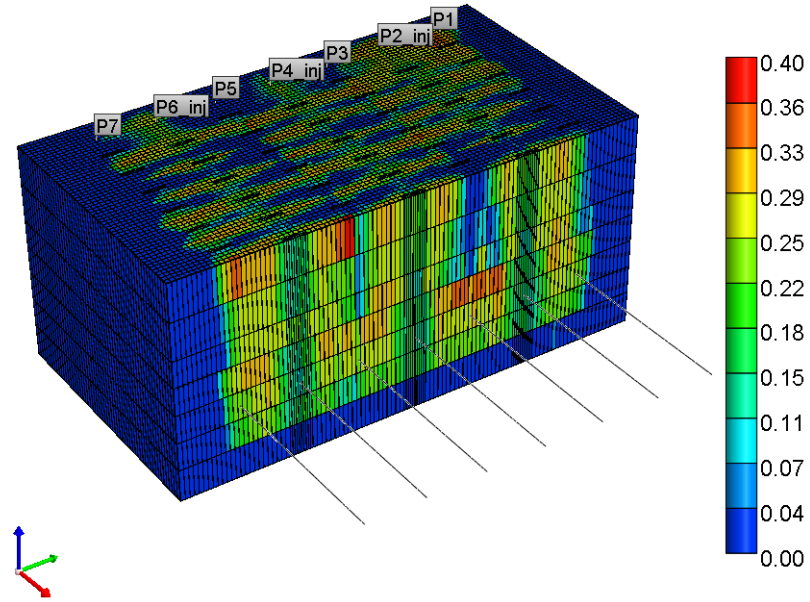
(b)



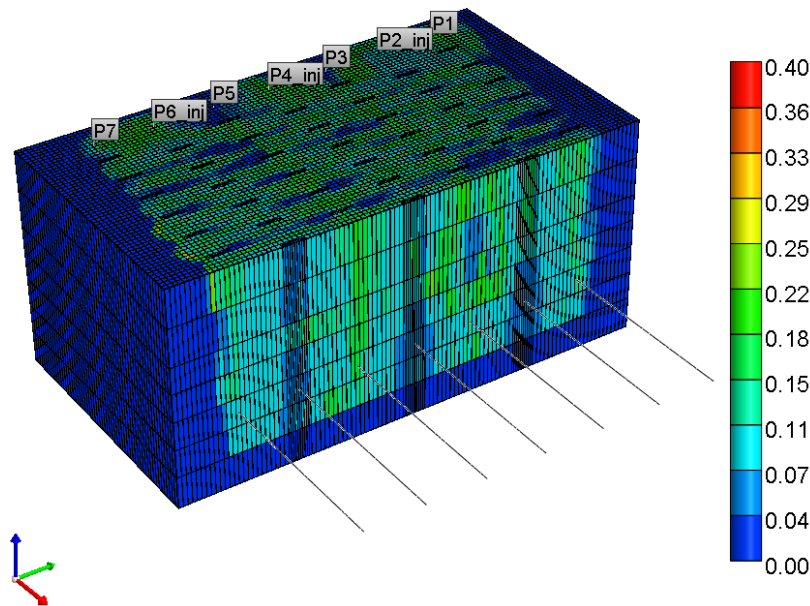
(c)



(d)



(e)



(f)

Figure 6-7: Cross-section view of spatial distribution of different phases in Run 67 (a) oil saturation and (b) water saturation distribution at the end of the water-flood scenario and the beginning of the WAG scheme; (c) oil saturation at the end of the WAG process (d) oil saturation at the conclusion of the project (e) CO₂ saturation at the end of the WAG process (f) CO₂ saturation at the conclusion of the project.

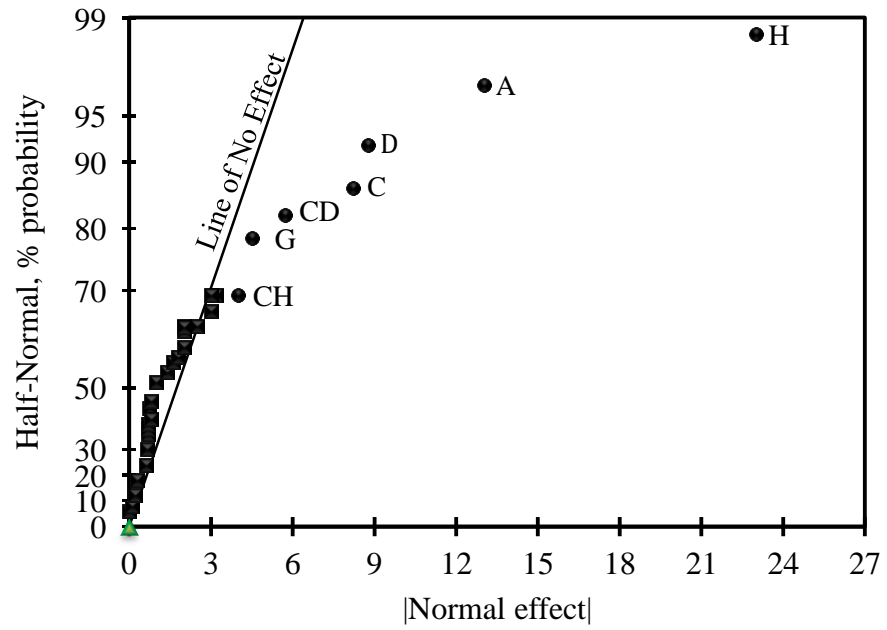
6-4- Simulation Results and Discussion

Upon the completion of all sensitivity runs performed using DOE (Table 6-7), the final

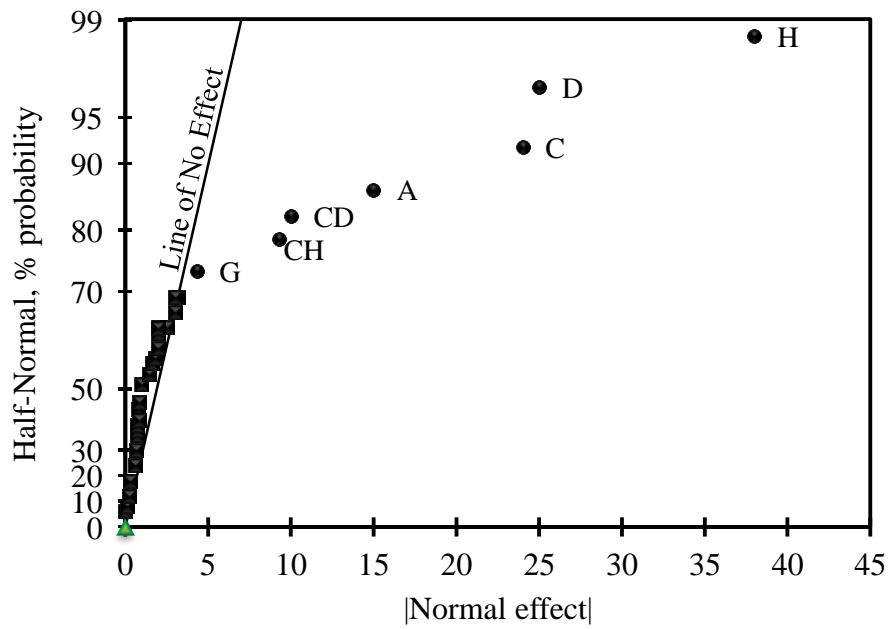
results for the objective functions values should be statistically evaluated. Preliminary review of the results indicates that the range of variation in oil recovery factor is between 36.9% and 60.6%, and for incremental oil recovery, 0.4% and 17.1% of OOIP. The amount of CO₂ storage fluctuates between 0.17 bcf and 3.59 bcf (note that each bcf of CO₂ at standard conditions is equivalent to 52 kilotonnes of CO₂). Finally, the maximum and minimum NPV are 8.6 and 38.1 MM\$, respectively. However, it should be emphasized that these values are solely associated with the runs listed in Table 6-7 and there might be other combination of factors that provide different maximal/minimal values.

A more sophisticated statistical analysis of the results allows us to find the most important parameters that affect each of the responses, and also to rank them in the order of importance. The results of such an analysis are depicted in Figure 6-8 in the form of “half-normal probability” plot, which is used to determine whether the entire set of factors and interaction effects are by coincidence (and thus, shows very little effect) or whether some factors and/or interactions have significant effect. This is a plot of the absolute value of the effect estimates against their normal cumulative probabilities. Any factors or interactions whose observed effects are due to chance are expected to be randomly distributed around zero. These effects will tend to fall along a straight line called “line of no effect”. The straight line on this plot always passes through the origin and should also pass close to the fiftieth percentile data value. The effects that might be significant have average values different from zero and are located at a substantial distance away from the straight line that represents no effect (Montgomery, 2007). In other words, the effect on the x axis specifies the changes in the response when a factor

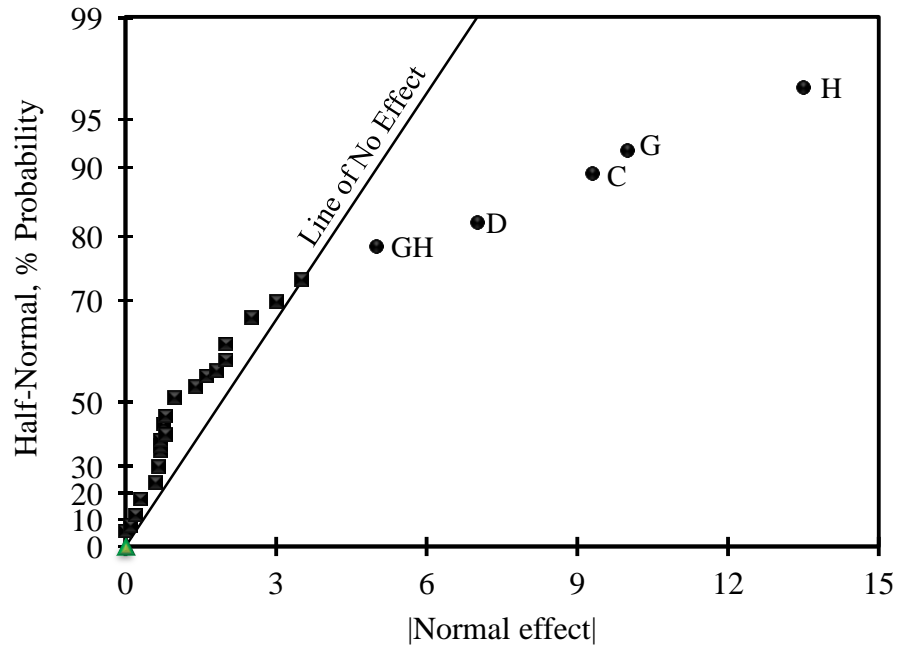
varies between its bounds of uncertainty.



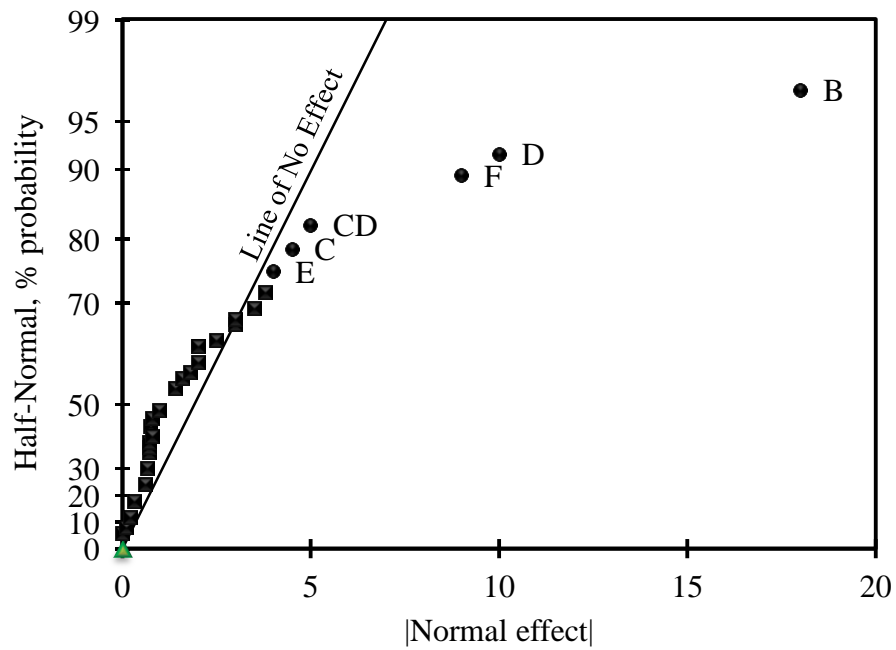
(a)



(b)



(c)



(d)

Figure 6-8: Half-normal probability plots showing the effect of parameters, and their ranking, on (a) oil recovery factor (b) incremental oil recovery factor (c) stored CO₂ volumes and (d) net present value (NPV) of the projects.

According to Figure 6-8-a, based on the parameters and the reservoir conditions in

this study, the greatest to least dominant factors for oil recovery factors are WAG ratio, well pattern, fracture half-length, fracture spacing, and finally CO₂ slug size. As Figure 6-8-b suggests, these same factors will impact the incremental oil recovery factor but in a different order. For storage purposes however (Figure 6-8-c), WAG ratio, CO₂ slug size, fracture spacing and fracture half-length will be the ordered impactful factors. The NPV of the projects is mostly driven by well completion method, and thereafter fracture spacing, WCUT while switching to WAG process, fracture half-length and finally average reservoir pressure while switching to water-flood. Therefore, for all three responses aimed at this study, the parameters associated with fracture design (fracture spacing and fracture half-length) play a role in changing the results considerably and therefore require special attention.

During the continuous CO₂ injection, or when the WAG ratio is equal to zero, the injected CO₂ will rather quickly override due to gravity segregation. On the other hand, low viscosity of the CO₂ will lead to very unfavorable mobility ratios which causes the gas to rapidly approach the producers' fractures. Both of these factors will bring about poor sweep efficiencies in the case of continuous injection. Moreover, in this case, once CO₂ breakthrough occurs, the average reservoir pressure quickly drops below MMP and therefore the process loses the advantages of a miscible flood (Ghaderi et al., 2012). Therefore, in comparison with higher WAG ratios, the lesser values of recovery and incremental recovery factor listed for continuous injection scenarios in Table 6-7 are understandable. From the storage perspective, the same reasons will undermine the stored CO₂ volumes. Therefore, a proper WAG ratio should be selected to fulfill the purposes of each objective (incremental recovery and storage).

Both decreasing the fracture spacing and increasing the fractures half-length improve the contact area of the well in the tight reservoir and hence the well's deliverability. Nevertheless, such an improvement is jeopardized by poorer sweep efficiency for miscible gas injection schemes. Basically, any design which decreases the distances between the fractures' tips along the producers and injectors (path of least resistance) will accelerate the gas breakthrough and impair the sweep efficiency and storage capacity. Again, quick breakthrough will be detrimental to the carbon dioxide storage potential of the projects.

Thus, the design elements that govern recovery factors, in one way or another, control the CO₂ storage potential of the projects. Intuitively, by increasing the total volume of injected CO₂, the likelihood of trapping larger quantities of CO₂ in the reservoir increases. Trapped CO₂ replaces the volume occupied by oil and therefore increases the recovery factors. In this regard, CO₂ slug size is an important factor for both objective functions.

Considering the half normal probability plot of all NPV results (Figure 6-8-d), it is revealed that well completion is the most influential factor in this situation. For economic evaluation, we have assumed that the completion cost of the cemented well is 1.5 times for that of open-hole completion (per well). All other costs being equal, using the cemented liner configuration will increase the initial required investment by 50%, which is a significant increase. As the NPV involves the time value of money, it is interesting to note that those factors which control the scheme switching times, namely *E* and *F*, emerged as effective parameters. It should be declared that any switch is initiated with a related capital investment. Once more, the fracture design parameters which can

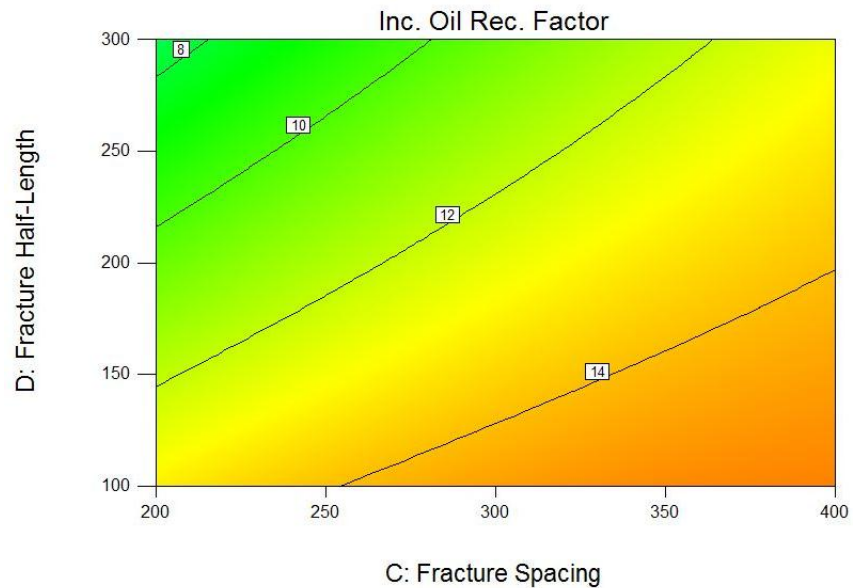
stimulate the production rates and also influence the capital costs (more and longer fractures demand higher initial capital cost), play a central role in NPV calculation.

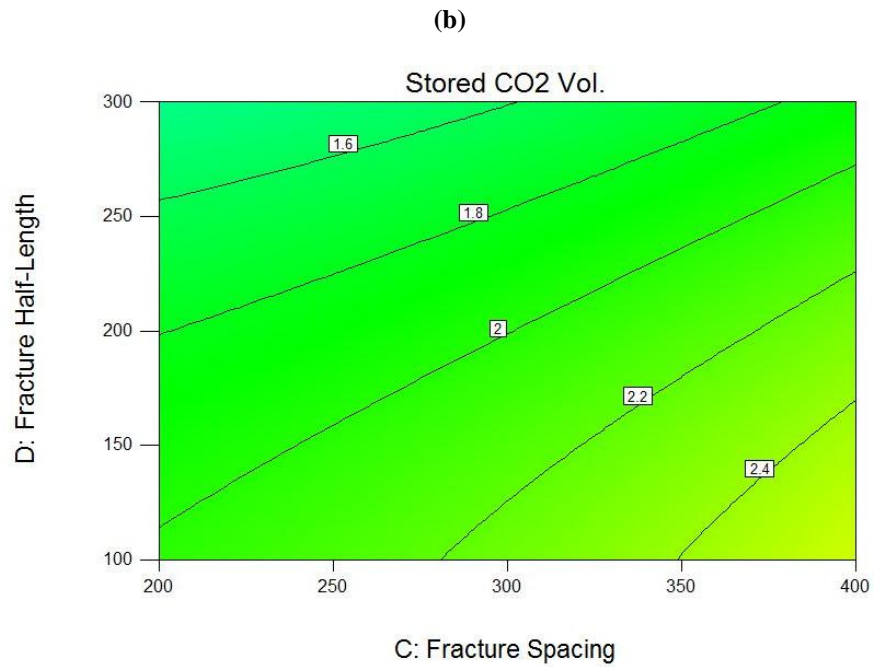
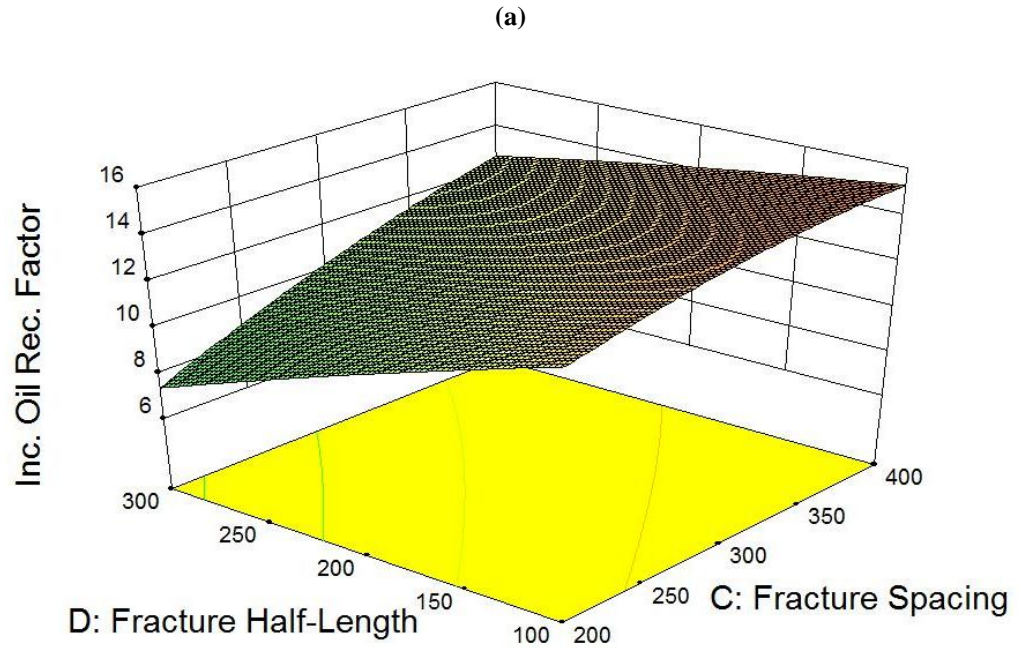
After identification of the sensitive parameters and ranking them with respect to their importance, the contour maps and response surfaces for each objective function can be generated. An important feature of the response surfaces is that they can provide an accurate estimate of the objective functions for the values other than those which have been used in their construction. These extra values are usually a continuous interval between the upper and lower bounds of the constituent factors.

Figure 6-9-a and Figure 6-9-b demonstrate the contour map and response surface for oil recovery factor with respect to factors *C* and *D*, respectively. Both figures indicate that the recovery factor is almost a linear function of fracture spacing and fracture half-length and increases as the number of fractures and their size decrease. The contour map and response surface for stored CO₂ volume can be seen in Figure 6-9-c and Figure 6-9-d and show very similar trends as oil recovery factors i.e. a smaller number of fractures, which are shorter in half-length, promote CO₂ storage potential. All other factors are fixed and are identical for the two generated responses (i.e., A=D1; B=Open-hole; E=1600 psi; F=0.5; G=0.5; H=1). The variation in NPV with respect to categorical factors, namely *A* and *B*, at two levels of *C* are shown in Figure 6-9-e (C=200 ft) and Figure 6-9-f (C=300 ft). Other relevant parameters are D=200 ft; E=1300 psi; F=0.5; G=0.5; H=1. According to these figures, the change in NPV imposed by the well pattern is minor in comparison with well completion strategy.

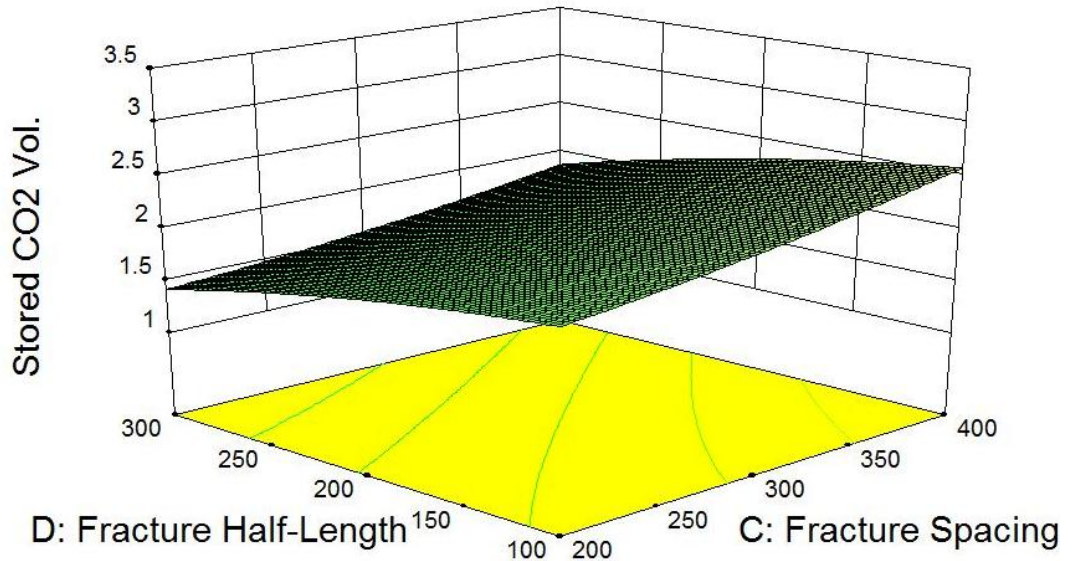
Mathematical form of the response surfaces can be used to find the value of each factor such that the optimum value for each of the objective functions can be obtained

individually or in combination with each other. By introducing weighting factors into combined objective functions, the preferential direction of the project can be dictated. Table 6-9 presents the values for any of the eight considered factors by which the maximum possible recovery, storage and the NPV can be obtained. The effect of optimization of one response (on the lost) on other responses has been provided as well. This is an excellent feature of experimental design and response surface analysis which allows the values of the objective functions to be evaluated with marginal error without any need to run the models at those specific values. According to these results, the highest achievable values for recovery, storage volume and NPV are 63.3%, 4.2 Bcf, and 40.3 MM\$, respectively. The optimal conditions for a combined response like *R4* are presented in the last column of Table 6-9. NPV gains the highest weighting factor for *R4* and therefore the process is mainly driven by economics and less by recovery and storage. The results for any other combined response with different weighting factors can be obtained in a similar manner.

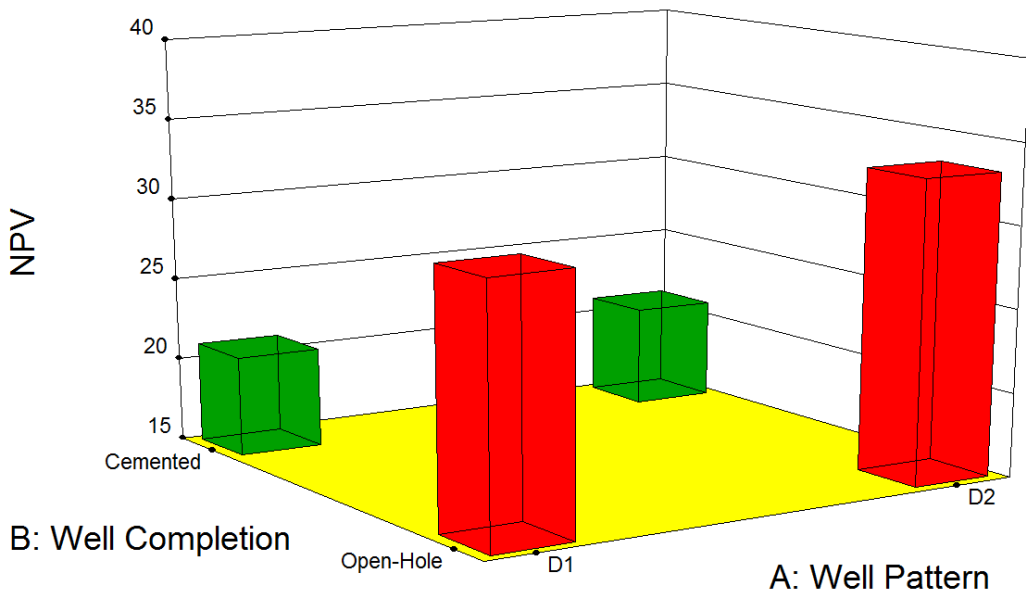




(c)



(d)



(e)

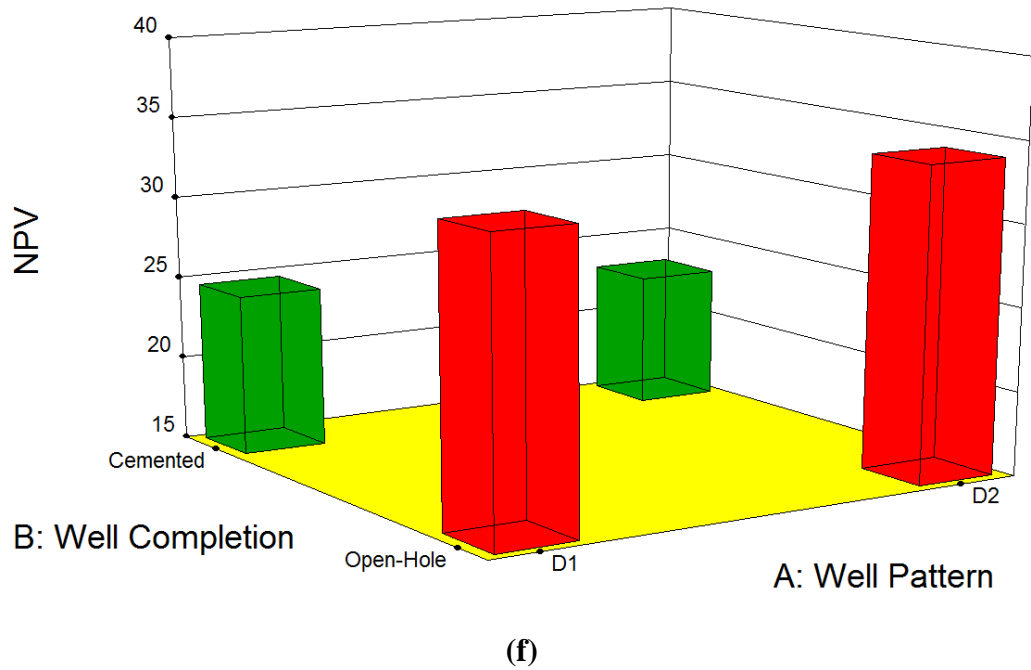


Figure 6-9: (a, b) contour plot and surface response for the incremental oil recovery (c, d) contour plot and surface response for stored CO₂ volume with respect to fracture half-length and fracture spacing. The other related parameters are A=D1; B=Open-hole; E=1600 psi; F=0.5; G=0.5; H=1.0. (e, f) Variation of NPV with respect to “well pattern” and “well completion” where C=200 ft (e) and C=300 ft(f); D=200 ft; E=1300 psi; F=0.5; G=0.5; H=1.0.

Table 6-9: The optimal values of factors for different responses

Response ►		R1: Maximizing oil recovery factor (%OOIP)	R2: Maximizing stored CO ₂ volume (Bcf)	R3: Maximizing NPV (MM\$)	R4: Combined response*
Factor ▼					
A: Well pattern		D1	D1	D2	D2
B: Well completion		Open-Hole	Cemented	Open-hole	Open-hole
C: Fractures' spacing, ft		400	400	290	352
D: Fractures' half-length, ft		100	110	100	100
E: Pavg while switching to WF, psi		1,530	1,590	1,360	1,425
F: WCUT while switching to WAG		0.9	0.9	0.5	0.5
G: CO ₂ slug size		0.75	0.75	0.45	0.75
H: WAG ratio		1.87	1.93	1.38	1.77
Response with optimal values	Oil recovery factor (%OOIP)	63.3	60.8	55.3	56.1
	Stored CO ₂ volume (Bcf)	3.9	4.2	2.5	3.3
	NPV(MM\$)	25.5	16.2	40.3	38.9
* $R4 = 0.25 \times R1 + 0.25 \times R2 + 0.5 \times R3$					

6-5- Summary

In this chapter, one section of the Pembina Cardium field was selected and compositional simulations were performed to evaluate and quantify the effect of different design parameters and operational constraints on the performance of the CO₂-EOR process. Eight factors were considered as important, including well parameters (well spacing and completion method), hydraulic fracture specification (fracture spacing and fracture half-length), time of switch between recovery schemes (between primary and water flood and later between water flood and WAG), and WAG parameters (CO₂ slug size and WAG ratio). By applying “D-optimal” method, the matrix of runs for the sensitivity study was built and a total of 105 compositional runs were performed.

Statistical analysis of the results was carried out to find the most effective parameters for the oil recovery factor (objective 1) and the CO₂ storage (objective 2). Based on the results, WAG and fracture parameters have a profound effect on both objective functions

with the WAG ratio being the dominant factor. It was also revealed that increasing the number of fractures and expanding the fracture half-length will unfavorably reduce the sweep efficiency of WAG injection and accelerates the short-circuiting of the injected gas at producers. This in turn reduces the oil recovery factor, incremental oil recovery factor, and CO₂ storage. This indirectly implies that applying longitudinal fractures might be a better option for gas injection into tight formation with close well spacing. Nevertheless, the reservoir heterogeneity still plays an important role in dictating the preferential path of fluids flow.

Due to differences in switching time between alternative recovery schemes, the effect of time was taken into account by determination of NPV (objective 3) for each scenario. It was shown that the important parameters affecting NPV are completion method (which affects the capital cost) and fracture parameters, and switching time, with completion method being the dominant factor. Cemented well completion with the assumed economic model is not the recommended method.

Response surfaces were generated to quantify the effect of different uncertain parameters on the objective functions. Thereafter, an optimization process was pursued to search for those combinations of factors which lead to maximum response. Based on the reservoir properties considered in this study the maximum achievable recovery, storage and NPV are 63.3% of OOIP, 4.2 Bcf CO₂, and 40.3 MM\$ respectively. The response surfaces allow any combination of objective functions (by applying weighting factors) to be optimized for the desired purposes.

Results from this study show that the CO₂-EOR potential in tight oil formation can be considerable if the design parameters and operating conditions are chosen properly. In

this regard, the parametric compositional models are very efficient proxies, and design of experiment method is powerful tools in identifying and optimizing these factors.

Acknowledgment

This research was made possible by funding provided by ISEEE-NRCan (project title “Co-optimization of CO₂ Storage and Oil Recovery in Tight Oil Formations”). The authors appreciate the constructive comments and helps provided by Ian Bryden from Penn West Exploration. Chris Clarkson would like to acknowledge Encana and AITF for support of his Chair position in Unconventional Gas and Light Oil Research at the University of Calgary, Department of Geoscience. He would also like to acknowledge the sponsors of Tight Oil Consortium (TOC), hosted at the University of Calgary.

References

- Clarkson, C.R., Pedersen, P.K., 2011. Production Analysis of Western Canadian Unconventional Light Oil Plays. Paper CSUG/SPE 149005 presented at the Canadian Unconventional Resources Conference held in Calgary, Alberta, Canada, 15-17 November.
- Computer Modeling Group, 2011. CMG-GEM (version 2011) Reference Manual.
- Danesh, A., 1998. PVT and Phase Behaviour of Petroleum Reservoir Fluids, Elsevier.
- Ghaderi, S.M., Clarkson, C.R., Chen, S., Kaviani, D., 2012. Evaluation of Recovery Performance of Miscible Displacement and WAG Processes in Tight Oil Formations, Paper SPE 152084, presented at SPE/EAGE European Unconventional Resources Conference and Exhibition, Vienna, Austria, 20-22

March.

- Ghomian, Y., Pope, G.A., Sepehrnoori, K., 2008. Hysteresis and Field-Scale Optimization of WAG Injection for Coupled CO₂-EOR and Sequestration, Paper SPE 110639 presented at SPE Symposium on Improved Oil Recovery, Tulsa, Oklahoma, USA, 20-23 April.
- Ghomian, Y., 2008. Reservoir Simulation Studies for Coupled CO₂ Sequestration and Enhanced Oil Recovery. Ph.D. dissertation, The University of Texas at Austin.
- Green, W.D., Willhite, G.P., 1998. Enhanced Oil Recovery. SPE, Richardson, Texas.
- Han, W.S., McPherson, B.J., Lichtner, P.C., Wang, F.P., 2010. Evaluation of Trapping Mechanisms in Geologic CO₂ Sequestration: Case Study of SACROC Northern Platform, a 35-Year Injection Site, American Journal of Science, vol. 310, 382-324.
- Harvey, A.H., 1996. Semiempirical Correlation for Henry's Constants over Large Temperature Ranges, AIChE J, vol. 42, 1491-1494.
- Hovorka, S.D., Tinker, S.W., 2010. EOR as Sequestration - Geoscience Perspective, paper presented at the Symposium on the Role of Enhanced Oil Recovery in Accelerating the Deployment of Carbon Capture and Storage, Cambridge, MA, USA, July 23. GCCC Digital Publication Series #10-12.
- Khan, S.A., Pope, G.A., Sepehrnoori, K., 1992. Fluid Characterization of Three-Phase CO₂/Oil Mixtures, Paper SPE/DOE 24130 presented at the 8th Symposium Oil Recovery, Tulsa, OK, USA, 22-24 April.

- Kovscek, A.R., 2002. Screening Criteria for CO₂ Storage in Oil Reservoirs, *Petroleum Science and Technology*, vol. 20, 841-866.
- Kovscek, A.R., Cakici, M.D., 2005. Geologic Storage of Carbon Dioxide and Enhanced Oil Recovery II: Co-optimization of Storage and Recovery, *Energy Conversion and Management*, vol. 46, 1941-1956.
- Jarrel, P.M., Fox, C.E., Stein, M.H., Webb, S.L., 2002. Practical Aspects of CO₂ Flooding, Monograph Series, SPE, Richardson, Texas.
- Lake, L.W., 1989. Enhanced Oil Recovery. Englewood Cliffs, NJ, Prentice-Hall.
- Li, Y.K., Nghiem, L.X., 1986. Phase Equilibria of Oil, Gas and Water/Brine Mixtures from a Cubic Equation of State and Henry's Law, *Can. J. Chem. Eng.*, vol. 64, 486-496.
- Mathews, P., 2005. Design of Experiments with MINITAB. Milwaukee, Wisconsin: ASQ Quality Press.
- Montgomery, D.C., 2007. Design and Analysis of Experiments. Seventh Edition, John Wiley & Sons Inc.
- Ozah, R., Lakshminarasimhan, S., Pope, G.A., Sepehrnoori, K., Bryant, S.L., 2005. Numerical Simulation of the Storage of Pure CO₂ and CO₂-H₂S Gas Mixtures in Deep Saline Aquifers, Paper SPE 97255 presented at SPE Annual Technical Conference and Exhibition, Dallas, TX, USA, 9-12 October.
- Pedersen, K.S., Fredenslund, A., 1987. An Improved Corresponding States Model for Prediction of Oil and Gas Viscosities and Thermal Conductivities. *Chem. Eng. Sci.*, vol. 42, 182-186
- Peng, D.Y., Robinson, D.B., 1976. A New Two-Constant Equation of State, *Ind.*

& Eng. Chem. Fund. vol.15, 59-64.

- Shaoul, J.R., Behr, A., Mtchedlishvili, G., 2007. Developing a Tool for 3D Reservoir Simulation of Hydraulically Fractured Wells. SPE Res Eval & Eng vol. 10, 50-59. SPE-108321-PA. DOI: 10.2118/108321-PA.
- Shing-Ming, C., Allard, D.R., Anli, J., 1984. Factors Affecting Solvent Slug Size Hydrocarbon Miscible Flooding Requirements in Hydrocarbon Miscible Flooding, Paper SPE 12636 presented at the 4th Symposium on Enhanced Oil Recovery, Tulsa, OK, USA, 15-18 April.
- Smyth, R.C., 2008. SACROC EOR and Sequestration Demonstration, DE-FC26-05NT42591: in Southwest Regional Partnership on Carbon Sequestration (SWP) Annual Meeting, Albuquerque, New Mexico, USA, October 23. GCCC Digital Publication #08-08.
- Spiteri, E.J., Juanes, R., Blunt, M.J., Orr, F.M., 2005. Relative Permeability hysteresis: Trapping Models and Application to Geological CO₂ Sequestration, Paper SPE 96448 presented at SPE Annual Technical Conference and Exhibition, Dallas, Texas, USA, 9-12 October.
- Stat-Ease, Inc. 2010. Design-Expert (version 8.0.6) Reference Manual.
- Viau, C., Nielsen, K., 2010. Unconventional Oil Production in the Cardium Formation, East Pembina Area, Alberta, Canada. Presented at the CSPG core conference held in Calgary, Alberta, Canada, 16-17 September.
- Wu, X., Ogbe, D.O., Zhu, T., Khataniar, S., 2004. Critical Design Factors and Evaluation of Recovery Performance of Miscible Displacement and WAG Process, Paper SPE 2004-192 presented at Canadian International Petroleum

Conference, Calgary, Alberta, Canada, 8-10 June.

- <http://www.energy.alberta.ca/Tenure/pdfs/FISREG.pdf>

Chapter 7

Investigation of Economic Uncertainties of CO₂ EOR and Sequestration in Tight Oil Formations¹

Advancement in drilling and production technologies, such as horizontal drilling with multi-stage fracturing, has enabled commercial production from more challenging reservoirs, namely, tight oil formations. However, high capital costs and relatively low recovery narrow the profit margin from such reservoirs. CO₂ EOR has provided not only an excellent opportunity to improve oil recovery, but also a chance to sequester CO₂ to reduce environmental footprint. Nevertheless, profitability of CO₂ EOR processes relies heavily on market conditions.

While CO₂ EOR recovery and CO₂ storage can be quantified through compositional simulation, thorough economic analyses need to be conducted to evaluate the viability of a CO₂ EOR project. The complexity of this study can be reduced significantly through experimental design. Randomized economic uncertainties, such as commodity prices, royalty scheme and incentives, CO₂ storage credits, capital and operating cost structure,

¹This chapter is a modified version of: Ghaderi, S.M., Clarkson, C.R., Taheri, S., and Chen, S., 2013. Investigation of Economic Uncertainties of CO₂ EOR and Sequestration in Tight Oil Formations, Paper SPE 165301, presented at 2013 SPE Enhanced Oil Recovery Conference, Kuala Lumpur, Malaysia, July 02 - 04.

CO₂ price, etc. can also be investigated with Monte Carlo simulation. This coupled approach allows us to stochastically search for the influential factors and quantify their financial impacts on CO₂ EOR projects. This methodology is extremely valuable in the assessment of risks in business, especially when uncertainties are high or the problem is rather complex, such as CO₂ EOR/storage in tight oil reservoirs.

The remaining oil in tight oil formations, after primary and water flood, is still significant. Hence, CO₂ EOR has attracted attention from industrial partners and government regulatory bodies. This paper provides a rigorous workflow for the industry to evaluate such projects, as well as a perspective for the governing bodies on how to transform their policies and incentives when market conditions change.

7-1- Introduction

Consumption of fossil fuels has continuously increased the level of carbon dioxide and other heat-trapping “green-house” pollutants in the atmosphere. Presumably as a result, the climate temperature has gradually increased and most likely will continue to increase over this century. Simulation of climate change indicates that the planet’s temperature could be between 2 to 9.7 °F higher than its current value in 2100 (Herring 2012). The exact value of temperature increase will depend heavily on the energy choices and courses of action we make now and in subsequent decades.

Several options have been suggested to reduce the CO₂ concentration in the atmosphere. Improving the efficiency of energy utilization systems, replacing fossil energy with low CO₂ emitting systems like renewable energy, and capturing/storing CO₂ from fossil fuel combustion are some of these methods to name a few. The extent to which each of these techniques is used will depend on other factors, including the

designated target for emission-reduction, costs, availability of alternative energy resources, environmental influence and public acceptance (Davison 2001). Among the aforementioned methods, underground storage/geological storage of CO₂ is currently the most promising short to medium-term option for reducing the net carbon emissions to the atmosphere (Bachu and Shaw 2003).

The annual rate of CO₂ emissions in Alberta, as a major North American energy supplier, reached 236 Mt (millions of tonnes) in 2010, which was the highest in Canada (Environment Canada 2012). While this level of emissions should be reduced, the sustainability of economic growth should be assured as well (Bachu and Shaw 2003). For Alberta, being a landlocked province with significant subsurface petroleum resources, underground storage of CO₂ is the best, and probably only, option available for mitigating large emissions rates (Bachu 2003).

Deep saline aquifers, unmineable coal seams and (depleted) oil and gas reservoirs are usually considered as the most applicable CO₂ storage formations (Bachu 2003). Although saline aquifers offer the largest potential for long-term storage, the regulatory framework of their application is not clear and the economic/commercial feasibility of aquifer storage is under question (McCoy and Rubin 2009). As for unmineable coal seams, while there has been significant development of coalbed methane (CBM) in Alberta in the past 10 years, primarily in the Horseshoe Canyon coals (Bastin et al 2005), they are not optimal storage targets because, in the case of the Horseshoe Canyon, there are multiple thin coal seams at a relatively shallow depth. Conversely, CO₂ storage through enhanced oil and gas recovery (EOR and EGR) can be quite attractive (Bachu 2003; Gaspar et al. 2005; Ghomian 2008; Singhal 2009; McCoy and Rubin 2009;

Jahangiri and Zhang 2011). Over decades of practice, industry has gained enough experience around CO₂ injection operation. When becoming miscible with the in-situ fluids, CO₂ can considerably reduce the declining production rates from some wells. Because of integrity of the sealing cap-rock in hydrocarbon reservoirs, secure storage of injected CO₂ can be achieved. Most importantly, the selling revenue from incremental production can partially (if not completely) offset the operating costs of the project. An additional benefit is that the infrastructure built today for CO₂-EOR can be utilized for future development of storage in saline aquifers (McCoy and Rubin 2009).

Based on the performance of Joffre Viking and Weyburn projects, there is a good awareness of potential reserve additions by CO₂ flooding, which can be applied to other sedimentary basins within Alberta. Nonetheless, the main barrier to widespread usage of CO₂-EOR in Alberta is the lack of supply and transportation infrastructure (Singhal 2009). Accordingly, these factors will influence the economic viability of CO₂ projects significantly. Therefore, in the absence of carbon credits, these projects would likely not be cost effective and attractive.

In this study, the economics of miscible CO₂-EOR/storage in the tighter portion of Pembina Cardium is investigated. With recent elevated activity in the exploitation of tight reservoirs and with high decline rates, the industry should be aware of the need for deploying secondary and tertiary recovery schemes. With current high oil prices, which may continue for the foreseeable future, CO₂-EOR may become attractive and feasible. High uncertainty around the flood performance within these tight formations necessitates an understanding of the risk associated with CO₂ injection/storage. The amount of incentive required for commercial development of such reservoirs should be explored as

well.

This chapter is organized as follows: First, the effect of uncertainty of reservoir heterogeneity on the performance of water-flood and CO₂ flood is investigated. Second, the key elements in economic assessment of CO₂ flood and the proposed economic model used in this paper is discussed. Third, the results of economic sensitivity and uncertainty are presented.

7-2- Effect of Reservoir Properties on the Flood Performance

Prior to reviewing the economics of EOR methods in tight oil formation, acquiring an understanding of the effect of different parameters on the performance of flooding schemes is crucial. In our previous study (Ghaderi et al. 2012, see Chapter 6), the effect of some of the development design parameters, such as well spacing, fractures spacing, and etc. on the performance of CO₂ miscible flood was investigated. It was also discussed how these parameters interact with each other and how they should be selected to achieve a specific goal like maximizing CO₂ storage. However, the method was applied to a reservoir with specific (and fixed) properties. It should be noted that, fluid and reservoir properties may change across a field and these variations (heterogeneity) should be taken into account during any flood performance evaluation. For example, Kerr (1980) discusses the noticeable changes in geology and fluid quality occurring in the Pembina Cardium field.

Therefore, in a follow-up to our previous study, the effect of reservoir heterogeneity on the performance of different recovery schemes in tight oil formations is investigated. Since permeability is likely the most important component of flow capacity of a reservoir, the focus of the current study is on permeability heterogeneity. In order to

introduce permeability heterogeneity in the simulation models, reservoir geo-models were built based on three different parameters which can describe the heterogeneity quantitatively. The first parameter is Dykstra-Parsons coefficient, which contributes to the permeability variation. The second and third parameters are the dimensionless correlation lengths in both horizontal and vertical directions, which define the pattern by which permeability field is distributed. In the following, a brief description of these parameters is provided.

Dykstra-Parson Coefficient - V_{dp} : Dykstra-Parsons coefficient is the most common measure of permeability variation in reservoir engineering (Jensen 2000). It is a dimensionless number that relates the changes in the permeability of the reservoir to the standard deviation of its mean. Mathematically, V_{dp} is defined as:

$$V_{dp} = \frac{k_{50\%} - k_{16\%}}{k_{50\%}} \quad (7-1)$$

where $k_{50\%}$ is the median of permeability and $k_{16\%}$ is the permeability one standard deviation below the median value on a log-probability plot. V_{dp} of zero means a perfectly homogenous medium with its permeability equal to $k_{50\%}$. For a hypothetical infinitely heterogeneous reservoir, V_{dp} approaches one. Sometimes the Dykstra-Parsons coefficient is referred to as the permeability variation or permeability variance (Arnold and Stewart 1998).

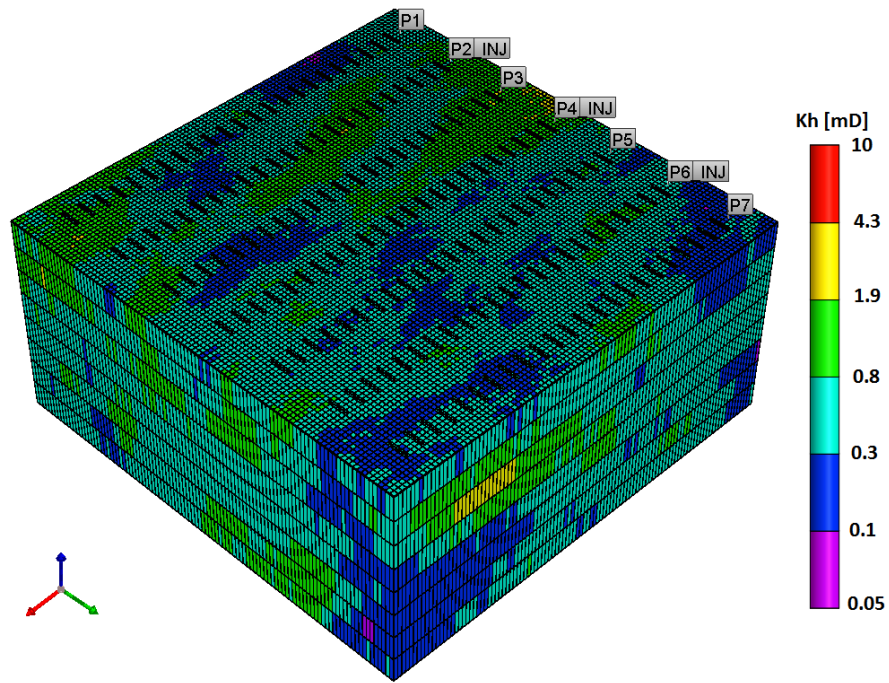
Dimensionless correlation length in horizontal direction - λ_{Dx} : correlation length for a spatial property like permeability is defined as the maximum length over which autocorrelation exists between the values of that parameter at different locations. In other words, the values of parameters over this length and in a specific direction (here horizontal) cannot change independently. In geostatistics, the semivariogram is the

common tool to delineate the auto-correlation structure (Garmeh and Johns 2009).

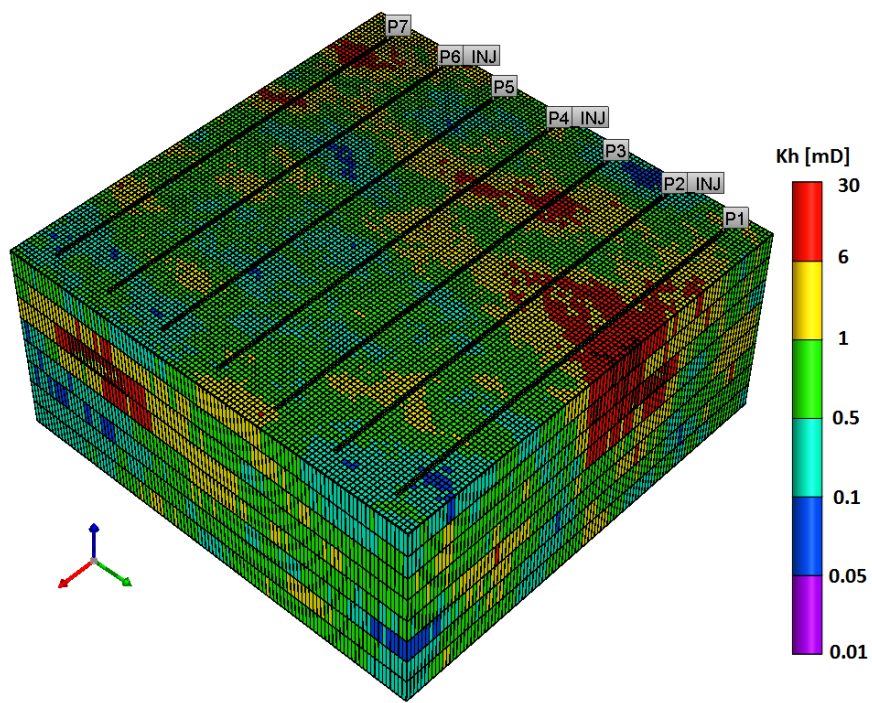
Dimensionless correlation length in vertical direction- λ_{Dz} : has the same definition as its horizontal counterpart but applied in the vertical direction.

Experimental design is used to conduct a sensitivity analysis based on six different parameters (one based on fracture design parameters and the rest based on reservoir permeability characteristics). It should be noted that the direction of propagating hydraulic fractures, longitudinal versus transverse, depends on the direction of maximum horizontal stress in the field. For example, a horizontal well designed for longitudinal fracture configuration should be drilled along the maximum horizontal stress (Economides et al. 2002). In this study, the wells can accept both fracture configurations without any limitation. For rational comparison of the two fracture design systems, however, the total length of the fractures along the wells for two systems are considered to be equal. 23 transverse fractures with a half-length of 100 ft each are equivalent to a single longitudinal fracture extending from toe to heel of the well lateral with a total length of 4600 ft.

Because the reservoir models are intended to be generic, SGeMS software (Remy et al. 2009) was used to generate the required geo-models with anticipated heterogeneity characteristics. As Geostatistics relies heavily on random functions to model uncertainty (Olea 2009), to reduce the effect of random errors for each set of parameters, two distinct realizations sharing the same properties are generated; the replicated realizations are denoted as R1 and R2, respectively. The median permeability of all geo-models is equal to 0.53 mD. Figure 7-1 displays prototypes of two geo-models with different properties.



(a)



(b)

Figure 7-1: Prototype of the model with reservoir properties for (a) “Run 1” in (b) “Run 2” in Table 7-3.

Table 7-1 provides a summary of the factors and the two levels assigned for each factor. Design of experiment and fractional factorial design is used to identify the

required runs. Based on this design, 16 simulation runs are needed to explore the effect of each individual parameter, as well as their combinations, on responses or objectives.

Table 7-1: Factors and levels for studying the effect of reservoir heterogeneity

Factor	Level1	Level2
A: Fracture design†	L	T
B: λ_{DX}	0.2	1.0
C: λ_{DZ}	0.25	0.5
D: Vdp	0.35	0.7
E: Heterogeneity direction††	0	90
F: k_v/k_h ratio	0.1	0.5

†L stands for longitudinal and T stands for transverse fracture

†† Preferential heterogeneity direction with respect to Y axis

In contrast, a conventional sensitivity study will require 64 (2^6) runs. Similar to our previous study, three consecutive recovery schemes are considered, namely one year of primary recovery followed by a water flood scenario, which ends when the water-cut reached 90%, and finally a CO₂-WAG scheme with a designated cumulative slug size of 50% HCPV. Table 7-2 summarizes the common properties of the simulation models. Fluid and SCAL data can be found from the other paper (Ghaderi et al. 2012, see chapter 6).

Table 7-2: Common inputs of simulation models

Property	Value
Length, ft	5,250
Width, ft	5,250
Thickness, ft	24.1
Depth at the top of formation, ft	6,120
Initial reservoir pressure, psi	2,520
Initial water saturation, %	36
Initial oil saturation, %	64
Fracture pressure gradient, psi/ft	0.9
WAG ratio	1.0
Length of well laterals, ft	4,600
Well spacing, ft	750
Rock compressibility at P^0 , psi^{-1}	5.0E-6
Number of grids ($N_x \times N_y \times N_z$)	105 \times 105 \times 7
Average grid size ($D_x \times D_y \times D_z$), ft	50 \times 50 \times 3

Table 7-3 contains the results of primary and water-flood scenarios for the 16 cases. The closeness of the responses between two realizations of each scenario suggests that the two models are similar to each other. At the bottom of the table, the range of variation in each response is shown. Table 7-4 tabulates similar results for CO₂-WAG process with recovery factor and CO₂ storage as the main responses.

Table 7-3: Sensitivity factors and different response values for 16 simulation runs for primary and water-flood scenarios

Run	Fracture Design	λ_{DX}	λ_{DZ}	V_{dp}	Het. Dir.	Kv/Kh Ratio	HCPV (MMBbl)		PR-RF† (%)		DU-WF†† (Year)		WF-RF††† (%)	
							R1	R2	R1	R2	R1	R2	R1	R2
1	T	0.20	0.25	0.35	90	0.1	7.35	7.35	4.6	4.6	11	11	22.6	22.4
2	L	0.20	0.25	0.70	0	0.5	7.44	7.44	6.1	6.3	9	8	19.9	19.1
3	L	1.00	0.25	0.70	90	0.1	7.44	7.44	6.6	6.4	8	8	18.9	18.3
4	T	0.20	0.50	0.35	0	0.5	7.35	7.35	4.9	5.0	11	11	22.1	22.0
5	T	1.00	0.50	0.35	90	0.1	7.35	7.35	4.6	4.6	11	11	22.3	22.2
6	L	0.20	0.50	0.35	90	0.5	7.44	7.44	4.6	4.6	11	12	24.0	24.5
7	T	0.20	0.25	0.70	90	0.5	7.35	7.35	6.4	6.5	8	8	17.7	17.4
8	L	1.00	0.50	0.35	0	0.1	7.44	7.45	4.6	4.6	12	11	24.5	24.1
9	T	0.20	0.50	0.70	0	0.1	7.35	7.35	5.8	6.0	8	8	17.7	17.3
10	L	1.00	0.25	0.35	90	0.5	7.44	7.44	4.7	4.6	11	11	24.0	23.8
11	L	0.20	0.25	0.35	0	0.1	7.44	7.44	4.6	4.6	12	11	24.5	24.1
12	L	0.20	0.50	0.70	90	0.1	7.44	7.44	5.7	5.8	10	10	20.6	20.5
13	T	1.00	0.50	0.70	90	0.5	7.35	7.35	6.8	6.6	8	9	17.0	18.0
14	T	1.00	0.25	0.35	0	0.5	7.35	7.35	5.2	5.1	10	10	21.2	21.4
15	L	1.00	0.50	0.70	0	0.5	7.44	7.44	6.3	6.2	9	9	19.5	20.2
16	T	1.00	0.25	0.70	0	0.1	7.35	7.35	7.0	6.7	7	7	15.6	15.9
Results Summary ►						Max	7.44	7.45	7.0	6.7	12	12	24.5	24.5
						Min	7.35	7.35	4.6	4.6	7	7	15.6	15.9

† Primary Recovery – Recovery factor

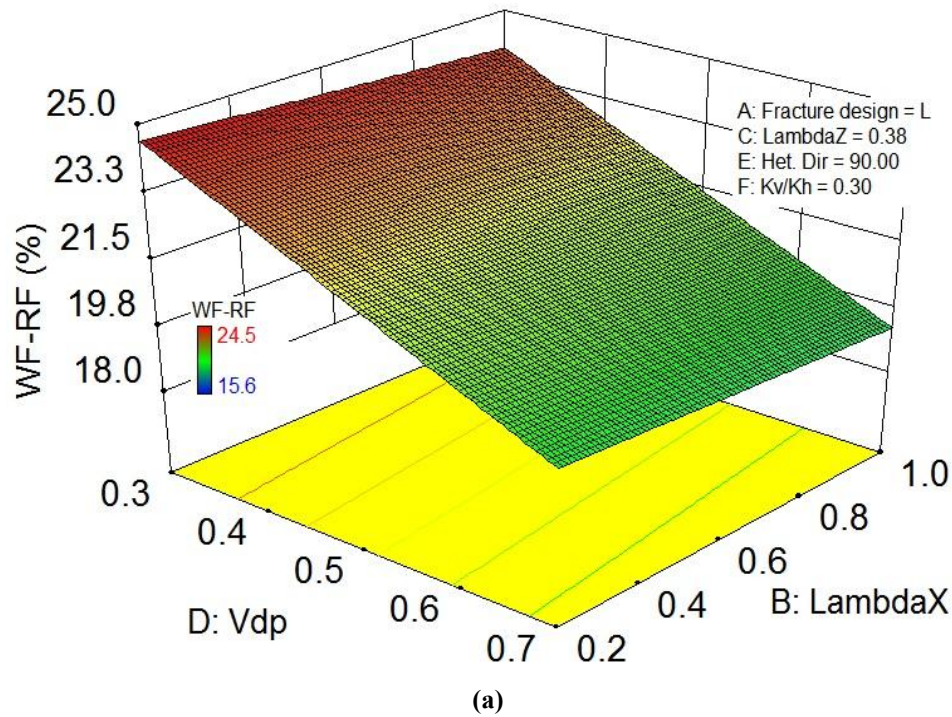
†† Duration of water flood until water cut reaches 90%

††† Water flood – Recovery factor

Table 7-4: Sensitivity factors and different response values for 16 simulation runs for CO₂-WAG scenarios

Run	Fracture Design	λ_{DX}	λ_{DZ}	Vdp	Het. Dir.	Kv/Kh Ratio	DU – WAG† (Years)		WAG-RF†† (%)		Stored CO ₂ (%HCPVI)		Total RF (%)	
							R1	R2	R1	R2	R1	R2	R1	R2
1	T	0.20	0.25	0.35	90	0.1	16	16	20.3	20.4	47.6	46.6	47.5	47.4
2	L	0.20	0.25	0.70	0	0.5	12	11	17.0	17.6	38.5	40.3	42.9	43.1
3	L	1.00	0.25	0.70	90	0.1	11	11	18.6	18.1	41.8	39.7	44.1	42.8
4	T	0.20	0.50	0.35	0	0.5	15	16	19.1	19.6	45.8	43.8	46.1	46.5
5	T	1.00	0.50	0.35	90	0.1	16	17	20.6	20.2	46.0	45.5	47.5	46.9
6	L	0.20	0.50	0.35	90	0.5	18	18	20.1	20.5	43.6	44.6	48.7	49.6
7	T	0.20	0.25	0.70	90	0.5	11	11	16.8	18.2	39.3	37.1	40.9	42.1
8	L	1.00	0.50	0.35	0	0.1	17	18	22.3	22.0	47.4	47.4	51.5	50.7
9	T	0.20	0.50	0.70	0	0.1	10	10	15.5	15.9	30.8	38.0	39.0	39.2
10	L	1.00	0.25	0.35	90	0.5	18	18	20.1	20.9	43.0	43.6	48.8	49.4
11	L	0.20	0.25	0.35	0	0.1	18	18	21.3	21.7	45.2	44.9	50.3	50.5
12	L	0.20	0.50	0.70	90	0.1	13	13	17.7	17.3	37.1	40.8	44.0	43.5
13	T	1.00	0.50	0.70	90	0.5	10	12	18.5	17.4	39.8	37.0	42.2	41.9
14	T	1.00	0.25	0.35	0	0.5	16	16	19.5	20.0	43.0	44.0	46.0	46.6
15	L	1.00	0.50	0.70	0	0.5	11	12	17.9	16.8	38.8	36.1	43.7	43.2
16	T	1.00	0.25	0.70	0	0.1	9	9	16.8	16.2	39.6	38.4	39.4	38.9
Results Summary ►						Max	18	18	22.3	22.0	47.6	47.4	51.5	50.7
						Min	9	9	15.5	15.9	30.8	36.1	39.0	38.9
† Duration of WAG process														
†† WAG process – Recovery factor														

Model outputs in Table 7-3 and Table 7-4 are utilized to create response surfaces covering the whole range of discrete factors as a continuous spectrum, Figure 7-2. Figure 6-2-a and Figure 6-2-b show the response surfaces of water-flood recovery factor and ultimate volume of stored CO₂ as a function of selected factors. The outputs of simulation are refined further to identify the important factors for each results of interest in a ranked order. Figure 7-3-a through Figure 7-3-d show the *Pareto* chart for duration of water-flood, recovery factor of water-flood, recovery factor of WAG scenario, and amount of stored CO₂ at the end of WAG scheme. For these four different objectives, Dykstra-Parson coefficient and fracture direction design are the most important factors, ranking first and second, respectively. In addition, both of these factors have a negative effect on the defined objective. This means that, moving from “level1” to “level2” for these factors (see Table 7-1) will decrease the value of the objective functions (see Figure 7-2).



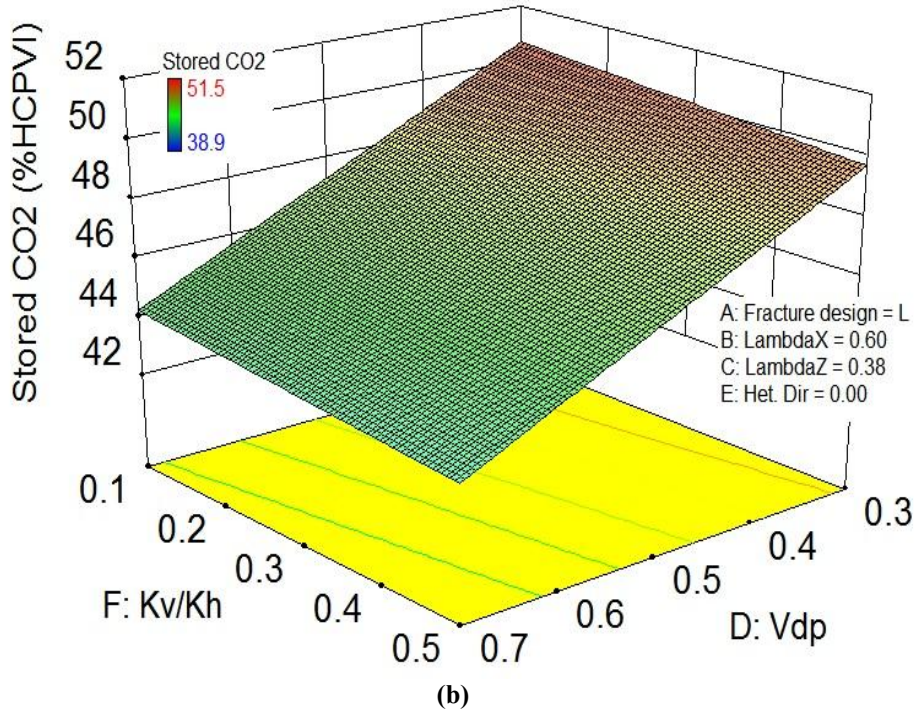
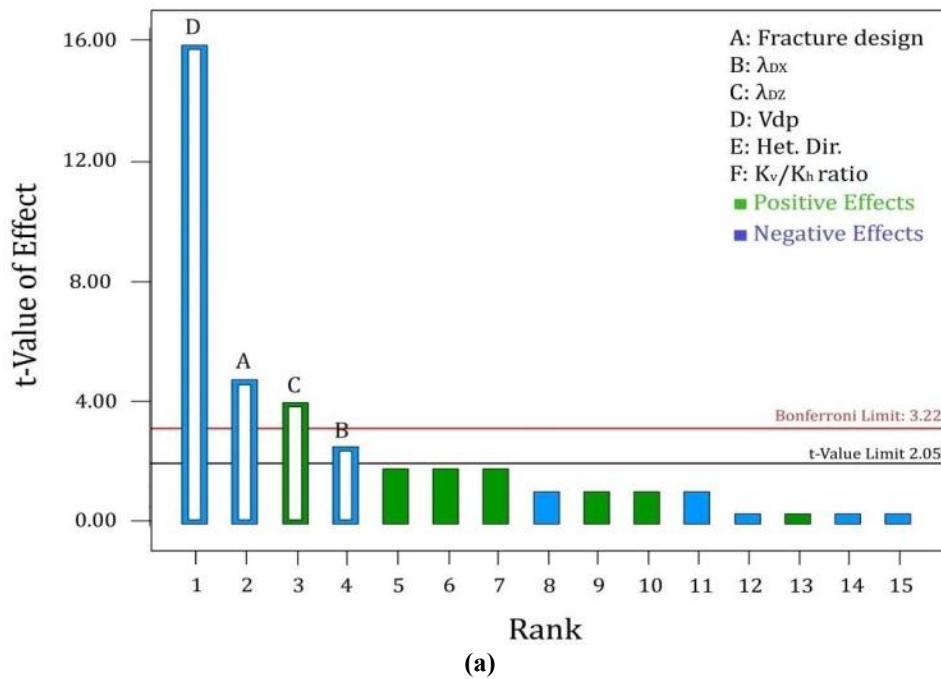
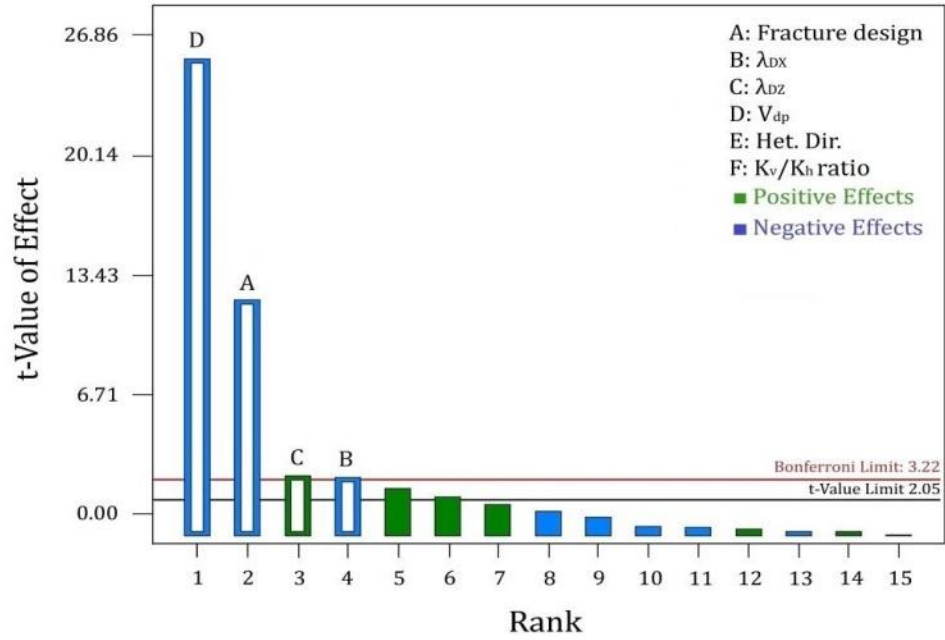
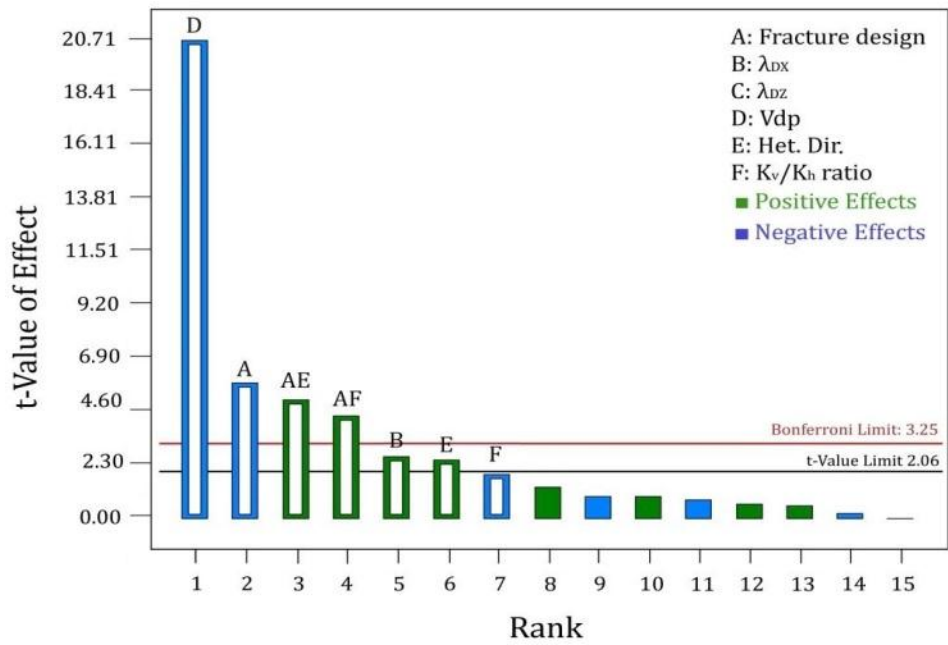


Figure 7-2: Example response surfaces exhibiting (a) the recovery of water flood (b) the amount of stored CO₂ as a function of some selected factors. The values of other factors have been indicated in the legend.





(b)



(c)

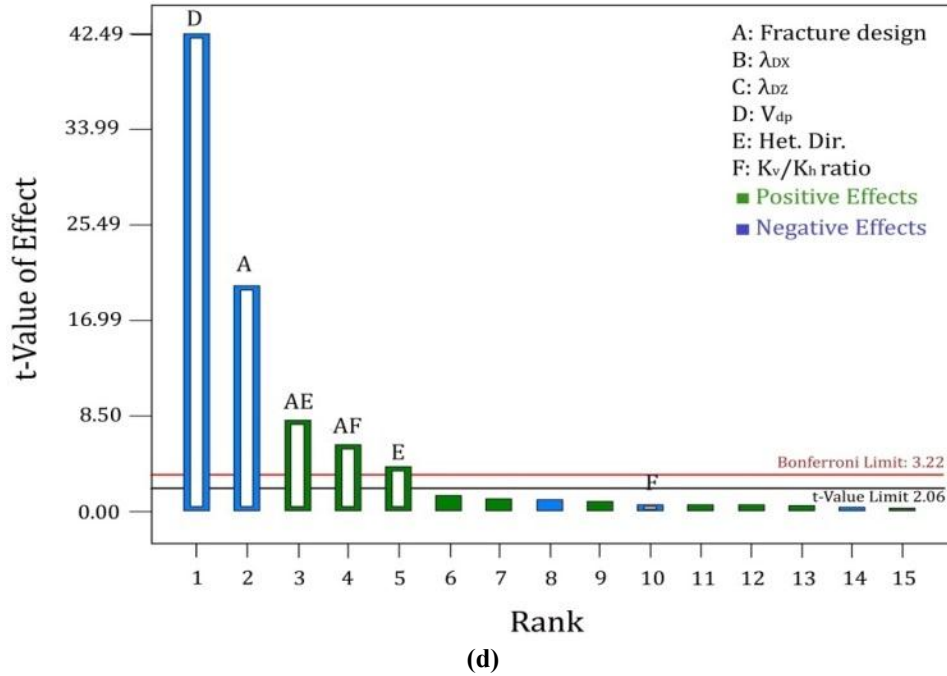


Figure 7-3: Pareto chart showing the rank of effective parameters on (a) duration of water-flood (b) recovery of water-flood scheme (c) recovery of CO₂-WAG scheme and (d) net storage of CO₂ during WAG process.

As its definition implies, higher V_{dp} values will impose higher permeability variation in the reservoir. This in turn will promote fingering, quicker and uneven breakthrough of injected fluid during injection, all of which reduce the sweep efficiency of the flood. Certainly, the shorter the well spacing of injection scenarios, the more dominant effect that permeability heterogeneity would have in reducing the sweep efficiency.

“Level 1” of fracture design is longitudinal and “Level 2” is transverse fractures. As mentioned before, we have defined the fracture dimensions such that both designs will provide identical stimulated rock volume (SRV). Nevertheless, transverse fractures will shorten the effective well spacing, which, to a lesser extent, has the same impact as increasing V_{dp} . Although, at least theoretically, the longitudinal fractures appear to be promising, their implementation is hampered by several issues. For instance, in addition to the requirement of drilling the horizontal well parallel to the maximum horizontal

stress, this fracturing orientation cause long-term formation stability issues (Economides et al. 2002).

Figure 7-3 indicates that the factors impacting permeability heterogeneity, namely V_{dp} and the correlation lengths, are important in water injection scenarios. For a complex miscible process like CO₂-WAG, however, additional reservoir characteristic factors are influencing yields such as the recovery and storage capacity of the models.

In short, reservoir heterogeneity characteristics are potentially very critical decision-making elements in the development plan for tight reservoirs. Specifically, because of the denser well spacing required in the exploitation of such reservoirs, other design factors should be adjusted to account for reservoir heterogeneity.

7-3- Economic Elements in CO₂ EOR/Storage

Implementation of carbon capture and storage (CCS) into a porous medium as a part of an EOR plan is usually associated with many cost components. When CO₂ is extracted from anthropogenic sources like electricity plants or petrochemical units, which is most likely the only option applicable to Alberta, the task of scrubbing CO₂ from the flue gas is expensive and can affect the economics of the project to a large extent (Nguyen and Allinson 2002). However, under such circumstances, if carbon credits are available, the cost of CO₂ storage will be partially offset and the storage component of the EOR process may become attractive as well. To reduce the uncertainty related to CO₂-EOR projects, comprehensive economic studies are required to minimize the risk of failure under different market conditions such as variable oil and gas prices. In the following, we outline the major costs of the process.

Capture and compression cost: The main sources of pollutant emissions into the

atmosphere include power plants, oil refineries, petrochemical, fertilizer and gas processing plants, as well as cement and steel factories. A considerable number of such contributors exist in Central Alberta (see Figure 7-4).

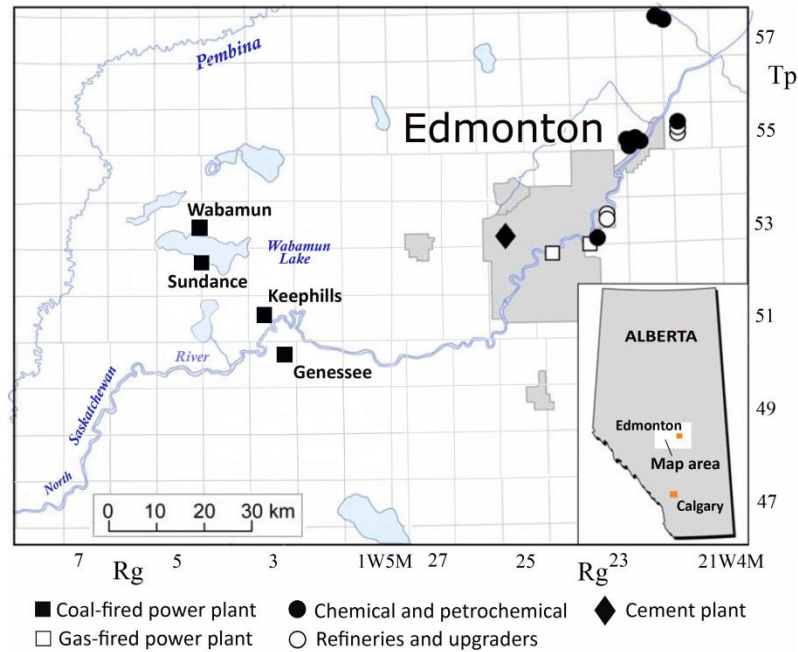


Figure 7-4: Location of main large CO₂ emitters in central Alberta (redrafted from Karsten and Bachu, 2007).

Among the above-mentioned sources, fossil fuel power plants are the most important sources as they account for 30% of global air pollution and naturally are the first candidates for curtailment. However, it should be realized that CO₂ is only a minor portion of the emitted gas stream from power stations and the CO₂ concentration depends on the utilized technology and the age of the plant. Figure 7-5 shows the flow rate of flue gas along with CO₂ from different kinds of power plants. Table 7-5 also provides some quantitative values for CO₂ volumetric concentration in the generated flue gas of power plants.

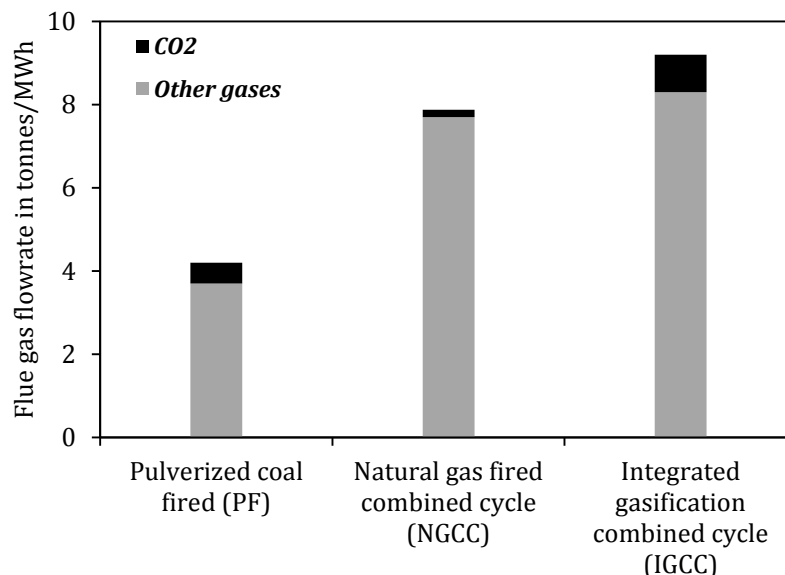


Figure 7-5: Flue gas flow rate from power plants using different technologies (redrafted from Nguyen and Allinson, 2002).

Table 7-5: CO₂ concentration (volume percentage) in the flue gas of power plants with different technologies (from Davison et al. 2001)

Utilized Technology	%Vol. CO ₂
Pulverized coal fired steam cycle	14
Coal fired integrated gasification combined cycles	9
Natural gas combined cycles	4

Because even a midsized power plant can supply CO₂ at high and stabilized rates, it would likely be a reliable supplier for implementing large scale CO₂-EOR projects with a relatively long life (15 to 30 years). For instance, a nominal 500 MW integrated gasification combined cycle (IGCC) power plant, operating at 80% capacity, can deliver 140 MMSCF of CO₂ per day which is approximately equivalent to 2.6 Mt of CO₂ per year. Nevertheless, the capital investment of power stations with carbon capture technology, as well as their operation and maintenance costs, can be quite significant (Jeremy and Herzog, 2000)¹.

Different techniques have been devised for separation of CO₂ from gaseous mixtures

¹Direct underground storage of the flue gas leaving a power station is not feasible because of two factors: (1) limited storage space available (2) the need for too much compression energy.

which have been summarized in Figure 7-6.

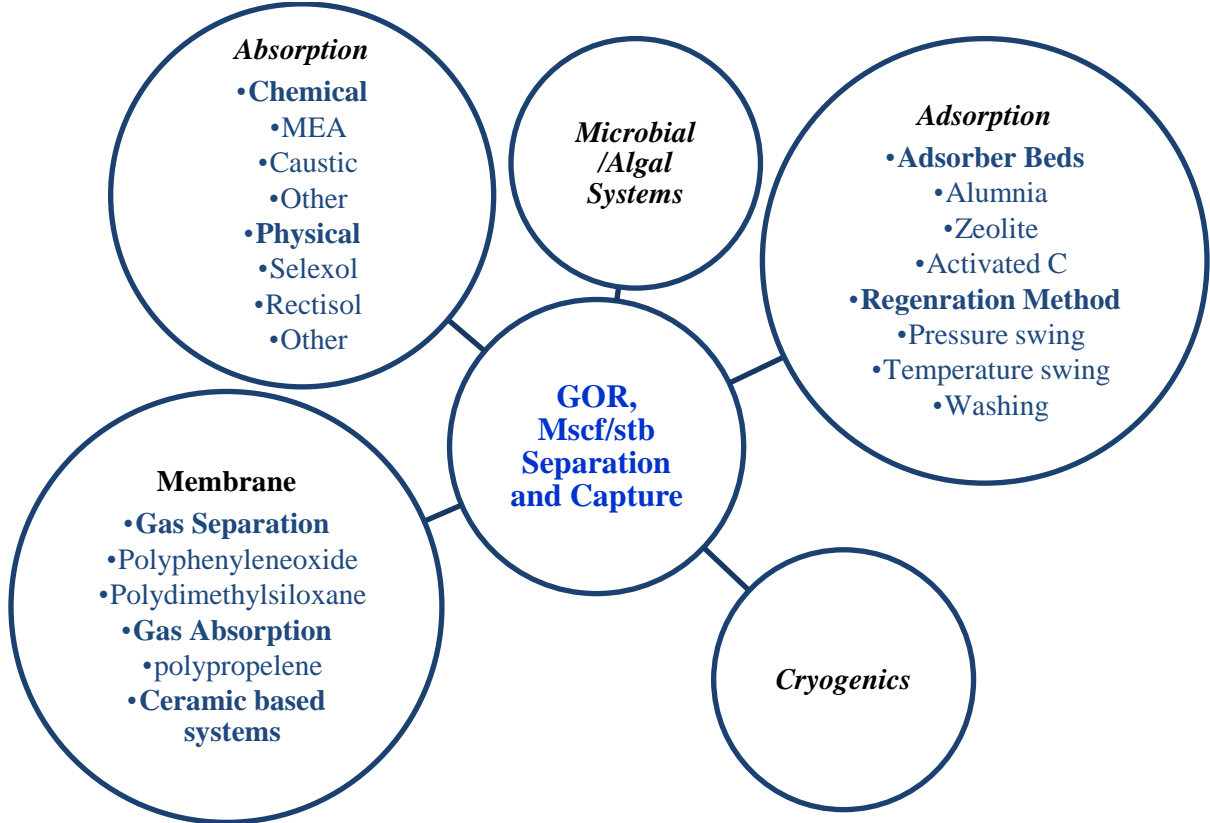


Figure 7-6: Available technical approaches for CO₂ separation and capture (derived from Rao and Rubin, 2002).

The selected approach depends on the intended purity and also the condition of the treated flue gas such as its temperature, pressure, and initial CO₂ concentration. The most widely used technique is chemical absorption by solvent scrubbing. An amine-based solvent like Mono-ethanolamine (MEA) has a CO₂ recovery rate of 98% with a final purity which can be in excess of 99%. The main issue with solvent methods, however, is high cost of the process, related to the rate of solvent degradation, and also the energy required for regeneration of the solvent. The energy consumption for the process can vary between 10 to 35% of the power plant capacity and involves CO₂ regeneration (Herzog, 2000).

In the context of CCS, the goal of the capture stage is to purify the CO₂ stream that

can be stored permanently in a geological formation. The required injection pressure under such circumstances is high. Therefore the separated CO₂ is first compressed to supercritical state, where it has liquid-like properties and can be transported easily. The compression step is usually considered as part of the capture system because it is almost always located at the CO₂ plant site where it is being captured.

The capture process is in general the most expensive part of the storage chain. Nonetheless, vigorous research and development programs, which are currently underway, and also governmental actions such as proposing different incentive programs or limiting CO₂ emissions, will finally bring about substantial and sustained decrease in the future cost of capture (Rubin et al. 2012). The available data in the literature indicates that the unit cost of capture can vary broadly as the assumptions made for each study are different. In a recent publication by IEA (Finkenrath 2011), the projected commercial CO₂ capture cost per tonne of CO₂ has been appraised at 55 US\$ for coal-fired stations and 80 US\$ for gas-fired plants, respectively. In a study by Rochelle et al. (2005), the final costs of capture and compression has been estimated as 45 US\$ per tonne of CO₂ for a nominal 500 MW IGCC power plant.

Transportation Cost: The most common method of CO₂ transportation, especially for higher volumes, is by pipeline¹. For efficient pipeline transportation, CO₂ should be shipped in the supercritical state. Therefore, temperature and pressure changes along the length of the CO₂ pipeline are important design parameters which can change the operation cost. While the temperature mostly depends on the temperature of the surrounding soil, pressure drop is governed by many other factors such as the roughness of steel, changes in elevation and etc. Accurate calculation of pressure drop is necessary

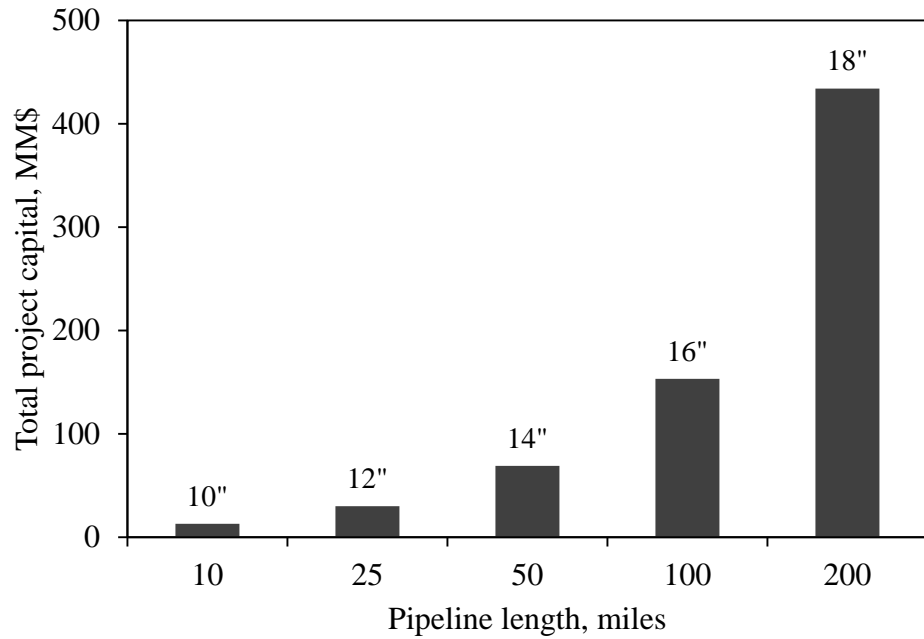
¹For smaller volumes, trucking is usually used.

to compute the initial compression pressure and to determine if additional boosters (with additional costs) are required along the way. Several models are available in the literature for this purpose (Essandoh-Yeddu and Gürcan 2009).

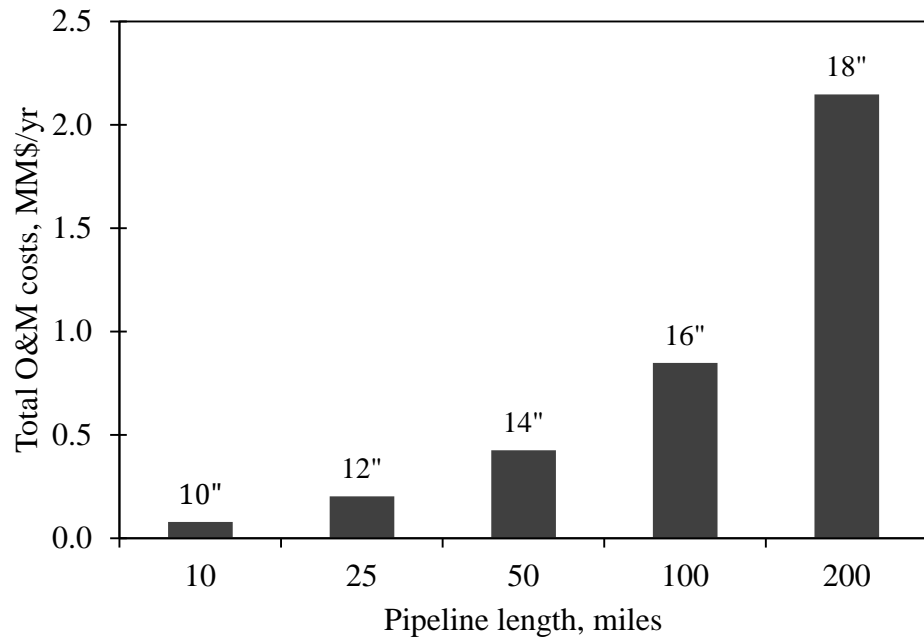
The total cost of pipeline construction can be broken down into four elements: Material, labor, right-of-way (ROW), and miscellaneous expenses. As the detailed construction data for actual CO₂ pipeline is rare, different studies have provided different cost models and most of them provide cost in \$/inch/km. For instance, in the MIT model (Heddle et al., 2003), the average cost has been quoted as \$20,989/inch/km while IEA model (2005) reports \$25,889/inch/km. In a more recent study by Essandoh-Yeddu (Essandoh-Yeddu and Gürcan, 2009), the authors have concluded that the minimum cost of construction cannot be less than \$50,000 per inch per km. In addition to the pipeline diameter and length, the designated flow rate is also an important factor and generally larger flow size reduces transportation cost. Fixed operation and maintenance costs (“O&M” costs) should be also taken into account.

Based on these facts, transportation cost can vary significantly for different projects. For transportation of CO₂ volumes (2.6 Mt/year) captured from the assumed IGCC plant in the previous section, Figure 7-7-a and Figure 7-7-b depict the capital and “O&M” cost of transportation versus the distance of power station to storage site and also the internal diameter of the selected pipeline. Figure 7-7-c displays the minimum required pipeline diameter versus its length to maintain supercritical conditions considering related pressure drop. Tarka and Wimer in NETL report (2010) have analyzed these data and calculated the normalized cost of CO₂ transportation for different distances and for a nominal 550MW gas-fired and coal-fired plants (Figure 7-7-d). Based on this analysis,

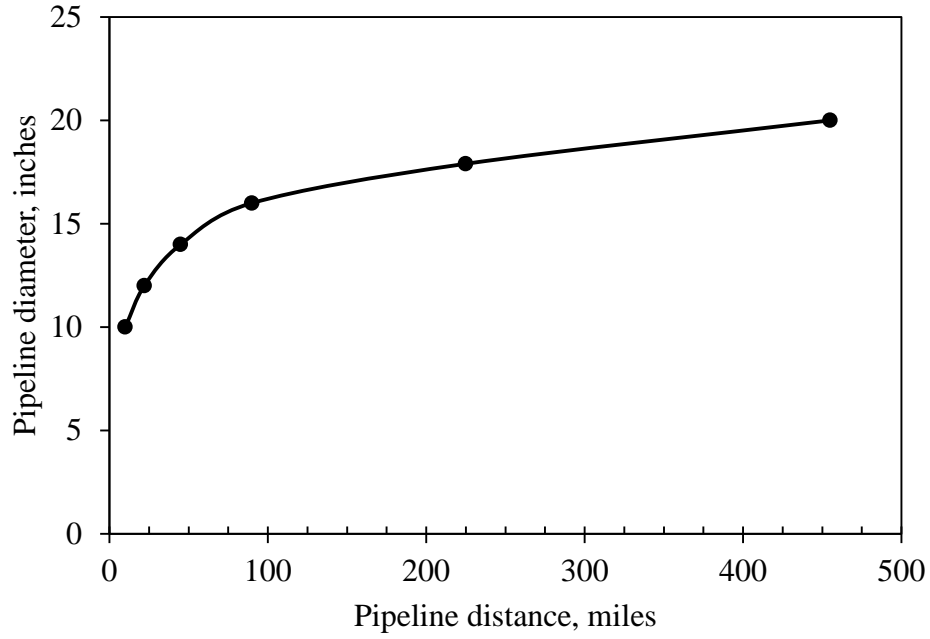
for distances in the range of 40 to 100 miles, the CO₂ removal costs will be in the range of 5 to 10 \$ per tonne of CO₂. A pipeline with this length can transport CO₂ from Wabamun Lake, where the main power plants of Alberta are located, to oil and gas reservoirs is Pembina Cardium field.



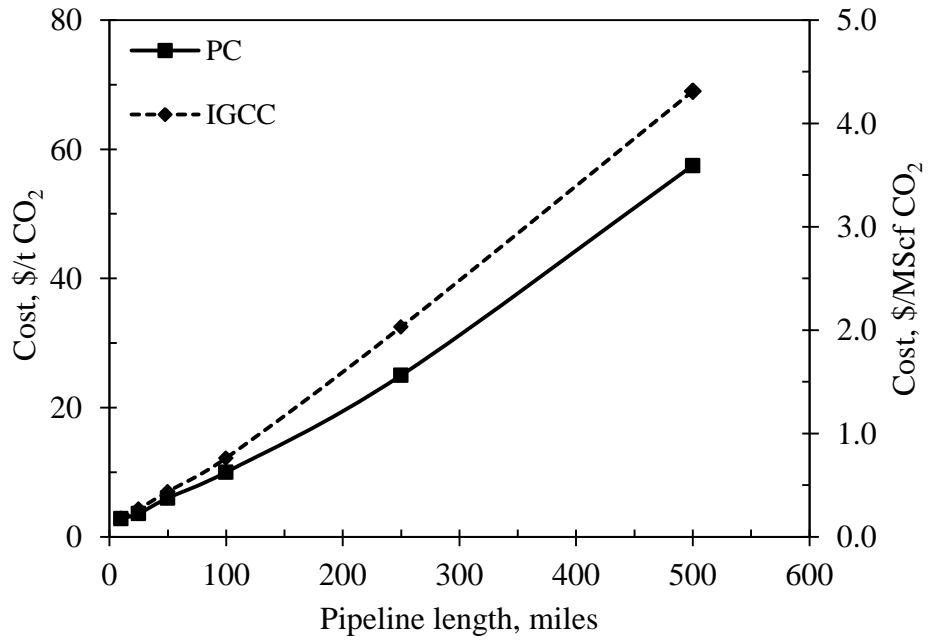
(a)



(b)



(c)



(d)

Figure 7-7: (a, b) Variation of capital and “O&M” cost with pipeline specifications (c) minimum required pipeline versus the transportation length for maintaining supercritical state of CO₂ (d) overall cost of CO₂ removal from power stations (redrafted from NETL 2010).

Storage cost: Cost components for CO₂ injection into hydrocarbon reservoirs

include mainly capital costs for drilling wells, and cost related to the operation,

maintenance and sometimes monitoring of the system (Nguyen and Allinson, 2002). EOR projects involve CO₂ recycling processes, and depending on the required process, the cost of process equipment can change dramatically. For simple compression and dehydration equipment, the process would be much cheaper than a complex facility which can separate NGL as well. Location, reservoir depth, reservoir temperature, and environmental regulatory framework can also affect the economics of the projects.

Consequently, the storage cost varies widely from reservoir to reservoir (different types) and from location to location. Nguyen and Allinson (2002) have pointed out that for most of the geological storage, the cost of storage can range from less than 5\$ to more than 20\$ per tonne of injected CO₂.

7-4- Economics of CO₂-EOR in Tight Reservoirs

CO₂ capture and storage combined with EOR can be utilized to recover oil which otherwise would not be extracted. Revenue from the sale of recovered products (oil, gas, NGL) can offset the cost of CO₂ storage (Gasper 2005). Therefore, CO₂-EOR probably will remain as the only economical method of storage. However, there exist many economic factors that drive the viability of the EOR/storage project. Some of them were presented in the previous section; additional economic factors include oil price, gas price, interest rate, flood performance, and etc. Thus far, almost all of the commercial scale CO₂ injection projects worldwide have been supplied by CO₂ from natural resources at a cheap price, and hence are/were economically very attractive¹. Based on the cost components listed above, should CO₂ be supplied by capture from anthropogenic sources

¹The only exception is the ongoing Weyburn CO₂-EOR/storage project in Saskatchewan, Canada. Carbon dioxide is piped 205 miles from North Dakota coal-gasification facility. The project has shown great success in fulfillment of both objectives of an EOR/storage project. The current oil production is approximately 16,000 stb/day with anticipated storage of 40 Mt of CO₂.

(like power plants), final CO₂ price becomes high and the CO₂-EOR projects may never become attractive/cost competitive. Therefore, to make these projects economic and compare with other investment opportunities for business decision-makers, incentives should be implemented in some form by the government. The purpose of this section is to explore the viability of CO₂-EOR/storage in a typical West Central Alberta tight reservoir, capturing the uncertainty of economic parameters. In the following, simulation models and related assumptions are first reviewed, followed by discussion of the economic model used.

7-5- Simulation Models and Assumptions

Compositional simulation models are used to investigate the effect of different major parameters on the flood performance of tight oil reservoir going through different recovery schemes. The exploitation of tight reservoirs is still in its infancy and currently most of the wells are under primary production. Two stages of primary and waterflood before CO₂ injection are considered in this work. The initial primary scheme lasts for one year in order to partially capture the Alberta royalty holiday benefit for primary production from horizontal wells; this will offset the significant drilling and completion costs in the first year.

The reservoir models considered in this study have properties typical of reservoirs in the tighter portion of Pembina Cardium field in Alberta. The Pembina Cardium pool is the largest conventional oil reservoir in western Canada and covers an area of 700,000 acres. The reservoir quality of the Cardium formation varies considerably, which can be related to deposition environment and subsequent diagenesis. Existence of higher reservoir quality conglomerate, which can act as a thief zone, is expected in the

formation. During the CO₂ injection process, thief zones can prevent CO₂ from contacting the majority of oil (less oil production and hence less revenue) and hence their existence is an important parameter to consider in a simulation study (Goretzky and Hawkins 2009).

Tight reservoirs require denser well spacing for improved oil recovery to be achieved. Well spacing, however, has a more complicated relationship with recovery and economic performance of enhanced recovery schemes. While smaller well spacing brings about better sweep efficiency and hence higher revenue, it would entail higher drilling and operational costs. Hydraulic fractures along a horizontal well not only increase the effective contact area of the well with reservoir but also can change the effective spacing between the wells and therefore their effect should be investigated.

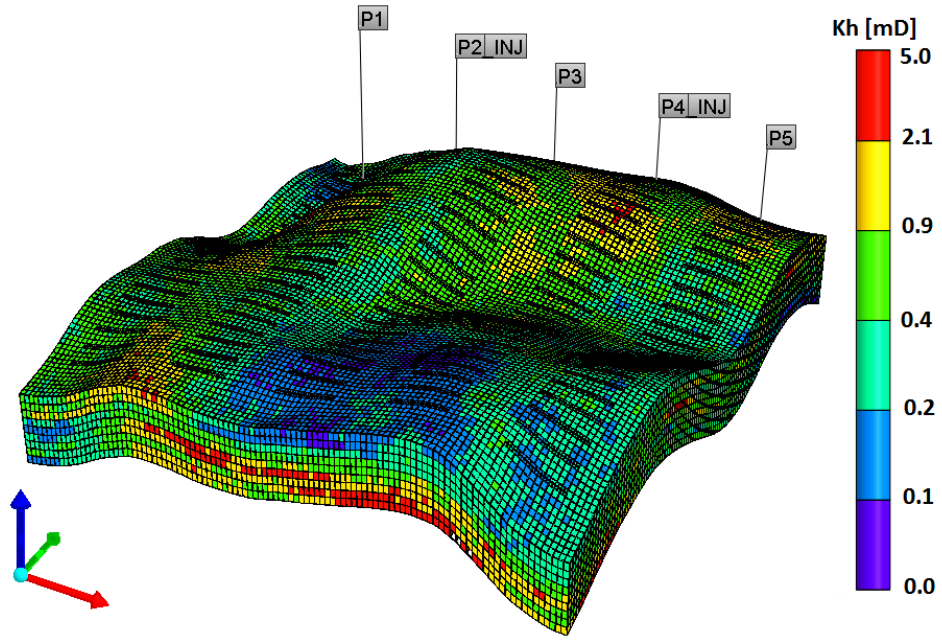
The CO₂ injection scheme is another design factor that can affect the economics of storage significantly. Compared to continuous CO₂ injection, CO₂-WAG could enhance the sweep efficiency and hence better oil recovery (Ghaderi et al. 2012) which ultimately results in better economic outcomes. On the other hand, continuous injection may be a better alternative for maximizing CO₂-storage.

Based on all of these technical factors, 24 field-scale compositional simulation models were built and run to investigate the performance of CO₂-EOR in the tighter portion of Pembina Cardium field. The properties of the base reservoir model (without a thief-zone) are summarized in Table 7-6.

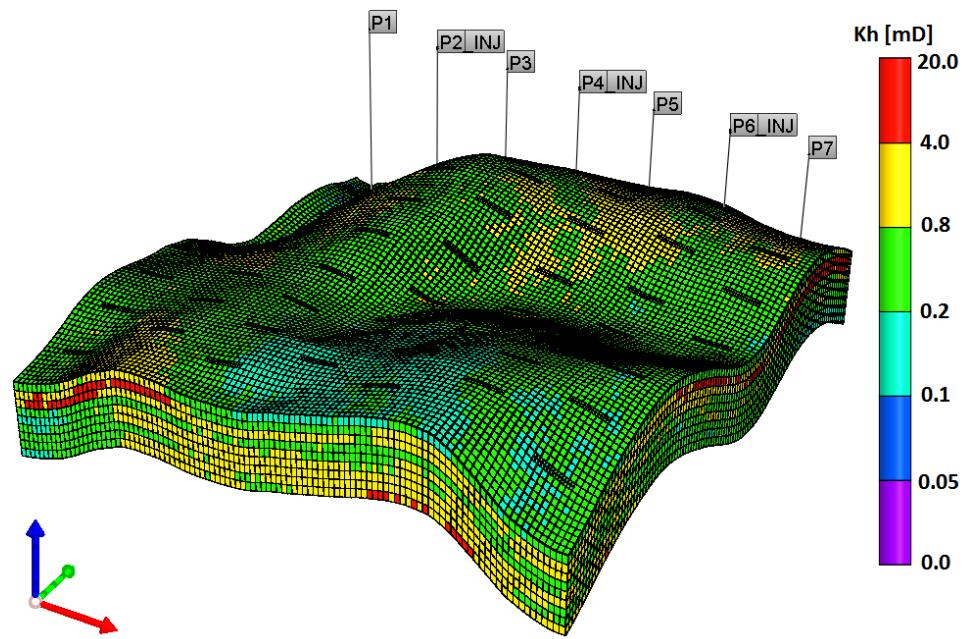
Table 7-6: Reservoir properties of the base geo-model used in economic study

Property	Value
Length, ft	5,250
Width, ft	5,250
Thickness, ft	27
Dykstra-Parsons coefficient	0.55
Dimensionless correlation length in horizontal direction	0.5
Dimensionless correlation length in vertical direction	0.5
Kv/Kh ratio	0.1
Average porosity	0.11
Average permeability, mD	0.53
Length of well laterals, ft	4,600
Number of grids (Nx×Ny×Nz)	105×105×9
Avg. grid size (Dx×Dy×Dz), ft	50×50×3

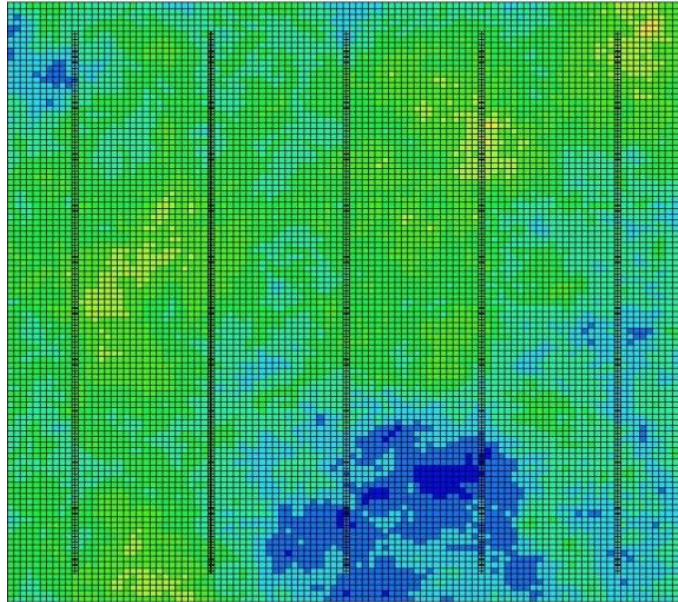
To generate the thief-zone model, permeability of the second and third layers from the top of the base model is multiplied by ten and porosity is modified accordingly in these two layers. Either 7 wells per section or 5 wells per section are considered to investigate the effect of well spacing. For injection, 3 wells are converted into injectors for the first well spacing scheme and 2 wells for the second one. The effect of hydraulic fracture orientation is investigated (longitudinal vs. transverse), as well as fracture spacing along each well lateral for the transverse fracture cases. Two configurations were considered for fracture spacing along the well. In the first configuration, and for the longitudinal fractures, the fractures are assumed to cover the whole length of the horizontal well, while for transverse fracture cases, 23 fractures are placed along the wellbore. In the second configuration, for both fracture directions, the number of fractures is reduced to 9 discrete fractures in a zipper (staggered) arrangement along each well. In the tabulated results presented later “(1)” and “(2)” refers to these fracture configurations (see Figure 7-8).



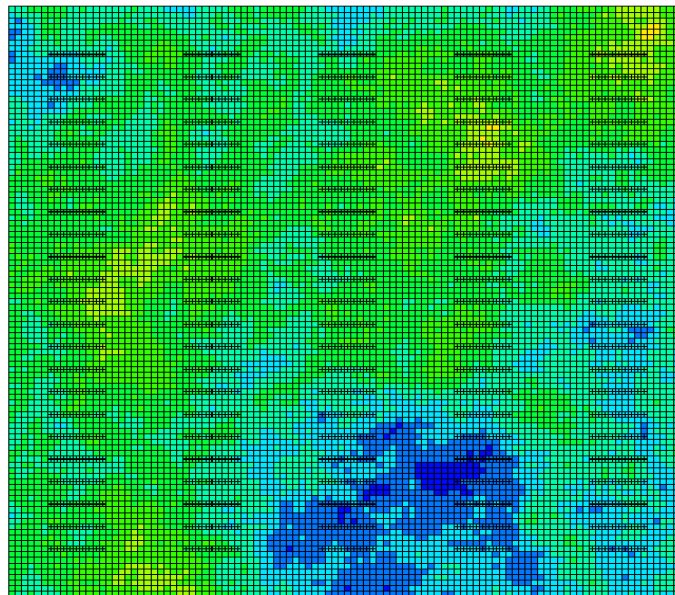
(a)



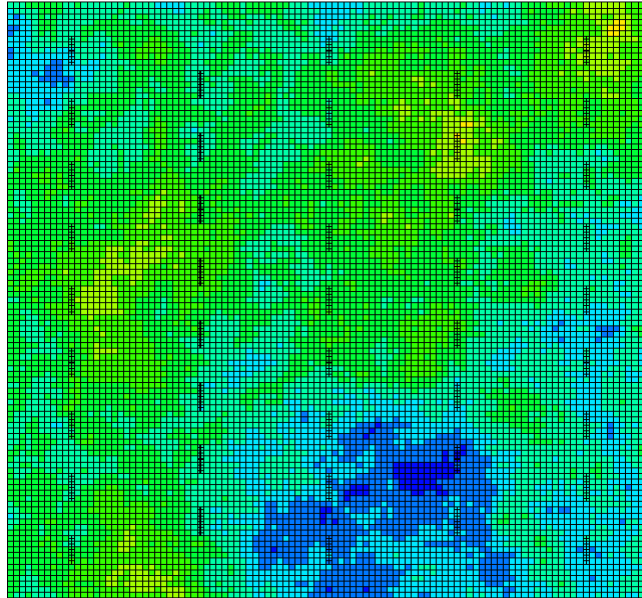
(b)



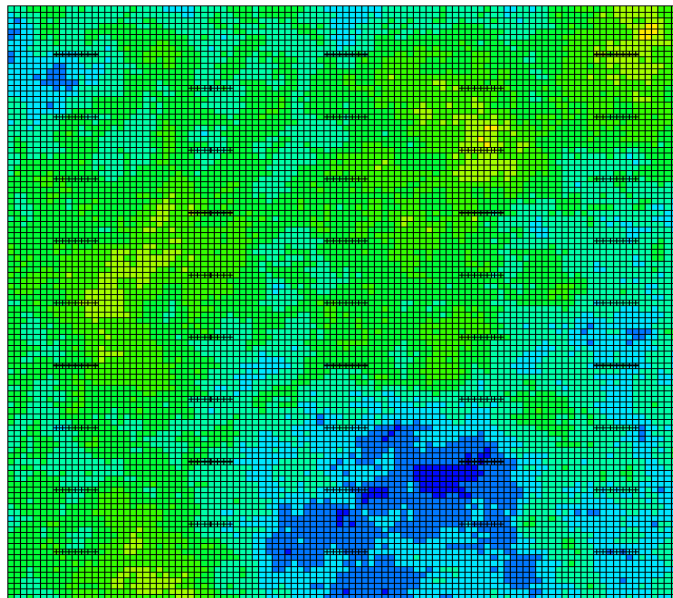
(c)



(d)



(e)



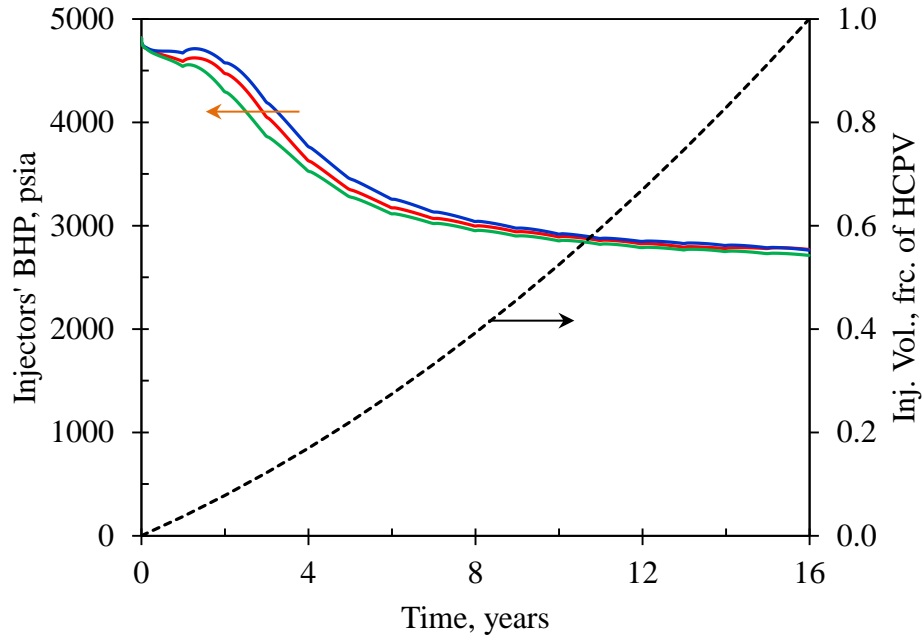
(f)

Figure 7-8: 3D view of the reservoir used in economic evaluation of the CO₂-EOR project (a) with base permeability properties and (b) with induced thief zone. Top view of the reservoir with five horizontal wells stimulated with (c) longitudinal (d) transverse fractures in configuration 1 and (e) longitudinal (f) transverse fractures in configuration 2.

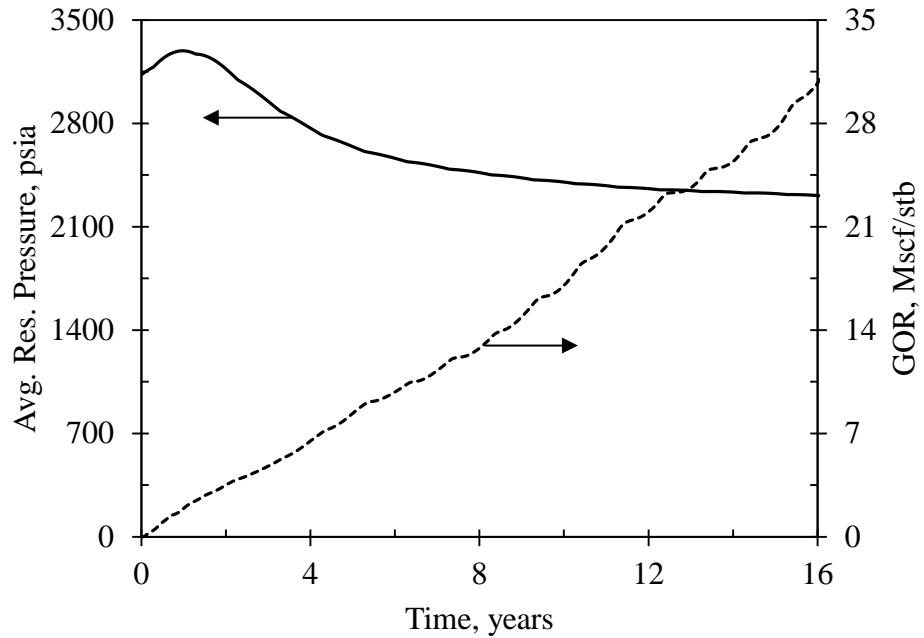
All the producers are operated under a constant bottom-hole pressure of 300 psia and injection occurs at a constant rate with pressure being monitored regularly to ensure a safe operation at 90% of fracture pressure or below. The water-flood scenario terminates

when the water-cut of the producers passes 95%. In the case of CO₂ injection, the operation concludes when the CO₂ cumulative injected volume reaches 100% HCPV. Figure 7-8-a and Figure 7-8-b display 3D prototypes of geo-models with two different well spacing and fracture design. Figure 7-8-c through Figure 7-8-f show the top view of the reservoir, where five wells are used with hydraulic fractures in two different configurations.

It should be mentioned that in the case of continuous CO₂ injection, because of the short distance between the adjacent producers and injectors and also effect of reservoir permeability heterogeneity, CO₂ breakthrough will occur rather quickly followed by rapid average reservoir pressure drop below the minimum miscibility pressure ($P_{avg} \ll P_{MMP}$). Under this condition, the recovery factor will reduce considerably and the operating cost of excessive CO₂ recycling and processing will increase drastically and henceforth will be impractical. Therefore, in such cases, the well operating condition should be modified. Consequently, we have increased the bottom-hole pressure of producers to 1200 psi and injection rates of CO₂ increase by 5% each year. Figure 7-9 shows the average reservoir pressure and bottom-hole pressure of injectors in the 7 well model (3 injectors and 4 producers) over the CO₂ injection period.



(a)



(b)

Figure 7-9: Variation in different parameters during continuous CO₂ injection with adjusted BHP of producers and injection rates of injectors for the “without thief-zone” model with 7 wells (3 injectors and 4 producers) and transverse fractures.

The output results from the simulation runs are used to accurately quantify the production and injection volumes of different fluids and also the amount of stored CO₂

mass in each model.

7-6- Economic Model

Besides the technical factors discussed above, several important economic parameters are considered to evaluate the viability of each project. Considering the high price of deliverable CO₂, the CO₂ injection part of the entire recovery scheme (primary-water flood-CO₂ flood) would likely be unfavorable and would require an appropriate level of incentives.

As net present value (NPV) is the main indicator of the profitability of the projects, a comprehensive economic model based on the Alberta oil and gas fiscal system was developed to calculate the NPV and associated profit of each scenario. NPV captures the time value of money and gives more importance to the near-term revenue and expense than the future. In this study, the economic analysis is performed on three different combinations of recovery mechanisms.

In the first scenario we consider only primary and water-flood stages. In such a scenario, a significant amount of capital investment is required to drill, frac, and complete the horizontal wells, but at the same time, the operating cost would be minimal which means a shorter payback period. Specially, the applicable royalty holidays during the primary recovery period can significantly improve NPV of the projects¹. In the second scenario, primary, water-flood and CO₂ injection (as continuous injection or WAG) are combined as a single project. In this situation, because the CO₂ injection (the most operationally expensive part) occurs at later times, its effect on NPV may be offset by the

¹ In this study, we neglected to compare the profitability of a scenario in which the wells produce under primary production for the whole life of the project with other scenarios due to our focus of this paper on CO₂-EOR and CCS.

early profitable periods. Lastly and in the third scenario, the CO₂ injection scenario is investigated individually and independently from preceding recovery schemes. In such a scenario, the required capital investment of drilling and other related expenses will be eliminated and the already available infrastructure (i.e. wells, pipelines) can be adapted for tertiary recovery purposes. For this scenario, the effect of providing direct incentive for the projects will be investigated.

To obtain a better understanding of the effect of different economic factors on the viability and performance of the projects, stochastic rather than deterministic analysis should be performed. As such, each evaluated parameter can acquire several values (levels). However, a sophisticated statistical analysis like experimental design is required to perform a complete sensitivity (uncertainty) analysis with a minimum number of runs. The response surface method can be utilized subsequently to search for the mathematical relationship between the object function (i.e. NPV) with these parameters. In the end, Monte Carlo simulation can be used to determine the risk (probability) of failure under uncertain economic and market conditions which is important for justification of investment.

7-7- Results of Economic Sensitivity Analysis

The large capital investment required for initial development of tight oil formations through drilling of long horizontal wells stimulated with hydraulic fractures, and factors such as oil price, gas price, oil and gas lift cost, interest/discount rate, and many others can change the fate of a project. For scenario 1 and 2 described previously, 13 economic factors listed in Table 7-7 were considered.

Table 7-7: Uncertain economic factors for economic evaluation of PR-WF-CO₂ flood

Factor	Unit	L1	L2	L3	L4
A: Oil price	\$/bbl	65	75	85	95
B: Gas price	\$/Mscf	1.5	2.5	3.5	
C: Well drilling cost	MM\$/HWell	2.0	2.67	3.33	4.0
D: Fracing job cost	M\$/stage	16	19.33	22.67	26
E: CO ₂ inj. Cost	\$/Mscf	1.5	2.5	3.5	4.5
F: Water inj. cost	\$/bbl	0.75	1.5	2.25	
G: Oil lift cost	\$/bbl	10	15	20	
H: Gas processing cost	\$/Mcf	0.25	0.5	0.75	
I: Water prod. cost	\$/bbl	0.5	1	1.5	
J : CO ₂ recycling cost	\$/Mcf	0.3	0.6	0.9	
K: Avg. unit operation cost	M\$/HWell	40	60	80	
L: Flood performance factor (FPF)	Dimensionless	0.7	0.9	1.1	1.3
M: Discount rate	fraction	0.05	0.083	0.116	0.15

Besides economic factors, one factor, referred to as “flood performance factor”, has been introduced to account for the uncertainty associated with the simulation results. This factor takes into account the uncertainty in production/injection performance arising from the uncertainty in proper characterization of the reservoir heterogeneity as well as uncertainty in properties of induced hydraulic fractures. These inevitable uncertainties, in addition to the assumption of static properties for the hydraulic fractures, could result in optimistic or pessimistic simulation outcomes.

Four different levels (values) were assigned to the factors which have a greater effect on the economics of the projects and the lower impact factors were assigned three levels. Because the matrix of input numerical parameters has an uneven number of levels for different factors, an optimal response surface method (RSM) should be chosen to specify the required runs for economic evaluation. In this study, optimal design of “IV” criterion was selected as it is the best choice where prediction is critical (Stat-Ease 2010). Based on optimal design, 230 runs will be required to determine the response surface of NPV with respect to the 13 economic factors. In comparison with conventional sensitivity

analysis, which would require 444528 ($6^4 \times 7^3$) runs, this will bring about vast computational savings and makes this sort of evaluation feasible. Table 7-8 shows a portion of the sensitivity analysis matrix and the value that each parameter would gain in each run.

Table 7-9 presents the max/min NPV and associated profit (NPV divided by the ultimate equivalent barrels of oil, boe¹ produced) for 24 simulation scenarios in columns with headings labeled “A”, “B”, “C”, and “D”. Sample 3D response surfaces of NPV with respect to some of these economics factors are depicted in Figure 7-10.

¹For boe calculation, the equivalency ratio for gas was assumed to be 10 Mscf.

Table 7-8: Table of runs for sensitivity analysis based on the 13 economic factors for scenarios 1&2 (coded factors)

Run	Factors													Responses		
	A	B	C	D	E	F	G	H	I	J	K	L	M	R1†	R2††	R3†††
1	-1	1	0.33	-1	1	-1	-1	1	0	-1	0	1	-1	27.5	21.9	30.6
2	-1	-1	0.33	1	-1	1	1	1	-1	1	1	-0.33	0.33	-14.6	-14.6	-14.3
3	-0.33	1	-0.33	-1	1	1	1	0	-1	0	-1	1	1	14.3	13.9	14.7
4	1	-1	0.33	1	0.33	-1	-1	1	-1	1	1	-1	0.33	5.8	4.4	6.1
5	0.33	0	-0.33	-0.33	-1	-1	0	1	0	0	0	0.33	0.33	13.7	15.4	15.8
6	-0.33	0	0.33	0.33	-0.33	1	0	-1	-1	1	0	0.33	-1	13.9	16.3	20.2
7	1	1	1	0.33	-1	-1	-1	-1	0	1	0	1	-1	56.9	77.0	82.0
8	1	1	1	1	1	1	1	1	1	1	-1	-0.33	1	-0.1	-1.0	-0.1
9	-1	-1	-1	1	-0.33	-1	-1	1	-1	1	1	1	-1	33.0	36.4	42.8
...
50	-1	1	1	-1	1	-1	0	-1	0	1	-1	0.33	-0.33	3.1	-2.7	2.1
51	-1	-1	-1	1	-1	0	1	1	1	-1	1	1	-1	12.1	19.4	21.1
52	1	-1	1	1	-1	1	1	-1	1	1	1	1	-0.33	25.9	33.3	33.6
53	1	1	1	-1	-1	-1	-1	0	-1	-1	-1	1	-0.33	50.7	61.0	62.2
54	-0.33	-1	1	-0.33	-1	0	0	1	1	0	-1	1	-1	21.0	33.3	36.5
55	1	-1	-1	-1	0.33	1	-1	1	-1	1	-1	-1	1	13.0	12.4	13.0
56	-0.33	-1	0.33	-1	-1	-1	-1	-1	1	1	-1	0.33	1	14.1	15.1	15.3
57	1	-1	1	-1	1	1	0	-1	1	0	-1	-1	0.33	-3.2	-5.9	-4.2
58	-1	-1	1	1	-1	1	1	-1	-1	-1	0	-1	0.33	-24.8	-25.0	-24.9
59	1	1	-1	-1	1	-1	-1	-1	-1	1	-1	-0.33	-1	42.0	34.8	43.6
...
120	1	1	0.33	0.33	1	-1	0	-1	-1	0	-1	1	-1	54.5	58.3	67.7
121	1	-1	-1	0.33	-0.33	0	-1	1	-1	-1	0	1	1	44.6	46.4	46.5
122	-1	-1	1	0.33	-1	-1	0	-1	0	-1	-1	-0.33	-0.33	-7.5	-6.0	-5.1
123	-1	1	0.33	1	-1	0	-1	-1	-1	-1	-1	1	-1	24.5	36.4	40.0
124	1	-1	1	-0.33	-1	0	-1	0	-1	-1	-1	-1	-1	8.8	15.6	17.0
125	-1	-1	-1	1	1	1	-1	1	1	-1	0	-1	0.33	-4.6	-8.5	-6.7
126	-1	1	-1	-0.33	-0.33	1	-1	-1	1	0	-1	-1	1	-2.3	-3.0	-2.6
127	-1	0	-0.33	0.33	-1	1	-1	1	1	-1	-1	1	0.33	17.1	19.5	19.4
128	-1	1	-0.33	-1	0.33	1	0	1	1	0	-1	-1	-0.33	-8.8	-15.1	-12.9
129	-0.33	-1	1	0.33	-0.33	0	1	1	0	1	-1	-1	0.33	-17.1	-18.5	-17.5
...

Run	Factors													Responses		
	A	B	C	D	E	F	G	H	I	J	K	L	M	R1†	R2††	R3†††
171	-1	0	1	-1	1	1	1	0	1	-1	1	1	0.33	-4.8	-6.7	-5.1
172	1	1	-0.33	1	-1	0	-1	1	1	0	-1	-0.33	1	19.2	20.4	20.3
173	-0.33	1	1	1	0.33	1	1	1	0	1	1	-1	-0.33	-19.4	-25.6	-23.0
174	-1	-1	-0.33	1	-0.33	1	1	0	1	1	-1	0.33	1	-4.7	-5.0	-4.6
175	-1	-1	1	1	-1	1	1	1	1	-1	1	-1	-1	-27.3	-29.5	-31.4
176	-1	1	0.33	1	1	1	1	-1	-1	1	-1	-1	1	-19.3	-21.5	-20.3
177	1	-1	-1	0.33	-1	0	1	-1	-1	0	0	0.33	0.33	28.3	31.2	31.4
178	1	1	1	-1	0.33	-1	0	-1	1	0	1	-1	-1	5.8	-2.1	2.4
179	1	-1	1	-1	-1	-1	1	-1	-1	0	-1	-1	1	-4.6	-4.1	-3.9
...
216	1	1	-1	-1	1	1	-1	1	1	-1	1	-0.33	1	23.4	23.0	23.6
217	1	0	-1	0.33	1	0	-1	1	0	-1	1	-1	-1	20.1	8.3	13.7
218	-1	1	1	-1	-1	1	-1	1	-1	1	0	1	1	7.7	8.7	8.8
219	-1	1	-1	-0.33	0.33	-1	-1	1	1	-1	-1	-1	1	0.4	-0.8	0.0
220	-1	1	1	0.33	0.33	-1	1	-1	0	-1	1	1	1	-3.7	-4.0	-3.3
221	-1	-1	1	1	1	-1	-1	1	1	-1	-1	-1	-1	-10.9	-29.9	-23.1
222	1	-1	1	1	1	-1	-1	-1	1	1	1	-1	1	-1.8	-3.1	-2.0
223	1	-1	-1	1	-1	-1	0	1	-1	1	-1	-1	-1	19.1	22.9	25.8
224	-1	1	-1	-1	-1	-1	-1	-1	1	-1	1	-1	-1	5.3	5.4	6.3
225	-0.33	1	-0.33	1	0.33	-1	1	1	0	-1	1	-1	1	-8.1	-9.2	-8.5
226	0.33	-1	-0.33	-0.33	-1	0	1	0	0	0	1	-1	-1	0.6	2.2	2.9
227	-0.33	0	0.33	0.33	-0.33	0	-1	0	0	0	0	-0.33	-0.33	7.3	7.6	9.3
228	-1	1	-1	1	-0.33	0	1	0	1	1	1	-1	1	-10.1	-11.1	-10.6
229	-1	1	-1	1	-0.33	1	-1	-1	-1	-1	0	-1	-1	-0.1	-5.4	-4.0
230	1	0	1	-1	0.33	0	0	-1	1	-1	-1	1	-1	46.6	56.6	61.9

†NPV (MM\$) of primary-waterflood recovery scheme

†† NPV (MM\$) of primary-waterflood-CO₂ flood (continuous) recovery scheme

††† NPV (MM\$) of primary-waterflood-CO₂ flood (WAG) recovery scheme

Table 7-9: Results of economic evaluation of different recovery schemes for considered reservoir models

Model Design			Primary – Waterflood					Primary – Waterflood – CO ₂					Primary – Waterflood – WAG				
			A	B	C	D	β	A	B	C	D	β	A	B	C	D	β
Without thief-zone	LHF	7 W	67.2	23.2	-27.1	-9.4	8.6	79.7	17.1	29.2	-6.3	88.5	85.7	15.4	-29.4	-5.3	3.7
		5 W	60.8	21.2	-17.2	-6.0	0.8	61.9	13.8	-17.3	-3.8	0.9	64.2	12.4	-17.2	-3.3	0.4
	THF	7 W	64.0	23.1	-27.3	-9.9	9.5	77.0	17.7	-29.9	-6.9	88.6	82.0	16.0	-31.4	-6.1	7.2
		5 W	55.8	21.4	-19.5	-7.5	3.3	58.6	14.6	-19.6	-4.9	4.5	59.5	13.2	-20.2	-4.5	2.4
With thief-zone (1)	LHF	7 W	57.8	19.7	-48.7	-16.6	31.4	58.2	16.4	-60.6	-17.1	85.5	69.1	16.0	-65.7	-15.2	76.4
		5 W	59.0	20.0	-29.3	-9.9	7.9	59.1	16.3	-33.5	-9.2	47.5	64.1	14.7	-33.9	-7.8	24.5
	THF	7 W	59.6	20.2	-46.8	-15.9	29.1	61.2	16.4	-55.9	-15.0	77.5	70.2	16.1	-61.2	-14.1	70.1
		5 W	55.9	19.4	-31.6	-11.0	13.7	57.2	15.6	-34.6	-9.4	45.0	59.9	14.0	-35.8	-8.4	32.8
With thief-zone (2)	LHF	7 W	84.8	23.1	-30.5	-8.3	4.1	95.4	19.4	-35.8	-7.3	20.8	105.6	18.2	-37.9	-6.5	8.2
		5 W	79.7	22.2	-16.6	-4.6	0.2	83.6	17.4	-17.7	-3.7	6.5	86.8	15.2	-17.6	-3.1	0.2
	THF	7 W	85.3	23.1	-27.6	-7.5	2.3	97.9	19.7	-31.5	-6.3	13.0	105.9	18.2	-33.6	-5.8	8.0
		5 W	79.6	22.3	-14.7	-4.1	0.5	85.1	17.4	-15.4	-3.2	0.4	87.6	15.2	-15.5	-2.7	0.1

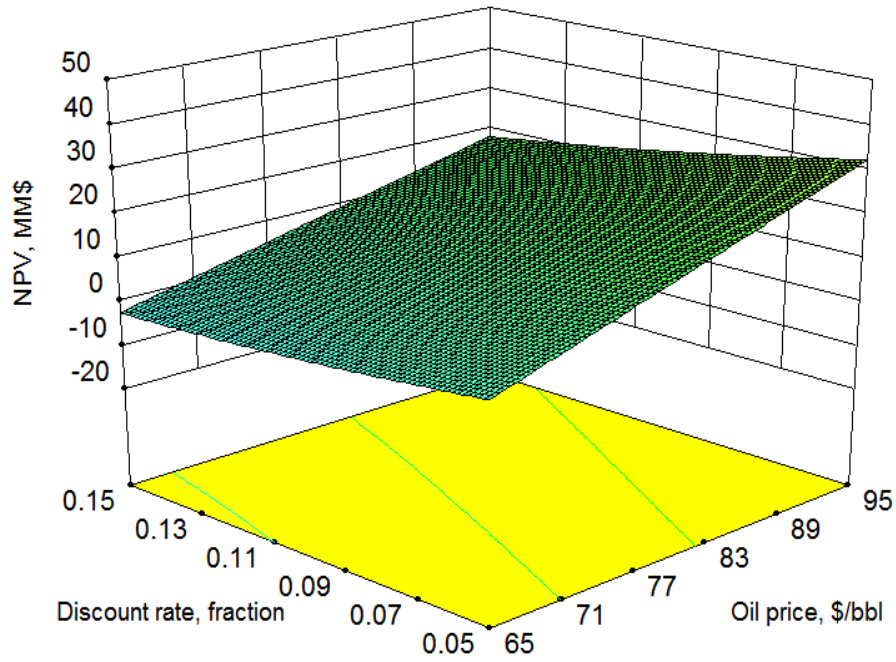
A: Maximum NPV (MM\$)

B: Maximum profit (\$/boe)

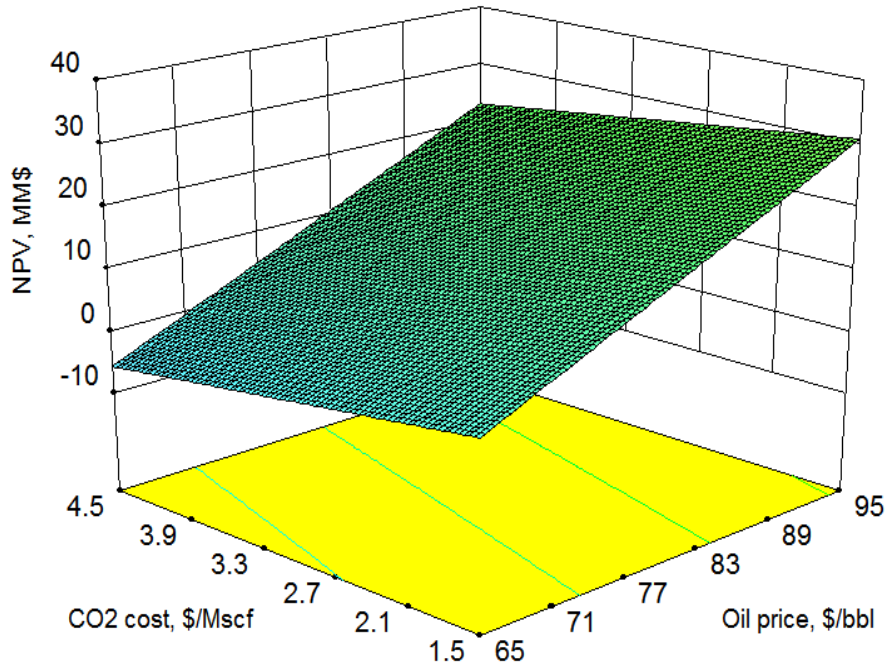
β: Probability of failure (NPV<0 @ 95% C.I.)

C: Minimum NPV (MM\$)

D: Minimum profit (\$/boe)



(a)



(b)

Figure 7-10: Response surfaces of NPV with respect to (a) oil price and discount rate for a primary-waterflood scenario (b) oil price and CO₂ cost for a primary-waterflood-CO₂ flood scenario. Other factors are at their mean value.

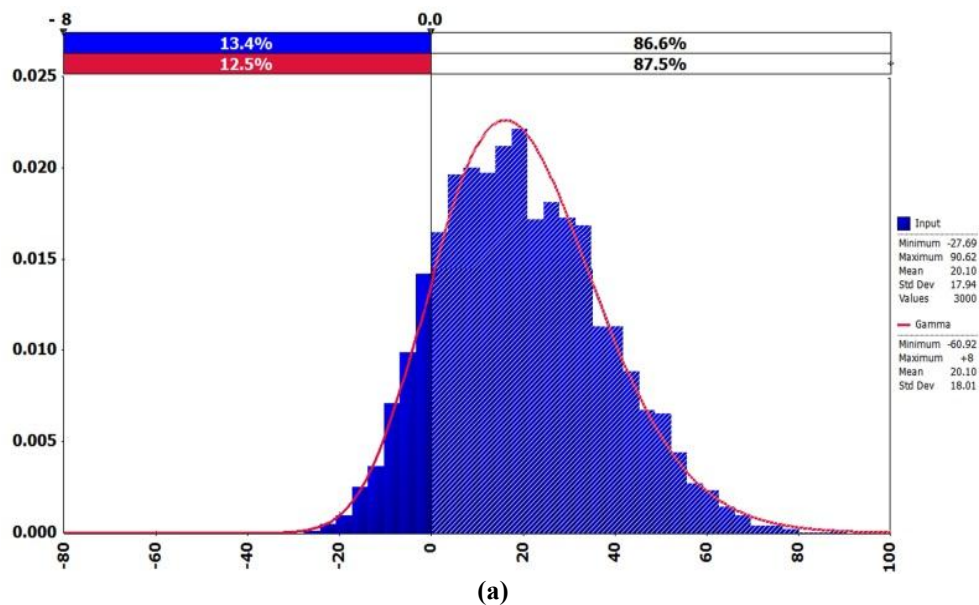
With response surfaces alone it would be difficult to track the behavior of the target objective (here NPV) when several input parameters can change simultaneously, and

especially when the relationship between input parameters and response surface is not linear. For example, in graphical form, at most the effect of two factors on the objective function can be visualized and examined simultaneously. Moreover, tracking the behavior of the desired response becomes important when the input parameters behave in a certain way, like following a certain probability distribution function. Under such circumstances, there is a chance that, over a certain combinations of input parameters, the response tends toward undesired, risky values. To evaluate such a risk, “*Monte-Carlo*” type of simulation can be applied to the resultant expression from the response surface to determine the chance of failure for each scenario. For this purpose, a probability distribution function (PDF) should be assigned to each economic factor. There are several types of PDFs such as uniform, triangular, and normal distributions which might be able to represent the possible behavior of each factor. However, in this study, the uniform distribution was selected to represent uncertainty as there is no prior information or strong evidence that suggests that a more complex PDF would be superior (McCoy and Rubin 2009). For this simple distribution, the maximum and minimum values that each factor can acquire are equal to the corresponding values in Table 7-7. Then, 3000 simulation runs based on the “Latin Hypercube¹” sampling technique were performed to explore the probability of getting negative NPV and hence failure of each project.

Based on these inputs, the probability and cumulative distribution functions for NPV can be obtained and further utilized to determine the chance of getting negative NPV and hence failure of the project. Monte-Carlo simulation results can also be used to rank the individual input parameters in order of their importance. Figure 7-11 shows those

¹In comparison with the conventional Monte-Carlo sampling algorithm, Latin Hypercube is a more robust approach as it can accurately recreate the probability distributions specified by distribution functions in fewer iterations (@Risk 2013).

expected outputs for a model with the following properties: a thief-zone geo-model with 7 wells having transverse fractures arranged in configuration 2 and recovery scheme sequence primary-waterflood-continuous CO₂ injection. According to simulation results illustrated in this figure, the probability of failure for this project is around 13%, which is relatively low. Moreover, the most important economic factors are oil price, oil-lift cost, drilling cost, discount rate, CO₂ injection cost; this order remains the same for other models in Table 7-8 which belong to scenario 1. The column below the heading labeled “ β ” in this table gives the probability of failure for different projects.



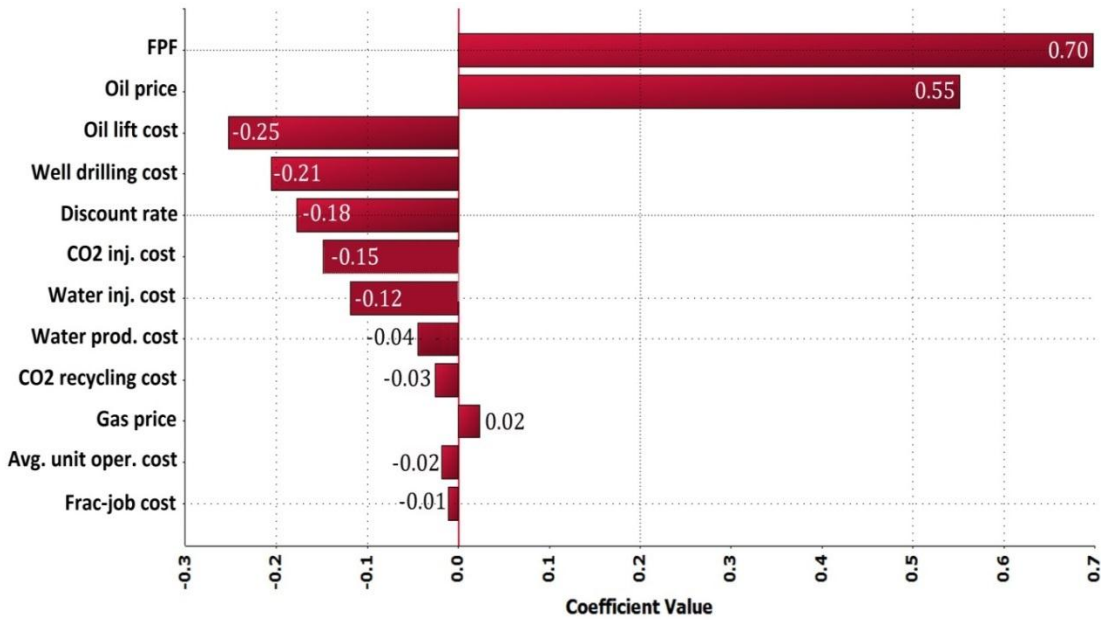
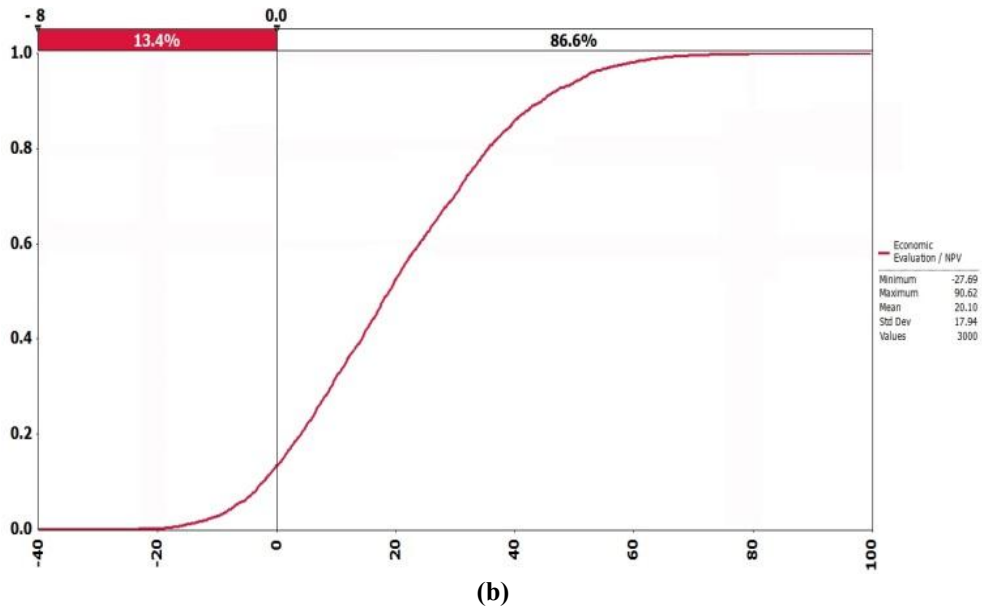


Figure 7-11: (a) probability density function and the best fit function (in red) for NPV (b) cumulative distribution function of NPV (c) Tornado graph of important economic factors of NPV for a primary-waterflood-continuous CO₂ injection scenario.

According to these results, under different conditions, the primary-waterflood scenarios have a high chance of success and this chance is higher in the absence of a thief-zone or when the fracture arrangement is modified in the presence of a thief zone (configuration 2). Furthermore, models with 5 wells per section respond better to this

recovery scheme. When CO₂ injection is implemented along with primary-waterflood as a single project, it is seen that the probability of failure increases. This increase is considerable in two situations: (1) continuous CO₂ injection with denser well spacing (7 wells/section) (2) for both continuous CO₂ injection and WAG injection when configuration (1) is used in development of a reservoir with a thief-zone. In the first situation, tighter well spacing causes breakthrough of CO₂ to happen earlier and hence the well operating cost, and in particular the cost of recycling, becomes dominant. In the second situation, because CO₂ tends to move upward and the thief zone is also located at the upper portion of the reservoir, the same issue of excessive recycling exists. According to these results, well spacing has an important effect on the profitability of the projects under uncertain economic conditions. Moreover, in the presence of an upper thief-zone (like the conglomerate zone in the Cardium formation), although the well design parameters may have a negligible effect on the economic viability of the primary-waterflood scenario, they would have a significant effect on the success of the subsequent CO₂ flood scenario. For this reason, in the exclusive investigation of the CO₂ injection projects, which is discussed next, configuration (1) is not used.

As mentioned previously, when the source of CO₂ supply for EOR projects is through capture from anthropogenic sources like power plants, the final cost of deliverable CO₂ would be high. Therefore, incentives would be required to make these projects attractive and even feasible. In this section, we assume that the reservoir has already gone through the primary and secondary recovery schemes and no capital expenditure is required for drilling and initial facility development. However, as the proposed time-frame for commercial implementation of CO₂ projects is on order of 10

years and beyond, fluctuation in cost components (especially for the commodity prices) could be significant over this long time interval. Therefore, a more conservative assessment of these projects would be necessary to guarantee success. Table 7-10 summarizes the price and cost elements used in evaluation of CO₂ injection projects alone. It should be mentioned that, when the escalation factor (factor B) is applied to oil price, the assumed maximum and minimum oil prices are \$60 and \$120, respectively. Gas and NGL prices and associated changes have been incorporated in the economic model as well.

Table 7-10: Uncertain economic factors for economic evaluation of the CO₂ flood projects

Factor	Unit	L1	L2	L3	L4
A: Oil price	\$/bbl	65	75	85	95
B: Oil price escalation factor	fraction/year	-0.01	0	0.01	
C: Gas price	\$/Mcf	1.5	2.5	3.5	
D: CO ₂ Inj. Cost	\$/Mscf	1.5	2.5	3.5	4.5
E: Water Inj. Cost	\$/bbl	0.75	1.5	2.25	
F: Oil lift cost	\$/bbl cost	10	15	20	
G: Gas processing cost	\$/Mcf	0.25	0.5	0.75	
H: Water prod. Cost	\$/bbl	0.5	1	1.5	
I: CO ₂ recycling cost	\$/Mcf	0.3	0.6	0.9	
J: Avg. unit operation cost	M\$/HWell	40	60	80	
K: Applied CO ₂ royalty	fraction	0.05	0.075	0.1	
L: Flood performance factor (FPF)	Dimensionless	0.7	0.9	1.1	1.3
M: Discount rate	fraction	0.05	0.08	0.116	0.15

As before, design of experiment (with 210 runs), method of response surface, and Monte-Carlo simulation were used to evaluate the risk of failure and hence the need to apply incentives for continuous and WAG injection into tight formations. Figure 7-12 depicts the tornado plot for parameters affecting the economics of CO₂ injection into such reservoirs. According to this plot, CO₂ injection cost and oil price are the most important economic driving factors. The final results for the economic evaluation of the injection with respect to different design conditions are presented in Table 7-11; note that three

different incentive schemes are included in the analysis.

Table 7-11: Results of economic evaluation of CO₂-EOR projects using different incentive schemes

Model Design				Incentive: Not Provided					Incentive: Royalty-Credit					Incentive: Storage-Credit				
				A	B	C	D	β	A	B	C	D	β	A	B	C	D	β
Without Thief-zone	LHF	7 W	CO ₂	35.7	20.4	-60.9	-35.0	79.9	39.7	22.8	-58.8	-33.8	66.6	60.8	34.9	-27.6	-15.8	24.8
			WAG	46.4	17.5	-49.0	-18.5	56.8	50.5	19.1	-43.4	-16.4	39.5	77.6	29.3	-9.9	-3.7	3.8
		5 W	CO ₂	23.7	15.0	-49.8	-31.4	86.3	26.7	16.8	-48.3	-30.5	75.4	52.8	33.4	-11.8	-7.5	14.5
			WAG	21.5	9.5	-24.8	-10.9	78.5	24.0	10.5	-23.1	-10.1	61.3	47.1	20.7	-4.2	-1.9	6.1
	THF	7 W	CO ₂	34.2	22.1	-61.4	-39.6	90.7	37.6	24.2	-58.7	-37.9	82.2	52.6	33.9	-37.0	-23.8	40.1
			WAG	41.4	17.7	-56.7	-24.3	93.6	45.1	19.3	-51.1	-21.9	83.3	67.8	29.0	-22.1	-9.5	5.3
		5 W	CO ₂	25.1	17.8	-52.4	-37.2	95.7	27.6	19.6	-50.4	-35.8	90.8	46.2	32.8	-24.3	-17.2	22.7
			WAG	22.4	12.0	-32.6	-17.4	95.9	24.2	12.9	-29.6	-15.8	89.7	45.0	24.1	-4.7	-2.5	1.2
With Thief-zone (2)	LHF	7 W	CO ₂	22.3	19.0	-76.5	-65.1	98.3	25.7	21.9	-73.8	-62.8	95.4	32.9	28.0	-62.4	-53.1	84.9
			WAG	39.2	19.3	-71.3	-35.0	95.6	42.6	20.9	-65.5	-32.2	88.7	58.2	28.6	-46.0	-22.6	48.5
		5 W	CO ₂	20.8	17.0	-67.6	-55.2	98.7	23.3	19.0	-64.6	-52.8	96.3	38.3	31.3	-44.3	-36.2	65.1
			WAG	31.6	15.1	-53.0	-25.4	96.3	34.4	16.5	-48.6	-23.2	89.4	56.9	27.2	-19.4	-9.3	3.7
	THF	7 W	CO ₂	25.9	21.1	-72.5	-58.9	96.3	29.5	24.0	-69.7	-56.7	92.2	37.1	30.2	-57.5	-46.8	77.7
			WAG	40.1	19.3	-70.9	-34.1	95.3	43.7	21.0	-65.1	-31.3	88.8	60.4	29.0	-44.1	-21.2	45.1
		5 W	CO ₂	24.1	18.6	-66.9	-51.5	97.8	26.7	20.6	-63.7	-49.1	94.3	42.0	32.4	-43.0	-33.1	58.9
			WAG	32.9	15.2	-53.8	-25.0	96.1	35.7	16.6	-49.3	-22.9	89.8	58.0	26.9	-20.4	-9.4	4.6

A: Maximum NPV (MM\$)

B: Maximum profit (\$/boe)

β: Probability of failure (NPV<0 @ 95% C.I.)

C: Minimum NPV (MM\$)

D: Minimum profit (\$/boe)

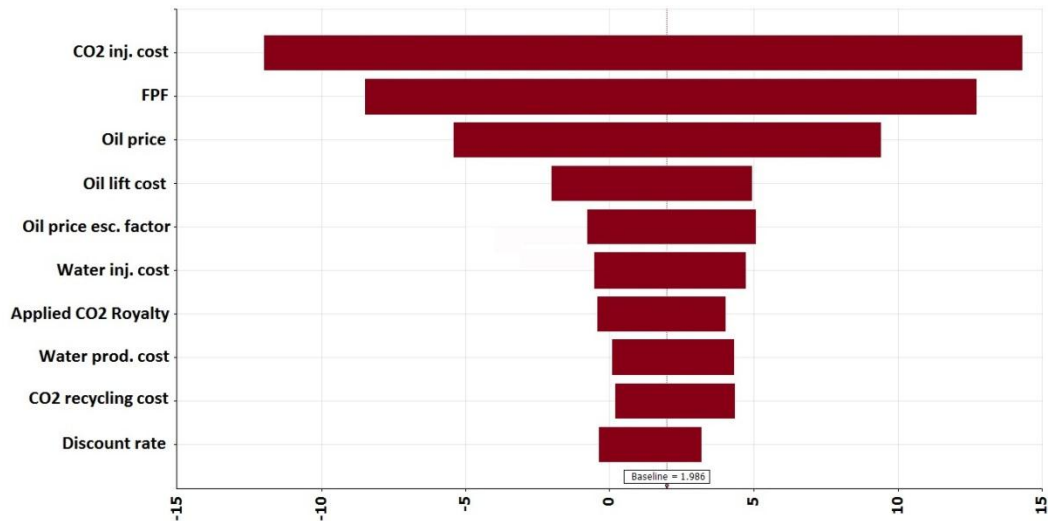


Figure 7-12: Tornado graph of important economic factors affecting NPV for CO₂ injection projects.

For the first scheme, no incentive is applied. Based on the calculated results, in this case, the chance of success under any conditions is very limited and it is even less for the continuous injection scheme. In the second and third schemes, and in order to encourage CO₂ storage, incentives in two different forms are provided. For royalty credit, the amount of royalty payout is decreased based on the amount of storage occurring and decreases from an initial value of 0.05 to 0. For storage credit, direct credit in the amount of \$10 per tonne of stored CO₂ is provided.

Based on the results presented in Table 7-11, royalty-credit has a minor effect on the viability of the projects. Results depicted in Figure 7-12 also suggest that the applied royalty value during CO₂ injection has a weak effect on the profitability of the projects. Thus, even using the minimum royalty from day one of CO₂ injection would not result in any significant change in the likelihood of success or failure of the projects.

On the other hand, considering the results for geo-model without a thief-zone (see Table 7-1), it can be observed that with 10\$ storage credit, substantial improvement in the profitability of the projects occur. For this reservoir condition, credit in the range of \$10

to \$11 would be enough to make all WAG projects economic at 95% confidence level. The required storage credit for continuous CO₂ injection, however, lies in the range of \$13 to \$15. The lower limit of each of the intervals is associated with larger well spacing and the upper limit is associated with smaller well spacing. As this in turn is associated with a reservoir containing a thief zone located at upper portion of the structure, the previous credit interval limits should be approximately multiplied by a factor of 1.5. The exception, however, is WAG injection through the 5 wells/section configuration, which is still economic at a storage credit of \$10.

In brief, direct carbon storage must be provided to CCS projects in tight oil formations and the reservoir conditions and well design have a significant effect on the amount of credit required. Denser well spacing, especially in the presence of a high permeability contrast, is not recommended for miscible CO₂ floods as it will dramatically increase the cost of handling produced volumes of costly injected fluids. Moreover, without performing technical and economical optimization, these projects can easily ended in failure.

7-8- Summary

In this work, we have provided a rigorous workflow for the industry to evaluate EOR and CO₂ storage in tight oil reservoirs, as well as a perspective for the governing bodies on how to transform their policies and incentives when market conditions change. Full-cycle economics are provided for various enhanced recovery schemes in a tight oil formation, which take into account both uncertainties in reservoir and cost structure. A novel approach, which includes compositional simulation, combined with design of experiment, method of response surface, and Monte-Carlo simulation was used to evaluate

profitability and the risk of failure for multiple recovery mechanism sequences, as well as the need for incentives to make continuous and WAG CO₂ injection profitable in tight formations.

The following specific conclusions resulted from the study:

- The primary-waterflood scenarios have a high chance of success and this chance is higher in the absence of a thief-zone or when the fracture arrangement is modified in the presence of a thief zone
- When CO₂ injection is implemented along with primary-waterflood as a single project, it is seen that the probability of failure increases.
- In the presence of an upper thief-zone (like the conglomerate zone in the Cardium formation), although the well design parameters may have a negligible effect on the economic viability of the primary-waterflood scenario, they would have a significant effect on the success of the subsequent CO₂ flood scenario.
- Royalty-credit incentive has a minor effect on the viability of standalone CO₂ injection projects (evaluated independently of preceding recovery schemes).
- The fixed storage credit incentive appears to have a greater effect on value for certain scenarios.

Acknowledgement

This research was made possible by funding provided by ISEEE-NRCan (project title “Co-optimization of CO₂ Sequestration and Oil Recovery in Tight Oil Formations”). The authors appreciate the constructive comments and help provided by Andrew Seto from Penn West Exploration. Chris Clarkson would like to acknowledge Encana and AITF for support of his Chair position in Unconventional Gas and Light Oil research at the

University of Calgary, Department of Geoscience. He would also like to acknowledge the sponsors of Tight Oil Consortium (TOC), hosted at the University of Calgary.

References

- Arnold, K., Stewart, M., 1998. Surface Production Operations, Volume 1: Design of Oil-Handling Systems and Facilities. Gulf Publishing Company.
- Bachu, S., 2003. Screening and Ranking of Sedimentary Basins for Sequestration of CO₂ in Geological Media in Response to Climate Change. *Environmental Geology*, vol. 44, no. 3, pp. 277-289.
- Bachu, S., Shaw, J., 2003. Evaluation of the CO₂ Sequestration Capacity in Alberta's Oil and Gas Reservoirs at Depletion and the Effect of Underlying Aquifers. *Journal of Canadian Petroleum Technology*, vol. 42, no. 9, pp. 51-61.
- Bachu, S., 2008. Legal and Regulatory Challenges in the Implementation of CO₂ Geological Storage: An Alberta and Canadian Perspective. *International Journal of Greenhouse Gas Control*, vol. 2, no. 2, pp. 259-273.
- Bastian, P.A., Wirth, O.F.R., Wang, L., Voneiff, G.W, 2005. Assessment and Development of the Dry Horseshoe Canyon CBM Play in Canada. Paper SPE 96899 presented at SPE annual technical conference and exhibition in Dallas, Texas, 9-12 October.
- Davison, J., Freund, P., Smith A., 2001. Putting Carbon Back into the Ground. IEA Greenhouse Gas R&D Programme.
- Dykstra, H., Parsons, R.L., 1950. The Prediction of Oil Recovery by Waterflooding in Secondary Recovery of Oil in the United States. Second edition, API publication.

- Economides, M.J., Oligney, R.E., Valkó, P., 2002. Unified Fracture Design: Bridging the Gap between Theory and Practice. Alvin, Texas, Orsa Press.
- Environment Canada, 2012. Canada's Emission Trends 2012.
- Essandoh-Yeddu, J., Gürcan, G., 2009. Economic Modeling of Carbon Dioxide Integrated Pipeline Network for Enhanced Oil Recovery and Geologic Sequestration in the Texas Gulf Coast Region. In proceedings of the ninth international conference on greenhouse gas control technologies, Washington DC, USA, pp. 1603-1610.
- Finkenrath, M., 2011. Cost and Performance of Carbon Dioxide Capture from Power Generation. no. 2011/5, International Energy Agency publication.
- Garmeh, G., Johns, R., 2009. Upscaling of Miscible Floods in Heterogeneous Reservoirs Considering Reservoir Mixing. Paper SPE 124000 presented at SPE Annual technical conference and exhibition in New Orleans, Louisiana, USA, 4-7 October.
- Gaspar, A.T., Suslick, S., Ferreira, D., Lima, G., 2005. Economic Evaluation of Oil-Production Project with EOR: CO₂ Sequestration in Depleted Oil Field. Paper SPE 94922 presented at SPE Latin American and Caribbean petroleum engineering conference in Rio de Janeiro, Brazil, 20-23 June.
- Ghomian, Y., Urun M., Pope, G., Sepehrnoori, K., 2008. Investigation of Economic Incentives for CO₂ Sequestration. Paper SPE 116717 presented at SPE annual technical conference and exhibition in Denver, Colorado, USA, 21-24 September.
- Ghaderi, S., Clarkson, C.R., Kaviani, D., 2012. Evaluation of Recovery

Performance of Miscible Displacement and WAG Processes in Tight Oil Formations. Paper SPE 152084 presented at SPE/EAGE European unconventional resources conference and exhibition in Vienna, Austria, 20-22 March.

- Ghaderi, S., Clarkson, C.R., Chen, Y., 2012. Optimization of WAG Process for Coupled CO₂ EOR-Storage in Tight Oil Formations: An Experimental Design Approach, Paper SPE 161884 presented at SPE Canadian unconventional resources conference in Calgary, Alberta, Canada, 30 October-1 November 2012.
- Goretzky, Q., Hawkins, B., 2009. CO₂ Enhanced Hydrocarbon Recovery: Incremental Recovery and Associated CO₂ Storage Potential in Alberta. Summary report prepared for the Alberta Energy Research Institute (AERI).
- Heddle, G., Herzog, H., Klett, M., 2003. The Economics of CO₂ Storage. Report No. MIT LFEE 2003-003, Laboratory for Energy and the Environment, Massachusetts Institute of Technology, 2003.
- Herzog, J.H., 2000. The Economics of CO₂ Separation and Capture. Technology-Elmsford-Journal of the Franklin Institute Then Journal of Science Serving Legislative Regulatory and Judicial Systems, Vol. 7, pp. 13-24.
- Herring, D., 2012. Climate Watch Magazine >> Global Temperature Projections. NOAA Climate Portal.
- Jensen, J.L., 2000. Statistics for Petroleum Engineers and Geoscientists. Elsevier.
- Jahangiri, H.R., Zhang D., 2011. Optimization of the Net Present Value of Carbon Dioxide Sequestration and Enhanced Oil Recovery. Paper OTC 21985 presented at offshore technology conference in Houston, Texas, USA, 2-5 May.

- Jeremy, D., Herzog, H., 2000. The Cost of Carbon Capture. In proceedings of the fifth international conference on greenhouse gas control technologies, Cairns, Australia, pp. 985-990.
- Karsten, M., Bachu, S., Buschkuehle, B.E., 2007. Assessment of a Carbonate Aquifer for CO₂ Geological Storage in the Wabamun Lake Area. CSPG CSEG convention, May 14-17.
- Kerr, W., 1980. A Geological Explanation for the Variation in Fluid Properties across the Pembina Cardium Field. Journal of Canadian Petroleum Technology, vol. 19, no. 2, pp. 76-84.
- Mace, M.J., Hendriks, C., Coenraads, R., 2007. Regulatory Challenges to the Implementation of Carbon Capture and Geological Storage within the European Union under EU and International Law. International Journal of Greenhouse Gas Control, vol. 1, no. 2, pp. 253-260.
- McCoy, S.T., Rubin, E.S., 2009. The Effect of High Oil Prices on EOR Project Economics. Energy Procedia, vol. 1, no. 1, pp 4143-4150.
- National Energy Technology Laboratory (NETL), 2010. Quality Guidelines for Energy Systems Studies: Estimating CO₂ Transport, Storage & Monitoring Costs. Tarka T.J., and Wimer, J.G., DOE/NETL-2010/1447.
- Nguyen, D.N., Allinson, W.G., 2002. The Economics of CO₂ Capture and Geological Storage. Paper SPE 77810 presented at SPE Asia Pacific oil and gas conference and exhibition in Melbourne, Australia, 8-10 October 2002.
- Olea, R.A., 2009. A Practical Primer on Geostatistics. US Geological Survey, Open- File Report 2009-1103.

- Palisade Corporation, 2013. @Risk (version 6) Reference Manual.
- Rao, A.B., Rubin, E.S., 2002. A Technical, Economic, and Environmental Assessment of Amine-based CO₂ capture Technology for Power Plant Greenhouse Gas Control. *Environmental Science & Technology*, vol. 36, no. 20, pp. 4467-4475.
- Remy, N., Boucher, A., Wu, J., 2009. *Applied Geostatistics with SGeMS: A User's Guide*. Cambridge University Press.
- Rochelle, G., Jassim, M., Beitler, C., Rueter, C., Searcy, K., 2005. Integrating MEA Regeneration with CO₂ Compression and Peaking to Reduce CO₂ Capture Costs. U.S. Department of Energy, Report No. DE-FG02-04ER84111.
- Rubin, E.S., Mantripragada, H., Marks, A., Versteeg, P., Kitchin, J., 2012. The Outlook for Improved Carbon Capture Technology. *Journal of Progress in Energy and Combustion Science*, vol. 38, no. 5, pp. 630-671.
- Singhal, A., 2009. CO₂ Flooding Potential in West-Central Alberta: Generalized Business Case of a Medicine River/Gilby Area Mature Waterflooded Reservoir. *Journal of Canadian Petroleum Technology*, vol. 48, no. 12, pp. 6-10.
- Stat-Ease, Inc. 2010. *Design-Expert (version 8.0.6) Reference Manual*.

Chapter 8

Summary, Conclusions and Future Work

Three available options for permanent CO₂ storage in Alberta include unmineable coal seams, saline aquifers, and hydrocarbon reservoirs. Because, in the case of the Horseshoe Canyon coals, where most CBM well penetrations occur, coal-seams are located at shallower depths and are relatively thin in thickness, they might not be an optimal storage target. Therefore, the focus of this study was on numerical simulation of CO₂ injection in the two remaining options, namely saline aquifers and tight oil reservoirs. The following conclusions and important observations can be drawn from this study:

8-1- CO₂ Injection into Aquifers

For aquifer storage, through compositional simulation it was indicated that CO₂ injection into a sour aquifer will cause the exsolution of initially dissolved H₂S in brine into the advancing gas plume. The volume swept by the plume is compositionally divided into two sub-regions. For pure CO₂ injection, the first sub-region is characterized by the absence of H₂S in both aqueous and gaseous phases. This sub-region occupies the interior cylindrical region centered at the injection point. On the other hand, in the outer cylindrical sub-region surrounding the first sub-region, the H₂S mole fraction gradually

increases toward the leading edge of the advancing gas front. The size of the evolved sub-region increases over time. The effect of different reservoir/flow conditions, and important fluid characteristics on the size of evolved sub-regions and maximum concentration of exsolved H₂S was examined. The results of this study are important in establishing monitoring strategies at CO₂ storage sites, and in evaluating the risks associated with the possible leakage of evolved H₂S during CO₂ and acid gas injection into sour saline aquifers.

In the next step towards studying CO₂ storage in the saline aquifers, the feasibility of injecting large volumes of CO₂ to fill up the enormous apparent storage capacity of the Nisku formation, was investigated. The target value of injection was 20 Mt/year, which continues for 50 years (storage target of 1000 Mt CO₂). It was shown that the capacity for injection is limited not by available pore space but by ability to inject without exceeding the fracture pressure of the formation. The capacity increases with the number of injectors, but increasing the number of wells has a limit, even considering a large well spacing. Very strong interference between pressure plumes occurs, which increases the average reservoir pressure substantially and rapidly and in turn reduces injectivity of the injectors. The saturation plumes remains discrete with no interference; n individual plumes of radius 4-5 km for each injector. The pressure field behavior is completely different from the saturation field. There are no individual pressure plumes but rather a single large (scale of hundreds of km) pressure disturbance. Results of simulations with either simplified homogenous or rigorous heterogeneous models indicate that, through vertical injectors, the maximum achievable storage volume is not in excess of 300 Mt over 50 years. Although, application of horizontal injectors and well fracturing

technology might be helpful in this regard, their benefit is not substantial. Sensitivity of capacity to reservoir permeability, rock compressibility and well placement was investigated and the minimum required properties to fulfill the target value were estimated.

8-2- CO₂ Injection into Low Permeability Hydrocarbon Reservoirs

For reservoir storage of CO₂, the performance of CO₂ injection into tight formations, and more specifically in the tighter portion of Pembina Cardium field in Alberta, was investigated. Due to poorer properties of these reservoirs, application of multi-stage fractured horizontal wells with denser well spacing is required. This configuration maximizes the contact area with the formation and considerably enhances the productivity/injectivity of the wells. For EOR schemes in these reservoirs, CO₂ injection, either through injection of pure CO₂ or WAG was considered. The results indicate that (for a fixed well pattern and hydraulic fractures properties) the achievable recovery from injection scenarios is quite influenced by the reservoir heterogeneity and also the mobility of the injected fluids. For continuous CO₂ injection, high mobility of the gas causes rapid breakthrough at the producers. As such, once the connection between the injector and producer fractures is established, the average reservoir pressure falls rapidly below the MMP and CO₂ becomes immiscible, losing the benefit of miscible flooding. WAG injection, on the other hand, can substantially improve the recovery by maintaining the pressure around the MMP and therefore develops an efficient miscible process. For WAG processes, however, different related properties such as WAG ratio, cycle length, and slug size should be designed carefully.

The compositional simulation study was then extended to evaluate and quantify the

effect of different design parameters and operational constraints on the performance of the CO₂-EOR process. Eight factors were considered as important, including well parameters (well spacing and completion method), hydraulic fracture properties (fracture spacing and fracture half-length), timing of the switch between recovery schemes, and WAG parameters (CO₂ slug size and WAG ratio). The matrix of runs for the sensitivity study was built based on a sophisticated experimental design approach. Statistical analysis of the results was carried out to find the most important parameters affecting oil recovery factor (objective 1) and CO₂ storage (objective 2). The results suggest that WAG and fracture parameters have a profound effect on both objective functions, with WAG ratio being the dominant factor. It is also seen that increasing the number of fractures and expanding the fracture half-length will unfavorably reduce the sweep efficiency of WAG injection and accelerates the short-circuiting of the injected gas at producers. This in turn reduces the oil recovery factor, incremental oil recovery factor, and CO₂ storage. This indirectly implies that applying longitudinal fractures might be a better option for gas injection into tight formation with close well spacing. Nevertheless, the reservoir heterogeneity still plays an important role in dictating the preferential path of fluids flow and requires a separate study. Due to differences in switching time between alternative recovery schemes, the effect of time was taken into account by using NPV (objective 3) for each scenario. It was found that the important parameters affecting NPV are completion method (which affects the capital cost) and fracture parameters and switching time, with completion method being the dominant factor.

Response surfaces were generated to quantify the effect of different uncertain parameters on the objective functions. Thereafter, an optimization process was pursued to

search for those combinations of factors which lead to maximum response. Results from this study show that the CO₂-EOR potential in tight oil formations can be considerable if the design parameters and operating conditions are chosen properly. In this regard, the parametric compositional models are very efficient proxies, and design of experiment methods are powerful tools in identifying and optimizing these factors.

The effect of reservoir heterogeneity and fracture design (with respect to orientation angle) on the performance of different recovery schemes in tight oil formations was also investigated. In order to introduce permeability heterogeneity in the simulation models, reservoir geo-models were built with different Dykstra-Parsons coefficients, dimensionless correlation lengths in both horizontal and vertical directions, preferential heterogeneity direction, and vertical to horizontal permeability ratio. Fracture design was limited to two extreme scenarios; longitudinal (0°) and transverse fractures (90°). It was shown that the Dykstra-Parson coefficient and fracture direction design are the most important factors, ranking first and second, respectively, for impact on WAG recovery factor, and amount of stored CO₂ at the end of WAG scheme. In addition, both of these factors have a negative effect on the defined objectives, meaning higher heterogeneity and higher orientation angles are detrimental to recovery factor and storage capacity.

In this study, a rigorous workflow was provided for industry to evaluate EOR and CO₂ storage projects in tight oil reservoirs subject to the Alberta oil and gas fiscal system. Full-cycle economics are provided for various enhanced recovery schemes in a tight oil formation, which take into account both uncertainties in reservoir and cost structure. A novel approach, which includes compositional simulation, combined with design of experiment, method of response surface, and Monte-Carlo simulation was used to

evaluate profitability and the risk of failure for multiple recovery mechanism sequences as well as the need for incentives to make continuous and WAG CO₂ injection profitable in tight formations. It was shown that in the presence of an upper thief-zone (like the conglomerate zone in the Cardium formation), although the well design parameters may have a negligible effect on the economic viability of the primary-waterflood scenario, they have a significant effect on the success of the subsequent CO₂ flood scenario. If CO₂ is intended to be supplied by capture from an anthropogenic source (the most likely case in Alberta) then the final cost of CO₂ injection and storage could be very high; provision of a direct credit incentive by government is therefore vital to make these project attractive and practical.

8-3- Recommendations and Future Work

The following summarizes limitations of the current study and lists recommendations for future research

- The dissolved impurity in the saline aquifer was limited to H₂S while other components may exist in the aquifer. The effect of other impurities such as CH₄, N₂, and SO₂, either as in-situ components or as constituents of the injection stream (each individually or in different combinations), can be studied in a similar manner.
- Engineering design should seek to make large volume injection practical in the Nisku Formation. One way of mitigating high pressure in the injection site is by keeping voidage replacement ratio (VRR) close to one through brine production. Numerical simulation results along with economic analysis can be used to find the optimal VRR value.

- Because of the short history of production/injection in tight oil formations, the models may need to be revisited in the future for better tuning. Specifically, the relative permeability data obtained from lab measurement should be validated against (long enough) historical field production/injection data.
- Due to the lack of data for the Pembina Cardium, the effect of relative permeability hysteresis was neglected in the simulation models. Such a measurement will be extremely useful for reliable estimation of the recovery and storage capacity of CO₂-EOR processes in tight oil formations.
- The effect of impurities in the injected CO₂ stream (which exist in the recycled CO₂) on the performance of the CO₂ injection projects was not considered and worth attention in future studies.

Appendix A: Copyright Permissions

Chapter 2

Supplier	Elsevier Limited The Boulevard,Langford Lane Kidlington,Oxford,OX5 1GB,UK
Registered Company Number	1982084
Customer name	Seyyed M Ghaderi
Customer address	University of Calgary Calgary, AB T2N 1N4
License number	3244281080765
License date	Oct 08, 2013
Licensed content publisher	Elsevier
Licensed content publication	International Journal of Greenhouse Gas Control
Licensed content title	Evolution of hydrogen sulfide in sour saline aquifers during carbon dioxide sequestration
Licensed content author	Seyyed M. Ghaderi,David W. Keith,Rob Lavoie,Yuri Leonenko
Licensed content date	March 2011
Licensed content volume number	5
Licensed content issue number	2
Number of pages	9
Start Page	347
End Page	355
Type of Use	reuse in a thesis/dissertation
Intended publisher of new work	other
Portion	full article
Format	both print and electronic
Are you the author of this Elsevier article?	Yes
Will you be translating?	No
Order reference number	
Title of your thesis/dissertation	Simulation Study of CO2 Injection and Storage in Alberta
Expected completion date	Oct 2013
Estimated size (number of pages)	270
Elsevier VAT number	GB 494 6272 12
Permissions price	0.00 USD
VAT/Local Sales Tax	0.0 USD / 0.0 GBP
Total	0.00 USD

Chapter 4

Copyright © 2013 IFP Energies nouvelles

Permission to make digital or hard copies of part or all of this work for personal or classroom use is granted without fee provided that copies are not made or distributed for profit or commercial advantage and that copies bear this notice and the full citation on the first page. Copyrights for components of this work owned by others than IFP Energies nouvelles must be honored. Abstracting with credit is permitted. To copy otherwise, to republish, to post on servers, or to redistribute to lists, requires prior specific permission and/or a fee: Request permission from Information Mission, IFP Energies nouvelles, fax. +33 1 47 52 70 96, or revueogst@ifpen.fr.

Chapter 5

License Number	3244271369503
License date	Oct 08, 2013
Licensed content publisher	Society of Petroleum Engineers
Licensed content publication	SPE Proceedings
Licensed content title	Evaluation of Recovery Performance of Miscible Displacement and WAG Process in Tight Oil Formations
Licensed content author	S.M. Ghaderi, SPE, and C.R. Clarkson, SPE, University of Calgary; S. Chen, SPE, PennWest Exploration; and D. Kaviani, SPE, University of Calgary
Licensed content date	2012
Type of Use	Thesis/Dissertation
Requestor type	author of the original work
SPE member	yes
SPE member number	3305901
Format	print and electronic
Portion	full article
Will you be translating?	no
Distribution	1
Order reference number	
Title of your thesis / dissertation	Simulation Study of CO2 Injection and Storage in Alberta
Expected completion date	Oct 2013
Estimated size (number of pages)	270
Total	0.00 USD
Terms and Conditions	

Chapter 6

License Number	3244280530069
License date	Oct 08, 2013
Licensed content publisher	Society of Petroleum Engineers
Licensed content publication	SPE Proceedings
Licensed content title	Optimization of WAG Process for Coupled CO2 EOR-Storage in Tight Oil Formations: An Experimental Design Approach
Licensed content author	S.M. Ghaderi, University of Calgary, Penn West Exploration, SPE; C.R. Clarkson, University of Calgary, SPE; S. Chen, Penn West Exploration, SPE
Licensed content date	2012
Type of Use	Thesis/Dissertation
Requestor type	author of the original work
SPE member	yes
SPE member number	3305901
Format	print and electronic
Portion	full article
Will you be translating?	no
Distribution	1
Order reference number	
Title of your thesis / dissertation	Simulation Study of CO2 Injection and Storage in Alberta
Expected completion date	Oct 2013
Estimated size (number of pages)	270
Total	0.00 USD
Terms and Conditions	

Chapter 7

License Number	3244280629578
License date	Oct 08, 2013
Licensed content publisher	Society of Petroleum Engineers
Licensed content publication	SPE Proceedings
Licensed content title	Investigation of Economic Uncertainties of CO2 EOR and Sequestration in Tight Oil Formations
Licensed content author	S.M. Ghaderi, C.R. Clarkson, University of Calgary; . Taheri, University of Calgary; S. Chen, Penn West Exploration
Licensed content date	2013
Type of Use	Thesis/Dissertation
Requestor type	author of the original work
SPE member	yes
SPE member number	3305901
Format	print and electronic
Portion	full article
Will you be translating?	no
Distribution	1
Order reference number	
Title of your thesis / dissertation	Simulation Study of CO2 Injection and Storage in Alberta
Expected completion date	Oct 2013
Estimated size (number of pages)	270
Total	0.00 USD
Terms and Conditions	